Title
Space-based constraints on NOx lifetime using high-resolution NO2 retrievals

Author
Laughner, Joshua L

Publication Date
2018

Peer reviewed|Thesis/dissertation

Space-based constraints on NO_x lifetime using high-resolution NO_2 retrievals

by

Joshua Lee Laughner

A dissertation submitted in partial satisfaction of the

requirements for the degree of

Doctor of Philosophy

in

Chemistry

in the

Graduate Division

of the

University of California, Berkeley

Committee in charge:

Professor Ronald C. Cohen, Chair
Professor Richard Saykally
Professor Inez Fung

Summer 2018

Space-based constraints on NO_x lifetime using high-resolution NO_2 retrievals

Joshua Lee Laughner

Abstract

Space-based constraints on NO_x lifetime using high-resolution NO_2 retrievals

by

Joshua Lee Laughner

Doctor of Philosophy in Chemistry

University of California, Berkeley

Professor Ronald C. Cohen, Chair

Satellite observations of NO_2 provide information about the spatial and temporal variability of NO_2 column densities that can be used to infer the processes controlling NO_2 concentrations. However, satellite observations require a priori information to properly transform the observed radiances into vertical column densities. Previous work has shown that using a priori data at equal or better spatial resolution to the satellite pixels significantly improves the retrieved NO_2. Of particular importance are the a priori vertical profiles that represent the vertical distribution of NO_2 within each satellite pixel.

In this dissertation, I show that the temporal resolution of the a priori NO_2 profiles, as well as the spatial resolution, is important to accurately retrieve NO_2. I show that using profiles with high spatial resolution, but coarse temporal resolution, overestimates the rate at which NO_2 is lost in the outflow from an urban source, and that high spatial and temporal resolution of these profiles is necessary to simultaneously retrieve the NO_2 column density and lifetime in an urban plume. To account for this, I design and validate an upgrade to the Berkeley High Resolution (BEHR) NO_2 retrieval that incorporates daily, high resolution profiles for over 7 years. With this retrieval, I show direct observations of the relationship between NO_x concentration and lifetime by examining the weekend-weekday changes in column density and lifetime from several US cities between 2005 and 2014. Specifically, I show that Chicago, IL and Dallas, TX are undergoing a transition from NO_x-suppressed to NO_x-limited chemistry, which may indicate that future reductions in NO_x emissions will be more effective at controlling O_3 production, but have less direct effect on NO_x concentrations.

To my parents, Jim and Lynn Laughner, and grandparents, Doris and Bob Bogert and Hazel and Clarence Laughner. I love you all.

Contents

List of Figures

List of Tables

Acknowledgments

First, I want to thank my adviser, Ron Cohen, for all his support and advice over the past five years. I've always appreciated your ability to give me the freedom to explore my own ideas, but always offer helpful insights, not to mention pull me back from the many rabbit holes I wandered into and help me see the big picture.

I also want to thank the other members of my dissertation and qualifying exam committees (Kristie Boering, Rich Saykally, Luciano Moretto, and Inez Fung) for their service and support.

Thank you to Cohen group alumni, Ben Nault for your mentorship in my first two and a half years and Ashley Russell for starting this project and answering my (many) questions as I was starting. To my friends and fellow grad students, thank you for your friendship and camaraderie from that first semester with quantum and stat mech to today, and for reminding me that there is life outside of lab. To my lab mates, for being an awesome group of people to spend the last five years with, and for having quite a penchant for bringing in delicious food. I can't think of a better group to go through this experience with. To my long time friends, Stephen and Nathan Boone for your continued friendship over the many years since we first met.

Finally, to my family and especially my parents, Jim and Lynn, who have always supported me in uncountably many ways.

The work in this dissertation was made possible by support from the NASA ESS Fellowship NNX14AK89H, NASA grants NNX15AE37G and NNX14AH04G, and the TEMPO project grant SV3-83019.

This work relied heavily on data freely available from NASA: the v3.0 NASA Aura OMI NO_2 standard product and OMI/Aura Ground Pixel Corners product were obtained from the Goddard Earth Science Data and Information Services Center (GES DISC) in Greenbelt, MD, USA. The MODIS Aqua Clouds 5-Min L2 Swath 1 and 5 km (MYD06_L2 Platnick et al., 2015) and MODIS Terra+Aqua BRDF/Albedo Parameters 1–3 Band3 and QA BRDF Quality Daily L3 Global 30ArcSec CMG V006 (MCD43D07, MCD43D08, MCD43D09, MCD43D31) were acquired from the Level-1 and Atmospheric Archive and Distribution System (LAADS) Distributed Active Archive Center (DAAC) located in the Goddard Space Flight Center in Greenbelt, MD (`https://ladsweb.nascom.nasa.gov/`). Additionally, Chapter 5 used Earth Network's Total Lightning Network data, provided to us freely by Earth Networks.

I would like to acknowledge high-performance computing support from Cheyenne (doi:10.5065/D6RX99HX) provided by NCAR's Computational and Information Systems

Laboratory, sponsored by the National Science Foundation. This research also used the Savio computational cluster resource provided by the Berkeley Research Computing program at the University of California, Berkeley (supported by the UC Berkeley Chancellor, Vice Chancellor for Research, and Chief Information Officer). I acknowledge use of the WRF-Chem preprocessor tools MOZBC, fire_emiss, etc. provided by the Atmospheric Chemistry Observations and Modeling (ACOM) laboratory of NCAR.

I would also like to thank Mary Barth for assistance with the lightning NO_x module in WRF-Chem (Chapter 3), as well as Eric Bucsela and Jim Gleason for very helpful discussions about the new formulation of the visible-only AMF in Chapter 4.

Chapter 1

Introduction

1.1 History and motivation of space based NO_2 observations

The challenge of measuring and understanding the atmosphere is one of scale. Processes operating at scales ranging from molecular to global must be known in order to understand the causes of changes to the earth-atmosphere system in the past and predict how it will change in the future. To do so requires measurements that can span that range of scales. Remote sensing of atmospheric trace gases from space is an important tool that can be used to observed the atmosphere locally to globally. *Remote sensing* describes a measurement made by interpreting electromagnetic radiation (or another signal[1]) that has interacted with the analyte, which is at some distance from the instrument. Specifically, in this context, satellite instruments orbiting at ∼700 km to ∼40 000 km observed reflected sunlight, emitted Earthshine (IR, microwave), or backscattered laser light to probe the concentration of trace gases in the atmosphere.

Many (though not all) satellite remote sensing instruments use some form of imaging spectroscopy to study the atmosphere. This means that the observations are integrated over some finite area of the Earth as pixels that can vary in size from just a few square kilometers (e.g. $<3\,km^2$, OCO-2, Crisp et al., 2017) to thousands of square kilometers (e.g. $\sim 13\,000\,km^2$, GOME, Burrows et al., 1999). Under cloudless conditions, this design allows these instruments to provide a gapless (or nearly so) map of trace gas concentrations over a region, which yields information about the spatial distribution of concentrations in a way that complements the detail at one location provided by in situ point measurements.

[1] The Gravity Recovery and Climate Experiment (GRACE) mission is one example of a satellite instrument that does not observe EM radiation; instead, it is designed to detect small variations in the Earth's gravitational field (Tapley et al., 2004).

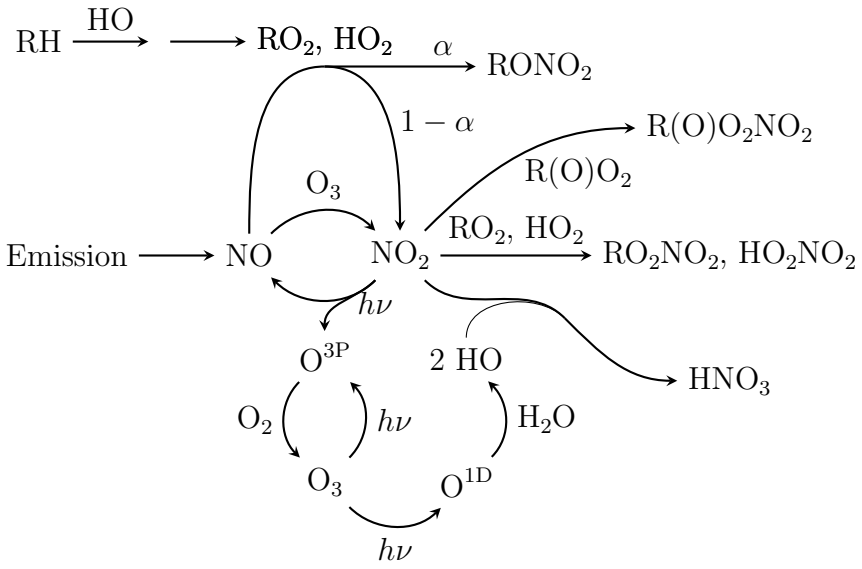

Figure 1.1: Schematic of the NO_x cycle and its interaction with the HO_x cycle.

Remote sensing of NO_2, specifically, plays a crucial role in understanding air quality. Haagen-Smit (1952) identified that the coincident emission of NO_x ($\equiv$ NO + NO_2) and volatile organic compounds (VOCs) led to the photochemical production of O_3 (Fig. 1.1), which in turn was responsible for the various ill effects arising from the Los Angeles photochemical smog. O_3 production occurs when NO is oxidized to NO_2 by an organic peroxide (RO_2, HO_2), which then photolyzes leading to a net production of O_3. NO_x lifetime is controlled by the production of HNO_3 and the formation of alkyl nitrates ($RONO_2$, Day, 2003).

Routine in situ monitoring of NO_x was established in the US with the Clean Air Act (US Environmental Protection Agency, 1970). Satellite observations have allowed us to expand this to understand the impact of NO_x on a regional scale. This is crucial for several reasons. First, due to its nonlinear chemistry, photochemical O_3 production can occur more rapidly downwind of a strong NO_x source (e.g. Apel et al., 2010), so understanding where and how NO_x is transported is a key part of evaluating its air quality impacts. Second, with recent reductions in NO_x emissions in the US and Europe (e.g. Kim et al., 2006; Russell et al., 2012; Curier et al., 2014; Lu et al., 2015; Krotkov et al., 2016; Miyazaki et al., 2017), non-anthropogenic sources of NO_x have risen in importance. Several of these are either difficult (e.g. lightning) or dangerous (e.g. biomass burning) to measure directly, so remote sensing provides a valuable means to constrain these sources. Third, with knowledge of wind fields, observations of NO_2 spatial distributions provide information about the temporal evolution of an NO_2 plume, which allows us to infer the dominant chemical kinetics in that plume (e.g. Valin et al., 2013).

The first observations of NO_2 from space were made by the Global Ozone Monitoring Exper-

iment (GOME) instrument onboard the ERS-2 satellite, launched in April of 1995 (Burrows et al., 1999; Richter and Wagner, 2011; Burrows and Noel, 2011). This instrument marked the beginning of now over two decades of observations of NO_2 from space. This was followed by the Scanning Imaging Absorption spectroMeter for Atmospheric CHartographY (SCIAMACHY) on board Envisat (launched in 2002, Noel et al., 1998), the Ozone Monitoring Instrument (OMI) onboard the Aura satellite (launched in 2004, Levelt et al., 2006), GOME-2 instruments on the MetOp-A and -B satellites (launched in 2006 and 2013, respectively, Munro et al., 2016), the Ozone Mapping and Profiler Suite (OMPS) Nadir Mapper (NM) onboard the Suomi-NPP satellite (launched in 2011, Yang et al., 2014), and most recently the Tropospheric Monitoring Instrument (TROPOMI) on board the Sentinel-5 Precusor satellite (launched 2017, Veefkind et al., 2012).

1.2 Applications of satellite NO_2 data

Given the utility of global coverage available from satellite instruments, such observations have been used in a wide range of applications to constrain and understand NO_x trends and transport, anthropogenic and natural NO_x emissions, and NO_x and HO_x chemistry across the over two decades years since the launch of GOME in 1995.

NO_x trends

Direct observations of trends in NO_2 columns (and, by inference, NO_x concentrations) is the most straightforward application of satellite NO_2 data. Such observations provide powerful evidence for or against the effectiveness of NO_x emissions controls. The effects are very clear, as shown in Fig. 1.2; the dramatic reduction in vertical column densities (VCDs) especially in the northeast US is a direct results of NO_x emissions controls. Numerous studies have evaluated NO_2 trends, particularly on regional scales. Here we will discuss a representative sample of these works with a focus on those using OMI.

Russell et al. (2012) analyzed US NO_2 emissions across several sectors between 2005 and 2011 using the BEHR v2 retrieval. They found that the largest decrease occurred from vehicles, the second largest from power plants, and the third largest from non-mobile urban sources. They and Lu et al. (2015) also identified larger decreases during the US economic recession (2007–2009) than before or after, thus demonstrating the capability of satellite observations to resolve the cause of changes in NO_x trends. Similarly, Duncan et al. (2013) found a trend of decreasing OMI NO_2 VCDs across the US that was similar but larger than EPA AQS ground site measurements.

Lamsal et al. (2015) investigated the challenging problem of connecting tropospheric NO_2 column measurements to surface NO_2 concentrations. Fully inverting the observed VCD to a surface concentration is difficult because it requires very accurate knowledge of the vertical distribution of NO_2; however, Lamsal et al. (2015) showed that a retrieval similar to the

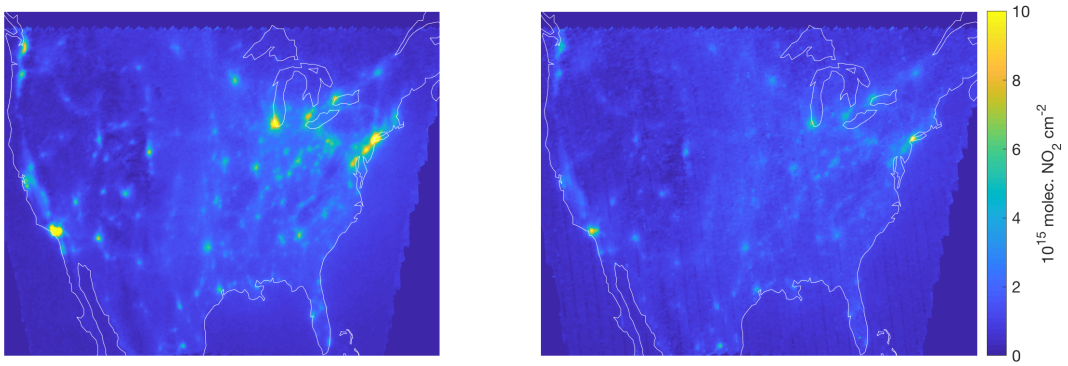

(a) (b)

Figure 1.2: NO_2 VCDs from the BEHR v3.0B product averaged over Apr-Sept 2005 **(a)** and 2016 **(b)**.

NASA SPv3 (1.25° × 1.0° a priori profiles with year-specific emissions) yielded trends in VCDs within 5 percentage points of the trends in surface concentrations when grouped by region or sector (except mobile sources). This affirms the utility of satellite observations to infer changes in surface concentrations of NO_2 that are most relevant for air quality.

Extended to the rest of the globe, Krotkov et al. (2016) analyzed OMI NO_2 trends in multiple regions across the world, finding unique trends in the US, Europe, China, India, and the Middle East. Likewise, Duncan et al. (2016) observed decreasing NO_2 over the US (except over several oil and gas production areas) and Europe, increasing NO_2 in Asia, and mixed trends in the Middle East. ul-Haq et al. (2015) studied trends over southeast Asia, finding increases of 40–77% between 2004 and 2015 for several major cities. van der A et al. (2006) used GOME and SCIAMACHY observations of the NO_2 trend in China between 1996 and 2005 and identified both an interannual increase in Shanghai and opposite seasonal trends between the eastern and western parts of the country. van der A et al. (2008) extended the analysis to the rest of the world and found reductions in NO_2 in the US and Europe and increases in the Middle and Far East.

Inter-continental transport

Long-range transport of O_3 has been examined as a driver for high O_3 events, especially in the Western US (e.g. Lin et al., 2014b; Verstraeten et al., 2015, and references therein). Intercontinental transport of NO_2 has received less attention as it is unusual for NO_x to have long enough lifetime for such transport to be important (e.g. Nault et al., 2016), but some studies have examined it. Wenig et al. (2003) studied NO_x transport from South Africa to Australia using GOME and concluded that an important fraction of Australia's NO_x burden

could be attributed to transport from South Africa; however, the percent contribution of lightning NO_x emission was highly uncertain. More recently, Lee et al. (2014) investigated transport between China, the Korean Peninsula, and Japan, and concluded that export of Chinese NO_x emissions could reconcile the decreasing Korean NO_x emissions in bottom-up inventories with increasing concentrations.

Anthropogenic emissions

Approaches to constrain anthropogenic emissions with satellite observations generally fall into two categories: mass balance or model constraint. The former uses observations of NO_2 plume amount and loss rate to calculate the necessary emissions to explain the equilibrium plume. The latter compares VCDs simulated in a model with prescribed emissions to observed VCDs. The model emissions are then modified, either *ad hoc* or by a formal assimilation process, until reasonable agreement between the modeled and observed VCDs is obtained.

The former method is best exemplified by the approach described by Beirle et al. (2011) and subsequent updates by Lu et al. (2015), Liu et al. (2016), and Liu et al. (2017). This method collects NO_2 VCDs transported out of a source under similar winds, either by dividing the data into groups based on the wind direction or rotating it so that the wind directions are aligned day-to-day. The resulting wind-aligned VCDs are then integrated perpendicular to the wind direction to yield a 1-dimensional line density, which can be fit to derive emissions based on the magnitude and downwind decay rate.

Beirle et al. (2011) applied this method to 9 large NO_x sources (8 cities, 1 power plant) and found reasonable agreement between their satellite-derived emissions and the EDGAR (Emissions Database for Global Atmospheric Research) inventory. Liu et al. (2016) expanded this to a larger number of locations (53 cities, 17 power plants) in the US and China. They compared against several bottom-up emissions inventories and found generally good agreement (better with power plants than cities), although they found that the EDGAR inventory underestimates the lowest emitters in China.

Lu et al. (2015) investigated US NO_x emissions between 2005 and 2014 and found overall good agreement between the emissions trends from this method and the US EPA NEI (National Emissions Inventory), although the absolute magnitude of the NEI emissions was greater than their top down estimates. Liu et al. (2017) likewise studied emissions trends in China, finding that bottom-up inventories generally captured the shape (increase to 2012 and decrease thereafter) but underestimated the peak magnitude.

As an example of *ad hoc* model constraints, Kim et al. (2006) studied reductions in power plant emissions in the US Ohio River Valley by comparing OMI NO_2 VCDs to VCDs simulated by WRF-Chem with two sets of power plant emissions: one kept at 1999-level and

one updated to reflected emissions decreases between 1999 and the time of this study. They found that using the updated emissions yielded much better correlation between the modeled and observed VCDs. From this, they also predicted lower O_3 across the northeastern US. Curier et al. (2014) carried out a similar study in Europe.

More formal assimilation methods also exist. Martin (2003) used a mass-balance approach, that related the NO_x emissions to NO_2 columns observed from GOME and the NO_x lifetime in GEOS-Chem, then calculated posterior emissions by weighting the bottom-up and top-down emissions by their respective errors. Chun and Yuhang (2009) used OMI NO_2 observations with a chemical transport model in an assimilation system where each day's NO_x emissions were scaled by the ratio of the previous day's simulated and observed NO_2 columns. Miyazaki et al. (2012b) used an ensemble Kalman filter approach (Hunt et al., 2007; Kalnay, 2010) to assimilate OMI observations in 2005 and 2006, and Miyazaki et al. (2017) used a similar approach to assimilate multiple species from several satellites to infer trends in emissions between 2005 and 2014. The advantage of such approaches is that they offer a formal, mathematical method by which OMI or other satellite observations can be incorporated into model simulations to adjust the assumed emissions.

Lightning NO_x production

Satellite observations provide a particularly powerful means to constrain lightning NO_x emissions. As lightning occurs principally in the upper troposphere, dedicated aircraft campaigns are needed to measure the NO_x in the outflow from convective events in situ. Such measurements cannot easily be carried out continuously, as they require significant planning and logistical support. However, satellite observations by their nature can provide daily observations of lightning produced NO_2.

Generally, there are two approaches. The first directly observes NO_2 downwind of a convective event and calculates a production rate per lightning flash by dividing the NO_2 concentration measured by observed flashes from a ground or satellite detector (e.g. Beirle et al., 2010a; Bucsela et al., 2010; Pickering et al., 2016). The second uses satellite observations to constrain a chemical transport model. Lightning NO_x production rates are varied in the model until good agreement with the satellite observations are obtained (e.g. Martin et al., 2007; Miyazaki et al., 2014).

These two approaches result in very different estimates of the production of lightning NO_x per lightning flash (Table 1.1. The first method (direct observation) generally yields results $\leq$100 mol flash^{-1} while the second (model constraint) gives values of $\sim$500 mol flash^{-1} in the midlatitudes ($\sim$250 mol flash^{-1} in the tropics).

Nault et al. (2017) proposed that the key difference between these approaches is that chemical loss is usually ignored in the direct observation methods, because it was assumed that NO_x

Method	Paper	Production rate (mol NO_x $flash^{-1}$)	Region
Direct obs.	Beirle et al. (2010a)	~ 30	Global
	Bucsela et al. (2010)	100–250	Costa Rica
	Pickering et al. (2016)	80 ± 45	Gulf of Mexico
Model constraint	Martin et al. (2007)	500 (midlatitudes); 125 (tropics)	Global
	Martini et al. (2011)	480	Cont. US
	Miyazaki et al. (2014)	310 (average)	Global
	Nault et al. (2017)	665 (midlatitudes); 330 (tropics)	Multiple

Table 1.1: Lightning NO_x production rates derived by key works using satellite observations

lifetime in the upper troposphere is on the order of days. However, recent work showed that the lifetime can be ~ 3 h when peroxy radicals derived from surface VOC emissions are present in the outflow (Nault et al., 2016).

Satellite observations are also starting to provide evidence that the existing assumption of two global production rates (one for midlatitudes, one for tropics) is too simple. Beirle et al. (2010a) noted that individual storms have very different production rates (0 mol $flash^{-1}$ to 250 mol $flash^{-1}$), and those over the US generally have higher rates. Nault et al. (2017) found that the difference in GEOS-Chem vs. OMI NO_2 VCDs varies among four regions (South America, southeast Asia, and north and south Africa). Satellite observations will likely play a key role in future efforts to understand the region-to-region variability around the world.

NO_x emitted by soil bacteria

Another important source of NO_x in rural areas is bacteria in soils. These bacteria can oxidize and reduce NH_4^+ and NO_3^-, respectively, producing NO as a byproduct (Zörner et al., 2016, and references therein). The emission of NO is controlled by multiple factors, including soil temperature and moisture, and fertilizer application (Yienger and Levy, 1995; Hudman et al., 2012). The interplay among these factors is complex; temperature and soil moisture play a role in determining persistent emissions, but large pulses of NO occur with application of fertilizer or rewetting after an extended dry spell. Since these parameters can vary significantly on reasonably small spatial scales, satellites provide an ideal platform to constrain that variability.

A number of studies have used satellite observations to constrain or apportion soil NO_x emissions, either globally or regionally (e.g. Jaeglé et al., 2004; Jaeglé et al., 2005; Wang et al., 2007; van der A et al., 2008; Zörner et al., 2016). The area nature of the soil NO_x source makes satellite observations a powerful tool for this, since they can capture spatial

variations that a sparse in situ network may miss. Satellite observations have also been highly instrumental in improving the parameterization of soil NO_x in models. Yienger and Levy (1995) created the first parameterization to account for precipitation- and fertilizer- induced pulsing, with fairly sparse observational data. As global satellite NO_2 measurements became widely available, numerous papers used those satellite observations to identify a significant underestimate in soil NO_x emissions in models using the Yienger-Levy parameterization (e.g. Boersma et al., 2008; Zhao and Wang, 2009; Lin, 2012). Efforts to improve the Yienger-Levy parameterization also made significant use of satellite observations. Bertram et al. (2005) used SCIAMACHY observations to show that the Yienger-Levy parameterization could be readily improved by incorporating local, high resolution information on precipitation and fertilizer application. Hudman et al. (2012) used OMI observations to validate a new soil NO_x parameterization that was a continuous function of soil moisture, rather than categorizing soil as wet or dry, as was done in the Yienger-Levy parameterization.

Biomass burning

Biomass burning is a significant tropospheric NO_x source ($\sim$6 Tg N yr^{-1}, Ciais et al., 2013). Individual biomass burning events can have NO_x emissions equal to major urban areas. Figure 1.3 shows OMI BEHR NO_2 columns over Los Angeles, CA and the King Fire, a moderately large forest fire that occured in September 2014. Although Los Angeles is a slightly larger source area, the King Fire has core NO_2 VCDs equal to or greater than those in central Los Angeles. Constraining these emissions is crucial to understanding their contribution to the tropospheric reactive nitrogen budget, but direct measurement is particularly challenging; it is simply too dangerous to carry out an on-the-ground in situ measurement.

Satellite observations can be an important tool for constraining biomass burning NO_x emissions, both because remote sensing is a much safer method of measuring the NO_2 released by a biomass burning event, and because their global reach allows them to capture the biomass burning events despite their episodic nature.

Studies aiming to derive a predictive relationship between the power of the fire and NO_x emissions have taken two approaches. The first relates the amount of NO_x emitted to fuel burned:

$$M_{NO_x} = A_{\text{burned}} \cdot F \cdot C \cdot EF_x \tag{1.1}$$

where M_{NO_x} is the mass of NO_x emitted, A_{burned} is the area burned, F is the fuel density per unit area, C is the fraction of fuel that burns ("combustion completeness") and EF_{NO_x} is the emission factor for NO_x, i.e. the mass of NO_x emitted per mass of fuel burned (Seiler and Crutzen, 1980; Wiedinmyer et al., 2006; Mebust et al., 2011). The goal is to estimate EF_{NO_x}

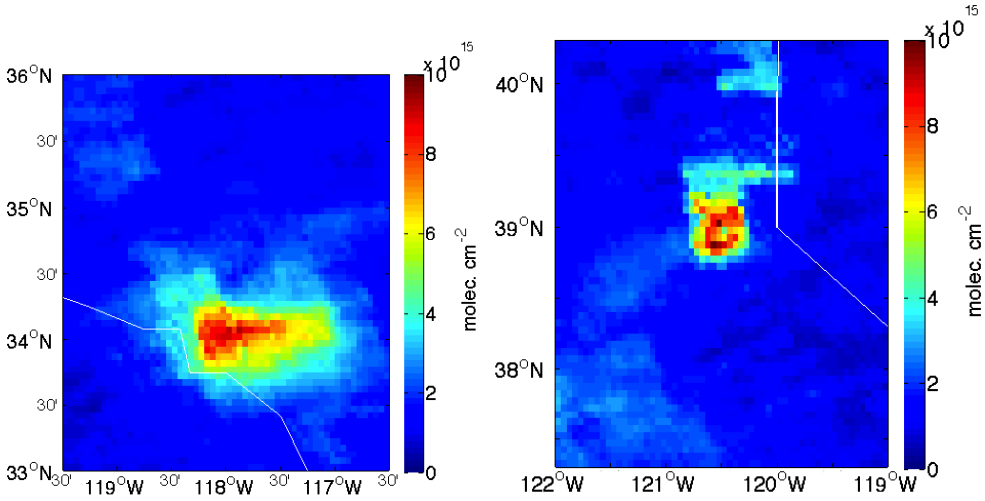

(a) (b)

Figure 1.3: BEHR NO_2 columns over Los Angeles, CA, USA **(a)** and the King Fire in eastern CA **(b)** during Sept. 2014.

using satellite observations to derive M_{NO_x}, but A_{burned}, F, and C can all have significant uncertainties themselves, and are highly variable (Mebust et al., 2011).

A second way connects the NO_x emissions to the observed radiative power of the fire:

$$M_{NO_x} = K \cdot EF_{NO_x} \cdot E_R \tag{1.2}$$

$$= EC_{NO_x} \cdot E_R \tag{1.3}$$

where E_R is the total radiative power of the fire and K is a coefficient that relates E_R and EF_{NO_x}. The product of K and EF_{NO_x} is usually termed the "emission coefficient" (EC_{NO_x}) to distinguish it from the fuel-based emission factor (Wooster, 2002; Wooster et al., 2005; Freeborn et al., 2008; Mebust et al., 2011).

While many studies use satellite observations of burned area to infer biomass burning emissions in combination with existing emission factors, other studies have taken advantage of satellite NO_2 observations to constrain either total fire NO_x emissions or emissions factors or emissions coefficients. Jaeglé et al. (2005), Miyazaki et al. (2012b), and Miyazaki et al. (2017) use satellite NO_2 columns to constrain model simulations in order to derive total global biomass burning NO_x emissions. Mebust et al. (2011) and Mebust and Cohen (2014) examined the spatial variation of emission coefficients in California and globally, respectively, using fire radiative power derived from MODIS, and found that emissions coefficients fall in a narrow range. Mebust and Cohen (2013) identified a seasonal cycle in emission coefficients

for woody savannas in Africa. Castellanos et al. (2014) found significant spatial and temporal variability in emissions factors in South America, and identified errors in the assumed emissions factors.

Despite these successes, retrievals of biomass burning events can still be improved. The episodic injection of significant amounts of NO_x into a normally clean area drastically perturbs the NO_2 profile, adding much more NO_2 near the surface compared to a typical rural profile. This perturbation is usually not well captured in the a priori profiles (Sect. 1.3), which would underestimate the actual VCDs. Mebust et al. (2011) notes this as a possible cause for deriving EC's at the low end of the established range. Second, biomass burning events emit large amounts of aerosol, significantly changing the radiative properties of the atmosphere. Investigation of this effect on retrievals by Leitão et al. (2010), Bousserez (2014), and Castellanos et al. (2015) found that accounting for the aerosols can introduce changes of up to 100% in the retrieved NO_2. Clearly, further development on a retrieval optimized to study biomass burning events would be very valuable.

NO_x/HO_x chemistry

Satellite observations of NO_2 can also be used to derive information about chemical processes in the atmosphere. This is usually done by examining the rate of change in NO_2 columns downwind of a NO_x source, using distance from the source and wind speed to calculate the plume age. Beirle et al. (2011) first introduced this method, dividing OMI NO_2 observations into eight bins based on wind direction, with subsequent refinements by Valin et al. (2013) and Liu et al. (2016).

With this method, Beirle et al. (2011) observed a factor of 2 difference in summer and winter lifetimes. Liu et al. (2016) also observed seasonal trends in the US and China; they further identified spatial patterns in the NO_x lifetime, finding it to be generally longer in highly polluted regions. Lu et al. (2015) found that US summertime NO_x lifetimes observed from OMI are slightly shorter than expected, and argue that this is because these lifetimes are a combination of chemical and dispersion lifetimes (de Foy et al., 2014; de Foy et al., 2015). Valin et al. (2013) used observations under different wind speeds around Riyadh, Saudi Arabia to infer changes in OH concentration due to feedbacks from NO_x concentration driven by dilution at faster wind speeds.

These studies take advantage of the higher spatial resolution available with OMI compared to prior NO_2 satellite instruments to resolve urban scale gradients of NO_2 in order to derive these lifetimes. The capability to probe both chemical and meteorological effects on NO_x lifetime opens the window to observing how changes in emissions drive not only changes in concentration, but in chemical processes in the atmosphere as well.

1.3 Principles of space based NO_2 observations

The challenge in interpreting remote sensing data is that factors other than the quantity of the trace gas of interest affect the observed radiance, especially atmospheric scattering and surface reflectivity. These factors need to be accounted for in the retrieval process. For NO_2, the goal of the retrieval is to calculate separate tropospheric and stratospheric VCDs.

The retrieval process

NO_2 is measured from space using the differential optical absorption spectroscopy (DOAS) technique, first developed for long path measurements within the atmosphere by Platt and Perner (1980). In space-based DOAS spectroscopy, absorption is measured as the ratio of intensity of reflected Earthshine to direct sunlight at the wavelengths of interest (I and I_0, Fig. 1.4). Absorbance due to certain broadband processes in the atmosphere, such as Rayleigh scattering, have a smooth dependence on wavelength. This is fit with a polynomial function of wavelength to provide a baseline against which narrower absorbances, such as those due to NO_2, are measured against. Fitting these absorption spectra yields a column density (molecules per area) as DOAS measurements in the UV/visible range have insufficient degrees of freedom to resolve vertical gradients in concentration. Since the spectra of various absorbing species in the atmosphere frequently overlap (e.g. NO_2, O_3, water vapor, and the Ring Effect all have absorption lines in the 400–460 nm range), the column densities of multiple species are fit simultaneously to account for overlapping absorption.

The resulting quantity is called a slant column density (SCD, Fig. 1.4) and is the total amount of a trace gas along all of the light paths through the atmosphere that reach the detector. The direct beam path depends on the position of the observing satellite and the sun relative to the point on the Earth's surface being observed, but is usually not normal to the Earth's surface (Fig. 1.4). Therefore, the SCDs must be corrected for the additional path length through the atmosphere. If a single light path from the sun, to the Earth's surface, and back to the satellite is assumed, this can be represented by a quantity called a geometric air mass factor (AMF_G, Palmer et al., 2001).

$$\mathrm{AMF_G} = \frac{\mathrm{SCD}}{\mathrm{VCD}} = \sec\theta_s + \sec\theta_v \tag{1.4}$$

which is simply the trigonometric ratio of the slant path length to the vertical path length. Dividing the SCD by this AMF_G yields a vertical column density (VCD, Fig. 1.4), which is the vertically integrated quantity of a trace gas between the Earth's surface and the top of the atmosphere.

This form implicitly assumes that sunlight passing through the atmosphere interacts with all vertical levels of the atmosphere equally. This is not true in practice. Rayleigh scattering,

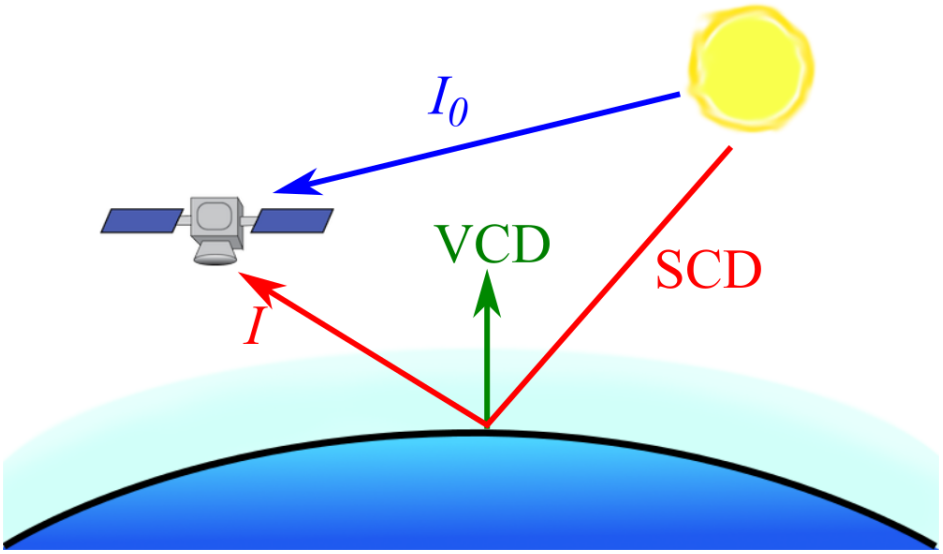

Figure 1.4: A graphic representation of the quantities involved in satellite remote sensing.

Mie scattering from aerosols, and reflection or absorption at surfaces (e.g. the ground or clouds) alter the probability that backscattered sunlight reaching an orbiting instrument has interacted with the trace gas of interest at a given vertical layer of the atmosphere.

Palmer et al. (2001) formulated an air mass factor that accounts for the vertically varying sensitivity:

$$\text{AMF} = \int_0^{z_{\text{top}}} g'(z) w(z)\, dz \tag{1.5}$$

$$g'(z) = \frac{\alpha(z) g(z)}{\int_0^{z_{\text{top}}} \alpha(z) g(z)\, dz} \tag{1.6}$$

$$w(z) = \left. \frac{\partial \ln I_B}{\partial \tau} \right|_z \tag{1.7}$$

where $g(z)$ is the vertical profile of the trace gas measured, $\alpha(z)$ is a vertically resolved factor accounting for pressure and temperature dependent changes in the trace gas absorption cross section, and $(\partial I_B / \partial \tau)_z$ is the dependence of the top-of-atmosphere (TOA) intensity of backscattered radiation on the optical depth of the trace gas at altitude z.

Conceptually, this AMF can be rewritten as:

$$\text{AMF} = \frac{\text{SCD}}{\text{VCD}} = \frac{\int_0^{z_{\text{top}}} g(z)w(z)\,dz}{\int_0^{z_{\text{top}}} g(z)\,dz} \tag{1.8}$$

where the numerator of the right hand side represents a modeled slant column density and the denominator represents a modeled vertical column density. In practice, an AMF is calculated with two models: a chemical transport model (CTM) simulates the trace gas vertical profile, $g(z)$, while a radiative transfer model (RTM) simulates the scattering weights, $w(z)$, that describe how the trace gas concentration at each altitude z affects the TOA backscatter intensity and therefore the retrieved SCD. These models, especially CTMs, can be very computationally intensive. Therefore, when designing a retrieval algorithm to compute the necessary AMFs to retrieve a trace gas, one must balance the resolution and accuracy of these models against the available computational resources. Different groups have taken a multitude of approaches to this balance; a summary of OMI NO_2 retrievals is provided in Appendix A.

Implications of the retrieval process on atmospheric observations

Because satellite observations of NO_2 rely on a priori data to interpret the SCDs, the choice of a priori data can have significant effects on the retrieved VCD. Generally, there are six major sets of a priori data needed in a satellite retrieval:

1. Surface pressure
2. Surface reflectance
3. Cloud fraction
4. Cloud pressure
5. NO_2 profile
6. Aerosol profile

The first four can be obtained from existing databases (surface pressure) or other satellite products (surface reflectance, cloud fraction, cloud pressure). The last two, as fully 3D fields, must be simulated with a chemical transport model if they are to be explicitly included. The NO_2 profiles are always needed; however, in many cases an aerosol profile is not explicitly simulated, instead a single simple profile is assumed for the radiative transfer calculations, and variations in the aerosol profile are assumed to be implictly accounted for in the cloud properties (Boersma et al., 2004; Boersma et al., 2011).

Improving the overall quality of the a priori data, especially its spatial resolution, has been a consistent theme in NO_2 retrievals in the last decade. The resolution of the NO_2 profile is especially important. Valin et al. (2011) showed that coarsening the CTM resolution not only loses information about the fine-scale spatial variability, but also changes the chemical kinetics occuring, and so affects the amount of NO_x simulated downwind of a source. Numerous works have implemented high resolution (1 km to 15 km) NO_2 profiles (Russell et al., 2011; Russell et al., 2012; McLinden et al., 2014; Kuhlmann et al., 2015; Goldberg et al., 2017) and found changes in the NO_2 VCDs of up to $-75\,\%$ to $100\,\%$. Increasing the resolution allows the model to resolve the difference between urban and rural profiles; urban profiles have much more NO_2 near the surface, where a satellite is less sensitive to it, than rural profiles. At coarse resolutions ($\sim$100 km and greater), urban and rural NO_2 profiles are averaged together within a grid cell containing a city, producing a profile that does not accurately represent either situation.

This is not to say other a priori data are not important. Surface reflectance generally has the second largest effect. Russell et al. (2011) and Zhou et al. (2010) found $40\,\%$ to $60\,\%$ changes in NO_2 VCDs when switching from a $0.5^\circ \times 0.5^\circ$ OMI surface reflectance product to a $0.05^\circ \times 0.05^\circ$ MODIS product. Global, high resolution surface reflectance products from the MODIS instruments have now become available, making it straightforward to incorporate into a retrieval. However, in contrast, global high resolution ($\leq$12 km) CTMs are just now becoming barely computationally feasible (e.g. Hu et al., 2018), therefore further exploring the importance of the NO_2 profiles' resolution remains an important step in improving NO_2 retrievals.

1.4 Development of a retrieval with high spatial and temporal a priori data

Clearly, the utilty of satellite instruments such as OMI that provide global measurements of NO_2 and other trace gases has allowed significant advancements in our understanding of episodic emissions and chemical processes. However, we have also learned that the spatial resolution of the a priori inputs is a crucial factor in the accuracy of the retrieval. This leads to the question: how well do current retrievals perform for situations where significant temporal variability of the a priori data is expected as well? In particular, in this dissertation, my goal was to design a retrieval optimized to study temporal correlations between changes in NO_2 VCDs and lifetimes.

I explore the importance of temporal variation in the NO_2 a priori profiles in Chapter 2 by implementing three sets of a priori profiles in the BEHR v2.1C retrieval: one using monthly average profiles at a similar spatial resolution to the NASA Standard Product v3 (108 km i.e. $\sim 1^\circ$), one using monthly average profiles at the 12 km resolution used in BEHR, and one using daily profiles at 12 km resolution. Using Atlanta, GA, USA as a case study, I

show that increasing the temporal resolution from monthly to daily affects the retrieved VCDs on individual days by as much as 40%. Further, I apply the VCDs retrieved to the emissions and lifetime fitting method described by Beirle et al. (2011), Valin et al. (2013), and Lu et al. (2015) where downwind pixels are aligned and averaged together. This enhances the systematic error resulting from using monthly profiles, which blur together profiles resulting from different wind speeds and directions much the same way that using spatially coarse profiles blurs together urban and rural profiles. I show that, to retrieve emissions (or VCDs) and lifetime simultaneously and accurately, daily high-resolution a priori profiles are necessary.

In Chapter 3, I evaluate the accuracy of various lightning parameterizations in the WRF-Chem model that I would use to generate the daily, high-resolution profiles demanded by the results in Chapter 2. Lightning is a strong source of upper tropospheric (UT) NO_x, and since UV-visible satellite remote sensing is very sensitive to the UT, it was generally expected that errors in lightning contributions to the NO_2 a priori profiles could have large impacts on an NO_2 retrieval, but this had not been directly quantified. I showed that omitting lightning NO_2 entirely would bias the AMFs low by $\sim$30 %, and that using either the standard 500 mol flash^{-1} (Hudman et al., 2007) or the more recently recommended 665 mol flash^{-1} (Nault et al., 2017) for midlatitudes gives AMFs with an error $<$5 %. I also show that using four-dimensional data assimilation nudging decreases the number of lightning flashes in WRF by a factor of 2, and that doubling the flash count is necessary to restore the $<$5 % error in AMFs calculated using a priori profiles derived from these WRF-Chem simulations.

In Chapter 4, I describe in detail the new version (v3.0B) of the BErkeley High Resolution (BEHR) OMI NO_2 retrieval, built primarily around using daily, high-resolution a priori profiles, but also including a number of other enhancements, particularly in the treatment of surface reflectivity, surface pressure, and tropopause pressure. I show that implementing updated a priori profiles with more accurate chemistry and emissions is the second largest change to the retrieved VCDs, second only to the new slant column fitting algorithm implemented in version 3 of the NASA Standard Product. I also show that, in regions with strong lightning influence in the a priori profiles, using daily profiles changes a multi-month average of VCDs by $\sim$50 %, due to the statistically skewed frequency of UT NO_2 concentrations in those regions.

Chapter 5 evaluates the new BEHR v3.0B product against in situ aircraft and ground-based total NO_2 column measurements. I show that the daily a priori profiles adequately capture the day-to-day variability in the real profiles by comparing the correlation of monthly average and daily profiles with aircraft measurements of NO_2 profiles and by qualitatively comparing modeled distributions of NO_2 to observed OMI slant column densities. Further, I find that using daily a priori profiles improves agreement between BEHR VCDs and aircraft and ground-based column measurements compared to using monthly average a priori profiles.

Finally, in Chapter 6, I use BEHR v3.0B to investigate how NO_x lifetime has changed in step with decreasing NO_x emissions in the US between 2005 and 2014. By comparing weekday and weekend VCDs and lifetimes, I find that Chicago, IL and Dallas, TX are transitioning or have transitioned from NO_x-suppressed to NO_x-limited chemistry between 2005 and 2014, as weekend lifetimes decrease compared to weekday lifetimes prior to 2010, but the reverse is true after 2010. Using BEHR v3.0B, we can also observe that Portland, OR and San Francisco, CA have been NO_x-limited since before 2005, and Detroit, MI and Philadelphia, PA were still NO_x-suppressed as of 2014. I show that this has important implications for top-down constraints of NO_x emissions. More generally, to my knowledge, this is the first direct observation of the relationship between NO_x concentration and lifetime. Future work can take advantage of this new capability to test our understanding of NO_x chemistry by using such top-down lifetime constraints to test for missing sinks of NO_x in urban outflow.

Chapter 2

Effects of daily meteorology on the interpretation of space-based remote sensing of NO_2

The chapter was adapted from: J. L. Laughner, A. Zare, and R. C. Cohen (2016). "Effects of daily meteorology on the interpretation of space-based remote sensing of NO_2". *Atmos. Chem. Phys.* 16.23, pp. 15247–15264. DOI: 10.5194/acp-16-15247-2016

2.1 Introduction

NO_x (= NO + NO_2) is an atmospheric trace gas family that plays an important role in regulating the production of O_3 and particulate matter. NO_x is emitted into the atmosphere by natural processes (e.g. lightning, biomass burning) and anthropogenic sources, notably combustion. Understanding the contribution of each source is vital to determining the effectiveness of current and future efforts to improve air quality and to understanding the chemistry of the atmosphere. Studies have utilized satellite observations to constrain NO_x emissions from lightning (e.g. Miyazaki et al., 2014; Beirle et al., 2010a; Martin et al., 2007; Schumann and Huntrieser, 2007), biomass burning (e.g. Castellanos et al., 2014; Mebust and Cohen, 2014; Mebust and Cohen, 2013; Miyazaki et al., 2012a; Mebust et al., 2011), anthropogenic NO_x emissions and trends (e.g. Ding et al., 2015; Lamsal et al., 2015; Tong et al., 2015; Huang et al., 2014; Vinken et al., 2014a; Gu et al., 2013; Miyazaki et al., 2012a; Russell et al., 2012; Lin et al., 2010; Kim et al., 2009), soil NO_x emissions, (e.g. Zörner et al., 2016; Vinken et al., 2014b; Hudman et al., 2012), and NO_x lifetime (Liu et al., 2016; Lu et al., 2015; Foy et al., 2014; Valin et al., 2013; Beirle et al., 2011).

The process of retrieving a tropospheric NO_2 column with UV/visible spectroscopy from satellites requires three main steps. First, the raw radiances are fit using Differential Opti-

cal Absorption Spectroscopy (DOAS) to yield slant column densities (Richter and Wagner, 2011). Then, the stratospheric NO_2 signal must be removed (Boersma et al., 2011; Bucsela et al., 2013). Finally, the tropospheric slant column density (SCD) must be converted to a vertical column density (VCD) by use of an air mass factor (AMF) and Eq. (2.1). Depending on the specific algorithm, NO_2 obscured by clouds may be ignored (producing a visible-only tropospheric NO_2 column, e.g. Boersma et al., 2002), corrected by use of an assumed ghost column (e.g. Burrows et al., 1999; Koelemeijer and Stammes, 1999), or corrected via the AMF (e.g. Martin et al., 2002). In all cases, the AMF must account for the varying sensitivity of the satellite to NO_2 at different altitudes, and therefore a priori knowledge of that sensitivity and the vertical profile of NO_2 is required. Over low-reflectivity surfaces, light scattered in the atmosphere is the primary source of radiance at the detector. The probability of back-scattered light penetrating to a given altitude is greater for higher altitudes; thus there is greater interaction with, and therefore greater sensitivity to, NO_2 at higher altitudes (Richter and Wagner, 2011; Hudson et al., 1995). Because of this, the correct AMF is smaller in locations influenced by surface NO_x sources. The relative contribution of errors in the calculated sensitivity and in the a priori profiles of NO_2 to error in the final VCD varies between polluted and clean pixels (Boersma et al., 2004). Previous work (e.g. Russell et al., 2011) has sought to reduce errors in both, and highlighted the importance of accurate a priori profiles in urban areas.

$$\mathrm{VCD} = \frac{\mathrm{SCD}}{\mathrm{AMF}} \tag{2.1}$$

A priori NO_2 profiles are generated using chemical transport models. Previous studies (e.g. Cohan et al., 2006; Wild and Prather, 2006; Valin et al., 2011; Vinken et al., 2014a; Schaap et al., 2015) have demonstrated these modeled NO_2 profiles are strongly dependent on the spatial resolution of the chemical transport model used. The impact of model spatial resolution on satellite retrievals has been evaluated through case studies (Valin et al., 2011; Heckel et al., 2011; Yamaji et al., 2014) and through what could be termed "regional" retrievals (Russell et al., 2011; McLinden et al., 2014; Kuhlmann et al., 2015; Lin et al., 2015) that trade complete global coverage for improved spatial resolution of the input assumptions. These studies recommend model resolution of < 20 km to accurately capture NO_x chemistry on a priori profiles. Russell et al. (2011) showed that increasing the spatial resolution of the input NO_2 profiles produces a retrieval that more accurately represents contrast in the spatial features of NO_2 plumes, reducing systematic bias by as much as 30%. Reducing these biases improves the clarity of the observed urban-rural gradients by providing unique urban and rural profiles, rather than one that averages over both types of locations. McLinden et al. (2014) showed that using 15 km resolution profiles increased the NO_2 signal of the Canadian oil sands by $\sim 100\%$ compared to the DOMINO and NASA SP products, which they state corrects a low bias in the retrieved column amounts.

Currently, only the Hong Kong-OMI retrieval has made use of daily a priori NO_2 profiles at < 20 km spatial resolution (Kuhlmann et al., 2015). Their retrieval covered the Pearl River Delta for the period October 2006 to January 2007. No operational retrieval covering the majority of the OMI data record does so. The current generation Berkeley High Resolution (BEHR) (Russell et al., 2011; Russell et al., 2012) and OMI-EC (McLinden et al., 2014) retrievals simulate monthly average NO_2 profiles at 12 and 15 km, respectively. Conversely, the DOMINOv2 (Boersma et al., 2011), POMINO (Lin et al., 2015), and DOMINO2_GC (Vinken et al., 2014a) retrievals simulate daily profiles at 3° lon × 2° lat (DOMINO) and 0.667° lon × 0.5° lat (POMINO and DOMINO2_GC), respectively, which is insufficient to capture the full spatial variability of NO_2 plumes, but does capture large scale variations in meteorology. Lamsal et al. (2014) quantitatively compared NO_2 average profile shapes measured from the P3-B aircraft for each of six sites in the DISCOVER-AQ Baltimore/DC campaign with the modeled profile shape from the GMI chemical transport model used to compute the NO_2 a priori profiles in the NASA Standard Product v2 retrieval, which uses monthly average NO_2 profiles at $2° \times 2.5°$ spatial resolution. They found up to 30% differences between the measured and modeled profile shape factors (i.e. $S(p)$ in Eq. 2.3) at any single pressure throughout the troposphere. Several sites (Edgewood, Essex, and Beltsville) had less NO_2 than the model throughout the free troposphere, and Edgewood also exhibited an elevated NO_2 layer at 970 hPa not captured in the model.

Lamsal et al. (2014) also noted that there was significant day-to-day variability in the measured profiles that cannot be captured by a monthly average model; however, they do not quantify those differences. These day-to-day differences can be significant in a priori NO_2 profiles. Valin et al. (2013) showed that the concentration of NO_2 downwind of a city increases significantly with wind speed, observing that NO_2 100–200 km downwind from Riyadh, Saudi Arabia was approximately 130–250% greater for wind speeds between 6.4–8.3 m s^{-1} than wind speeds < 1.9 m s^{-1}. When monthly average a priori profiles are used, this is not accounted for in the retrieval. The effect on the AMF is illustrated in Fig. 2.1c. Compared to the monthly average a priori profiles, daily profiles from a day with fast winds would contain greater near-surface NO_2 further from the city. As discussed before Eq. (2.1), UV/visible satellite observations of NO_2 are less sensitive to NO_2 at low altitudes, so this requires smaller AMFs at a greater distance from the city on days with fast winds to compensate through Eq. (2.1).

These day-to-day variations may be particularly important for methods such as Beirle et al. (2011), Valin et al. (2013), Lu et al. (2015), and Liu et al. (2016) that use observations sorted by wind speed to derive detailed information about NO_x chemistry and emissions from space-borne observations. This is a very valuable tool because of the wealth of data available from OMI (Levelt et al., 2006) and expected from upcoming instruments such as TROPOMI (Veefkind et al., 2012), TEMPO (Chance et al., 2013), Sentinel-4 (Ingmann et al., 2012), and GEMS (Bak et al., 2013; Choi and Ho, 2015). However, the act of sorting data by wind speed transforms errors in the profile shape resulting from day-to-day variability in wind

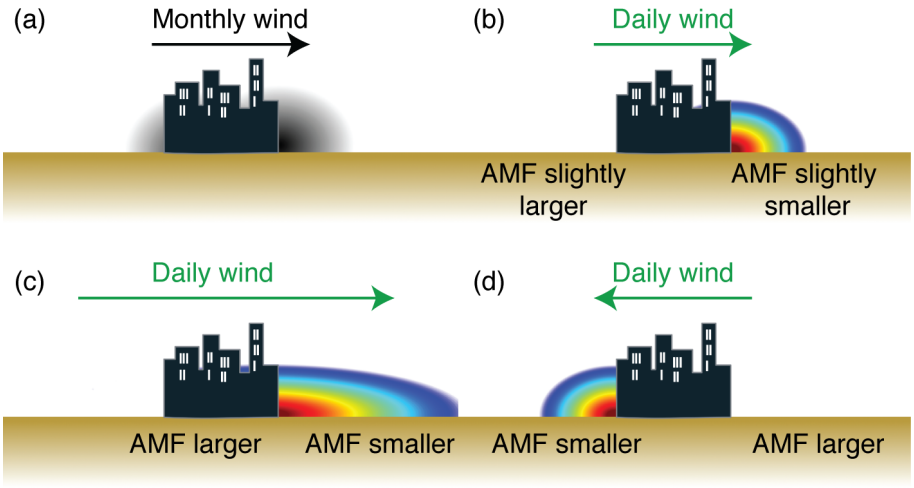

Figure 2.1: An illustration of the central issues that will be discussed in this paper. (a) The monthly average a priori profiles, shown as the grayscale plumes. (b) A case when the daily wind is similar to the monthly average wind. (c) A case where the daily wind is significantly faster than average, but blows in the same direction. (d) A case where the daily wind direction is different than average. The text below each panel describes how the AMF derived from the daily profile would compare with those derived from the monthly a priori.

speed from random to systematic. For example, Beirle et al. (2011), Valin et al. (2013), and Lu et al. (2015) derive an effective NO_x lifetime using data with fast wind speed, and Liu et al. (2016) does so by fitting a function with a component derived at slow wind speeds to data derived from days with fast wind speeds. On a day when the wind speed is faster than average, a priori NO_2 profiles taken from a monthly average model would have less near-surface NO_2 further from the city than is actually present for that day (i.e. Fig. 2.1c vs. 2.1a). The resulting incorrect AMFs would lead to an underestimation of the spatial extent of the plume, and could lead to an underestimate of the NO_x lifetime as a consequence.

In this paper we explore how day-to-day changes in the a priori NO_2 profiles affect satellite retrievals of urban NO_2. Several scenarios are illustrated in Fig. 2.1. In each case the change in the AMF results because, over low albedo surfaces, a UV/visible satellite spectrometer is less sensitive to near surface trace gases, necessitating a smaller AMF to account for the reduced sensitivity. In Fig. 2.1a, the monthly average NO_2 plume is shown as the grayscale gradient, to emphasize that it is static from day to day. Most of the plume follows the prevailing wind direction (here, to the right), but because days with different wind directions are averaged together, there is some influence of the plume upwind of the city. Figure 2.1b shows a case where the daily winds are similar to the monthly average. This leads to a similar NO_2 plume as in the monthly average, but because we are not averaging different wind directions, the upwind plume influence is removed (increasing the AMF, reflecting the reduction in near-surface NO_2) and conversely the downwind AMFs are slightly smaller, due

to a slight increase in near-surface NO_2 from not averaging in days when the wind direction is different. Figure 2.1c shows a case where the daily winds are faster than the average. Here the AMFs within the city need to be larger, as near-surface NO_2 is being removed more efficiently and transported downwind, where the AMFs must therefore be smaller. Finally, Fig. 2.1d has the wind change direction from the monthly average. Left of the city must have smaller AMFs to account for the presence of the plume not seen in the monthly average, and the opposite change occurs to the right.

We combine the high spatial resolution a priori previously developed as part of the BErkeley High Resolution (BEHR) algorithm (Russell et al., 2011) with high temporal resolution to demonstrate the impact of day-to-day variations in the modeled NO_2 profiles on the calculated AMFs surrounding a major urban area such as Atlanta, GA, USA. Atlanta provides an example of a strong NO_x area source relatively isolated from other sources, with straightforward response of the day-to-day a priori profiles to meteorological variables. Our point is not to derive exact answers for the size and frequency of the effects of daily profiles, but rather to illustrate that these effects are large enough that their role should be assessed in any future analysis that does attempt to interpret space-based remote sensing of NO_x. We show that the variability in the a priori profiles is largely due to changes in wind speed and direction. We first consider the effects of day-to-day variations in a priori profile on AMFs for the region surrounding Atlanta for a fixed grid of OMI pixels, simplifying day-to-day comparisons. We then fully implement 91 days of retrieval to examine the effect on both day-to-day and monthly average NO_2 columns. Finally, we apply the exponentially-modified Gaussian (EMG) fitting method of Lu et al. (2015) to the new retrieval and show that the spatial and temporal resolution of the a priori profiles can significantly alter the derived emission rate and lifetime.

2.2 Methods

The Ozone Monitoring Instrument

The Ozone Monitoring Instrument (OMI), onboard the Aura satellite, is a polar-orbiting, nadir-viewing, UV/visible spectrometer with a swath width of 2600 km and a pixel size at nadir of 13×24 km^2. It observes backscattered solar radiation in the range of 270–500 nm with an average spectral resolution of 0.5 nm. (Levelt et al., 2006). It has a continuous data record since 1 Oct 2004, with global daily coverage for the first ~ 3 years of operation. Since 25 June 2007, anomalous radiances have been observed in several of the pixel rows. These have been classified as the "row anomaly" (`http://projects.knmi.nl/omi/research/product/rowanomaly-background.php`). As of 5 July 2011, one-third of OMI pixels are flagged as affected by the row anomaly, indicating that data from these pixels should not be used. Using only the pixels unaffected by the row anomaly, it takes two days to observe the entire globe. There are two publicly available global NO_2 products, the

KNMI DOMINO product (Boersma et al., 2011) and the NASA Standard Product (Bucsela et al., 2013).

BErkeley High Resolution (BEHR) Retrieval

The BEHR retrieval is described in detail in Russell et al. (2011), and updates are described on the BEHR website (`http://behr.cchem.berkeley.edu/Portals/2/Changelog.txt`). The product is openly available for download at `http://behr.cchem.berkeley.edu/`. Briefly, the BEHR retrieval is based on the NASA Standard Product v2 (SP v2) retrieval (Bucsela et al., 2013). The total slant column densities (SCDs) are from OMNO2A v1.2.3 (Boersma et al., 2002; Bucsela et al., 2006; Bucsela et al., 2013), and have been recently evaluated by van Geffen et al. (2015) and Marchenko et al. (2015). The stratospheric subtraction and destriping used is that of the NASA SP v2 retrieval. The tropospheric AMF is then recalculated similarly to the AMF formalism described in Palmer et al. (2001). Clear and cloudy AMFs are calculated as shown in Eq. (2.2). p represents the vertical coordinate as pressure. $w(p)$ represents scattering weights derived from the NASA SP v2 look up table. $g(p)$ represents the mixing ratio NO_2 a priori profile taken from WRF-Chem, simulated at 12 km resolution in the published BEHR product. p_0 represents the surface pressure (clear sky AMF) or cloud pressure (cloudy AMF) of the satellite pixel, and p_{tp} the tropopause pressure. The cloud pressure is that provided in the NASA SP v2 product, and is retrieved using the OMI O_2-O_2 cloud algorithm (Acarreta et al., 2004; Sneep et al., 2008; Bucsela et al., 2013). A static tropopause pressure of 200 hPa is used. p_{surf} in Eq. (2.3) is the terrain surface pressure. The integration is carried out using the scheme described in Ziemke et al. (2001) which allows integration of mixing ratio over pressure.

$$\mathrm{AMF} = \int_{p_0}^{p_{\mathrm{tp}}} w(p) S(p)\, dp \tag{2.2}$$

where

$$S(p) = \frac{1}{\int_{p_{\mathrm{surf}}}^{p_{\mathrm{tp}}} g(p)\, dp} g(p) \tag{2.3}$$

The scattering weights, $w(p)$, depend on the viewing geometry, surface albedo, and terrain pressure altitude. The BEHR algorithm uses the $0.05^\circ \times 0.05^\circ$ combined MODIS MCD43C3 black-sky albedo product and a surface pressure derived from the Global Land One-km Base Elevation project database (`http://www.ngdc.noaa.gov/mgg/topo/globe.html`; Hastings and Dunbar, 1999) with a 7.4 km scale height as inputs to the clear sky scattering weights. Cloudy scattering weights treat the cloud pressure as the surface pressure and use an assumed cloud albedo of 0.8 (Stammes et al., 2008; Bucsela et al., 2013). The final AMF is computed as the cloud radiance fraction (f_{rad}) weighted average of the clear and cloudy AMFs (Eq. 2.4). The cloud radiance fraction is taken from the SP v2 data product (Bucsela et al., 2013).

$$\mathrm{AMF}_{\mathrm{total}} = f_{\mathrm{rad}}\mathrm{AMF}_{\mathrm{cloudy}} + (1 - f_{\mathrm{rad}})\mathrm{AMF}_{\mathrm{clear}} \tag{2.4}$$

WRF-Chem

Modeled NO_2 a priori profiles are simulated using the WRF-Chem model v3.5.1 (Grell et al., 2005). The domain is 81 (east-west) by 73 (north-south) grid cells centered on 84.35° W, 34.15° N on a Lambert Conformal map projection (approximate edges of the domain are 89.5° W to 79.2° W and 30.3° N to 38° N). Meteorological initial and boundary conditions are driven by the North American Regional Reanalysis (NARR) dataset. Anthropogenic emissions are taken from the National Emissions Inventory 2011 (NEI11) and scaled to 88.9% to account for 2011–2013 NO_x reductions (EPA, 2016); total emissions of NO for the domain are approximately 3.1×10^6 kg NO day^{-1}. The MEGAN model (Guenther et al., 2006) is used to determine biogenic emissions. Chemical initial and boundary conditions for the domain are obtained from the MOZART chemical model (Emmons et al., 2010). The RACM2 (Goliff et al., 2013) and MADE-SORGAM schemes are used to simulate gas-phase and aerosol chemistry respectively; the RACM2 scheme is customized to reflect recent advancements in understanding of alkyl nitrate chemistry using Browne et al. (2014) and Schwantes et al. (2015) as a basis. Lightning NO_x emissions were inactive.

The model is run from 27 May to 30 August, 2013. Similar to Browne et al. (2014), the five day period 27–31 May is treated as a spin up period, thus we use 1 June to 30 August as our study time period. Model output is sampled every half hour; the two output files from the same hour (e.g. UTC 1900 and 1930) are averaged to give a single hourly set of profiles. These hourly NO_2 profiles are used as the a priori NO_2 profiles in the BEHR retrieval (Section 2.2). To produce monthly average profiles, each hourly profile is weighted according to Eq. (2.5), where l is the longitude of the profile and h is the hour (in UTC) that WRF calculated the profile for. The weights are clamped to the range $[0, 1]$. These are used as the weights in a temporal average over the month in question. This weighting scheme gives higher weights to profiles closest to the OMI overpass time around 1330 local standard time.

$$\begin{aligned} w_l &= 1 - |13.5 - (l/15) - h| \\ w_l &\in [0, 1] \end{aligned} \tag{2.5}$$

The weighting scheme in Eq. (2.5) was chosen over simply using the model output for 1400 local standard time for each longitude to create smooth transitions between adjoining time zones. This attempts to account for the day-to-day variability in OMI overpass tracks as well as the fact that pixels on the edge of a swath can be observed in two consecutive overpasses at different local times. More detail is given in Appendix B.

A spatial resolution of 12 km is used as the high spatial resolution a priori. To determine the effect of coarser spatial resolution, the model is also run at 108 km resolution. At 12 km resolution, profiles are spatially matched to OMI pixels by averaging all profiles that fall within the pixel bounds. At 108 km resolution, the profile closest to the pixel is used. When using daily profiles, they are temporally matched by identifying those closest to the scan time defined in the Time field of the NASA SP v2 data product.

Implementation of daily profiles

Two retrievals are used to study the effects of incorporating daily a priori profiles in the BEHR algorithm. The first is what we term a "pseudo-retrieval." To create this retrieval, an 11×19 (across $\times$ along track) subset of pixels from OMI orbit 47335 centered on the pixel at 84.2513° W and 33.7720° N is used to provide the pixel corners, solar and viewing zenith and azimuth angles, terrain pressure, and terrain reflectivity. This swath places Atlanta near the nadir view of the OMI instrument (therefore providing pixels with good spatial resolution) while also remaining outside the row anomaly. This same subset of pixels is used for all days in the pseudo-retrieval. Cloud fractions are set to 0 for all pixels to consider clear-sky AMFs and simplify the pseudo-retrieval. AMFs are calculated for this subset of pixels with WRF-Chem NO_2 profiles from 1 June to 30 Aug 2013 in Eq. (2.2). This pseudo-retrieval will allow a simplified discussion of the effects of daily a priori profiles by:

1. Using a fixed set of OMI pixels. Because OMI pixels do not align day-to-day, using each day's true pixels makes a day-to-day comparison more difficult to see. In this pseudo-retrieval, that is alleviated.

2. Using a fixed set of OMI pixels also keeps the scattering weights ($w(p)$ in Eq. 2.2) constant as the parameters that the scattering weights depend on (solar and viewing zenith angles, relative azimuth angles, terrain albedo, and terrain height) are fixed.

3. Setting cloud fractions to 0 ensures that the AMF for every pixel is calculated with the full a priori profile, rather than just the above cloud part. Day-to-day variations in cloud fraction also lead to large changes in AMF because the presence of clouds changes both the scattering weights (due to high assumed reflectivity of clouds and smaller effective surface pressure compared to ground) while also obscuring the NO_2 profile below the cloud.

Essentially, the pseudo-retrieval is a idealized experiment in which we hold all other variables except the a priori profile constant to compute the theoretical magnitude of the effect of using daily a priori profiles on the AMF. It will be used in Sect. 2.3 to demonstrate the effect of incorporating daily a priori profiles. The daily a priori profiles are also implemented in the full BEHR retrieval (no longer using a fixed set of pixels or forcing cloud fractions to 0)

to determine the impact of including daily a priori profiles on the VCDs in a realistic case. When averaging in time, all pixels are oversampled to a $0.05^\circ \times 0.05^\circ$ grid. The contribution of each pixel is weighted by the inverse of its area.

Evaluation of exponentially-modified Gaussian (EMG) fits

Lu et al. (2015) and Valin et al. (2013) used NO_2 data from the DOMINO retrieval to study NO_x emissions and lifetime from space, accounting for the effects of wind speed variation. To evaluate the impact of the a priori resolution on methods such as these, a similar procedure to fit an exponentially modified Gaussian function to NO_2 line densities is used. The surface wind direction and speed are calculated as the average of the first five layers ($\sim$ 500 m) of the 9 WRF 12 km grid cells closest to Atlanta at 1400 local standard time for each day. WRF wind fields are given relative to the model grid; however, the x and y coordinates of the grid do not correspond directly to longitude and latitude. Therefore, the wind fields must be transformed from grid-relative to earth-relative (`http://www2.mmm.ucar.edu/wrf/users/FAQ_files/Miscellaneous.html`) as:

$$U_{\text{earth}} = U_{\text{model}} \times \cos(\alpha) - V_{\text{model}} \times \sin(\alpha) \tag{2.6}$$

$$V_{\text{earth}} = V_{\text{model}} \times \cos(\alpha) + U_{\text{model}} \times \sin(\alpha) \tag{2.7}$$

where U and V are the longitudinal and latitudinal wind fields, and $\cos(\alpha)$ and $\sin(\alpha)$ are outputs from WRF as the variables COSALPHA and SINALPHA.

As in Valin et al. (2013), the satellite pixels are rotated so that wind direction (and therefore NO_2 plumes) for each day lie along the x-axis. Pixels affected by the row anomaly or with a cloud fraction $> 20\%$ are removed. Pixels within 1° upwind and 2° downwind are gridded to $0.05^\circ \times 0.05^\circ$, averaged in time (weighting by the inverse of the pixel area), and integrated across 1° perpendicular to the x-axis. This produces line densities, which are a one-dimensional representation of the NO_2 concentration at various distances downwind of the city. Three a priori sets are used to create the retrievals used in this section: coarse (108 km) monthly average, fine (12 km) monthly average, and fine (12 km) daily profiles.

We use the form of the EMG function described in Lu et al. (2015) to fit the calculated NO_2 line densities, after expanding the definition of the cumulative distribution function:

$$F(x|a, x_0, \mu_x, \sigma_x, B) = \frac{a}{2x_0} \exp\left(\frac{\mu_x}{x_0} + \frac{\sigma_x^2}{2x_0^2} - \frac{x}{x_0}\right) \operatorname{erfc}\left(-\frac{1}{\sqrt{2}}\left[\frac{x-\mu_x}{\sigma_x} - \frac{\sigma_x}{x_0}\right]\right) + B \tag{2.8}$$

where erfc is the error function complement, i.e. $\text{erfc}(x) = 1 - \text{erf}(x)$. $F(x|a, x_0, \mu_x, \sigma_x, B)$ serves as an analytical function that can be fitted to the observed line densities. We find the values of a, x_0, μ_x, σ_x, and B that minimize the sum of squared residuals between $F(x|a, x_0, \mu_x, \sigma_x, B)$ and the line densities, $\text{NO}_2(x)$:

$$Resid(a, x_0, \mu_x, \sigma_x, B) = \sum_x \left(F(x|a, x_0, \mu_x, \sigma_x, B) - \text{NO}_2(x)\right)^2 \tag{2.9}$$

Eq. (2.9) is minimized using an interior-point algorithm, finding the values of a, x_0, μ_x, σ_x, and B that best fit the line densities. The values of a, x_0, μ_x, σ_x, and B have physical significance and so their optimum values yield information about the NO_x emission and chemistry occurring within the plume (Beirle et al., 2011; Foy et al., 2014; Lu et al., 2015). Specifically:

- a describes the total amount of NO_2 in the plume (referred to as the burden)
- x_0 is the distance the plume travels in one lifetime, τ. It relates to τ by $x_0 = \tau \times w$, where w is wind speed.
- u_x describes the effective center of the emission source. In the supplement to Beirle et al. (2011), it is represented by X which is the point at which exponential decay of the NO_2 plume begins.
- σ_x is the standard deviation of the Gaussian component of the EMG function. Lu et al. (2015) terms this a "smoothing length scale," which describes smoothing of the data due to the spatial resolution and overlap of OMI pixels (Boersma et al., 2011). It can also be thought of as capturing effects of both the spatial extent of emissions and the turbulent wind field.
- B is the background line density.

For each parameter, uncertainty from the fitting process itself is computed as the 95% confidence interval calculated using the standard deviation obtained from the fitting process. This is combined in quadrature with 10% uncertainty due to across wind integration distance, 10% uncertainty due to the choice of wind fields, and 25% uncertainty from the VCDs, similar to Beirle et al. (2011) and Lu et al. (2015). Technical details of the EMG fitting and uncertainty calculation are given in Appendix B.

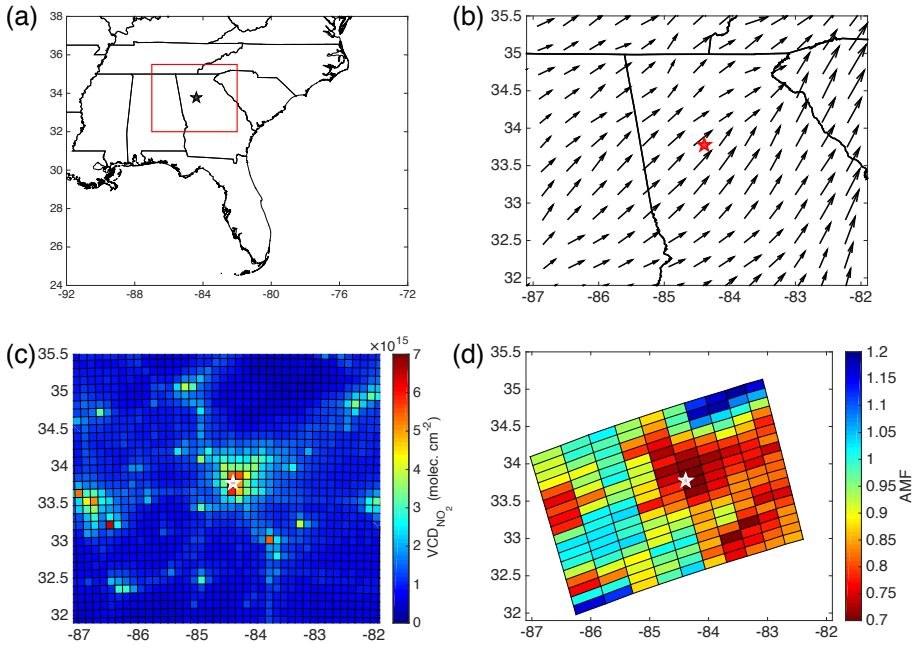

Figure 2.2: Average conditions for June 2013. (a) The red box indicates the part of the SE US being considered. (b) Surface wind directions from the WRF model; average wind speed is 5.0 m s^{-1} (min 1.7 m s^{-1}, max 12.7 m s^{-1}). (c) WRF-Chem tropospheric NO_2 columns. (d) AMFs for the pseudo-retrieval calculated using the average monthly NO_2 a priori. The direction of the colorbar is reversed in (d), as small AMFs correspond to high modeled VCDs. In all panels, the star (★) indicates the position of Atlanta. Longitude and latitude are marked on the x- and y- axes, respectively.

2.3 Results

Daily variations

Fig. 2.2 shows the average wind and modeled NO_2 columns for June 2013, and the AMF values for the psuedo-retrieval around Atlanta, GA, USA. Atlanta was chosen as the focus of this study because it represents a strong NO_x source relatively isolated from other equally large sources. This ensures that changes to the a priori profiles on a daily basis can be attributed to a local cause. The prevailing wind pattern advects NO_2 to the northeast of Atlanta (the location of Atlanta is marked by the star), as can be seen in the wind field shown in Fig. 2.2b and the WRF-Chem NO_2 columns in Fig. 2.2c. The average surface wind speed over Atlanta for June is 5.0 m/s. This distribution of NO_2 leads directly to the lower AMFs seen to the northeast of Atlanta in Fig. 2.2d through Eq. (2.2).

To illustrate the effect of incorporating daily a priori profiles into the retrieval, we consider two days: 18 and 22 June 2013. These provide an illustration of the effect of changes

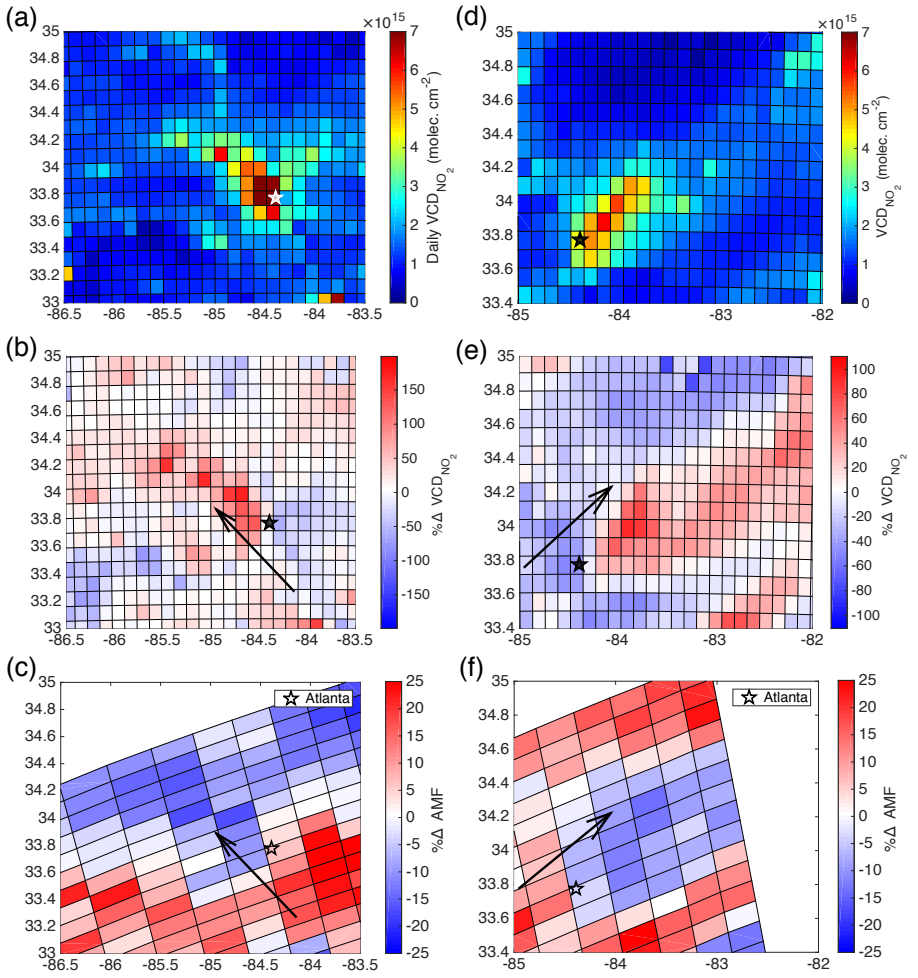

Figure 2.3: Results from 22 June (a–c) and 18 June (d–f). (a,d) WRF-Chem tropospheric NO_2 columns for 1900 UTC. (b,e) The percent difference in WRF-Chem tropospheric NO_2 columns at 1900 UTC for that day vs. the monthly average. (c,f) Percent difference in AMFs using hybrid daily profiles vs. the monthly average profiles in the pseudo-retrieval. In all panels, the star (★) indicates the position of Atlanta, and the wind direction around Atlanta is shown by the arrow in the lower four panels. Longitude and latitude are marked on the x- and y- axes, respectively.

in both wind speed and direction. Figure 2.3a–c shows the result from implementing the daily profiles for 22 June. On this day, the winds over Atlanta blow out of Atlanta to the northwest, with a speed at the surface of 4.5 m/s. This is similar to the monthly average speed (5.0 m s^{-1}) but are rotated 90° counterclockwise compared with the monthly average. The change in direction results in much greater near-surface NO_2 to the northwest compared to the monthly average (Fig. 2.3b) as the wind direction advects NO_2 into an area with low NO_2 in the monthly average.

Figure 2.3c shows that the greater near-surface NO_2 to the northwest results in lower AMFs than average (red), while the opposite is true to the east (blue). The greater near-surface NO_2 in profiles to the northwest weights $S(p)$ in Eq. (2.2) more heavily towards lower altitudes, where $w(p)$ is less, thus decreasing the overall AMF by ∼15%. The increase in AMFs to the east reflects the inflow of cleaner air from the shift in winds. This reduces near-surface NO_2 and increases the weight of higher altitudes of $S(p)$, increasing the AMFs by ∼10–35% (the colorbar saturates at ±25% to make the decrease to the northwest easier to see).

Wind speed also plays an important role in determining the a priori profile shape through transport and chemistry. Fig. 2.3d–f shows results from 18 June, where the wind speed over Atlanta averaged 9.1 m/s. This results in faster advection away from emission sources, with 10–15% increases in modeled NO_2 columns to the west as the plume is driven east more strongly. The greatest decreases in AMF (and thus increases in VCD) are as much as −13% and occur between 84° and 83° W where the increased wind speed has advected the NO_2 plume farther than the average. There is also a 2–13% increase along the east edge of Atlanta, resulting from the shift of the plume center east.

When the change in AMF from using the hybrid daily a priori profiles is averaged over the full time period studied (1 June–30 Aug), the percent change in AMF is on average +3.6% throughout the domain with a maximum of +9.8%. All pixels show a positive change. This occurs because 77% of the daily profiles have less NO_2 than the corresponding monthly average profile, as most pixels will be upwind from the city on any given day and will see a decrease in NO_2 when upwind and downwind days are no longer averaged together. This reduces the denominator in Eq. (2.3) and increases the contribution of upper tropospheric scattering weights to the AMF. Scattering weights increase with altitude; therefore, this results in a systematic increase of the AMF throughout the domain for the pseudo-retrieval.

We also consider the relative importance of day-to-day changes in the boundary layer of the a priori profiles versus day-to-day changes in the free troposphere of the a priori profiles by running the pseudo-retrieval with a set of hybrid daily profiles that only include day-to-day variability below 750 hPa and use a monthly average profile above that. The changes in AMFs using these hybrid profiles versus monthly average profiles are very similar to those observed when using the full daily profiles. In general, the hybrid profiles has a slightly greater average increase in AMFs (+3.2% vs. +2.7%) and slightly less extreme changes, but the overall distribution of changes in AMFs is very similar. From this, we can conclude that changes in the boundary layer of the a priori profiles are the dominant reason for changes to the AMFs. However, the WRF-Chem simulations used to produce the a priori profiles did not include lightning NO_x, so this should be considered a lower bound for the effect of day-to-day changes in the free troposphere. The detailed comparison is described in Appendix B.

Effects on retrieved vertical column densities in full retrieval

To determine the effect the inclusion of daily a priori profiles has on the final retrieved vertical column densities (VCDs), the daily profiles were implemented in the full BEHR retrieval. Effects on individual days and multi-month average VCDs are presented here. The cities of Birmingham, AL, USA and Montgomery, AL, USA are included to demonstrate that this effect is significant for cities of various sizes. Atlanta, GA, USA is the largest with approximately 5.7 million people, followed by Birmingham, AL, USA with 1.1 million, and Montgomery, AL, USA with 374,000 (*Annual Estimates of the Resident Population: April 1, 2010 to July 1, 2015. Metropolitan and Micropolitan Statistical Area; and for Puerto Rico.*).

Table 2.1 describes how frequently significant changes in the retrieved VCD occur for pixels within 50 km of Atlanta, Birmingham, and Montgomery. Changes are considered significant by two different criteria. First, we consider the global mean clear-sky uncertainty from Bucsela et al. (2013). As we are modifying the a priori profiles, and thus potentially the uncertainty associated with the choice of profiles, this gives us a fixed value to compare against. Second, we use the quadrature sum of uncertainties from spectral fitting (0.7×10^{15} molec. cm^{-2}, Boersma et al., 2007; Boersma et al., 2011), stratospheric separation (0.2×10^{15} molec. cm^{-2}, Bucsela et al., 2013), and AMF calculation (20%, Bucsela et al., 2013), assuming that these are independent and so can be added in quadrature (Boersma et al., 2004). We consider the fraction of days with at least one pixel exhibiting a significant change in VCD (rather than the fraction of pixels) because the main NO_2 plume may only fall within a small number of pixels. Up to 54% of days exhibit changes in the VCDs greater than 1×10^{15} molec. cm^{-2}, and up to 43% exhibit changes greater than the quadrature sum of uncertainties. This indicates that when considering individual daily measurements, a considerable fraction of days with any valid pixels would have biases in the retrieved VCDs above the uncertainty due to the temporal resolution of the a priori NO_2 profiles.

For both significance criteria, Table 2.1 also indicates that Birmingham and its surrounding area exhibits the largest and most frequent changes when using a daily a priori profile. Figure 2.4a shows the NO emissions throughout this domain. Birmingham has the second largest NO_x emission rate, after Atlanta, while Montgomery has the smallest of the three cities considered. We note that the largest changes are not associated with the city with the greatest NO_x emissions. Both Atlanta and Birmingham fall entirely within the NO_x suppressed regime in the model, so the larger changes in Birmingham are not because NO_x chemistry transitions between the NO_x suppressed and NO_x limited regimes. Instead, the magnitude of these changes is due to Birmingham's intermediate size, where significant NO_2 is present, but emission occurs over a small enough area that changes in wind direction can significantly affect NO_2 concentration at a short distance from the source. When considering changes to be significant if they exceed 1×10^{15} molec. cm^{-2}, Montgomery has the least frequent significant changes because it has the smallest VCDs, so a change to the AMF needs to be rather large to produce a significant change in the VCD by this metric, since the AMF

	Percent of days with ΔVCD $> 1 \times 10^{15}$ molec. cm^{-2}	Percent of days with ΔVCD $> [\sum_i \sigma_i]^{1/2}$	Min. change (molec. cm^{-2})	Max. change (molec. cm^{-2})
Atlanta	39%	23%	-2.4×10^{15}	$+2.5 \times 10^{15}$
Birmingham	54%	43%	-3.8×10^{15}	$+3.9 \times 10^{15}$
Montgomery	27%	20%	-2.2×10^{15}	$+1.9 \times 10^{15}$

Table 2.1: Statistics on the frequency and magnitude of changes in the retrieved VCDs using a daily vs. monthly average profile for pixels with centers within 50 km of Atlanta, GA, USA (84.39° W, 33.775° N), Birmingham, AL, USA (86.80° W, 33.52° N) and Montgomery, AL, USA (86.30° W, 32.37° N). The "percent of days" values are calculated as the number of days with at least one pixel in that subset with a change greater than the given uncertainty divided by the number of days with at least one pixel unobscured by clouds or the row anomaly. The uncertainty represented by $[\sum_i \sigma_i]^{1/2}$ is the quadrature sum of uncertainties from spectral fitting (0.7×10^{15} molec. cm^{-2}, Boersma et al., 2007; Boersma et al., 2011), stratospheric separation (0.2×10^{15} molec. cm^{-2}, Bucsela et al., 2013), and AMF calculation (20%, Bucsela et al., 2013).

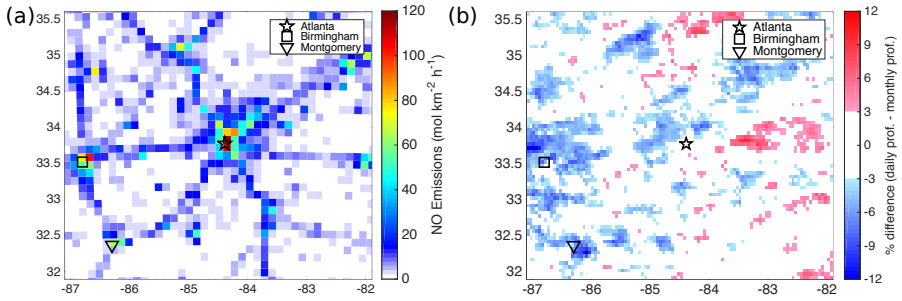

Figure 2.4: (a) 24 h average NO emissions from WRF-Chem at 12 km resolution. (b) The change in retrieved VCDs averaged over 1 June to 30 Aug. Pixels with a cloud fraction $> 20\%$ or that are affected by the row anomaly are excluded from the average. The color scale is reversed from Fig. 2.3c,f to reflect the inverse relationship between VCD and AMF. Longitude and latitude are marked on the x- and y- axes, respectively, for both panels.

is a multiplicative factor. When considering the quadrature sum of errors as the significance criterion, Montgomery and Atlanta both demonstrate significant changes $\sim 20\%$ of the time.

Implementing the daily profiles also changes the average VCDs, in addition to the day-to-day changes in VCDs discussed above. Figure 2.4b shows the changes in VCDs averaged over the period studied. The largest decrease around Atlanta is to the northeast, along the direction that the monthly average model results placed the NO_2 plume, but clear decreases can also be seen to the northwest and southwest. In these directions, a systematic decrease of up to 8% (4×10^{14} molec. cm^{-2}) is observed. Although this change is small, it is expected to

be systematic. Statistically, a pixel's a priori profile is more likely to have less surface NO_2 when different wind directions are no longer averaged in, thus decreases in the VCD when using a daily a priori profile are more common.

Greater relative changes are observed around the smaller cities of Birmingham (down to -12.9%, 5×10^{-14} molec. cm^{-2}) and Montgomery (down to -13%, 4×10^{-14} molec. cm^{-2}). This appears to be due primarily because the areas of emissions are smaller which makes shifts in wind direction have a greater average relative effect on the plume shape.

We also compare this average change to the measurement uncertainty. The uncertainty due to random errors in the retrieval should reduce as the square root of the number of observations, but delineating random and systematic errors in the retrieval is challenging (Boersma et al., 2004). The most optimistic approach assumes that the global average uncertainty of 1×10^{15} molec. cm^{-2} (Bucsela et al., 2013) can be treated entirely as random error, and can be reduced by $\sqrt{40}$ for the number of observations (not impacted by clouds or the row anomaly), to a lower bound of $\sim 1.6 \times 10^{14}$ molec. cm^{-2}. Most of the changes near the three cities exceed this lower limit. More realistically, the spectral fitting and stratospheric uncertainty may be considered largely random, but only part of the error in the AMF calculation is random, due to spatial or temporal autocorrelation in the models or ancillary products (Boersma et al., 2004). For simplicity, we assume that the spectral fitting and stratospheric subtraction errors are entirely random, while only half of the error in the AMF is random. This reduces the error from $\sqrt{(0.7 \times 10^{15})^2 + (0.2 \times 10^{15})^2 + (20\%)^2}$ to $\sqrt{(0.11 \times 10^{15})^2 + (0.03 \times 10^{15})^2 + (11.6\%)^2}$. Only the largest changes near Birmingham and Montgomery exceed this threshold. This more conservative estimate suggests that the changes in averages are primarily important for smaller or very geographically concentrated cities, where wind direction can have a large effect. Nevertheless, larger cities may exhibit important changes as well.

Unlike the pseudo-retrieval, where we only allowed the a priori profiles to vary day-to-day and clouds were set to zero, there is a some spatial structure to these average changes. This is primarily a statistical phenomenon. We use only pixels with cloud fraction $< 20\%$, which reduces the number of pixels in the average. Within this subset, the wind blows to the southeast out of Atlanta more frequently than other directions; so the increases due to properly accounting for the presence of surface NO_2 average with the more typical decreases to give a small average change. The other directions exhibit the expected average decrease in VCDs due to the average increase in AMFs discussed in section 2.3. We expect that over longer periods of time all directions would see a 2–6% decrease in the average VCDs.

2.4 Discussion

Importance of model uncertainty

WRF-Chem has generally been found to reproduce wind fields, especially above 2 m s^{-1} (Tie et al., 2007; Zhang et al., 2009), and spatial variability of trace gases (Follette-Cook et al., 2015) well. Nevertheless, a natural concern when modeling daily NO_2 profiles for satellite retrievals is the accuracy of the plume location. We, however, note that the transition from monthly average to daily profiles does not necessarily result in increased model uncertainty, but rather a change in the type of uncertainty.

When using monthly average profiles, the uncertainty in the modeled NO_2 concentrations compared to the true mean will be reduced (assuming at least some component of the error is random in nature), but the true day-to-day variability not captured by the monthly average effectively becomes a new error term. In contrast, when using daily profiles, the random model error is not reduced, but the day-to-day variability is also not averaged out. Ideally, the error in a set of daily profiles will manifest as deviation from the true set of profiles for that day, rather than the monthly profiles' smaller deviation from a mean set of profiles that itself may not represent any single day.

An important step in managing the uncertainty in the daily profiles is to constrain the modeled meteorology with observations or reanalysis datasets. By default, meteorology in WRF is constrained via initial and boundary conditions only. With larger domains and longer runs, further constraints using four-dimensional data assimilation (FDDA, Liu et al., 2006) and/or objective analysis (Follette-Cook et al., 2015; Wang et al., 2014; Yegorova et al., 2011), possibly combined with periodic model reinitialization (Otte, 2008) are strongly recommended.

Effects on space-based lifetime and emissions constraints

Recently several authors have used wind-sorted satellite NO_2 observations to probe NO_x chemistry and emissions from space (Beirle et al., 2011; Valin et al., 2013; Foy et al., 2014; Lu et al., 2015; Liu et al., 2016). We apply the EMG fitting method of Lu et al. (2015) to NO_2 line densities derived from NO_2 columns retrieved using the daily and monthly average a priori profiles, as well as a monthly average profile simulated at 108 km resolution for both Atlanta and Birmingham. To match the method of Lu et al. (2015) as closely as possible, we use 3 m s^{-1} as the division between slow and fast winds.

We acknowledge that a 91 day averaging period is significantly shorter than those used in Beirle et al. (2011), Valin et al. (2013), or Lu et al. (2015) (5 years, summer half-year for 7 years, and summer half-year for 3 year periods, respectively). However, since the goal of this section is to compare the results obtained using three different sets of a priori profiles with all other variables equal, we believe that 91 days is sufficient for this purpose.

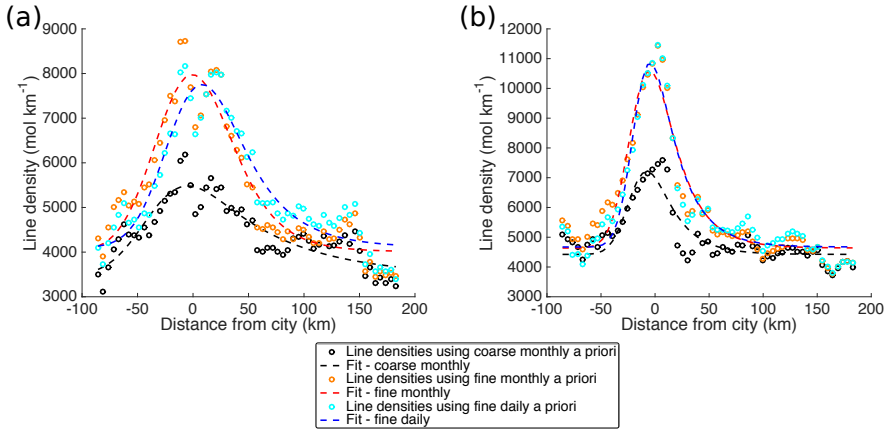

Figure 2.5: Line densities around Atlanta, GA, USA averaged over the study period when using monthly average and daily a priori (open circles), and the corresponding fits of exponentially-modified Gaussian functions (dashed lines). Black series are derived from a retrieval using a monthly average a priori at 108 km resolution; red series from a monthly average a priori at 12 km resolution, and blue from the daily profiles at 12 km resolution. (a) Average of days with wind speed ≥ 3.0 m/s. (b) Average of days with wind speed < 3.0 m/s.

Additionally, we do not include days around Atlanta in which the wind blows towards the southeast (specifically 0° to −112.5°, 0°, is defined as east, negative values are clockwise from east). Significant suburban NO_2 columns near 83.5° W, 33° N add a secondary maximum to the line densities which can erroneously lengthen the decay time of the fit. All wind directions are used for Birmingham.

Accounting for the spatial and temporal variability of NO_2 in the a priori profiles leads to several notable changes in the line densities and the resulting EMG fits. Figure 2.5 shows the line densities and the corresponding EMG fits around Atlanta for the average over the 91 day study period. Table 2.2 enumerates the values obtained for the fitting parameters in Eq. (2.8) for the fits of the Atlanta NO_2 plume in Fig. 2.5 and fits for the Birmingham NO_2 plume (not shown).

The spatial scale of the a priori makes the greatest difference to the maximum value of the line density, causing a significant increase in a when the spatial resolution of the a priori profiles increases from 108 km to 12 km. This reflects the impact of the blurring of urban and rural profiles described in Russell et al. (2011).

Both the spatial and temporal resolution impact the determination of x_0, the distance traveled in one lifetime. This parameter is determined at fast wind speeds (Lu et al., 2015; Valin et al., 2013), so we consider only the results for wind speed ≥ 3.0 m s^{-1}. For Atlanta, using a daily a priori results in an x_0 value 37% greater than that obtained using a monthly average

		Wind $\geq$ 3.0 m/s			Wind $<$ 3.0 m/s		
		Monthly 108 km	Monthly 12 km	Daily 12 km	Monthly 108 km	Monthly 12 km	Daily 12 km
Atlanta	a (mol NO_2)	$3. \pm 1 \times 10^5$	$4. \pm 1 \times 10^5$	$3. \pm 1 \times 10^5$	$1.5 \pm 0.6 \times 10^5$	$3. \pm 1 \times 10^5$	$3. \pm 1 \times 10^5$
	x_0 (km)	74 ± 30	27 ± 11	37 ± 15	23 ± 10	24 ± 10	24 ± 10
	μ_x (km)	-37 ± 15	$-20. \pm 8$	$-14. \pm 6$	$-21. \pm 8$	$-19. \pm 8$	$-17. \pm 7$
	σ_x (km)	28 ± 11	29 ± 12	27 ± 11	$14. \pm 6$	$15. \pm 6$	$13. \pm 5$
	B (mol NO_2 km^{-1})	$3. \pm 1 \times 10^3$	$4. \pm 2 \times 10^3$	$4. \pm 2 \times 10^3$	$4. \pm 2 \times 10^3$	$5. \pm 2 \times 10^3$	$5. \pm 2 \times 10^3$
Birmingham	a (mol NO_2)	$1.6 \pm 0.5 \times 10^5$	$3. \pm 1 \times 10^5$	$3. \pm 1 \times 10^5$	$4. \pm 1 \times 10^5$	$3. \pm 1 \times 10^5$	$3. \pm 1 \times 10^5$
	x_0 (km)	41 ± 14	32 ± 11	44 ± 15	230 ± 80	34 ± 12	59 ± 20
	μ_x (km)	$-20. \pm 7$	$-24. \pm 8$	$-14. \pm 5$	-51 ± 17	$-24. \pm 8$	$-24. \pm 8$
	σ_x (km)	$26. \pm 9$	$27. \pm 9$	$23. \pm 8$	$23. \pm 8$	$26. \pm 9$	$22. \pm 8$
	B (mol NO_2 km^{-1})	$4. \pm 1 \times 10^3$	$4. \pm 1 \times 10^3$	$4. \pm 1 \times 10^3$	$4. \pm 1 \times 10^3$	$5. \pm 2 \times 10^3$	$5. \pm 2 \times 10^3$

Table 2.2: Values of the five fitting parameters for the EMG functions (Eq. 2.8) used to fit the distributions of line densities around Atlanta and Birmingham. a represents the total NO_x burden, x_0 is the distance the plume travels in one lifetime, μ_x is the center of emissions relative to the city center, σ_x describes the Gaussian smoothing, and B the background line density.

profile at the same spatial resolution (12 km). Birmingham also shows a 38% increase in x_0 between the monthly and daily 12 km a priori.

μ_x represents the apparent center of the NO_2 plume relative to the geographic center of the city. This moves downwind (positive) when changing from the monthly average 12 km or 108 km a priori to the daily 12 km a priori. This reflects the ability of the daily a priori to capture how the wind distorts the plume shape.

σ_x is the Gaussian smoothing length scale, representing both the width of the upwind Gaussian plume and smoothing of the NO_2 signal due to the physical extent of the source, the averaging of NO_2 within one OMI pixel, and daily variability in the overpass track (Beirle et al., 2011). There is a slight decrease when going from a monthly average to daily profiles, which reflects the general increase in upwind AMFs (i.e. compare Fig. 2.1a and 2.1b), but because this is outside of the main NO_2 plume, the effect is small.

Finally, B is the background line density. Ideally, it is derived sufficiently far from any NO_x sources that spatial and temporal variability should be minimal. In several cases there is a $\sim 25\%$ increase when improving the spatial resolution of the a priori profiles. This is likely attributable to the general increase in urban signal discussed several times so far pulling the edges of the line density upward. However, a greater selection of cities is necessary to demonstrate this more conclusively.

Ultimately, the goal of this method is to extract information about chemically relevant quantities such as emission rate and lifetime. Since Foy et al. (2014) and Valin et al. (2013)

		Atlanta			Birmingham		
	Wind speed bin	Monthly 108 km	Monthly 12 km	Daily 12 km	Monthly 108 km	Monthly 12 km	Daily 12 km
E (Mg NO_x h^{-1})	WRF-Chem NEI		**13.74**			**10.49**	
	≥ 3.0	$4. \pm 2$	$15. \pm 9$	$11. \pm 6$	$4. \pm 2$	$11. \pm 6$	$8. \pm 4$
	≥ 4.0	$5. \pm 3$	17 ± 10	$10. \pm 6$	$4. \pm 2$	$13. \pm 7$	$9. \pm 5$
	≥ 5.0	-	-	-	$6. \pm 4$	$16. \pm 9$	$11. \pm 6$
τ (h)	≥ 3.0	$4. \pm 2$	1.4 ± 0.6	1.8 ± 0.8	2.2 ± 0.8	1.7 ± 0.6	2.3 ± 0.8
	≥ 4.0	2.1 ± 0.9	1.2 ± 0.5	2.0 ± 0.8	2.2 ± 0.8	1.5 ± 0.5	2.1 ± 0.8
	≥ 5.0	-	-	-	1.8 ± 0.7	1.3 ± 0.5	1.7 ± 0.7

Table 2.3: Values of the emission rates (E) and effective lifetime (τ) obtained when the separation between slow and fast winds is set at 3, 4, and 5 m s^{-1}. For comparison, the total NO_x emission for all 12 km WRF-Chem grid cells within 50 km of each city is given. These emissions are derived from NEI 11 and scaled to 88.9% to account for 2011–2013 reductions. Uncertainties calculated as described in Appendix B.

showed that choice of wind speed bins affects the values obtained, we also consider if the effect of implementing the daily a priori profile changes if the observations are binned by different wind speed criteria. Table 2.3 compares the values of the NO_x emission rate, E, and effective lifetime, τ_{eff}, derived from different wind speed bins for Atlanta and Birmingham. Restricting the analysis to days with wind speed greater than 5 m s^{-1} results in too few days for a meaningful analysis around Atlanta (due to the need to remove days with winds to the southeast), so results for Atlanta are restricted to ≥ 3 m s^{-1} and ≥ 4 m s^{-1} only.

τ_{eff} and E are each computed from several of the EMG fitting parameters. τ_{eff} depends on x_0 and w (the mean wind speed) through Eq. (2.10):

$$\tau_{\text{eff}} = \frac{x_0}{w} \tag{2.10}$$

E depends on a, x_0, and w through Eq. (2.11):

$$E = 1.32 \times \frac{a \times w}{x_0} = 1.32 \times \frac{a}{\tau_{\text{eff}}} \tag{2.11}$$

where the factor of 1.32 accounts for the NO_x:NO_2 ratio throughout the tropospheric column (Beirle et al., 2011).

Both Valin et al. (2013) and Foy et al. (2014) show that lifetime should decrease at faster wind speeds. We see this trend clearly for Birmingham but not Atlanta. Foy et al. (2014) also saw that, for a chemical lifetime of 1 h, greater derived emissions were found at faster

wind speeds. This is also better seen in our results for Birmingham than Atlanta. Previous measurements of NO_x lifetime in urban plumes average 3.8 h and range from 2-6 h (Beirle et al., 2011; Ialongo et al., 2014; Nunnermacker et al., 1998; Spicer, 1982), and, using the EMG method, Lu et al. (2015) saw effective lifetimes between 1.2 and 6.8 h. The lifetimes we calculate are at the low end of the previously observed ranges. However, this is similar to the instantaneous lifetime of 1.2 ± 0.5 h and 0.8 ± 0.4 h calculated from the WRF-Chem model for days in June 2013 with wind speed ≥ 3 m s^{-1} and grid cells within 50 km of Atlanta and Birmingham, respectively (see Appendix B for the calculation details). The sole exception is the lifetime calculated for Atlanta using the coarse monthly profiles with all wind speeds ≥ 3 m s^{-1}. However, several points near the peak of the line densities for this case are abnormally low compared to their neighbors. This results from the inclusion of negative VCDs in the average to avoid biasing the data; if negative VCDs are not included, the lifetime is instead 1.58 h. We expect that with studies expanded over longer time periods, the impact of negative VCDs will be reduced.

The differences in the lifetimes and emissions derived using the daily and monthly 12 km a priori profiles are systematic. In all cases, the lifetime derived using the daily profiles is 30–66% longer. When using monthly average a priori profiles, profiles resulting from different wind directions are averaged together. The AMFs calculated from these profiles thus reflect the average distance from the city the plume reaches in a given direction, e.g. east of the city, with smaller AMFs near the city and greater AMFs more distant (Fig. 2.1). In this hypothetical example, when the wind blows to the east, the spatial extent of the plume is underestimated because the average AMFs towards the end of the plume will be too large, so the VCDs will be too small by Eq. (2.1). On days when the wind does not blow east, the reverse is true: the plume extent is overestimated because the AMFs nearer to the city are too small (Fig. 2.1d). If one considers a simple average change in the VCDs, these two errors will partially cancel and we will see the average change from Sect. 2.3. However, in the EMG fitting approach, these errors do not cancel at all because the EMG method both rotates the NO_2 plumes so that the wind directions align before calculating the line densities and systematically selects fast winds to determine τ_{eff}, so we are always dealing with the first case and the plume extent is always underestimated. In the EMG fit, this manifests as a too short lifetime. As the emissions are inversely proportional to lifetime (Eq. 2.11), emissions derived using the monthly 12 km a priori profiles will be too great. Therefore, when using a retrieval with a priori profile at fine spatial resolution, daily temporal resolution of the a priori profiles is necessary to prevent underestimating the lifetime. Further, the spatial resolution of the a priori profiles has a large impact on the magnitude of the derived emissions. To reduce the systematic biases in emissions and lifetime from the choice of a priori profile, it is necessary to simulate these profiles at fine spatial and daily temporal resolution.

We also use 2-sample t-tests at the 95% confidence level (Harris, 2010) to determine if differences in emissions and lifetimes given in Table 2.3 are significantly different among the results derived from using the three different a priori profile sets for a given city and

wind speed bin (i.e. we compare the three values of emissions derived using different a priori profiles for Atlanta and wind speeds ≥ 3 m s^{-1}). This found that, for emissions, the choice of a priori leads to statistically different emissions for all five cases. For the derived lifetimes, in all but one cases the monthly 108 km and daily 12 km a priori are statistically indistinguishable, but the monthly 12 km a priori is statistically different. The exception again is Atlanta for all winds ≥ 3 m s^{-1}, which as explained above, is spuriously affected by negative VCDs. We note that a Durbin-Watson test indicates some spatial autocorrelation remains, and so the uncertainty may be underestimated and the t-tests may be incorrectly identifying the differences as significant in this case (Chatterjee and Hadi, 2012). Even if this is true, with a longer averaging period such as those in Beirle et al. (2011), Valin et al. (2013), and Lu et al. (2015), we would expect the random uncertainties to reduce while the systematic difference from the choice of a priori profile remains. Therefore, the choice of a priori profiles does have an important effect on derived emissions and lifetimes.

We also compare the derived emissions rates to the emissions in a 12 km WRF-Chem model driven by the NEI 11 emission inventory with NO_x emissions scaled to 88.9% of the 2011 values to account for the decrease between 2011 and 2013 (EPA, 2016). WRF-Chem emissions are calculated as the sum of all grid cells within a 50 km radius of the city. 50 km was chosen as the line densities were integrated for ~ 50 km to either side perpendicular to the wind direction. The coarse monthly a priori are 42–70% lower than the NEI-driven emissions, while emissions derived using daily 12 km a priori are within 5–27% (both greater and less than the NEI emissions). Recent work (e.g. Travis et al., 2016, and references within) suggests that the NEI inventory is overestimated by ~ 50% using both satellite and in situ observations. Emissions derived using daily 12 km show the best agreement to the current NEI inventory, and emissions derived using monthly 108 km a priori profile agree with the NEI inventory reduced by 50%. Therefore, we cannot say which a priori profiles provide the best measurement of emissions by comparing to NEI. It is likely that emissions derived using the monthly 12 km a priori profiles are an overestimate, because the systematically low lifetimes discussed above increase E through Eq. (2.11); that these emissions are consistently higher than the NEI emission reinforces this likelihood. Conversely, we expect that emissions derived using the coarse monthly a priori profiles are biased low due to the known underestimate of urban NO_x signals using coarse a priori (Russell et al., 2011). From this, it is clear the choice of a priori profiles has a substantial impact on emissions derived from satellite observations, and that both spatial and temporal resolution of the a priori profiles contribute to that difference. This explains why the OMI derived emissions from Lu et al. (2015) are lower that the bottom up NEI inventory, but needs to be reconciled with work by Travis et al. (2016) which indicates that NEI is overestimated.

In summary, the two most important parameters (a and x_0) and values derived from them (E, τ_{eff}) are significantly affected by the spatial and temporal resolution of the a priori. a is most affected by increasing the spatial resolution of the a priori, while using daily profiles corrects a systematic bias in x_0 when the profiles are simulated at high spatial resolution. E

is affected by both the spatial and temporal resolution of the a priori profiles, increasing by $\sim 100\%$ between the retrievals using coarse monthly and fine daily a priori profiles. Therefore the use of daily a priori NO_2 profiles at high spatial resolution significantly alters the results obtained from fitting wind aligned retrieved NO_2 columns with an analytical function.

2.5 Conclusions

We have demonstrated that incorporating daily NO_2 a priori profiles simulated at sufficiently fine spatial scales to capture the spatial variation of an NO_2 plume leads to significant changes in the final VCDs when compared to monthly average profiles at the same spatial resolution. Changes to VCDs on a single day are up to 50% (relative) and 4×10^{15} molec. cm^{-2} (absolute). This is attributable to changes in the direction of the NO_2 plume. Up to 59% of days with valid observations exhibit changes in VCDs $> 1 \times 10^{15}$ molec. cm^{-2} in at least one pixel. Additionally, the inclusion of daily profiles affects a systematic change in time-averaged VCDs around Atlanta, GA, USA. Pixels downwind in the average exhibited VCD decreases up to 8% (4×10^{14} molec. cm^{-2}). Larger relative changes of as much as -13% were found around the nearby cities of Birmingham, AL and Montgomery, AL. Day-to-day variations in the free troposphere have a smaller impact on the value of the AMF, and average out to no net change over the period studied. These results were obtained using WRF-Chem without lightning NO_x emissions; it is likely that the inclusion of lightning NO_x would increase the magnitude of positive changes to the AMF due to the presence of NO_2 at altitude to which OMI is highly sensitive.

When the methods of Lu et al. (2015) are applied to these prototype retrievals, significant changes in derived NO_x emissions are found, increasing by as much as 100% for Atlanta compared to emissions derived from a retrieval using coarse a priori profiles. Using high spatial resolution, monthly average a priori profiles results in the highest derived emissions rates, followed by high spatial resolution, daily a priori, with spatially coarse a priori leading to the lowest derived emissions. Emissions derived using the fine daily a priori are within 25% of the bottom up number from the NEI inventory, a smaller reduction than that suggested by Travis et al. (2016). Future work will aim to resolve this difference. Lifetimes derived from satellite observations using a spatially fine but monthly averaged a priori are systematically biased low due to the spatial pattern of AMF imposed by such a priori; consequently, emissions derived using these a priori profiles are likely biased high. The use of daily profiles at fine spatial resolution corrects this systematic bias.

Having shown that the use of daily a priori NO_2 profiles in the retrieval algorithm significantly alters emissions and lifetimes derived from this retrieval, we plan to implement such profiles for several years at the beginning and current end of the OMI data record to investigate how NO_x lifetimes have changed in urban plumes over the past decade. Such work can provide a greater understanding of the most effective means of improving air quality in years to come,

as it will allow us to determine whether reductions in NO_x or VOC emissions will provide the most benefit in ozone reduction.

Chapter 3

Quantification of the effect of modeled lightning NO_2 on UV-visible air mass factors

The chapter was adapted from: J. L. Laughner and R. C. Cohen (2017). "Quantification of the effect of modeled lightning NO_2 on UV–visible air mass factors". *Atmos. Meas. Tech.* 10.11, pp. 4403–4419. DOI: 10.5194/amt-10-4403-2017

3.1 Introduction

NO_x ($\equiv$ NO + NO_2) is a short-lived (typical summer lifetime 2–7 h) trace gas in the atmosphere. NO_x is emitted by both anthropogenic and natural processes; the former is primarily due to combustion, while the latter includes biomass burning, soil bacteria nitrification or denitrification, and lightning. NO_x regulates ozone production throughout the troposphere; therefore accurate measurements of NO_x and understanding of NO_x chemistry is essential to describe and predict the role of ozone as both an air quality hazard, oxidant, and a greenhouse gas.

Space-borne measurements of NO_2 as an indicator of total NO_x, such as those from the Global Ozone Monitoring Experiment (GOME and GOME-2), SCanning Imaging Absorption SpectroMeter for Atmospheric CHartographY (SCIAMACHY), and Ozone Monitoring Instrument (OMI) are a valuable tool in understanding NO_x emissions and chemistry because of their global reach and long data records. Use of these observations includes assessment of NO_x chemistry (e.g. Beirle et al., 2011; Valin et al., 2013) anthropogenic emissions (e.g. Miyazaki et al., 2012a; Russell et al., 2012; Lu et al., 2015; Liu et al., 2016; Liu et al., 2017) and natural emissions (e.g. Martin et al., 2007; Beirle et al., 2011; Hudman et al., 2012; Mebust et al., 2011; Mebust and Cohen, 2013; Mebust and Cohen, 2014; Miyazaki et al., 2014; Zörner et al., 2016).

Retrieval of tropospheric NO_2 from a UV-visible satellite spectrometer requires three main steps: fitting the measured absorbance to produce a slant column density (SCD), separation of the stratospheric and tropospheric signals, and conversion of the tropospheric SCD to a vertical column density (Boersma et al., 2011; Bucsela et al., 2013). This final step accounts for the effect of variable path length through the atmosphere, surface elevation and reflectance, and the vertical distribution of NO_2 (Palmer et al., 2001). For observations over low reflectivity surfaces, the sensitivity of the satellite to NO_2 decreases towards the surface, as photons penetrating into the lower atmosphere may scatter into the surface, where most are absorbed; thus, there is a higher probability that a photon that reaches the detector has interacted only with the higher levels of the atmosphere (Hudson et al., 1995; Richter and Wagner, 2011). That is to say, a given number of NO_2 molecules in the upper troposphere produce a greater signal than the same number of NO_2 molecules at the surface would. Thus, a priori knowledge of the vertical profile of NO_2 is necessary to account for this effect in the retrieval.

These vertical profiles are simulated using chemical transport models (CTMs) such as TM4 (used in Boersma et al., 2011), the Global Modeling Initiative CTM (used in Bucsela et al., 2013), or the Weather Research and Forecasting—Chemistry (WRF-Chem, used in Russell et al., 2011). These models must account for atmospheric transport, chemistry, emissions, and deposition to accurately simulate the required NO_2 profiles. Most emission of NO_2 occurs at or very near the surface. There are comparatively weaker sources of NO_2 in the upper troposphere, limited to transport from the surface, aircraft, stratospheric mixing, and lightning (Jaeglé et al., 1998).

Simulation of lightning NO_x emission in these models is typically done by assuming each flash emits a set number of molecules of NO. The number and location of lightning flashes is often parameterized using the method of Price and Rind (1992), which relates lightning flash rates to cloud top heights, which in turn are calculated from the model's meteorology. In CTMs focused on simulating surface chemistry to understand or predict air quality, such as WRF-Chem or the Community Multi-scale Air Quality (CMAQ) model, including NO_x produced by lightning may be disabled by default or require the user to prepare additional input files. As these models are often used to simulate high resolution a priori profiles (e.g. Russell et al., 2011; Russell et al., 2012; Kuhlmann et al., 2015; Laughner et al., 2016; Goldberg et al., 2017), the absence of lightning NO_x from the a priori profiles may contribute to a significant bias in the interpretation of the measurements (e.g. Travis et al., 2016).

In the upper troposphere, NO_x lifetime has previously been assumed to be long (2–8 days, Schumann and Huntrieser, 2007). Recently, work from the Deep Convective Clouds and Chemistry (DC3) campaign showed that the lifetime of NO_x is short near thunderstorms due to active alkyl-, peroxy-, and multifunctional- nitrate chemistry with peroxy radicals formed in the near field from organic precursors lofted from the boundary layer ($\sim$ 3 h, Nault et al., 2016), but longer (12–48 h, Nault et al., 2016) away from thunderstorms once

these radical species are consumed and other controlling factors take over (Bertram et al., 2007; Apel et al., 2012). In either case, lightning NO_x can affect upper tropospheric NO_x concentrations distant from active storms; thus, simulated lightning NO_x will have wide-reaching and persistent effects on a priori NO_2 profiles throughout a model domain. Previous work by, e.g. Beirle et al. (2009) and Pickering et al. (2016), has provided careful analysis of the effect of lightning on AMFs in the near field of a thunderstorm, with the goal of improving direct satellite measurements of the mean production of NO per flash. Goldberg et al. (2017) compared high resolution NO_2 profiles from the Community Multiscale Air Quality (CMAQ) model with those from a lower resolution Global Modeling Initiative (GMI) model and found that the CMAQ profiles had less upper troposphere (UT) NO_2 than the GMI profiles, despite greater lightning emissions in CMAQ. Our goal here is to consider the broader impact of modeled lightning NO_x on satellite retrievals on the full domain both near and far from the lightning event.

In this work, we evaluate the impact of modeled lightning NO_x on NO_2 a priori profiles simulated with the WRF-Chem chemical transport model for a domain covering the central and eastern US. We first consider the problem in a general sense, with a sensitivity test using three profiles simulated with different amounts of lightning NO_x. We then compare modeled profiles to observations from the DC3 campaign to determine the accuracy of AMFs derived using the simulated profiles, and finally implement these profiles in an NO_2 retrieval to demonstrate the spatial pattern and significance of this effect in a real application.

3.2 Methods

The Deep Convective Clouds and Chemistry Campaign

The Deep Convection Clouds and Chemistry (DC3) Campaign is an aircraft measurement campaign that took place between 18 May and 22 June 2012 throughout the central and southeastern US (Barth et al., 2015). The NASA DC-8 aircraft sampled outflow from convective systems, studying direct and aged lightning NO_x emissions. We use NO_2 measurements made by laser induced florescence at 1 second resolution in this study (Thornton et al., 2000; Nault et al., 2015).

Weather Research and Forecasting—Chemistry Model

We use the Weather Research and Forecasting—Chemistry (WRF-Chem) model v. 3.5.1 (Grell et al., 2005) to simulate NO_2 profiles across a domain that covers the same region as the DC3 campaign at 12 km model resolution with 29 vertical levels. Meteorological initial and boundary conditions are driven by the North American Regional Reanalysis (NARR) dataset. Chemical initial and boundary conditions are driven by output from the Model for Ozone and Related chemical Tracers (MOZART; Emmons et al., 2010) provided by the National Center for Atmospheric Research. Anthropogenic emissions are driven by the

National Emissions Inventory 2011 (NEI 11); each emitted species is scaled domain-wide by the ratio of its total annual 2012 to 2011 emissions provided by the Environmental Protection Agency (EPA, 2016), e.g. 2012 NO_x emissions are given at 13.657 million tons, 94% of the 2011 value of 14.519 million tons; the gridded 2011 NO emissions are multiplied by 0.94 to obtain 2012 emissions. Biogenic emissions are driven by the Model of Emissions of Gases and Aerosol from Nature (MEGAN; Guenther et al., 2006). The chemical mechanism is a customized version of The Regional Atmospheric Chemistry Model, version 2 (RACM2; Goliff et al., 2013) that includes updates to alkyl nitrate chemistry from Browne et al. (2014) and Schwantes et al. (2015), as well as formation, dissociation and photolysis of methylperoxy nitrate (Browne et al., 2011, see also `http://wiki.seas.harvard.edu/geos-chem/images/GEOS_changes_MPN_chemistry.pdf`) Instantaneous values of the model output are sampled every half hour.

WRF can be run such that the meteorology within the domain is driven by the model physics chosen, constrained by reanalysis meteorology data only through the initial and boundary conditions. Alternatively, four dimensional data analysis (FDDA) nudging (Liu et al., 2006) can be used to nudge the model meteorology towards a reanalysis meteorology product throughout the domain. We use this capability in two WRF-Chem simulations, nudging towards the NARR meteorology. In all other simulations, the meteorology evolves according to the model physics.

Lightning NO_x emissions are calculated by the standard modules in WRF-Chem 3.5.1, with a slight modification to the assumed emission profile (described below). The flash rates (number of lightning flashes per unit time) are determined by the Price and Rind level of neutral buoyancy parameterization (Price and Rind, 1992), which depends on cloud top height, calculated using the Grell 3D cumulus physics (Grell, 1993; Grell and Dévényi, 2002) with Lin microphysics (Lin et al., 1983). This number of flashes calculated may be scaled by a constant factor, we use this functionality for one run in Sect. 3.3, otherwise the scaling factor is 1. The intra-cloud/cloud-to-ground ratio is prescribed using the Boccippio et al. (2001) climatology; both intra-cloud and cloud-to-ground flashes are specified to generate the same number of mol NO per flash (Cooray et al., 2009; Ott et al., 2010), which for this study is 0, 500, or 665 mol $flash^{-1}$. These values are chosen to represent no lightning, the standard midlatitude assumption (500 mol $flash^{-1}$ Hudman et al., 2007), and the recently proposed 33% increase in lightning NO_x emissions of Nault et al. (2017) (665 mol $flash^{-1}$).

The vertical distribution of NO emissions is driven by a modified version of the profiles from Ott et al. (2010). Several recent studies (Allen et al., 2012; Seltzer et al., 2015) suggest that the standard Ott profiles place too much NO_x in the mid-troposphere. Ott et al. (2010) calculated these profiles using a polynomial fit to profiles of the post-convection vertical distribution of lightning NO_x simulated by a cloud resolving model. The midlatitude profile generated by the cloud resolving model has a bimodal distribution not captured by the polynomial fit; therefore we replace the standard (polynomial fit) Ott et al. (2010)

midlatitude profile in WRF-Chem with the bimodal profile.

Matching aircraft and model data

We match WRF-Chem data to DC3 observations to evaluate the accuracy of the chosen lightning parameterization. Each 1 second DC3 NO_2 observation is paired with the corresponding WRF-Chem data point. Data points are matched in time by finding the WRF-Chem output file (available every half-hour) nearest in time to a given DC3 observation.

Horizontally, a WRF-Chem data point is said to match with a DC3 observation if the latitude and longitude of the DC3 observation lie within the box defined by the midpoints of the WRF-Chem grid cell edges. These midpoints are computed as the average of the relevant corner coordinates (e.g. the western edge point is the average of the northwestern and southwestern corners); the corner coordinates are calculated by assuming that corners not on the edge of the domain are the average of the four surrounding centers. Corners on the domain edge are calculated by extrapolating from the internal corners.

Vertically, we find the matching WRF-Chem data point from the column of such points identified by the previous two steps by finding the WRF-Chem grid point with the smallest difference in pressure compared to the DC3 observation. The result is two vectors of NO_2 concentrations (DC3 and WRF-Chem) that are the same length; WRF-Chem data points that correspond to multiple DC3 observations are repeated, thus inherently giving them more weight and reflecting the sampling of the aircraft. Matching the vertical position in this way inherently restricts the model data to the vertical range of the observations.

The Ozone Monitoring Instrument

The Ozone Monitoring Instrument is a polar-orbiting, nadir-viewing UV-visible spectrometer on board the Aura satellite, launched in 2004. It has a nadir pixel size of 13×24 km^2. The primary detector is a 2D CCD array that observes a swath width of 2600 km and a spectral range of 270–500 nm (Levelt et al., 2006). It provides daily global observation for the first three years of operation; after 2007 several detector rows developed anomalous radiances (termed the "row anomaly", `http://projects.knmi.nl/omi/research/product/rowanomaly-background.php`) that have expanded over time; from July 2011 on, this affects approximately one-third of the pixels. There are two publicly available global products of NO_2 column densities, the KNMI DOMINO product (Boersma et al., 2011) and the NASA Standard Product v3 (Krotkov et al., 2017), and numerous regional products, including OMI-EC (McLinden et al., 2014), Hong Kong OMI NO_2 (Kuhlmann et al., 2015), Peking University OMI NO_2 (POMINO Lin et al., 2015), Empa OMI NO_2 (EOMINO, `http://temis.empa.ch/index.php`), DOMINO2_GC (Vinken et al., 2014a), and the Berkeley High Resolution OMI NO_2 retrieval (Russell et al., 2011; Russell et al., 2012).

Berkeley High Resolution OMI NO_2 retrieval

Retrieval product

To demonstrate the impact of modeled lightning NO_x on retrieved NO_2 column densities, we use v2.1C of the BErkeley High Resolution (BEHR) NO_2 retrieval. Details of the algorithm are given in Russell et al. (2011); more recent updates are given in the changelog (`http://behr.cchem.berkeley.edu/Portals/2/Changelog.txt`). This product is available for download at `http://behr.cchem.berkeley.edu/DownloadBEHRData.aspx`.

Version 2.1C of the BEHR product is based on the NASA Standard Product version 2 (SP v2). It uses the OMI total slant column densities (SCDs) from the OMI NO_2 product OMNO2A v1.2.3 (Boersma et al., 2002; Bucsela et al., 2006; Bucsela et al., 2013), as well as the stratospheric separation and destriping from the NASA Standard Product v2 (SP v2). Version 3 of the NASA Standard Product was released in 2016, and includes new spectral fitting and tropospheric AMF calculations. The change from SP v2 to v3 does not affect any of the AMF calculations in this work. Krotkov et al. (2017) indicates that the tropospheric VCDs over unpolluted areas are similar between SP v2 and v3, therefore, when effects on retrieved VCDs are considered here, we expect our conclusions to be unaltered when BEHR is updated to use SP v3 data.

The BEHR product recalculates the tropospheric air mass factor (AMF) using the formulation in Palmer et al. (2001). In previous versions of BEHR, the tropospheric AMFs and resulting vertical column densities (VCDs) were always "total" tropospheric columns, i.e., they included an estimated ghost NO_2 column below clouds. The ghost column was estimated by using as the AMF the ratio of the visible modeled slant column (derived from the a priori NO_2 profile, scattering weights, and radiance cloud fraction) to the total modeled tropospheric vertical column. Thus, dividing the observed slant column by this AMF produced a total tropospheric vertical column via a multiplicative correction. This approach is identical to that described in Boersma et al. (2002).

Starting in v2.1C, "visible-only" tropospheric AMFs and VCDs are included (which do not include the below-cloud ghost column), in addition to the "total" tropospheric VCDs. In both cases, separate AMFs for clear and cloudy scenes are calculated using Eq. (3.1)

$$\text{AMF} = \int_{p_0}^{p_{\text{tp}}} w(p) S(p)\, dp \tag{3.1}$$

where p_0 is the surface or cloud pressure (for clear and cloudy scenes, respectively), p_{tp} is the tropopause pressure (fixed at 200 hPa), $w(p)$ are the pressure-dependent scattering weights from the TOMRAD look-up table used in the NASA SP v2 (Bucsela et al., 2013), which must be corrected for the temperature dependence of the NO_2 cross section:

$$w(p) = w_0(p)\,[1 - 0.003(T(p) - 220)] \tag{3.2}$$

where $w_0(p)$ is the scattering weight from the look-up table and T is the temperature in Kelvin for a given latitude, longitude, and month; T is taken from the same temperature profiles used in the NASA SP v2 (Bucsela et al., 2013). Recently, an error in the temperature profile lookup for BEHR v2.1C was identified. This caused a $\sim 5\%$ bias in the AMFs, but has been corrected for this study.

Finally, $S(p)$, the shape factor, is computed as:

$$S(p) = \left(\int_{p_s}^{p_{\text{tp}}} g(p)\,dp\right)^{-1} g(p) \tag{3.3}$$

where $g(p)$ is the NO_2 vertical profile, and p_s is either the surface or cloud pressure, depending on whether a total (visible + ghost) or visible-only tropospheric VCD is desired. BEHR v2.1C provides both. For clear scenes, p_s is always the surface pressure. For cloudy scenes, p_s is the surface pressure when calculating the total tropospheric VCD and the cloud pressure when calculating the visible-only VCD.

The clear and cloudy AMFs for a given pixel are combined as:

$$\text{AMF}_{\text{trop}} = (1 - f)\text{AMF}_{\text{clear}} + f\text{AMF}_{\text{cloudy}} \tag{3.4}$$

where f is the radiance cloud fraction, i.e. the fraction of light from the pixel that is reflected off of clouds. The final VCD is computed as:

$$\text{VCD} = \frac{\text{SCD}}{\text{AMF}_{\text{trop}}} \tag{3.5}$$

where the SCD is the tropospheric slant column density from the NASA SP v2.

The vector of scattering weights, $w(p)$, chosen from the TOMRAD look-up table depends on five parameters: solar zenith angle (SZA), viewing zenith angle (VZA), relative azimuth angle (RAA), albedo, and surface pressure. The SZA, VZA, and RAA are directly provided or can be calculated from data provided in the NASA SP v2. The surface albedo for a given pixel is calculated by averaging the black sky albedo product MCD43C3 (Schaaf and Wang, 2015) values that fall within the pixel. This product is generated by the Moderate Resolution Imaging Spectroradiometer (MODIS) instruments on board the Aqua and Terra satellites.

Parameter	Abbreviation	Values	Unit
Solar Zenith Angle	SZA	0, 11, 22, 33, 44, 55, 66, 77, 88	deg.
Viewing Zenith Angle	VZA	0, 14, 28, 42, 56, 70	deg.
Relative Azimuth Angle	RAA	0, 45, 90, 135, 180	deg.
Albedo (clear sky)	Alb	0, 0.009, 0.018, 0.027, 0.036, 0.044, 0.053, 0.062, 0.071, 0.080	unitless
Albedo (cloudy sky)	Alb	0.700, 0.722, 0.744, 0.767, 0.789, 0.811, 0.833, 0.856, 0.878, 0.900	unitless
Surface Pressure (clear)	Surf P	1013, 989, 965, 940, 916, 892, 868, 843, 819, 795	hPa
Cloud Pressure (cloudy)	Cld P	1003, 930, 857, 783, 710, 637, 564, 490, 417, 344	hPa

Table 3.1: The values used for the five input parameters to the AMF TOMRAD lookup table in the sensitivity tests. Albedo and surface pressure have different sets of values when the sensitivity test is looking at clear sky and cloudy sky scenarios. For cloudy scenes, the cloud pressure is used as the surface pressure.

Clouds are assumed to have an albedo of 0.8 (Stammes et al., 2008). Surface pressures are calculated by averaging elevation data from the Global Land One-km Base Elevation project (Hastings and Dunbar, 1999) that falls within the pixel and assuming a scale height of 7.4 km; cloud pressures are from the OMI O_2-O_2 algorithm (Acarreta et al., 2004; Sneep et al., 2008; Bucsela et al., 2013) and are included in the NASA SP v2.

When averaging over time for the results in Sect. 3.3 we only use pixels with the OMI geometric cloud fraction < 0.2, XTrackQualityFlags $= 0$, and an even integer for VcdQualityFlags. The averages weight each pixel's contribution by the inverse of the pixel area. Unless otherwise stated, all results in this work use the total tropospheric column.

AMF sensitivity tests

To understand the sensitivity of the AMF to the profile shape under different conditions, we carry out sensitivity tests by varying the five input parameters to the TOMRAD look-up table. Table 3.1 lists the input parameters and the values used for each parameter. For albedo and surface pressure, two sets of values are used; one represents common values seen for clear (unclouded) scenes, the other cloudy scenes. In cloudy scenes, the cloud pressure is used as the surface pressure. The range of values for SZA, VZA, and RAA span the values defined in the TOMRAD look-up table. The range of values for Albedo (clear sky), Surface Pressure (clear sky), and Cloud Pressure (cloudy) span the average 5th and 95th percentiles of those values observed in seven days of BEHR data (2012-06-01 to 2012-06-07). The limits for Albedo (cloudy) are chosen as 0.8 ± 0.1, i.e. the assumed cloud albedo plus a reasonable range to explore.

Scattering weights are calculated for every combination of clear or cloudy parameters (27000 combinations). We choose the temperature correction (Sect. 3.2, Eq. 3.2) assuming the June temperature profile at 37.5° N, 95° W. Using a single NO_2 profile, an AMF is calculated for every combination of input parameters.

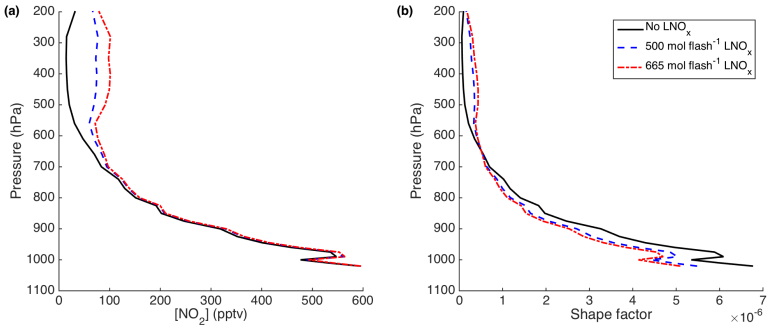

Figure 3.1: Domain-wide mean WRF-Chem NO_2 profiles. (a) profiles in mixing ratios; (b) profiles in shape factor as defined in Palmer et al. (2001), i.e. number density divided by VCD.

We use three types of NO_2 vertical profiles for the AMF sensitivity tests.

1. One derived from the 1 sec DC3 NO_2 data (Sect. 3.2)
2. One using WRF-Chem output matched to the DC3 flight path (Sect. 3.2)
3. One using WRF-Chem output averaged over the entire domain between 1700 and 2200 UTC (roughly the times during which OMI is over North America)

In all cases the data points (modeled or measured) used to generate the NO_2 profiles are binned by pressure to generate a profile defined at the same pressures (using pressure as a vertical coordinate) as the scattering weights in the look-up table. Each data point is placed in the bin with the scattering weight pressure closest to the pressure of the data point. When using the DC3-WRF matched profiles (Sect. 3.2), the two greatest surface pressures (1013 and 989) will have essentially no difference, as the matched profiles only extend down to 990 hPa.

3.3 Results

Parameter sensitivity study using modeled profiles

We begin by demonstrating the sensitivity of the AMF to modeled lightning NO_x emissions in a general sense. Profiles used in this section are those derived by binning WRF-Chem output from the entire domain for simulations with 0, 500, and 665 mol NO $flash^{-1}$ without FDDA nudging (Fig. 3.1). Figure 3.2 shows the percent difference in the AMF when using the profile simulated with 500 mol NO $flash^{-1}$ versus 0 mol NO $flash^{-1}$. In each plot, two of the look-up table inputs are varied and two are held constant. Each plot represents the

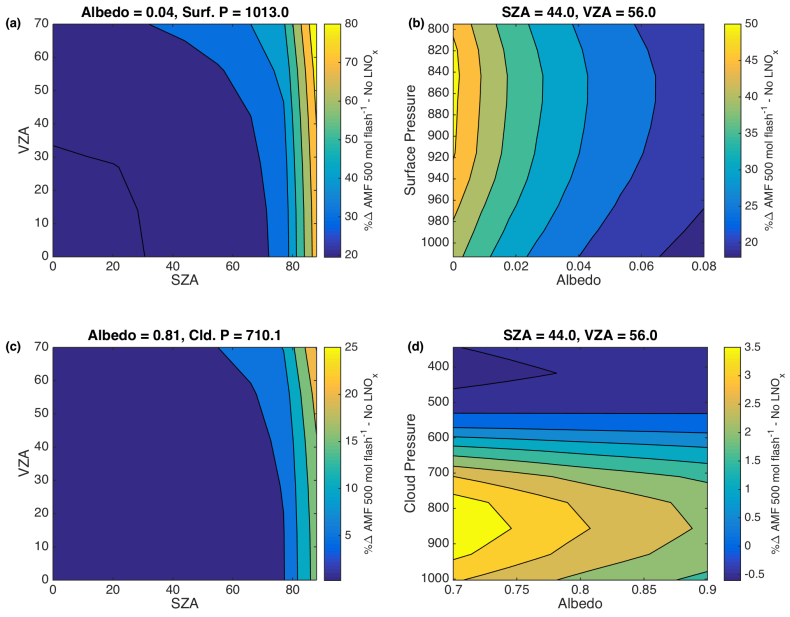

Figure 3.2: Contour plots of the percent change in the AMF when changing from the mean profile without lightning NO_x to the mean with lightning NO_x (500 mol flash^{-1}), averaged over the whole WRF-Chem domain. The differences are averaged over all values of RAA. In each plot, two parameters are varied while the other two are held constant. The values of the constant parameters are given above each plot. (a) and (b) use a range of albedos and surface pressure representative of clear pixels; (c) and (d) for cloudy pixels.

change averaged over all values of relative azimuth angle (RAA), since RAA has a small impact on the AMF (see Fig. C.1).

Under both clear and cloudy conditions, the largest differences in AMF between the two profiles are seen at large SZAs (Fig. 3.2a and c). This reflects the longer average optical path through the upper troposphere (UT) at larger SZAs, causing greater sensitivity to UT NO_2. A similar, though smaller, effect is also seen for larger VZAs.

If viewing geometry is held constant and albedo and surface pressure varied, the largest sensitivity of the AMF to simulated lightning NO_x can be seen at very low albedo and moderate surface pressure ($\sim$ 860 hPa) for clear conditions (Fig 3.2b). The cause for this is illustrated in Fig. 3.3; Fig. 3.3c shows how the scattering weight vectors change with albedo and Fig. 3.3d shows how they change with surface pressure. Lower albedos yield lower sensitivity to near-surface NO_2 (note that scattering weights are proportional to sensitivity) because a photon that reaches the near-surface NO_2 will likely be absorbed if it scatters into the surface (Hönninger et al., 2004). The 500 mol flash^{-1} profile does have more NO_2 in the

boundary layer than the no lightning profile, especially below 900 hPa. This partly balances the increase in UT NO_2 from lightning, as there are increases at both low and high sensitivity altitudes. As surface pressure decreases (i.e. higher in elevation), the altitude of minimum sensitivity moves up. The surface integration limit for Eq. (3.1) and (3.3) reduces as well, removing part of the boundary layer profile. Taken together, these changes put more weight on the UT profile and remove the < 900 hPa increase that counteracts part of the change in the UT (thus increasing the impact of lightning NO_x) until ~ 860 hPa. At ~ 860 hPa, most of the boundary layer is no longer included in the AMF calculation. Figure 3.1 shows that above ~ 800 hPa, the WRF-Chem profiles start to diverge due to the different amounts of lightning NO_x in each simulation. Therefore, as surface pressure moves above 850–800 hPa, the sensitivity to lightning NO_x begins to decrease because the entire extent of the profile that is integrated changes with changes in the simulated lightning NO_x. Since the profile is normalized to the column amount (Eq. 3.3), only the relative distribution of NO_2 matters, and the relative distribution changes very little with the magnitude of lightning NO_x emitted when only considering the part of the profile influenced by lightning NO_x.

The effect of changing surface pressure in a regular retrieval will likely be different than that described above, because the above analysis assumes that the profile does not change with surface pressure, where in fact it should, since surface-based emissions will move up with the surface. Consequently, the boundary layer maximum would not be cut off in that case. The effect described here is more consistent with the effect of clouds or an aerosol layer that creates an effectively higher altitude surface (due to scattering), or if using coarse enough a priori profiles that the surface pressure of a pixel is significantly different than the surface pressure in the model used to simulate the profile.

Cloudy conditions exhibit less sensitivity than clear conditions to the amount of lightning NO_x in the modeled profiles due to this shielding effect: in many cases, the cloud is at sufficiently high elevation to obscure the part of the NO_2 profile influenced by surface emissions, and therefore restricts the profile to the component influenced by lightning NO_x. As previously discussed with respect to surface pressure, this means that the relative distribution of NO_2 in the visible component of the profile does not change significantly. This is apparent in Fig. 3.2, where (c) and (d) show responses roughly $\frac{1}{4}$ and $\frac{1}{10}$ times, respectively, compared to (a) and (b).

Cloudy conditions also tend to have more uniform scattering weights (Fig. 3.4) due in large part to their high albedo. At high albedo, the probability of "losing" photons to absorption at the surface is significantly reduced, so the reduction in sensitivity towards the surface found with low albedos does not occur. At sufficiently high albedos, there is an enhancement in sensitivity near the cloud due to the possibility of extended optical paths near the surface from multiple scattering (Richter and Wagner, 2011).

From Fig. 3.4, it is clear why the impact of lightning NO_x is small in Fig. 3.2d. For

all but the most extreme sun-satellite geometries, the scattering weights are fairly uniform across all altitudes, thus the impact of changes to the relative distribution of NO_2 within the UT is minimized since a UV/visible satellite instrument is similarly sensitive to NO_2 at any altitude under these conditions. At larger SZAs and VZAs, the cloudy scattering weights do decrease towards the cloud because Rayleigh scattering has a greater effect on the transmitted light along the longer beam paths, scattering photons at higher altitudes and so reducing the fraction of photons observed by the satellite that penetrate to the cloud (Richter and Wagner, 2011). However, the impact is less than in clear conditions. From Fig. 3.2c, at the largest SZA and VZA simulated, the difference in AMF between the no lightning and 500 mol flash^{-1} profiles is +20–25%—large, but only one-fourth that of clear conditions.

The difference in the AMF obtained using profiles with 665 and 500 mol NO flash^{-1} follows essentially the same pattern as shown in Fig. 3.2, but with $\frac{1}{10}$ to $\frac{1}{5}$ the magnitude (Fig. C.2). The only difference in the shape of the contours is that the maximum difference occurs at greater (i.e. lower altitude) surface pressures, because the 665 and 500 mol flash^{-1} profiles are mostly identical in the boundary layer, so the slight countervailing increase in boundary layer NO_2 between the 0 and 500 mol flash^{-1} profiles that offset part of the UT increase is not present.

Comparison with observed profiles

Given the large sensitivity of AMFs to the presence of lightning NO_x in the a priori profiles, it is necessary to use a priori profiles that are consistent with observations. Figure 3.5 compares the average NO_2 profile measured in the DC3 campaign (Sect. 3.2) with WRF-Chem profiles averaged along the DC3 flights (Sect. 3.2) for five simulations. It is immediately apparent that the WRF-Chem simulation with no lightning is missing a significant amount of UT NO_2 compared to the observed DC3 profile. Both unnudged WRF-Chem simulations with lightning NO_x enabled do qualitatively capture this UT NO_2; however the vertical distribution is biased compared to the DC3 observations with a maximum at 500 hPa not seen in the observed profile and less NO_2 between 300–200 hPa than in the observed profile.

We consider how significant these differences between the simulated and observed profiles are in the context of the AMF calculation. To focus only on the effect of the UT profile, we use hybrid profiles. The hybrid profiles for the unnudged 500 mol flash^{-1} are illustrated in Fig. 3.5b. The free troposphere hybrid uses the DC3 profile up to 750 hPa and the WRF-Chem profile above that, while the mid-troposphere hybrid only uses the WRF-Chem profile between 750 and 375 hPa. The free tropospheric hybrid profile focuses on the effect of lightning NO_2 on the AMF by removing the difference in the boundary layer between the WRF-Chem and DC3 profiles, while the mid-troposphere hybrid similarly focuses on the effect of the local NO_2 maximum around 500 hPa that is not present in the DC3 profile.

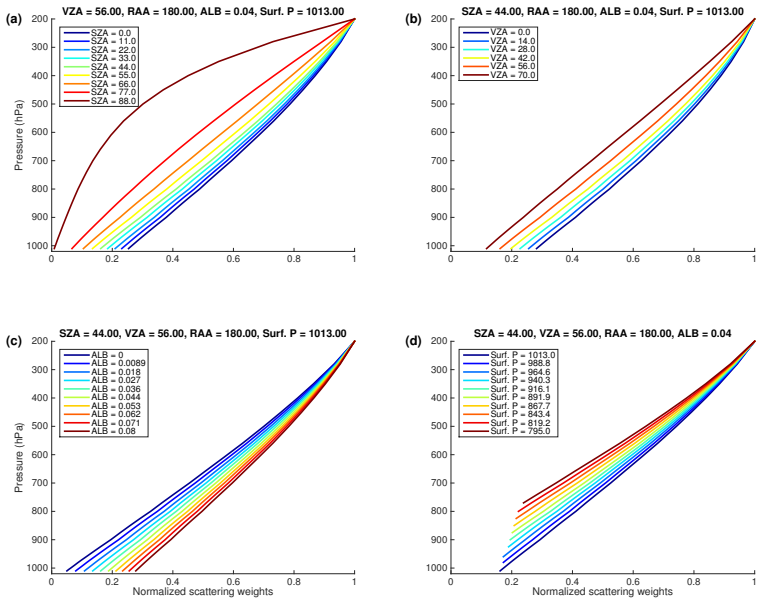

Figure 3.3: Vectors of scattering weights and their variation with each of the four most important look-up table input parameters. Values are representative of clear-sky conditions. Each scattering weight vector is scaled so that the top most entry is 1. Scattering weights are only shown above the surface pressure.

Table 3.2 gives the results of AMF sensitivity tests (Sect. 3.2) on various hybrid combinations of the profiles in Fig. 3.5a. We present the average AMF obtained in the sensitivity test using each hybrid profile, and its percent difference relative to the mean AMF obtained using the DC3 profile. Because OMI experiences a more limited range of solar zenith angles during summer over the US ($\sim$30°$\pm$ 6°, on average) than are defined in the TOMRAD look-up table, we also compare a subset of the AMF sensitivity tests with the SZA $<$ 40°.

Comparing the 0 mol flash^{-1} WRF-Chem profiles to the DC3 profile, we see that difference NO_2 above 375 hPa has a large impact on the AMF, causing a 25–35% low bias in the AMF, depending on the SZAs considered. Adding lightning NO_x to the WRF-Chem simulation (the 500 and 665 mol flash^{-1} profiles) corrects this bias. Recent work (Nault et al., 2017) suggests that the previous mean value of mol NO flash^{-1} (500 mol flash^{-1}) is 33% low; comparing the AMFs obtained from profiles generated with 500 and 665 mol flash^{-1} changes the sign of the AMF bias relative to the DC3 profile, but not its magnitude.

The purpose of including the mid-troposphere hybrid profiles, which only use the WRF-Chem profile between 700 and 375 hPa, is to evaluate the impact of the simulated NO_2 maximum around 500 hPa. In almost all cases, the bias of these hybrid profiles against the

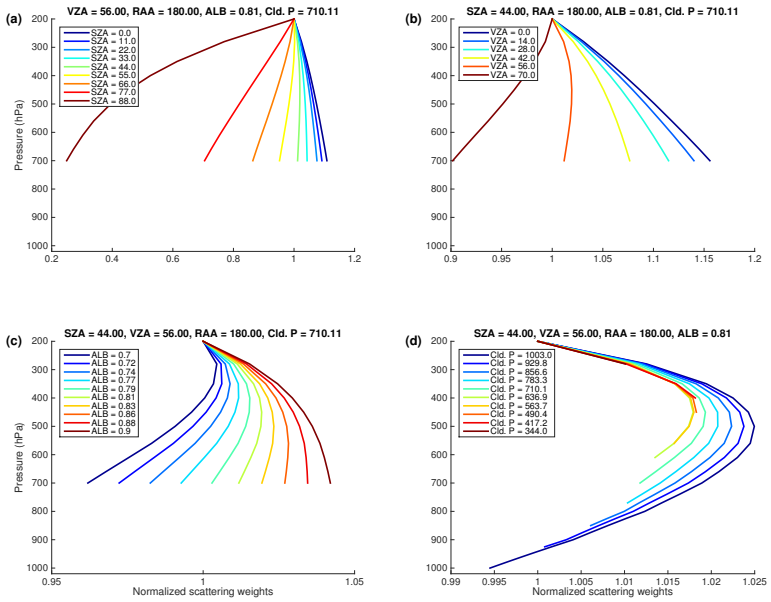

Figure 3.4: As in Fig. 3.3, but for cloudy conditions. Note that the x-axis limits are different from Fig. 3.3 and each other.

Profile	Avg. AMF	%Δ AMF vs. DC3	Avg. AMF SZA $< 40°$	%Δ AMF(SZA $< 40°$) vs. DC3
DC3	1.59	–	1.33	–
Free Trop. Hybrid-0	1.04	−34.42	0.99	−25.51
Mid. Trop. Hybrid-0	1.58	−0.80	1.31	−1.02
Free Trop. Hybrid-500	1.54	−3.56	1.31	−1.07
Mid. Trop. Hybrid-500	1.63	2.12	1.36	2.69
Free Trop. Hybrid-665	1.64	3.24	1.39	4.37
Mid. Trop. Hybrid-665	1.64	3.23	1.38	3.98
Free Trop. Hybrid-500, nudge	1.29	−19.18	1.15	−13.73
Mid. Trop. Hybrid-500, nudge	1.59	−0.07	1.33	−0.07
Free Trop. Hybrid-500, nudge, 2x flashrate	1.51	−5.52	1.29	−3.13
Mid. Trop. Hybrid-500, nudge, 2x flashrate	1.61	1.11	1.34	1.26

Table 3.2: Results of the AMF sensitivity tests on the hybrid profiles in Fig. 3.5

DC3 profile is less than the corresponding free-troposphere hybrid. Thus, that anomalous maximum at 500 hPa has a smaller impact than the overall presence or absence of lightning NO_2, as one would expect.

An additional complication arises when considering the effect of nudging the model meteorology. By default, the meteorology in WRF is driven by the model's internal physics and is constrained by reanalysis meteorology only through the initial and boundary conditions. WRF has the option, however, to constrain meteorology throughout the domain using four dimensional data analysis (FDDA) nudging. Temperature and water vapor mixing ratio can

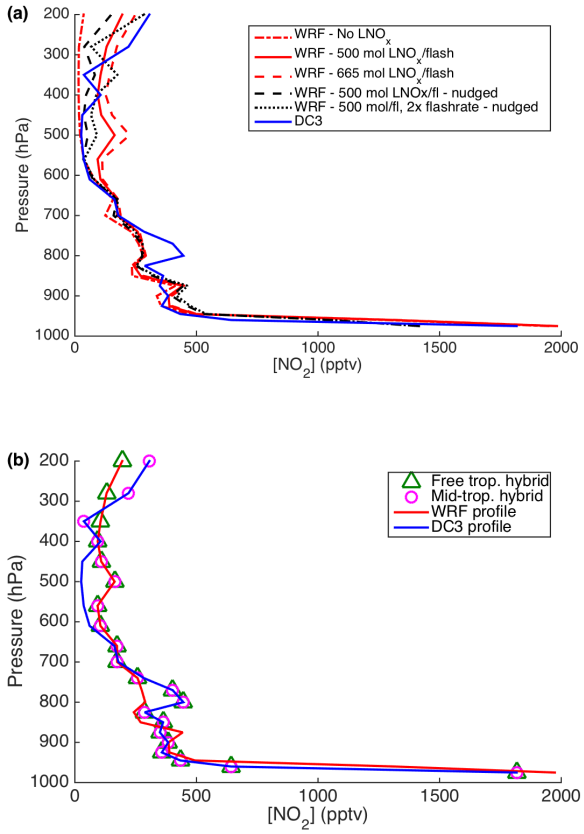

Figure 3.5: (a) Comparison of the NO_2 profiles obtained from binning all DC3 data and WRF-Chem output along the DC3 flight track (Sect 3.2) to pressure bins centered on the pressure the scattering weights are defined at. (b) The binned DC3 and WRF-Chem (500 mol flash^{-1}, no nudging) profiles; green triangles mark pressure levels from each profiles used in the free troposphere hybrid profile, magenta circles mark pressure levels used in the mid-troposphere hybrid profile.

both be nudged, and both are used in the Grell 3D cumulus physics calculation in WRF (Grell, 1993; Grell and Dévényi, 2002), which outputs the cloud top height that is used by the Price and Rind (1992) parameterization of flash rate.

With FDDA nudging, lightning flash rates throughout the domain decreased by approximately a factor of 2 compared to the unnudged case (Fig. C.3). Comparing both temperature and water vapor mixing ratios from nudged and unnudged simulations, we find that nudged and unnudged temperature profiles only differ by $\sim$ 1–2 K at each model level on average, and both agree well with DC3 measurements. The water vapor profiles change more significantly, and the profiles resulting from the nudged simulation agree better with those measured during DC3 (Fig. C.4). Therefore, we conclude that the changes to the water vapor profiles are responsible for the 2x change in lightning flash rates.

Using the NO_2 profiles resulting from the nudged simulation with 500 mol flash^{-1}, we see in Fig. 3.5a that there is significantly less simulated NO_2 near 200 hPa than in the unnudged run and the DC3 observations. The AMF sensitivity tests show that this reintroduces a 14–19% low bias compared to the AMF derived from the DC3 profile, a significant increase in the bias compared to the unnudged simulation. Doubling the flash rate largely corrects this bias by increasing the NO_2 found in the upper part of the profile (Fig. 3.5a).

Effect of varied lightning emissions on BEHR AMFs

To illustrate the impact of missing lightning NO_x on a full retrieval, we use the unnudged WRF-Chem NO_2 profiles simulated with 0, 500 and 665 mol NO flash^{-1} as a priori profiles in the BEHR retrieval and examine the change in both AMF and retrieval NO_2 vertical column density (VCD) with the change in simulated lightning NO_x.

Figure 3.6 shows the average percent change in AMFs (top) and absolute change in VCDs (bottom) between retrievals using profiles generated using 0 and 500 mol NO flash^{-1} (Fig. 3.6a, c) and between 500 and 665 mol NO flash^{-1} (Fig. 3.6b, d). These results were obtained by averaging data from 18 May to 23 June 2012, treating the data as described in Sect. 3.2.

Most importantly, we see in Fig. 3.6a that the change due to the inclusion of lightning NO_2 is not constant throughout the domain, but is regionally specific. The SE US sees the greatest change in AMF, as it has very active lightning (Hudman et al., 2007). This leads to changes in the retrieved VCD of 1 to 2×10^{15} molec. cm^{-2}.

We consider two uncertainty values to determine if this change is significant. Bucsela et al. (2013) calculated a global mean uncertainty of 1×10^{15} molec. cm^{-2} for tropospheric NO_2 VCDs. Boersma et al. (2004) calculated a typical uncertainty of 23% in tropospheric AMFs for polluted conditions. Since, on average, 32 ± 6 (mean $\pm$ 1 σ) pixels contribute to each value in our average, the reduced uncertainty is $\sim 0.2 \times 10^{15}$ molec. cm^{-2} and 4%, respectively. The changes we find in the tropospheric VCD due to the inclusion or exclusion of lightning

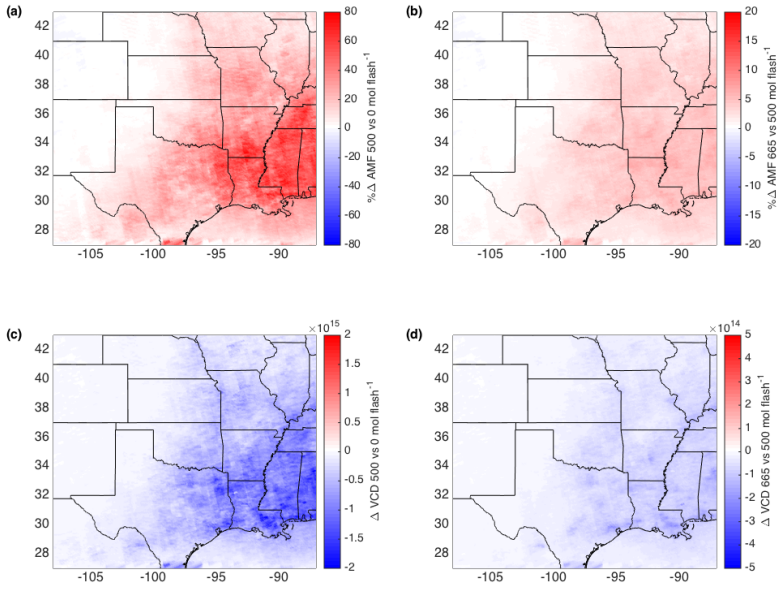

Figure 3.6: Average percent difference in AMFs (a,b) and absolute difference in VCDs (c,d) averaged over the time period 18 May–23 June 2012. (a,c) Difference between profiles generated using 500 mol NO flash^{-1} and 0 mol NO flash^{-1}; (b,d) Difference between profiles generated using 665 mol NO flash^{-1} and 500 mol NO flash^{-1}. Note that in (c) and (d) the color scale is one-fourth that of (a) and (b).

NO_2 from the a priori profiles exceed that uncertainty in $\sim 50\%$ of the domain; the changes in the AMF exceed the uncertainty in $\sim 70\%$ of the domain.

The effect on the retrieval from increasing the mol NO flash^{-1} from 500 to 665 is about 5–10x smaller, as seen in Fig. 3.6b, d. In Fig. 3.1 and Fig. 3.5, we saw that the change in the UT profile was smaller when increasing the mol flash^{-1} from 500 to 665 compared to increasing from 0 to 500 as expected. The nonlinear nature of the AMF calculation also contributes to the smaller change in AMFs and VCDs between 500 and 665 mol flash^{-1} profiles; as the contribution of lightning NO_2 increases, both the numerator (at the relevant pressure levels) and denominator of Eq. (3.3) increase. The increasing denominator will cause the same magnitude increase in the numerator to have a smaller effect on the overall AMF.

3.4 Discussion

Accurately representing lightning NO_2 in a priori profiles for retrieval of NO_2 from space is vital not only when retrieving lightning events, but any retrieval in a region and time period

influenced by lightning. Work from the DC3 campaign has shown that the lifetime of NO_x in the near field of thunderstorms is remarkably short ($\sim$ 3 h, Nault et al., 2016) due to active chemistry with peroxy radical species convected from the surface. We note that the WRF-Chem model used here may not be adequately capturing this near-field chemistry as the simulated concentrations of methyl peroxy nitrate (MPN) are significantly lower than those measured by the DC3 campaign, particularly in the range of 300 to 400 hPa. We suspect that modeled concentrations of the methyl peroxy radical precursor are too low, but have not investigated this. However, we do not believe this significantly impacts our conclusions, as when we bin the DC3 MPN data as in Fig. 3.5, the MPN concentration is $\frac{1}{5}$ to $\frac{1}{10}$ that of NO_x, so the effect on the AMF is expected to be less than the effect of increasing the modeled mol NO flash^{-1} from 500 to 665.

As discussed in Nault et al. (2017), once those peroxy radicals are depleted, the UT lifetime of NO_x in the far-field from thunderstorms is in the range of 0.5 to 1.5 days (Nault et al., 2016; Nault et al., 2017). As shown in Sect. 3.3, this means that the presence or absence of lightning NO_2 in the a priori profiles has a large effect on the retrieval AMFs in clear-sky conditions which are used to obtain information about boundary layer NO_x (e.g. Lamsal et al., 2010; Beirle et al., 2011; Valin et al., 2013; Lamsal et al., 2015; Lu et al., 2015; Liu et al., 2016; Liu et al., 2017). Since many of these studies focus on summer months when thunderstorms are common over the US (Barth et al., 2015), the inclusion of lightning NO_2 in the a priori profiles is necessary to accurately constrain the emissions. Lightning is less frequent in wintertime, but the southeast US does experience winter lightning (Orville et al., 2001; Hunter et al., 2001). Therefore, wintertime retrievals will likely see significantly less but nonzero impact from the inclusion of lightning NO_2 in the a priori profiles. Future work will verify this as new a priori profiles are planned for inclusion in the next generation of the BEHR retrieval. These new a priori profiles will correct the absence of modeled lightning NO_2 in the BEHR v2.1C a priori profiles.

Effect of nudged meteorology on flash counts

Although our results showed that the NO_2 profile resulting from the nudged run without doubled flash counts had less UT NO_2 than the average DC3 profile, we cannot conclude that the flash rates calculated with nudged meteorology are underestimated, particularly as Wong et al. (2013) found the opposite result when comparing to the National Lightning Detection Network. A direct comparison with Wong et al. (2013) is complicated by the different choices of model options (such as cumulus physics: Grell 3D in ours vs. Grell-Devenyi in Wong; Lin vs. Thompson microphysics; NARR vs. NCEP Global Forecasting System Final meteorology). A full analysis of the reason that activating FDDA nudging causes the flash rates to decrease by 50% in our case is beyond the scope of this paper. Empirically, we see that the NO_2 profile generated by the FDDA run with 1x the base flash rate has less UT NO_2 than was observed during DC3 (Fig. 3.5). Therefore, we cannot say whether this discrepancy in the profile is due to the reduced number of flashes or a too-low

average number of moles of NO emitted per flash. Our correction of doubling the nudged flash rate to improve agreement between the modeled and observed profiles was the most straightforward based on the differences between the nudged and unnudged runs.

Laughner et al. (2016) showed the importance of using daily, high-spatial resolution a priori profiles to accurately resolve differences in NO_2 VCDs upwind and downwind of a city, and suggested the use of nudging to reduce the uncertainty due to wind direction, especially. Those results also indicated that using daily, high spatial resolution profiles is essential to directly constrain emissions with satellite observations. Our results here indicate that (1) missing lightning NO_2 in the a priori profiles will lead to large overestimations of VCDs, which, among other things, would lead to overestimates of NO_x emissions based on such a retrieval, and (2) that when using nudging within a WRF-Chem simulation to constrain the meteorology, its effect on lightning flash rates must be checked to ensure it does not inadvertently affect the upper tropospheric NO_2 profile.

Relevance to cloud slicing

In the context of work using cloud-slicing techniques to derive NO_2 profiles (e.g. Choi et al., 2014), our results suggest that profile shape is a minor contribution to the uncertainty. By using a simulated retrieval with a known NO_2 concentration profile, Choi et al. (2014) estimated 20–30% uncertainty in the NO_2 concentration derived from their cloud-slicing approach. Our work here shows that, for fully cloudy conditions, the change in the AMF between a no lightning and 500 mol flash^{-1} NO_2 profile is $\leqslant 5\%$ (Sect. 3.3). Since Choi et al. (2014) used a typical C-shaped NO_2 profile that included lightning NO_2 (e.g. Pickering et al., 1998), based on our results, we expect that any uncertainty should be closer to the difference we observed between the 500 and 665 mol flash^{-1} profiles, $\leqslant 1\%$, although we acknowledge that the analysis in Choi et al. (2014) may include additional sources of uncertainty not captured by our work.

Relevance to global and geostationary retrievals

To the best of our knowledge, the chemical transport models used to generate the a priori profiles in the NASA Standard Product and KNMI DOMINO product for OMI NO_2 include lightning NO_x in the simulation. However, for researchers wishing to generate high spatial resolution a priori profiles using models such as WRF-Chem or the Community Multiscale Air Quality (CMAQ) model that have thus far focused on lower troposphere chemistry for air quality implications, it is important to verify whether that model setup includes lightning NO_x. Retrievals that use a priori profiles without a lightning NO_x parameterization will suffer from a regionally dependent, systematic positive bias in retrieved VCDs. This is particularly difficult to account for given that the bias is unlikely to be reduced by averaging, nor is it constant enough spatially to be addressed as a coarse, ad hoc correction to the AMF.

The next generation of polar orbiting (TROPOMI) and geostationary (TEMPO, Sentinel-5, GEMS) UV-visible spetrometers will have even greater spatial resolution than OMI. To get the most value out of these high spatial resolution detectors, high spatial and temporal resolution a priori profiles are necessary (e.g. Russell et al., 2011; Laughner et al., 2016; Goldberg et al., 2017). High resolution air quality models, such as WRF-Chem or CMAQ, are one avenue to produce a priori profiles with resolution of 1 to 10 km. Ensuring that lightning NO_x is adequately parameterized in the models is essential for any retrieval, but especially for geostationary satellites such as TEMPO, which will retrieve NO_2 at larger solar zenith angles than polar orbiting satellites. At such large SZAs, the relative importance of accurate UT NO_2 profiles is even greater than for OMI retrievals.

3.5 Conclusions

We quantify the impact of lightning NO_2 on a priori profiles used in satellite retrievals of NO_2. We find that, on average, compared to an average NO_2 profile constructed from measurements taken during the DC3 campaign, excluding lightning NO_2 leads to a -35% bias in the AMF if all solar zenith angles are considered, and -25% for solar zenith angles relevant to the OMI instrument in the summer. We find that, using the Price and Rind (1992) parameterization in WRF-Chem with the Grell-3D cumulus model, 500 to 665 mol NO flash^{-1} yields AMFs within $\sim 5\%$ of those obtained using the DC3 profile. We also find that, if FDDA nudging is used, flash rates must be multiplied by a factor of 2 to get the same agreement with this model configuration.

Implementing profiles generated with 0, 500, and 665 mol NO flash^{-1} in the BEHR retrieval, we find that the effect on the AMF is very regionally dependent. For summertime retrievals, changing from profiles using 0 mol NO flash^{-1} to 500 mol NO flash^{-1} shows the largest increase in the AMF of 50–80% occurring in the SE US. This results in changes to the VCD of 1 to 2×10^{15} molec. cm^{-2}. The effect is nearly 0 on the west edge of the domain, over the Rocky Mountains. Further increasing the mol NO flash^{-1} from 500 to 665 only results in a $\sim 5\%$ change to the AMF.

Chapter 4

The Berkeley High Resolution Product

The chapter was adapted from: J. L. Laughner, Q. Zhu, and R. C. Cohen (2018b). "The Berkeley High Resolution Tropospheric NO_2 Product". *Earth Syst. Sci. Data Discuss.* 2018, pp. 1–33. DOI: 10.5194/essd-2018-66

4.1 Introduction

Nitrogen oxides (NO + $NO_2 \equiv NO_x$) are trace gases in the atmosphere and are key species controlling air quality and affecting radiative balance. NO_x regulates the chemical production of tropospheric ozone (Jacob et al., 1993), which affects the radiative balance in the upper troposphere (Myhre et al., 2013) and is harmful to plants (Haagen-Smit et al., 1952; Heath, 1975), animals, and humans (Menzel, 1984) at the surface. NO_x directly affects the radiative balance of the atmosphere (e.g. Kiehl and Solomon, 1986). It also plays a role in the formation of aerosol particles (Izumi and Fukuyama, 1990; Pandis et al., 1992; Carlton et al., 2009; Rollins et al., 2012), which also affect the radiative balance of the atmosphere (Boucher et al., 2013). Exposure to fine particles is also a strong factor controlling life expectancy (Pope et al., 2009). Additionally, NO_x itself is harmful (Kagawa, 1985; Chauhan et al., 1998; Wegmann et al., 2005; Kampa and Castanas, 2008).

NO_x is emitted from a variety of sources, both anthopogenic and natural. Anthropogenic sources typically involve combustion, including motor vehicles and fossil fuel electrical generation. Natural sources include biomass burning, lightning, and soil bacteria. Understanding all of these sources is crucial to understanding the reactive nitrogen budget and predicting how future changes in emissions will affect air quality and climate change.

Satellite observations provide uniquely comprehensive spatial maps of NO_2, allowing inference of NO_x emissions. Early instruments (i.e. the Global Ozone Monitoring Experiment,

GOME, and the SCanning Imaging Absorption SpectroMeter for Atmospheric CHartographY, SCIAMACHY) allowed inferences at the scale of entire continents or entire metropolitan regions, including cities and their surroundings. More recent instruments (the Ozone Monitoring Instrument, OMI, and Tropospheric Monitoring Instrument, TROPOMI) have much higher resolution, allowing inferences about individual point sources and urban cores. Ground based measurements sample emissions at specific points in great detail; however, extrapolating such measurements to an entire region requires assumptions that are difficult to test, such as fleet composition and operating mode (e.g. Fujita et al., 2012; Anderson et al., 2014), that can bias estimates of the total vehicle emissions from a region. Satellite observations cannot currently provide the same level of detail as a roadside measurement, but by observing the entire city, provide a top-down constraint on its total NO_x emissions that include observations on every point in the domain. Satellite observations have been used in a wide variety of applications in this vein, including direct observation of emissions and trends (e.g. Russell et al., 2012), plume analysis to derive emissions and chemical lifetime (e.g. Beirle et al., 2011; Valin et al., 2013; Lu et al., 2015; Liu et al., 2016; Liu et al., 2017), model constraint (e.g. Travis et al., 2016), and data assimilation (e.g. Miyazaki et al., 2012a; Miyazaki et al., 2017).

Satellite measurements have also been used to constrain natural NO_x sources as well, predominantly biomass burning (e.g. Mebust et al., 2011; Huijnen et al., 2012; Mebust and Cohen, 2013; Mebust and Cohen, 2014; Bousserez, 2014; Schreier et al., 2014; Castellanos et al., 2015; Marle et al., 2017), lightning (e.g. Beirle et al., 2004; Martin et al., 2007; Beirle et al., 2010a; Bucsela et al., 2010; Miyazaki et al., 2014; Pickering et al., 2016; Nault et al., 2017), and soil NO_x (e.g. van der A et al., 2008; Hudman et al., 2010; Hudman et al., 2012; Zörner et al., 2016). The episodic and geographically disparate nature of these sources (especially lightning and biomass burning) make satellite observations an ideal method to constrain their emissions, given satellites' continuous data record and broad geographic coverage.

The absorption of NO is in the UV, making it too difficult to observe. In contrast, the visible absorbance of NO_2 is strong and inferences about total NO_x are made from NO_2 measurements. For a measurement of tropospheric NO_2, several steps are required. First, a UV-visible spectrometer records geolocated solar reflectances from the Earth's surface and a reference spectrum of the sun. Then, absorbances in backscattered sunlight are fit using differential optical absorption spectroscopy (DOAS) or a similar technique to yield a total slant column density (SCD). This quantity represents the amount of NO_2 per unit area, integrated along all light paths that reach the detector (Boersma et al., 2002; Richter and Wagner, 2011). Next, the tropospheric and stratospheric NO_2 columns are separated. There are several approaches; some examples include using a data assimilation system to constrain modeled stratospheric columns (Boersma et al., 2011) and an iterative process assuming that areas known a priori to have little tropospheric NO_2 are all stratospheric NO_2 and interpolating to fill in polluted areas (Bucsela et al., 2013). Finally, the tropospheric SCD is converted into a vertical column density (VCD) in order to account for pixel-to-pixel

differences in path length and sensitivity to NO_2. The conversion factor from the SCD to the more geophysically relevant and easily understood VCD is called the air mass factor (AMF, Palmer et al., 2001; Burrows et al., 1999; Slusser et al., 1996; McKenzie et al., 1991).

An AMF is computed by simulating an SCD and VCD for each retrieved pixel. Typically, an a priori NO_2 profile is simulated with a chemical transport model (CTM) such as GEOS-Chem, WRF-Chem, the GMI-CTM, or TM4. The modeled VCD can be calculated by integrating this profile over the troposphere. The modeled SCD requires a radiative transfer model, such as TOMRAD, SCIATRAN, VLIDORT, etc., in combination with the a priori NO_2 profile in order to compute the light absorbed by NO_2 and thus the SCD that yields that absorbance.

The radiative transfer calculations also require a priori inputs: the sun-satellite geometry, surface reflectance, and surface elevation are all necessary. Knowledge of the cloud and aerosol properties in the pixel is also necessary to account for their effects on light scattering in the radiative transfer calculations. Aerosol effects are often assumed to be implicitly accounted for in cloud properties (e.g. Boersma et al., 2011) but have been treated explicitly by some retrievals (e.g. Lin et al., 2015).

The accuracy of these input data has a significant impact on the accuracy of the retrieved columns. Lorente et al. (2017) compared seven retrievals and found that input assumptions were responsible for a 42% structural uncertainty in AMFs over polluted areas. A key concern is the resolution of the input data. CTMs are computationally expensive, requiring a trade-off between spatial and temporal resolution and domain size. For global retrievals, model resolutions of $3^\circ \times 2^\circ$ (Boersma et al., 2011) to $1^\circ \times 1^\circ$ (Krotkov et al., 2017) are typical. Russell et al. (2011) found that increasing the resolution of the NO_2 profiles to 4 km altered the retrieved VCDs by up to 75%, primarily by capturing the urban-rural gradient in surface NO_2 concentrations. McLinden et al. (2014) found that increasing the a priori profiles' resolution to 15 km resulted in a factor of 2 increase in NO_2 column over the Canadian Oil Sands. Laughner et al. (2016) examined the effect of the profiles' temporal resolution, and identified up to 40% changes in individual VCDs using day-to-day NO_2 profiles compared to monthly averaged profiles. The current trade off to obtain such high resolution profiles is that the retrieval is restricted to a region of the world.

The Berkeley High Resolution (BEHR) Ozone Monitoring Instrument (OMI) NO_2 retrieval is one such regional retrieval that provides tropospheric NO_2 VCDs over the continental United States using high resolution a priori inputs. Here we describe the updates from v2.1C to v3.0B. There are eight primary changes:

1. Updated to use the v3.0 NASA tropospheric SCDs
2. Surface reflectance updated from version 5 MODIS black sky albedo to version 6

MODIS BRDF product

3. A more physically intuitive visible-only AMF calculation was implemented (the standard total tropospheric AMF calculation is unchanged)
4. New a priori NO_2 profiles, with specific changes:
   a) Lightning NO_2 included
   b) Monthly profiles use 2012 emissions
   c) Daily profiles used for as many years as possible
5. Temperature profiles taken from WRF-Chem instead of the previous coarse climatology
6. A new gridding method was implemented
7. A variable tropopause height derived from WRF simulations replaced the previous fixed 200 hPa tropopause in the AMF calculations.
8. Surface pressure calculation was changed to follow Zhou et al. (2009) using GLOBE terrain elevation and WRF surface pressure

In this paper, we describe each change in detail and examine the effect of each individual change on the retrieved VCDs. Changes implemented in v3.0A are described first, followed by those implemented in v3.0B. The evaluation of v3.0B is described in Chapter 5.

4.2 Methods: BEHR

NO_2 VCD calculation

The BEHR product calculates tropospheric vertical column densities (VCDs) starting with the tropospheric slant column densities (SCDs) from the NASA Standard Product, v3.0 (Krotkov et al., 2017; Krotkov and Veefkind, 2016), by:

$$V_{\mathrm{BEHR}} = \frac{S_{\mathrm{NASA}}}{A_{\mathrm{BEHR}}} \tag{4.1}$$

where V_{BEHR} and S_{NASA} are the BEHR VCD and NASA SCD, respectively, and A_{BEHR} is a custom tropospheric air mass factor (AMF), computed with

$$A_{\mathrm{BEHR}} = \frac{(1-f)\int_{p_{\mathrm{surf}}}^{p_{\mathrm{trop}}} w_{\mathrm{clear}}(p)g(p)\,dp + f\int_{p_{\mathrm{cloud}}}^{p_{\mathrm{trop}}} w_{\mathrm{cloudy}}(p)g(p)\,dp}{\int_{p_{\mathrm{surf}}}^{p_{\mathrm{trop}}} g(p)\,dp} \tag{4.2}$$

where f is the cloud radiance fraction, and w_{clear} and w_{cloudy} are the scattering weights for clear and cloudy subscenes (i.e. parts of the pixel), respectively, p_{trop} is the tropopause pressure, p_{surf} is the ground surface pressure, p_{cloud} is the cloud optical centroid pressure, and $g(p)$ is the NO_2 a priori profile.

This method produces VCDs that include an estimated below cloud component, and thus can be considered a total tropospheric column. This is desirable for applications focusing on near-surface NO_2. Other applications (e.g. cloud slicing) benefit from having a "visible-only" tropospheric AMF that only retrieves NO_2 above the cloud in a cloudy subscene. For these "visible-only" AMFs, Eq. (4.2) is replaced with:

$$A_{\text{BEHR,vis}} = \frac{(1-f)\int_{p_{\text{surf}}}^{p_{\text{trop}}} w_{\text{clear}}(p)g(p)\,dp + f\int_{p_{\text{cloud}}}^{p_{\text{trop}}} w_{\text{cloudy}}(p)g(p)\,dp}{(1-f_g)\int_{p_{\text{surf}}}^{p_{\text{trop}}} g(p)\,dp + f_g\int_{p_{\text{cloud}}}^{p_{\text{trop}}} g(p)\,dp} \tag{4.3}$$

where f_g is the geometric cloud fraction. The numerator is the same as in Eq. (4.2); in both cases representing a modeled slant column density. The denominator Eq. (4.2) is the total modeled tropospheric column, while in Eq. (4.3) it is only the visible modeled column. Replacing A_{BEHR} in Eq. (4.1) with $A_{\text{BEHR,vis}}$ yields a visible-only NO_2 column as the output.

The scattering weights (w_{clear} and w_{cloudy}) are computed from the same look-up table (LUT) as the NASA SP v2.1 and v3.0 (Bucsela et al., 2013; Krotkov et al., 2017). The scattering weights depend on the solar zenith angle (SZA, θ_S), viewing zenith angle (VZA, θ_V), relative azimuth angle (RAA, ϕ_R), surface reflectance, and surface pressure. A vector of scattering weights is looked up using 5D multilinear interpolation to obtain the scattering weights for the above input parameters. Note that the RAA is calculated as

$$\phi_{R,\text{tmp}} = |180 + \phi_S - \phi_V| \tag{4.4}$$

$$\phi_R = \begin{cases} \phi_{R,\text{tmp}} & \text{if} \quad \phi_{R,\text{tmp}} \in [0, 180] \\ 360 - \phi_{R,\text{tmp}} & \text{if} \quad \phi_{R,\text{tmp}} > 180 \end{cases} \tag{4.5}$$

where ϕ_S and ϕ_V are the solar and viewing azimuth angles, respectively, defined in degrees, and $\phi_{R,\text{tmp}}$ is a temporary variable. The extra factor of 180 in Eq. (4.4) accounts for the RAA definition used in the scattering weight look up table (where $\phi_R = 0$ indicates that the satellite is opposite the sun, i.e. in the forward scattering position), while Eq. (4.5) ensures that ϕ_R is between 0°and 180°.

A temperature correction, $\alpha(p)$ is applied to the scattering weights interpolated from the look-up table, such that $w(p)$ in Eqs. (4.2) and (4.3) is equal to $\alpha(p)w_0(p)$, where $w_0(p)$ is the pressure-dependent scattering weights from the look-up table and $\alpha(p)$ is

$$\alpha(p) = 1 - 0.003 \cdot (T(p) - 220) \tag{4.6}$$
$$\alpha(p) \in [0.1, 10] \tag{4.7}$$

where Eq. (4.7) indicates that $\alpha(p)$ is constrained to the range 0.1 to 10. $T(p)$ is a temperature profile taken from the same WRF-Chem simulation as the NO_2 a priori profiles.

Surface reflectivity

Over land

BEHR v3.0B uses a bidirectional reflectance factor (BRF) to represent surface reflectivity over land. The BRF is given by (Stahler et al., 1999)

$$R(\theta_S, \theta_V, \phi_R, \Lambda) = f_{\text{iso}}(\Lambda) + f_{\text{vol}}(\Lambda)K_{\text{vol}}(\theta_S, \theta_V, \phi_R) + f_{\text{geo}}(\Lambda)K_{\text{geo}}(\theta_S, \theta_V, \phi_R) \tag{4.8}$$

where R is the surface reflectivity, f_{iso}, f_{vol}, and f_{geo} are coefficients representing the relative contributions of different types of scattering, and K_{vol} and K_{geo} are kernels representing the directional dependence of the reflectivity. Λ represents a wavelength band, which here is band 3 of the MODIS instrument (459–479 nm).

K_{vol} is the RossThick kernel (Roujean et al., 1992) and K_{geo} is the LiSparse kernel (Wanner et al., 1995), corrected to be reciprocal in θ_S and θ_V. BEHR calculates both kernels using the formulations given in Stahler et al. (1999). The coefficients, f_{iso}, f_{vol}, and f_{geo}, are taken from the MODIS MCD43D07 (Schaaf, 2015a), MCD43D08 (Schaaf, 2015b), and MCD43D09 (Schaaf, 2015c) BRDF products, respectively. Quality information for these coefficients is obtained from the MCD43D31 product (Schaaf, 2015d). (The combination of these four products will henceforth be referred to as MCD43Dxx.) These products represent a 16-day average; in version 006 (used here), the file date is in the middle of that 16-day averaging window. BEHR uses the file dated for the day being retrieved for the BRF coefficients.

An average surface reflectance for a given OMI pixel is calculated by computing R for each set of MCD43Dxx coefficients within the bounds of the pixel given by the FoV75 corners from the OMPIXCOR product (Kurosu and Celarier, 2010) and using the SZA, VZA, and RAA of the pixel as inputs to the kernels. All values of R from MCD43Dxx coefficients with non-fill quality flags are averaged to produce the overall surface reflectance for the pixel; however, since coefficients with quality 3 are significantly lower quality than quality 0 to 2, if the average quality of all MCD43Dxx coefficients within the OMI pixel is ≥ 2.5, the pixel is flagged as low quality. The pixel is also flagged if $\geq 50\%$ of the MCD43Dxx coefficients have a fill value for the quality (see Sect. D.1).

Wavelength	430 nm (v3.0A), 460 nm (v3.0B)
Atmospheric profile	MLS
Boundary layer aerosol model	MODTRAN Maritime
Stratospheric aerosol model	Background stratosphere
Total aerosol loading	AOD at 500 nm = 1
Wind speed	5 m s^{-1}
Ocean depth	100 m
Chlorophyll	0.2 mg m^{-3}
Ocean particle scattering	Petzold Average, $bb/b = 0.0183$
Bottom surface albedo	0.1

Table 4.1: Additional settings for the COART model used to simulate ocean reflectivity.

Over water

The MCD43Dxx products do not contain coefficients over deep water; therefore, an alternate measure of surface reflectance is needed. We use the University of Maryland land map (`ftp://rsftp.eeos.umb.edu/data02/Gapfilled/Land_Water_Mask_7Classes_UMD.hdf`, accessed 28 Nov 2017) to classify OMI pixels as land or water. Land classes 0 (shallow ocean), 6 (moderate or continental ocean), and 7 (deep ocean) are considered ocean; all others are considered land. The mask is given at 30 arc second resolution; if $> 50\%$ of the mask data points within the FoV75 bounds of the OMI pixel are ocean, the pixel is treated with an ocean surface reflectance.

Ocean surface reflectance is parameterized by SZA using output from the Coupled Ocean Atmosphere Radiative Transfer (COART) model (Jin et al., 2006, hosted at `https://satcorps.larc.nasa.gov/jin/coart.html`, accessed 2 Mar 2018). The ratio of upwelling to downwelling radiation was simulated for solar zenith angles between 0° and 85° at 5° increments. Additional settings are given in Table 4.1. The ratio of upwelling to downwelling radiation is linearly interpolated to the SZA of the OMI pixel, and that interpolated ratio is taken as the surface reflectance of the ocean pixel.

Surface pressure

The surface elevation of each OMI pixel is computed by averaging all surface elevation values from the Global Land One-kilometer Base Elevation (GLOBE) database (Hastings and Dunbar, 1999) within in FoV75 bounds of the pixel. In BEHR versions prior to v3.0B, this is converted to a surface pressure with

$$p = (1013.25\,\text{hPa})e^{-z/7400\,\text{m}} \tag{4.9}$$

where z is the average surface elevation in meters. From v3.0B on, pixel surface pressure is calculated using the method recommended by Zhou et al. (2009):

$$p = p_{\mathrm{WRF}} \left(\frac{T_{\mathrm{WRF}}}{T_{\mathrm{WRF}} + \Gamma \cdot (h_{\mathrm{WRF}} - h_{\mathrm{GLOBE}})} \right)^{-g/R\Gamma} \tag{4.10}$$

where p is the pixel surface pressure, p_{WRF}, T_{WRF}, and h_{WRF} are the surface pressure, temperature, and elevation from the WRF model, h_{GLOBE} is the averaged GLOBE surface elevation, g is gravitational acceleration (9.8 m s^{-2}), R is the gas constant for dry air (287 J kg^{-1} K^{-1}) and Γ the lapse rate (0.0065 K m^{-1}).

Tropopause Pressure

BEHR v3.0A and prior versions used a fixed tropopause pressure (200 hPa), BEHR v3.0B utilizes thermal tropopause pressure derived from the temperature profile from the same WRF-Chem simulation as the NO_2 a priori profiles. The thermal tropopause is defined as the lowest level at which the average lapse rate between this level and all higher levels within 2 km does not exceed 2 K km^{-1} by the World Meteorological Organization (1957). The calculation operationally works in most regions, however, occasionally a discontinuity occurs between adjacent pixels where both pixels approach the 2 K km^{-1} threshold at the same model level but only one exceeds the threshold at that level. As this discontinuity is only due to the choice of the standard threshold for lapse rate in the criteria, an additional filtering is implemented to identify pixels with abrupt transition in calculated tropopause pressure. New tropopause pressures for these pixels are derived by linear interpolation of tropopause pressures from the nearest valid pixels after filtering.

Cloud products

BEHR v3.0B contains several cloud fraction products: an OMI-derived geometric and radiance cloud fraction, a geometric cloud fraction derived from the Aqua MODIS instrument, and cloud pressure from the OMI O_2-O_2 algorithm (Acarreta et al., 2004). The OMI-derived quantities are the same as those in the NASA SP v3.0. The MODIS cloud product used is MYD06_L2 (Platnick et al., 2015). As with the MODIS BRDF product, all values of cloud fraction given in MYD06_L2 within each OMI pixels bounds defined by the FoV75 pixel corners are averaged to yield the MODIS-derived cloud fraction for that OMI pixel. Unlike the BRDF product, only Level 2 MODIS granules with times between the start and end time of the current OMI orbit are used.

A priori profiles

WRF-Chem configuration

NO_2 and temperature a priori profiles are generated using version 3.5.1 of WRF-Chem (Grell et al., 2005) run at 12 km resolution across the continental United States (Fig. D.1). The North American Regional Reanalysis (NARR) dataset is used to drive the meteorological initial and boundary conditions, as well as four-dimensional data analysis (FDDA) nudging (Liu et al., 2006). U and V winds, as well as temperature and water vapor are nudged at all levels with nudging coefficients of 0.0003 s^{-1}.

Anthropogenic emissions are driven by the National Emissions Inventory 2011 (NEI 11) gridded to 12 km resolution. Each years' emissions are scaled by the ratio of that year's total annual emissions to 2011 emission. These total emissions are provided by the Environmental Protection Agency (EPA, 2016). Biogenic emissions are driven by the Model of Emissions of Gases and Aerosols from Nature (MEGAN, Guenther et al., 2006). Lightning emissions are driven by the recommended settings in Laughner and Cohen (2017) for a simulation using FDDA nudging.

Chemistry in WRF-Chem is simulated using the RACM2_Berkeley2 mechanism (Zare et al., 2018), which is based on the Regional Atmospheric Chemistry Mechanism, version 2 (RACM2, Goliff et al., 2013) with updates to alkyl nitrate and nighttime chemistry (Browne et al., 2014; Schwantes et al., 2015) and the inclusion of methylperoxy nitrate (MPN) chemistry (Browne et al., 2011; Nault et al., 2015; Nault et al., 2016).

For model years 2007 and later, output from the Model for Ozone and Related chemical Tracers (MOZART, Emmons et al., 2010) provided by the National Center for Atmospheric Research (NCAR) at `https://www.acom.ucar.edu/wrf-chem/mozart.shtml` is used, converted to boundary conditions for WRF-Chem using the MOZBC utility. MOZART data is not available for model years 2005–2006; instead, the chemical data is taken from the GEOS-Chem model v9-02, with updates from Nault et al. (2017). These updates are detailed in Sect. D.2 of Appendix D. GEOS-Chem instantaneous output is sampled every three hours. This output is transformed into netCDF files for input into the MOZBC utility by use of the gc2moz utility of the AutoWRFChem package (Laughner, 2017).

Each year is simulated with a 1 month spinup at the anthropogenic emissions levels for that year. The year is simulated continuously, without reinitialization. Instantaneous WRF-Chem output is sampled hourly. For 2007, since MOZBC data was not available for December 2006, boundary conditions for 1 Jan 2007 were repeated for the first 32 days of the simulation (1 Dec 2006 to 1 Jan 2007) to allow the model time to spin up from the initial conditions.

In the BEHR AMF calculation, the profiles are interpolated, with extrapolation, to the same pressures that the scattering weights are defined on. The NO_2 mixing ratio profiles

are interpolated in log-log space (e.g., $\ln(NO_2)$ given at $\ln(p_{WRF})$ is interpolated to $\ln(p_{std})$, Bucsela et al., 2008). Temperature is interpolated in semilog space (T given at $\ln(p_{WRF})$ is interpolated to $\ln(p_{std})$), since lapse rates assume a linear relationship between temperature and altitude, and altitude is proportional to $\ln(p)$. Once interpolated, all profiles within the FoV75 bounds of the OMI pixel are averaged to give the profiles used in calculating the AMF.

Daily a priori profiles

As recommended in Laughner et al. (2016), we make use of daily profiles where possible. Both NO_2 a priori profiles and the temperature profiles necessary for the scattering weight temperature correction are drawn from the same simulation. WRF-Chem is configured to provide instantaneous output at the top of every hour. In v3.0A, the last WRF-Chem profile before average time of the OMI pixels over the domain is chosen to provide the a priori NO_2 and temperature profiles. In v3.0B, the profile closest in time to the average OMI time is used.

Monthly a priori profiles

Given the computational cost in producing daily a priori profiles, we continue to use monthly average profiles as well to cover years for which daily a priori profiles are unavailable. Monthly profiles are generated from 2012 WRF-Chem output. As in Laughner et al. (2016), an average of all available hourly profiles for a given month weighted by:

$$\begin{aligned} w_l &= 1 - |13.5 - (l/15) - h| \\ w_l &\in [0, 1] \end{aligned} \tag{4.11}$$

where l is the profile longitude and h is the UTC hour of the profile. This formulation gives highest weight to profiles near OMI overpass time (approximately 13:30 local standard time) while smoothly interpolating between adjoining time zones. The appropriate month's profiles are spatially matched to OMI pixels in the same manner as the daily profiles.

4.3 Changes in BEHR v3.0A

NASA v3.0 slant columns

Version 3.0 of the NASA Standard Product introduced a new method of fitting the observed Earthshine radiances to yield total SCDs (Krotkov et al., 2017; Marchenko et al., 2015). This new fitting approach eliminates a positive bias identified by Belmonte Rivas et al. (2014), and reduces the total SCDs retrieved. For much of the globe, this reduction is attributed

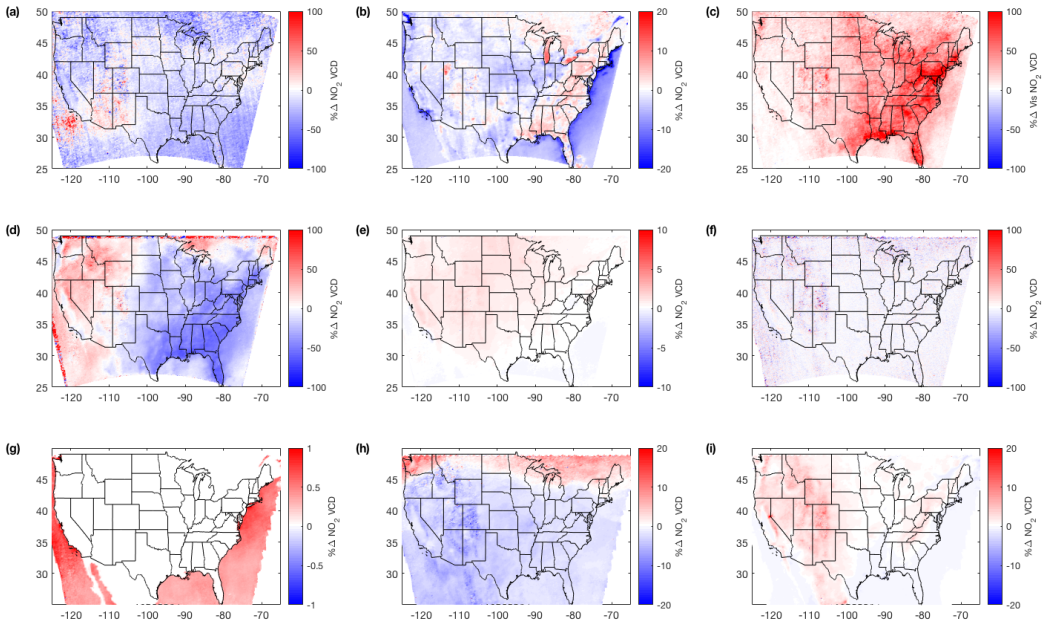

Figure 4.1: Percent change in the tropospheric NO_2 column due to each of the algorithm improvements. (c) is for the visible-only column; all others are the total tropospheric column. Changes due to (a) new NASA SCDs, (b) new surface reflectance, (c) new visible AMF calculation, (d) new monthly NO_2 profiles, (e) new temperature profiles, (f) new gridding method, (g) change in ocean reflectance LUT from 430 to 460 nm, (h) switch to WRF-derived tropopause pressure, (i) switch to Zhou et al. (2009) surface pressure methodology. Note that the color scale varies among the plots. Averages are for Jun–Aug 2012 and exclude pixels affected by the row anomaly and with cloud fraction > 0.2. Monthly average a priori profiles are used for all differences. Wintertime changes and histograms are given in Sect. D.5.

		JJA		DJF	
		Mean	Median	Mean	Median
Monthly	SCDs	-14 ± 14	-13^{+9}_{-9}	-21 ± 15	-21^{+9}_{-9}
	Surf. refl	-1.5 ± 2.8	$-1.4^{+1.8}_{-1.8}$	0.17 ± 6.87	$0.22^{+3.63}_{-4.29}$
	Vis. AMF formulation*	24 ± 18	20^{+15}_{-10}	18 ± 14	15^{+11}_{-8}
	NO_2 profiles	-9.8 ± 24.3	-11^{+20}_{-16}	-0.5 ± 7.7	$0.32^{+3.33}_{-4.23}$
	Temperature profiles	0.5 ± 0.4	$0.44^{+0.38}_{-0.29}$	1.5 ± 0.9	$1.4^{+0.8}_{-0.7}$
	Gridding	-0.66 ± 6.65	$-0.65^{+4.00}_{-4.05}$	-0.58 ± 10.45	$-0.64^{+6.28}_{-6.19}$
	Ocean LUT/profile time**	0.42 ± 0.12	$0.38^{+0.12}_{-0.05}$	0.41 ± 0.16	$0.43^{+0.10}_{-0.11}$
	Variable trop.	-2.4 ± 1.5	$-2.2^{+0.6}_{-1.0}$	1.9 ± 2.4	2^{+1}_{-1}
	Hypsometric Surf. Pres	0.55 ± 0.87	$0.3^{+0.7}_{-0.4}$	0.7 ± 0.9	$0.4^{+0.7}_{-0.4}$
Daily	NO_2 profiles	0.86 ± 20.14	$-0.54^{+15.46}_{-12.27}$	-1.3 ± 10.0	$-0.033^{+4.693}_{-6.724}$
	Temperature profiles	0.62 ± 0.48	$0.62^{+0.33}_{-0.38}$	1.5 ± 1.2	$1.2^{+1.0}_{-0.6}$
	Gridding	-0.82 ± 6.83	$-0.84^{+4.15}_{-4.13}$	-0.61 ± 10.58	$-0.69^{+6.36}_{-6.25}$
	Ocean LUT/profile time	0.036 ± 0.666	$0.044^{+0.403}_{-0.406}$	-0.084 ± 0.557	$-0.036^{+0.282}_{-0.371}$
	Variable trop.	-1.9 ± 2.4	$-2.3^{+1.6}_{-1.2}$	2.6 ± 2.6	$2.3^{+1.8}_{-1.2}$
	Hypsometric Surf. Pres	0.61 ± 1.01	$0.36^{+0.86}_{-0.43}$	1 ± 1	$0.58^{+1.22}_{-0.60}$

Table 4.2: Percent differences in averaged NO_2 VCDs for each increment. The first column indicacted which set of a priori profiles was used. Means are given with 1σ uncertainties; medians are given with uncertainties as the distance to the upper and lower quartiles. Outliers were removed before calculating these statistics. *Statistics for visible-only NO_2 column. **Statistics only for ocean pixels.

to the stratospheric SCD, but over the continental US, it is attributed to the tropospheric SCD. Thus, the broad reduction in tropospheric VCDs seen here (Fig. 4.1a, Tables 4.2 and 4.3) due to the new SCD fitting is consistent with Krotkov et al. (2017).

Surface reflectance: BRF

Generally, UV-vis AMFs increase (thus NO_2 VCDs decrease) with increasing surface reflectance, due to greater sensitivity to near surface NO_2. This pattern is apparent comparing Fig. 4.1b and Fig. 4.2a, as the NO_2 VCDs show the expected inverse relationship to the surface reflectance.

The changes in average surface reflectance are due primarily to the upgrade from version 5 to version 6 of the MODIS product. Figure D.4 breaks down the change in surface reflectance due to the upgrade from version 5 to 6 of the MODIS products separately from the change from black-sky to BRF surface reflectance. From Fig. D.4a and b, it is evident that the spatial pattern seen in the surface reflectance changes are due primarily to the differences between version 5 and 6. Differences between version 5 and 6 were listed at `https://lpdaac.usgs.gov/dataset_discovery/modis/modis_products_table/mcd43c3_v006` as of 5 Feb

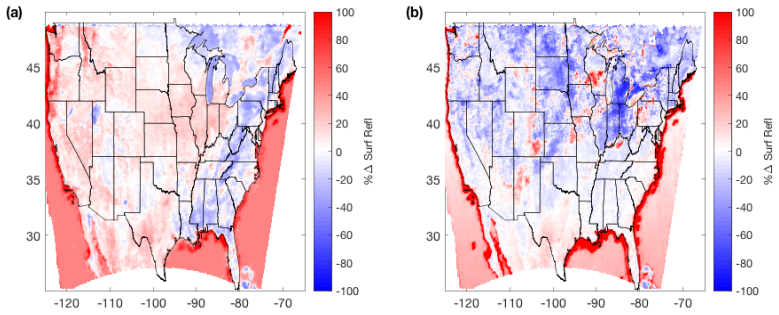

Figure 4.2: Difference in surface reflectance between BEHR v2.1C (MODIS MCD43C3 black-sky albedo, old ocean look up table) and BEHR v3.0B (MODIS MCD43Dxx BRF, new look up table) for (a) summer (JJA) and (b) winter (DJF).

2018. Two improvements of note are:

- Change from a land cover-based backup database to one based on full inversions. Notably, the summertime decreases along the east coast (Fig. 4.2a, D.4a) are somewhat spatially correlated with deciduous broadleaf forest, mixed forest, and woody savanna land cover types that are rare elsewhere in the country (Fig. D.5).
- Change from using the majority snow or no-snow status from the 16-day observation window to the current day status. In Fig. D.4b, the largest changes are seen sporadically in the northern half of the country, which suggests snow cover is impacting the surface reflectance.

We have not rigorously tested these specific changes as the cause for the spatial pattern of changes in surface reflectance; rather, our point is that the change from version 5 to 6 of the MODIS products is a larger driver of the change in average surface reflectance than the change from black-sky to BRF. However, Fig. D.4e illustrates that the change in individual pixels' surface reflectance due to the switch to a BRF is significant. The switch to a BRF surface reflectance is expected to improve retrieval accuracy of individual pixels and therefore is valuable to users interested in day-to-day variations in NO_2 VCDs (Vasilkov et al., 2017).

New visible-only AMF calculation

The formula for the v3.0 visible-only AMF is given in Eq. (4.3). Conceptually, this is the model SCD divided by the modeled VCD. In v2.1C, an alternate formulation was used:

$$A_{\text{BEHR,vis}} = (1 - f)A_{\text{clear,vis}} + fA_{\text{cloudy,vis}} \tag{4.12}$$

where f is again the cloud radiance fraction and

$$A_{\text{clear,vis}} = \frac{\int_{p_{\text{surf}}}^{p_{\text{trop}}} w_{\text{clear}}(p) g(p)\, dp}{\int_{p_{\text{surf}}}^{p_{\text{trop}}} g(p)\, dp} \tag{4.13}$$

$$A_{\text{cloudy,vis}} = \frac{\int_{p_{\text{cloud}}}^{p_{\text{trop}}} w_{\text{cloudy}}(p) g(p)\, dp}{\int_{p_{\text{cloud}}}^{p_{\text{trop}}} g(p)\, dp} \tag{4.14}$$

This earlier method assumes that each pixel can be treated as two totally independent subpixels, one clear and one cloudy. This seems a logical extension of the independent pixel approximation (Cahalan et al., 1994; Marshak et al., 1998), but the physical interpretation is less clear than the new formulation.

Although both approaches are conceptually valid, they are not mathematically identical, and so the retrieved visible tropospheric NO_2 column increases between v2.1C and v3.0A (Fig. 4.1c). The increase approaches 100% over the eastern US, decreasing to 0 towards the west coast.

The reason for this change is how the two approaches weight the clear vs. cloudy contributions to the pixel. In the v2.1C approach (Eqs. 4.12–4.14), the visible-only AMF is simply a cloud radiance fraction-weighted average of clear and above-cloud AMFs. Above-cloud AMFs are typically large, as the sensitivity of a remote sensing instrument to an above-cloud column is high both because of the altitude at which the column resides and the highly reflective cloud. As cloud fraction increases, the v2.1C visible AMF is weighted more heavily toward the above-cloud AMF, which leads to smaller retrieved visible NO_2 columns.

In contrast, the v3.0A visible AMF is the ratio of the modeled SCD to modeled visible VCD. The modeled visible VCD is calculated as the sum of to-ground and above-cloud VCDs weighted by the *geometric* cloud fraction, which tends to be smaller than the radiance cloud fraction. Thus, the v3.0 visible AMF should better account for the fact that the clear part of the pixel scatters less light than the cloudy part of the pixel. This leads to smaller AMFs than the v2.1C formulation, reflecting the fact that fewer photons interact with the clear part of the pixel, especially below the cloud top height.

Figure 4.3 shows the percent difference between the v2.1C and v3.0A visible-only VCDs as a function of several relevant input variables. We note the following patterns:

1. Greater percent difference with lesser cloud pressure
2. Greater percent difference with greater surface NO_2 concentration in the a priori profiles

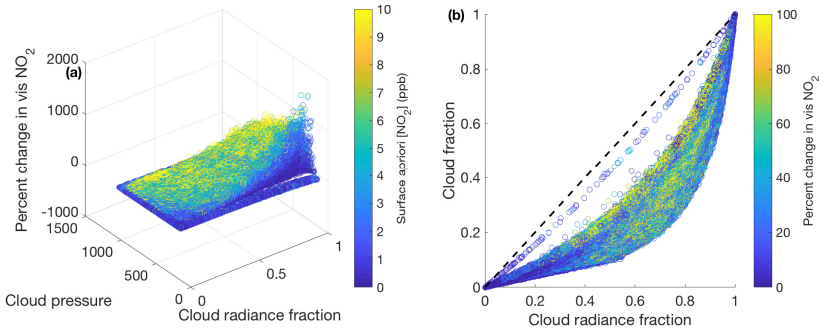

Figure 4.3: **(a)** The percent change in the visible-only NO_2 VCD versus cloud radiance fraction, cloud pressure, and surface NO_2 concentration in the a priori profiles. **(b)** The percent change in visible-only NO_2 VCD as a function of cloud radiance fraction and geometric cloud fraction. The color scale saturates at 10 ppbv in (a) and 100% in (b) to emphasize the distribution of the percent changes. The black dashed line is the 1:1 line.

3. Greater percent difference with greater difference between the geometric and radiance cloud fractions

All of these follow the conceptual difference between the two AMF formulations; the v2.1C AMF is retrieving the visible VCDs weighted by the amount of light that interacted with the clear and cloudy parts of the pixel; this will tend to be weighted towards the above-cloud part of the visible VCD. In contrast, the v3.0A AMF is designed to account for the difference between the radiance and geometric cloud fraction. Thus, as the amount of lower troposphere NO_2 increases or the gap between the amount of the pixel physically covered by cloud and the fraction of light from the cloud increases, the difference in the visible-only VCDs will be larger. Note in Fig. 4.3b that as both cloud fractions converge to 0 or 1 the difference in the visible-only VCDs tends towards 0, as expected since both the old and new visible-only AMF formulations reduce to the same expression if $f = f_g = 0$ or $f = f_g = 1$.

New WRF-Chem profiles

Update to new monthly average profiles

There are three significant changes from the old monthly average profiles used in v2.1C and before:

1. Lightning NO_x emissions are included in the profiles; these were not available in WRF-Chem when the previous profiles were simulated.

2. The anthropogenic emissions used now are from the National Emissions Inventory, 2011 (NEI 2011), scaled based on total annual emission to 2012 levels. 2012 boundary

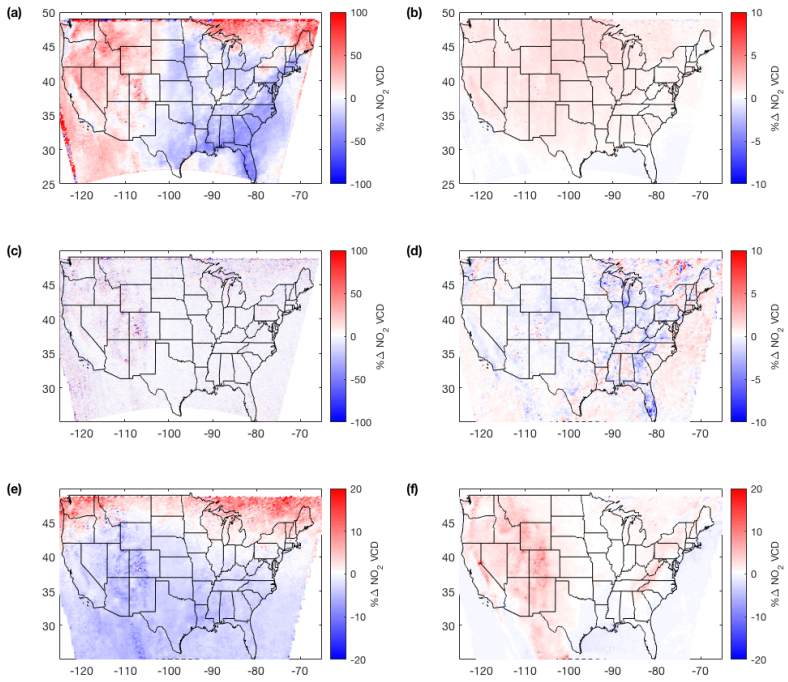

Figure 4.4: Percent change in the total tropospheric NO_2 column due to each of the algorithm improvements for the subproduct using daily profiles. Changes due to (a) new NO_2 profiles, (b) new temperature profiles, (c) new gridding, (d) change in profile time selection and ocean reflectance LUT from 430 to 460 nm, (e) switch to WRF-derived tropopause pressure, (f) switch to the Zhou et al. (2009) surface pressure methodology. Note that in (a), the difference is against an increment using monthly average profiles; also note that the color scale varies among the plots. Averages are for Jun–Aug 2012 and exclude pixels affected by the row anomaly and with cloud fraction > 0.2. Wintertime changes and histograms are given in Sect. D.5.

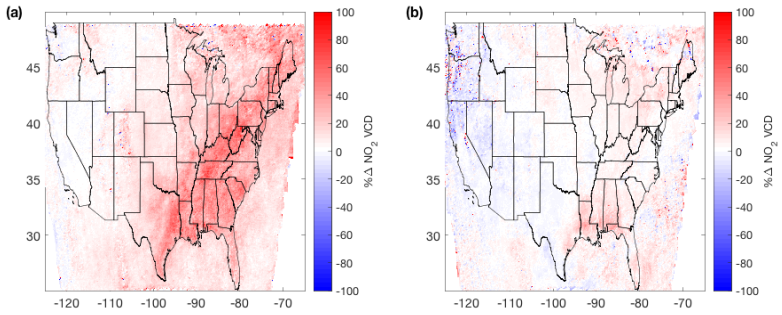

Figure 4.5: (a–b) Percent difference in NO_2 VCDs using daily instead of monthly profiles averaged over (a) Jun–Aug and (b) Jan, Feb, Dec 2012. Averages exclude pixels affected by the row anomaly and with cloud fraction > 0.2.

conditions and meteorology also used. In v2.1C and earlier, NEI 2005 emissions were used.

3. The chemical mechanism was updated from the Regional Acid Deposition Model, version 2 to the custom mechanism described in Sect. 4.2.

The changes in the summer average VCDs due to the profile update is shown in Fig. 4.1d. The effect of including lightning NO_x emissions is most apparent, causing the $\sim 30\%$ decrease (5th/95th percentiles: 8% and 55%) in VCDs in the SE US (averaged east of 95°and south of 45°). This is due to the increased contribution of UT NO_2 to the a priori profiles compared to the v2.1C profiles. As this NO_2 is located at higher sensitivity altitudes, the AMF is increased (and the retrieved VCD decreased) to reflect that higher sensitivity.

The increased VCDs along the west coast are caused by changes to the UT NO_2 profiles. The UT NO_2 over the west decreased compared to the old a priori profiles. This may be due either to the change in chemical mechanism or to a change in the O_3 boundary condition, which would affect the simulated UT NO:NO_2 ratio.

Daily vs. monthly profiles

Figure 4.5 shows the difference in v3.0B in the average total tropospheric NO_2 columns when using daily NO_2 profiles rather than monthly average profiles. Figure 4.5a is the summer (JJA) average, and shows a significant increase in VCDs along the eastern US, which is not present in the winter (DJF) average (Fig. 4.5b). The timing and location suggests that this difference is due to lightning, as the southeast US especially has very active lightning (Laughner and Cohen, 2017; Travis et al., 2016; Hudman et al., 2007).

		JJA		DJF	
		Mean	Median	Mean	Median
Monthly	SCDs	-15 ± 49	-16^{+27}_{-27}	-21 ± 48	-20^{+24}_{-28}
	Surf. refl	-1.6 ± 4.7	$-1.3^{+2.8}_{-3.4}$	-0.29 ± 8.60	$0.16^{+5.21}_{-6.07}$
	Vis. AMF formulation*	6.7 ± 10.6	$0.88^{+10.25}_{-0.88}$	-0.052 ± 0.770	0^{+0}_{-0}
	NO_2 profiles	-8.3 ± 25.7	$-6.9^{+15.8}_{-19.9}$	-2.1 ± 8.5	$-0.95^{+3.59}_{-5.70}$
	Temperature profiles	0.49 ± 0.51	$0.44^{+0.40}_{-0.31}$	1.2 ± 1.3	1^{+1}_{-1}
	Gridding	N/A	N/A	N/A	N/A
	Ocean LUT/profile time**	0.41 ± 0.17	$0.37^{+0.14}_{-0.08}$	0.44 ± 0.29	$0.46^{+0.19}_{-0.19}$
	Variable trop.	-2.2 ± 1.8	$-2.1^{+0.9}_{-1.2}$	1.5 ± 2.8	$1.6^{+1.6}_{-1.5}$
	Hypsometric Surf. Pres	0.49 ± 0.78	$0.26^{+0.70}_{-0.26}$	0.69 ± 0.87	$0.32^{+0.90}_{-0.32}$
Daily	NO_2 profiles	1 ± 25	$2.3^{+13.7}_{-15.2}$	-2.7 ± 12.5	$-1.4^{+6.2}_{-8.8}$
	Temperature profiles	0.53 ± 0.91	$0.43^{+0.66}_{-0.53}$	1.1 ± 1.7	$0.87^{+1.27}_{-0.98}$
	Gridding	N/A	N/A	N/A	N/A
	Ocean LUT/profile time	0.092 ± 0.613	0^{+0}_{-0}	0.053 ± 0.573	0^{+0}_{-0}
	Variable trop.	-1.9 ± 2.9	$-1.8^{+1.5}_{-1.8}$	2.1 ± 3.7	$1.7^{+2.6}_{-1.6}$
	Hypsometric Surf. Pres	0.53 ± 0.91	$0.24^{+0.88}_{-0.24}$	0.5 ± 0.9	$0.081^{+0.893}_{-0.081}$

Table 4.3: Percent differences in individual pixels' NO_2 VCDs for each increment. Means are given with 1σ uncertainties; medians are given with uncertainties as the distance to the upper and lower quartiles. Outliers were removed before calculating these statistics. *Statistics for visible-only NO_2 column. **Statistics only for ocean pixels.

Since the averages in Fig. 4.1 and Fig. 4.5 only use pixels with cloud fraction ≤ 0.2, a reasonable hypothesis is that the daily profiles for those less-cloudy pixels tend to have less upper tropospheric NO_2 than do the monthly average profiles (which include all days regardless of cloudiness). However, this is not the case, as Fig. 4.6 shows that cloud filtering does not change the distribution of UT NO_2 in the a priori profiles. Rather, it is seems to be caused by the order of averaging. The average daily and monthly profiles in the SE US are similar, but the median profiles are quite different (Fig. D.3). This is expected, as profiles influence by lightning are less frequent than those not influenced, but the amount of NO_2 introduced into the UT by lightning is large, leading to a skewed distribution of UT NO_2 concentrations (Fig. 4.6). When shape factors are considered, it is evident that this skewed distribution causes monthly shape factors to place more weight on UT NO_2 than do the daily shape factors (Fig. 4.6c).

WRF-Chem temperature profiles

Simulated or recorded temperature profiles are necessary to correct for the temperature dependence of the NO_2 cross section (Sect. 4.2 of this paper, also Bucsela et al., 2013). BEHR v2.1C used temperature profiles provided by NASA at $5^\circ \times 2^\circ$ resolution. Recently,

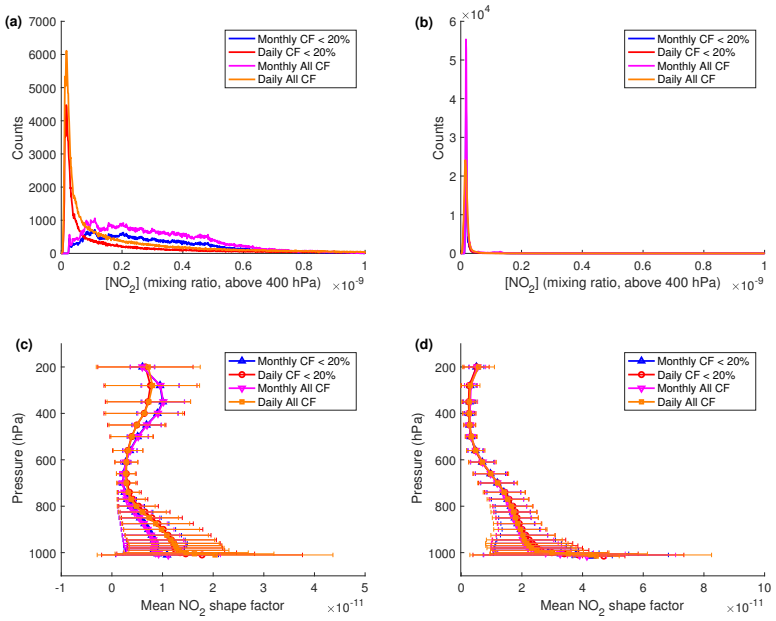

Figure 4.6: (a–b) Frequency distribution of average NO_2 above 400 hPa in the a priori profiles for the southeast US (a) and northwest US (b), from Jun–Aug 2012. (c–d) Mean a priori NO_2 shape factors over the southeast US (c) and northwest US (d) for Jun–Aug, 2012. The error bars are $\pm 1\sigma$. In all plots, the red and blue lines are only profiles from pixels with cloud fraction $\leq 20\%$, the purple and orange lines use all pixels. The regions (SE and NW US) are shown in Fig. D.2.

an error was identified in the temperature profile lookup used in BEHR v2.1C. Correcting this error changes the v2.1C VCDs by $-1.7 \pm 3.8\%$ (summer, $-0.9 \pm 11.2\%$ winter, Fig. D.6). Therefore the impact was small in both seasons, but more variable in the winter.

BEHR v3.0A uses temperature profiles from WRF-Chem at 12 km resolution instead. The effect on total tropospheric VCDs is shown in Fig. 4.1e. It is also small, $0.5 \pm 0.4\%$ on average in summer using monthly average profiles. Using daily temperature profiles, the change is slightly more variable ($0.6 \pm 0.5\%$). Therefore, high resolution temperature profiles are significantly less important than NO_2 profiles, which is expected, as temperature should not vary as rapidly in space as NO_2.

Gridding method

BEHR v2.1C used a constant value method (CVM) gridding algorithm to oversample the native pixel data to a fixed $0.05° \times 0.05°$ grid. A constant value method assigns the VCD of a given pixel to any grid points within the pixel bounds; this works well when the grid

resolution is significantly finer than the native pixel resolution. It was found that the existing algorithm was at times overly conservative, and did not assign values to grid cells near the border of two pixels.

We tested the two gridding algorithms described in Kuhlmann et al. (2014), a different CVM algorithm and the parabolic spline method (PSM), with updates from Schütt (2017). The PSM attempts to recover maxima in NO_2 between adjacent pixels by fitting the NO_2 VCDs with 2D splines and sampling the grid points along those splines. While this algorithm should be an ideal match with our retrieval (as our high resolution profiles are able to better resolve urban-rural NO_2 gradients), two technical challenges persisted. First, non-physical oscillations in the NO_2 VCDs would appear, especially on the edge of the row anomaly. Second, in one test, the PSM algorithm resulted in much greater VCDs than the CVM algorithm over a large area. As this is not the expected behavior, v3.0A uses the new CVM method from Kuhlmann et al. (2014). Both the PSM and CVM algorithms are adapted from those available at `https://github.com/gkuhl/omi`.

Figures 4.1f and 4.4c shows the percent change in the VCDs resulting from the change in gridding method. The average effect is small and no spatial pattern is evident, as would be expected, although individual effects are quite variable (4.2). The new CVM algorithm correctly assigns grid cells near the border of two pixels to one or the other. If two pixels overlap, an average of their values weighted by the inverse of their area (FoV75Area from the OMPIXCOR product) is assigned.

4.4 Changes in BEHR v3.0B

v3.0B implemented six main changes from v3.0A:

1. Retrievals using daily WRF-Chem profiles use the profile nearest in time to OMI overpass, rather than the last profile before the OMI overpass
2. Ocean surface reflectance calculated at 460 nm instead of 430 nm
3. Variable tropopause pressure (derived from WRF simulations) implemented in the AMF calculation
4. The method for calculating surface pressure from Zhou et al. (2009) was implemented
5. Clear and cloudy scattering weights are included separately in the native pixel files
6. The summary bits in the BEHRQualityFlags field were corrected.

Changes #1–4 directly affect the retrieved VCDs. #5 is intended for advanced users that wish to implement custom profiles. #6 makes rejecting low quality data easier for standard users.

Profile time and ocean LUT effects

Figures 4.1g and 4.4d show the changes to the NO_2 VCD caused by the change to the wavelength of the ocean reflectance LUT and the selection of the closest profile in time. Figure 4.1g only shows the effect due to the ocean LUT, as the monthly a priori profiles are not affected by the change in how the closest daily profile in time is selected.

In v3.0A, the ocean surface reflectance was calculated at 430 nm as the approximate midpoint of the wavelength fitting window for an NO_2 retrieval (402–465 nm, Krotkov et al., 2017). In v3.0B, this was changed to be 460 nm, which is more consistent with the MODIS band used (459–479 nm). The change in VCD retrieved over ocean is very small ($< 1\%$, Tables 4.2, 4.3), as expected.

In v3.0A, when using daily profiles, the last set of profiles before the OMI overpass time was used. In v3.0B, this was changed to be the nearest profile in time. The overall average is near 0 ($-0.01 \pm 4.6\%$), and the absolute magnitude of the average changes is $< 4 \times 10^{14}$ molec. cm^{-2}. As expected, a difference of 1 hour some of the selected profiles makes very little difference to the average retrieved column density.

Implementation of variable tropopause height

BEHR v3.0B uses variable tropopause pressure derived from WRF simulations while in prior versions tropopause pressure is set to be 200 hPa. Figures 4.1h and 4.4e reflect the effect of changes in tropopause pressure on NO_2 VCD. The changes in NO_2 are consistent with the variation in tropopause pressure. In summertime, the WRF-derived thermal tropopause pressure in lower latitudes ($< 45°$ N) is less than 200 hPa. This increases the contribution of the UT, with high sensitivity, to the AMF, which in turn reduces the retrieved NO_2 VCDs. In higher latitudes ($> 45°$ N), the thermal tropopause pressure is greater than 200 hPa and leads to a slight increase in NO_2 VCD. The changes in average NO_2 VCD caused by changes in tropopause pressure are small, $-1.6 \pm 5.3\%$ using monthly average profiles and $-1.1 \pm 8.2\%$ using daily profiles. In wintertime, the WRF tropopause is below the previous 200 hPa value over most of the US and it causes a broad enhancement of NO_2 VCD in most US domain ($>30°$ N) by approximately 2% (Figs. D.9, D.12, Tables 4.2, 4.3).

Surface pressure calculation

Figures 4.1i and 4.4f show the impact of switching from a fixed scale height calculation to using the hypsometric equation to adjust WRF modeled surface pressure to the GLOBE

terrain elevation. As expected, the changes are similar whether monthly or daily WRF output is used and are greatest over the Rocky and Appalachian mountains (up to a maximum of $\sim 10\%$). This is similar to the 5% effect Zhou et al. (2009) found in the summer, indicating that a simple scale height calculation is insufficient and that a meteorological surface pressure correction is necessary in mountainous regions even when using a high resolution terrain elevation database.

Publishing separate clear and cloudy scattering weights

In v3.0A and prior versions, an array of scattering weights used in the retrieval was included in the published files in order to allow advanced users to recalculate an AMF using their own a priori NO_2 profiles but retain the scattering weights computed using the high resolution surface reflectance and elevation data. These scattering weights were the cloud radiance fraction weighted average of the temperature-corrected clear and cloudy scattering weights (Eqs. 4.2, 4.6). Using these scattering weights along with the published a priori profiles, users could reproduce BEHR AMFs well, to within $0.5 \pm 1.9\%$. However, publishing the clear and cloudy weights separately increases the precision of reproduced AMFs by three orders of magnitude. Using these with the provided BEHR a priori profiles allows users to reproduce BEHR AMFs effectively exactly (Fig. D.7). This also permits users to use different cloud fractions in their custom AMF calculations.

BEHR Quality Flags

Starting with v3.0A, the BEHRQualityFlags field summarized key quality issues from both the NASA and BEHR processing steps. The first and second bits in these values are summary bits, so that users who want high quality data can very easily identify such data. Due to a bug in v3.0A, these bits did not filter out all low quality data. This has been rectified in v3.0B. See Sect. 4.6 for the proper use of this flags.

4.5 Overall difference

Overall, the two changes that had the largest impact on the retrieved VCDs were the new NASA slant column fitting and the new a priori NO_2 profiles ($-14 \pm 14\%$ and $0.86 \pm 20.14\%$, respectively, Table 4.2). Although the overall average effect of the new profiles is small, this is only because it causes both positive and negative changes to the VCDs. The large standard deviation reflects how different areas do have very significant changes. The effect of the a priori profiles was especially strong in the SE US where lightning has a strong influence on the profile shape in the summer (Fig. 4.7). Given the high sensitivity of NO_2 retrievals to upper tropospheric NO_2, this is not surprising. The omission of lightning NO_2 from the original BEHR product was a limitation of WRF-Chem at the time the product was created (Russell et al., 2012); lightning NO_x emission was not added to WRF-Chem until v3.5.0,

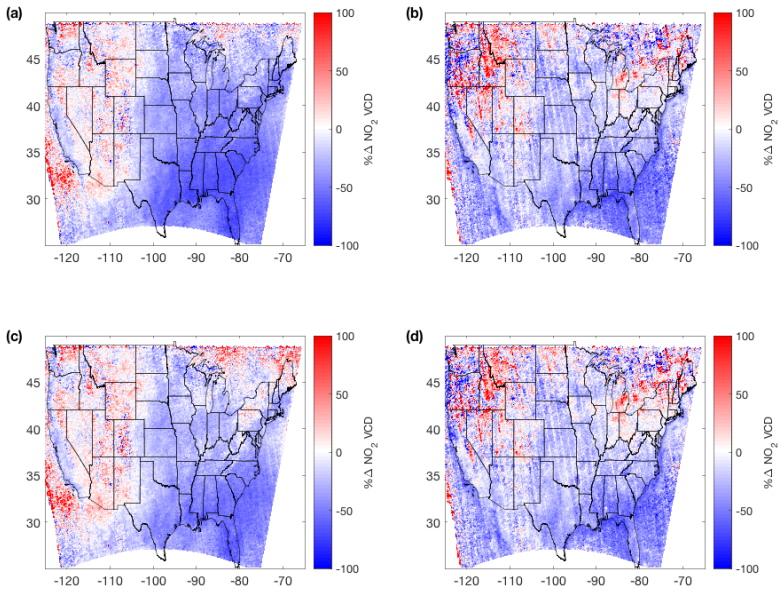

Figure 4.7: Overall average differences in total tropospheric NO_2 VCDs between v2.1C and v3.0B for Jun–Aug (a,c) and Jan, Feb, Dec (b,d) of 2012. (a,b) using monthly NO_2 profiles in v3.0B, (c,d) using daily profiles in v3.0B.

released in April, 2013 (`http://www2.mmm.ucar.edu/wrf/users/download/get_sources.html#WRF-Chem`). The change due to the SCD fitting resulted in a fairly uniform decrease in NO_2 VCDs across the domain.

The difference in the averages using daily (Fig. 4.7c,d) vs. monthly profiles (Fig. 4.7a,b) is not large, as noted in Laughner et al. (2016), because averaging over time periods greater than a month eliminates the temporal variability captured by the daily profiles. The effect of the daily profiles is on the average strongest in the SE US, as discussed in Sect. 4.3, and is still an overall decrease compared to the v2.1C profiles, due to the inclusion of lightning and the reduction in surface emissions. It should be noted that the difference between retrievals with daily and monthly profiles will be greater in years other than 2012, since the daily profiles incorporate year-specific emissions, while monthly profiles always assume 2012 anthropogenic emissions.

4.6 Recommendations for use

For most users, the quantity of interest will be the standard total tropospheric column contained in the file variable BEHRColumnAmountNO2Trop. (A note for historical consistency:

documentation for v2.1B indicated incorrectly that BEHRColumnAmountNO2Trop was the visible only column and that a ghost column correction was necessary to get the total column. BEHRColumnAmountNO2Trop has always in fact been the total tropospheric column.) In order to obtain high quality data, in v3.0B and later, only use pixels or grid cells for which BEHRQualityFlags is an even number (i.e. the quality summary bit is 0). This will automatically remove pixels affected by the row anomaly, with cloud fraction > 0.2, with low quality surface reflectance, or for which an error occurred during processing. (The quality flags in v3.0A do not properly remove all pixels meeting these criteria.)

Users are encouraged to use years with daily profiles if possible for their application, for two reasons. First, Laughner et al. (2016) showed that using daily profiles significantly changes day-to-day VCDs, and that some applications of satellite data can be biased when monthly profiles are used. Second, the daily profiles also use year specific emissions (Sect. 4.2, so will better capture trends in VCDs as the surface contribution to the a priori profiles is reduced.

For users using BEHR data to evaluate trends, mixing daily and monthly profile retrievals is *not* recommended, as systematic differences between them (i.e. Sect. 4.3 of this paper; Laughner et al., 2016) will bias any trends observed. Second, caution is advised if comparing 2005 or 2006 data using daily profiles to other years; the different WRF-Chem boundary conditions (Sect. 4.2) may also bias observed trends.

4.7 Conclusions

Here we present v3.0 of the Berkeley High Resolution OMI NO_2 product (BEHR NO_2). This version incorporates a number of changes, including updated a priori NO_2 profiles with lightning NO_x emissions, daily NO_2 profiles for select years, a directional surface reflectance product, variable tropopause height, a new gridding algorithm, and improved surface pressure calculation, in addition to using the current NASA OMI NO_2 Standard Product. The new a priori profiles and the upgrade to the new NASA product had the largest effect on the retrieved total tropospheric VCDs. Retrieved visible-only tropospheric VCDs were most strongly affected by the new visible-only AMF formulation, but otherwise were similarly affected by each change.

Code and data availability

BEHR data is stored in monthly compressed files as four subproducts on the University of California DASH archive (Laughner et al., 2018c; Laughner et al., 2018e; Laughner et al., 2018d; Laughner et al., 2018f). All BEHR data is also available for download as individual files at `behr.cchem.berkeley.edu`. The BEHR code is hosted on GitHub at `https://github.com/CohenBerkeleyLab/BEHR-core/tree/master` (Laughner and Zhu, 2018a). WRF-Chem simulations for 2005, 2007–09, and 2012–14 are available at the time

of writing; due to the large file size, access can be arranged by contacting the corresponding author. The analysis code (and its dependencies) along with the incremental averages are available at `https://doi.org/10.5281/zenodo.1247564` (Laughner and Zhu, 2018b).

The v3.0 NASA Aura OMI NO_2 standard product (Krotkov and Veefkind, 2016) and OMI/Aura Ground Pixel Corners product (Kurosu and Celarier, 2010) was obtained from the Goddard Earth Science Data and Information Services Center (GES DISC) in Greenbelt, MD, USA. The MODIS Aqua Clouds 5-Min L2 Swath 1 and 5 km (MYD06_L2 Platnick et al., 2015) and MODIS Terra+Aqua BRDF/Albedo Parameters 1–3 Band3 and QA BRDF Quality Daily L3 Global 30ArcSec CMG V006 (Schaaf, 2015a; Schaaf, 2015b; Schaaf, 2015c; Schaaf, 2015d, pp. MCD43D07, MCD43D08, MCD43D09, MCD43D31) were acquired from the Level-1 and Atmospheric Archive and Distribution System (LAADS) Distributed Active Archive Center (DAAC) located in the Goddard Space Flight Center in Greenbelt, MD (`https://ladsweb.nascom.nasa.gov/`).

Chapter 5

Evaluation of version 3.0B of the BEHR OMI NO_2 product

5.1 Introduction

NO_x ($\equiv$ NO + NO_2) is an atmospheric trace gas emitted by anthropogenic activity (predominantly combustion, e.g. motor vehicles and power plants), lightning, biomass burning, and soil microbes. It plays an important role in air quality, as a major controlling factor in ozone and aerosol production, as well as being toxic itself.

Satellite observations of NO_2 have proven to be extremely useful in constraining anthropogenic (e.g. Richter et al., 2005; Kim et al., 2006; Kim et al., 2009; van der A et al., 2008; Konovalov et al., 2010; Russell et al., 2010; Beirle et al., 2011; Castellanos and Boersma, 2012; Russell et al., 2012; Zhou et al., 2012; McLinden et al., 2014; Lu et al., 2015; Liu et al., 2016; Liu et al., 2017; Miyazaki et al., 2012a; Miyazaki et al., 2017), lightning (e.g. Beirle et al., 2004; Martin et al., 2007; Beirle et al., 2010a; Bucsela et al., 2010; Miyazaki et al., 2014; Pickering et al., 2016; Nault et al., 2017), soil (e.g. Bertram et al., 2005; van der A et al., 2008; Hudman et al., 2010; Hudman et al., 2012; Zörner et al., 2016), and biomass burning (e.g. Mebust et al., 2011; Huijnen et al., 2012; Mebust and Cohen, 2013; Mebust and Cohen, 2014; Bousserez, 2014; Schreier et al., 2014; Castellanos et al., 2015; Marle et al., 2017) emissions.

Satellite observations of NO_2 relate absorption of light in the $\sim$ 400–460 nm range of reflected Earthshine radiances to a total column measurement of NO_2 using differential optical absorption spectroscopy (DOAS, Boersma et al., 2002; Richter and Wagner, 2011) or a similar technique (e.g. van Geffen et al., 2015). Most applications of satellite NO_2 observations to constrain emissions or otherwise study air quality are focused on the tropospheric contribution to the total column; therefore the stratospheric column must be removed. Several methods have been implemented to do so (e.g. Boersma et al., 2007; Bucsela et al., 2013).

The tropospheric slant column density (SCD) is then converted to a vertical column density (VCD) through the use of an air mass factor (AMF, McKenzie et al., 1991; Slusser et al., 1996; Burrows et al., 1999; Palmer et al., 2001) that accounts for the effect of path length, surface reflectivity and elevation, NO_2 vertical distribution, clouds, and aerosols.

There have been numerous studies evaluating OMI NO_2 products against in situ aircraft profiles and ground based column measurements. This is not meant to be an exhaustive list, but to provide a summary of the results of evaluations of existing standard OMI NO_2 products.

The first-generation NASA Standard Product (SP) and KNMI DOMINO products were evaluated by Bucsela et al. (2008) and Hains et al. (2010) using aircraft profiles from multiple campaigns and Russell et al. (2011) using an extrapolation method with ARCTAS-CA aircraft data. These studies all identified a high bias in the DOMINO VCDs; by comparing the DOMINO a priori profiles to aircraft and lidar profiles Hains et al. (2010) found evidence that this was caused by insufficient vertical mixing in the DOMINO a priori profiles, which was corrected in DOMINO v2.

Lamsal et al. (2014) undertook a detailed evaluation of the NASA SP v2, primarily focusing on data from the Deriving Information on Surface Conditions from COlumn and VERtically Resolved Observations Relevant to Air Quality (DISCOVER-AQ) campaign in Baltimore, MD, USA. This work combined evaluation of the a priori profile against aircraft measurements along with validation of OMI VCDs with aircraft and ground-based VCDs. They found that the NASA SP v2 VCDs were generally biased low in urban areas and high in rural or suburban areas. This is consistent with the effect of coarse a priori profiles (Russell et al., 2011); in a large urban area like the Baltimore/Washington D.C. urban corridor, a coarse profile can capture the average urban characteristic profile, but on the edge, a coarse profile cannot capture the transition from urban to rural.

Krotkov et al. (2017) and Goldberg et al. (2017) both evaluated the NASA SP v3, primarily using ground based VCD observations. They found it to be biased low by $\sim 50\%$ in the Baltimore area (Goldberg et al., 2017) and low by 50% or more Hong Kong (Krotkov et al., 2017), but better than v2 in remote areas, due to the improved total column fitting implemented in version 3. Ialongo et al. (2016) also compared versions 2 and 3 of the NASA SP and version 2 of DOMINO against ground based column measurements in Helsinki, one of only a few studies at high latitudes ($> 60°$). They found that SP v3 was biased 30% low, while the version 2 products were not. They attributed this to cancellation of errors in the version 2 products, namely the high bias in the total OMI columns corrected by van Geffen et al. (2015), and the representativeness mismatch between OMI pixels and Pandora measurements.

Here we present an evaluation of version 3.0B of the BErkeley High Resolution (BEHR) OMI

NO_2 retrieval. Version 3.0B implements several changes over v2.1C:

- Daily profiles for selected years
- Updated 12 km WRF-Chem NO_2 profiles with a more complete chemical mechanism (Zare et al., 2018), updated anthropogenic emissions, and lightning NO_x emissions added
- Use of v3.0 NASA Standard Product (SP) tropospheric SCDs
- Directional surface reflectance
- Variable tropopause height
- Surface pressure combining a high resolution terrain database with WRF-simulated surface pressure

The motivation for this upgrade stems from ideas developed in Laughner et al. (2016), where we showed that daily, high resolution a priori profiles are necessary for a retrieval to simultaneously retrieve NO_x VCDs and lifetime to accuracies better than 30%. As our goal is to study the relationship between changes in NO_x VCDs/emissions and NO_x lifetime across the US, and resolving open questions requires higher relative precision and higher accuracy than prior retrievals, we have developed a new product with daily 12 km a priori profiles. Therefore, in this work, we first evaluate the simulated WRF-Chem profiles against aircraft measurements and OMI SCDs to demonstrate that the daily profiles accurately represent the real atmosphere. We then directly evaluate the retrieved VCDs using both aircraft and Pandora observations and show that v3.0 is generally superior to v2.1C, and that using daily profiles improves the overall quality of the retrieval.

5.2 Methods: models and observations

BEHR

The BEHR OMI NO_2 retrieval is described in detail in Chapter 4. Briefly, the BEHR retrieval calculates a tropospheric air mass factor (AMF) using high resolution a priori input data for surface reflectance, surface elevation, and NO_2 vertical profiles; the NO_2 profiles are simulated with WRF-Chem. To capture the day-to-day variation in NO_2 profiles, daily profiles are used. Currently, 2005, 2007–2009, and 2012–2014 are available. Other years will be posted as processing is completed. A second subproduct uses monthly average profiles (simulated for 2012) to retrieval all years of the OMI data record.

The BEHR AMF is used to convert the tropospheric slant column densities (SCDs) available in the NASA OMI NO_2 standard product to tropospheric vertical column densities (VCDs).

For full details of the AMF calculation, see Laughner et al. (2018b). The BEHR product is available for download as HDF version 5 files at `behr.cchem.berkeley.edu`.

WRF-Chem

WRF-Chem version 3.5.1 (Grell et al., 2005) is used to simulate the a priori NO_2 profiles for BEHR v3.0B. The model domain is 405 (east-west) by 254 (north-south) 12 km grid cells centered on 39° N 97° W with 29 vertical levels. Meterological initial, boundary, and nudging conditions are taken from the North American Regional Reanalysis (NARR) product; boundary conditions and four-dimension data analysis (FDDA) nudging (Liu et al., 2006) are applied every 3 hours. Temperature, water vapor, and U/V winds are nudged with nudging coefficients of 0.0003 s^{-1}.

The chemical mechanism used is described in Zare et al. (2018), which has a very detailed description of alkyl nitrate and nighttime chemistry. Methyl peroxynitrate (MPN) chemistry was added (Browne et al., 2011) to improve upper tropospheric chemistry. Anthropogenic emissions are from the National Emissions Inventory, 2011, scaled by EPA annual total emissions (EPA, 2016) to the model year. Biogenic emissions are from the Model for Emissions of Gases and Aerosols from Nature (Guenther et al., 2006). Lightning emissions are parameterized following Laughner and Cohen (2017) for a simulation with FDDA active (500 mol NO $flash^{-1}$, 2x base flashrate).

Chemical initial and boundary conditions are interpolated to the WRF grid using the MOZBC utility (`https://www2.acom.ucar.edu/wrf-chem/wrf-chem-tools-community`). For 2007 and later model years, chemical data is obtained from the MOZART model runs available at `https://www.acom.ucar.edu/wrf-chem/mozart.shtml`. For 2005 and 2006, chemical data is obtained from a GEOS-Chem model run, described in Laughner et al. (2018b).

Pandora ground-based columns

Evaluation of satellite NO_2 VCDs usually uses one of two methods. First, total satellite columns can be directly compared to a ground-based column measurement, such as a Pandora spectrometer (Herman et al., 2009) or multi-axis DOAS (MAX-DOAS) instrument (Hönninger et al., 2004). In the case of a direct-sun measurement, such as a Pandora spectrometer, the AMF required is only a geometric AMF to account for the difference in path length between the slant and vertical columns, since the multiple scattering that necessitates the use of a more complex AMF in the satellite retrieval is a much smaller signal than the direct-sun signal (Herman et al., 2009).

We compare against Pandora ground based column measurements taken during the four DISCOVER-AQ campaigns. For each OMI overpass, pixels are matched with Pandora sites

Data field	Condition
XTrackQualityFlags	Must be 0
VcdQualityFlags	Must be an even number
CloudFraction	Must be ≤ 0.2
BEHRAMFTrop	Must be a non-fill value $> 10^{-6}$

Table 5.1: Criteria that OMI pixels must meet to be used in any comparison.

that lie within the pixel boundaries defined by the FoV75 corners in the OMPIXCOR product (Kurosu and Celarier, 2010). Only pixels meeting the criteria in Table 5.1 are used. If multiple valid pixels from the same overpass encompass the Pandora site, their VCDs are averaged. As in Goldberg et al. (2017), the stratospheric VCD from the NASA Standard Product is added to the tropospheric VCD to obtain a total column, since the Pandora columns do not separate stratospheric and tropospheric contributions.

Pandora observations are matched in time to the OMI observations using the exact time of observation for each pixel given in the OMI data files. As in Goldberg et al. (2017), Pandora observations ± 1 h from the OMI observation are averaged.

In situ aircraft profiles

The other common method of evaluating satellite VCDs is to use in situ measurements of NO_2 by an instrumented aircraft that flies a vertical profile to calculate a VCD by integrating the NO_2 concentrations vertically. Ideally, the aircraft should fly a spiral path that provides a complete vertical sampling of the troposphere over a ground footprint similar in scale to the satellite pixel; the DISCOVER-AQ campaigns held in Maryland, California, Texas, and Colorado between 2011 and 2014 were designed to provide this sampling over the lower troposphere. In other cases, the VCD calculated from integrating the aircraft profiles is often matched to satellite pixels in which the boundary layer is sampled (e.g. Bucsela et al., 2008; Hains et al., 2010), on the assumption that differences in the UT between adjacent pixels is minimal.

We calculate tropospheric VCDs from in situ NO_2 profiles measured from aircraft. We use six campaigns: the four DISCOVER-AQ campaigns (`https://www-air.larc.nasa.gov/missions/discover-aq/discover-aq.html`) in Maryland (2011), California (2013), Texas (2013), and Colorado (2014), the Southeast Nexus campaign (2013, southeast US, SENEX Science Team, 2013), and the Studies of Emissions and Atmospheric Composition, Clouds, and Climate Coupling by Regional Surveys (SEAC4RS, 2013, Toon et al., 2016). For the DISCOVER-AQ and SEAC4RS campaigns, we use 1 second NO_2 data from the TD-LIF instrument (Nault et al., 2015; Wooldridge et al., 2010; Day et al., 2002; Thornton et al., 2000). For the SENEX campaign, we use 1 second data from the chemiluminescence

instrument (Ryerson et al., 1999).

We draw on methodology from several papers (Bucsela et al., 2008; Hains et al., 2010; Lamsal et al., 2014) for our approach. Similar to (Hains et al., 2010), only profiles with a minimum radar altitude < 500 m and at least 20 measurements below 3 km above ground level (AGL) are used. In the DISCOVER-AQ campaigns, individual profiles are demarcated in the data by a profile number. In the SENEX and SEAC4RS data, profiles were identified manually as periods when the aircraft was consistently ascending or descending. The profile measurements are binned to the same pressure levels used in the BEHR algorithm and the final profile uses the median of each bin.

Profiles are spatially matched to OMI pixels if any of the 1 second measurements in the bottom 3 km AGL lies within the FoV75 pixel boundaries. As with Pandora data, OMI pixels must meet the criteria in Table 5.1 to be included; all VCDs from valid pixels intersecting the profile are averaged to yield a single VCD to compare against the profile. Only profiles with a mean observation time of all points in the bottom 3 km AGL within 1.5 h of the mean OMI observation time for the orbit are used.

To calculate a VCD from the in situ measurements, the aircraft profiles are integrated from the average surface pressure to the average tropopause pressure of the matched pixels. The surface and tropopause pressure are used from the product being evaluated, i.e. aircraft profiles are integrated between BEHR surface and tropopause pressure for comparison with BEHR VCDs and NASA surface and tropopause pressures for comparison with NASA VCDs. For BEHR v2.1C comparisons, 200 hPa is used as the fixed tropopause pressure. Aircraft profiles that do not span the necessary vertical extent are extended similarly to Lamsal et al. (2014). The aircraft profile is extended to the surface by using the ratio of modeled concentrations at each of the missing levels to the lowest level with aircraft data to scale the bottom bin with aircraft data. Missing profile levels above the top of the aircraft profile are replaced with model data. We use modeled NO_2 profiles from v9.02 of the GEOS-Chem global chemical transport model (Bey et al., 2001), with the updated chemistry and lightning emission rates described in Nault et al. (2017). The NO_2 profiles are monthly averages of model output from 2012 sampled between 12:00 and 14:00 local standard time. We avoid using the a priori WRF-Chem profiles for this so that the aircraft VCDs are independent of the retrieved VCDs.

We also used the extrapolation method from Hains et al. (2010), where the median of the top 10 and bottom 10 points are extrapolated to the tropopause and surface pressures, respectively. The median of the top 10 points must be < 100 pptv. As in Hains et al. (2010), a detection limit of 3 pptv is assumed, and if the median to be extrapolated is less than 3 pptv, it is set to one-half of the detection limit, 1.5 pptv.

In addition, we directly compare the a priori profiles to the in situ aircraft profiles. This is

done as in Laughner and Cohen (2017); for each 1 second data point in the aircraft data, the nearest WRF-Chem output time is selected, and the model grid cell containing the aircraft location is sampled. This effectively samples the model output as if the aircraft were flying through the model world.

We use a similar set of aircraft campaigns here as for the VCD evaluation (Sect. 5.2); the only difference being that we use the Deep Convective Clouds and Chemistry campaign (Barth et al., 2015) instead of SENEX. The DC3 campaign focused on outflow from convective systems (i.e. thunderstorms) and so is used to evaluate the lightning NO_x parameterization. The DC3 campaign had better UT sampling but far fewer profiles than SENEX. The DISCOVER-AQ campaigns focused on satellite validation, flying repeated spirals over 6–8 sites during each campaign; however, for the average comparison, we use all data, not just that taken during the spirals.

5.3 WRF-Chem profile evaluation

Comparison with in situ aircraft profiles

Figure 5.1 shows campaign averaged profiles matched with WRF profiles from the four DISCOVER-AQ campaigns, the DC3 campaign, and the SEAC4RS campaign. We compare the monthly average NO_2 profiles from BEHR v2.1C and v3.0B for all campaigns, as well as the daily v3.0B profiles. The plots shown only use data between 12:00 and 15:00 local standard time, since the v3.0 monthly average profiles are calculated as a weighted average that only includes contributions from ± 1 h from OMI overpass; this way all profiles get a fair comparison to the observations.

In general, the v3.0 profiles show better agreement with observed profiles than the v2.1 profiles, except during the California DISCOVER-AQ campaign. The most dramatic example is the Maryland DISCOVER-AQ campaign, where the factor of ~ 2 reduction in NO_2 concentration (likely due to updating emissions from 2005 to 2012) brings the modeled profiles into substantially better agreement with the observed profiles. In the California DISCOVER-AQ campaign, the v2.1 profiles managed to capture an elevated layer of NO_2 that the v3.0 profiles did not; though we note that transport in California's central valley is notorious difficult to model (Hu et al., 2010, and references therein). In Texas, the v3.0 profiles and v2.1 profiles lie on opposite sides of the observed profiles, possibly suggesting that emissions in Houston did not decrease as much in fact as in the NEI inventory driving the v3.0 WRF simulations. In Colorado, both the v3.0 and v2.1 profile match observations reasonably well. The daily profiles do a better job capturing the decrease in NO_2 between 750 and 600 hPa than the v3.0 monthly or v2.1 profiles; this may be due to day-to-day variability in recirculation from the upslope/downslope winds (e.g. Sullivan et al., 2016).

We include the SEAC4RS and DC3 campaigns to check the simulation of lightning NO_x

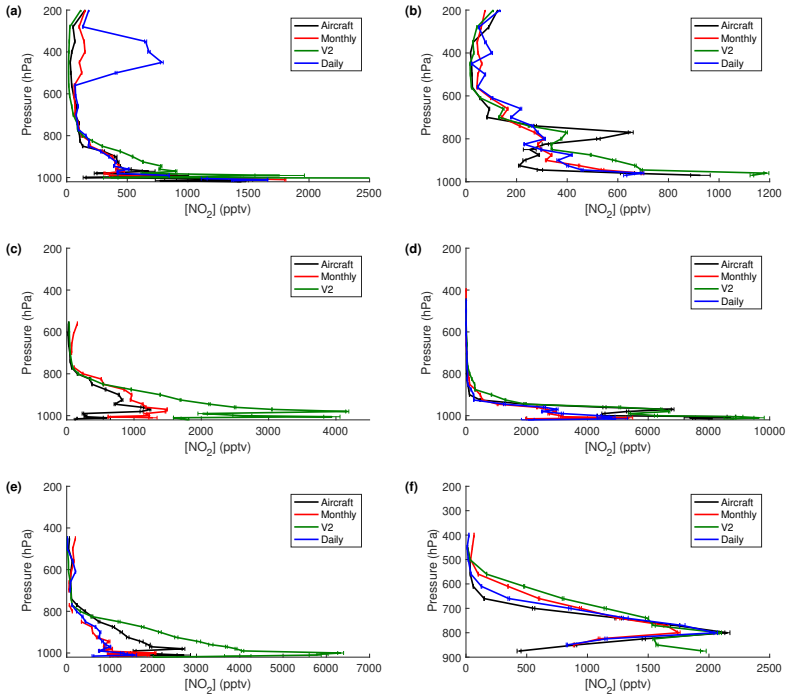

Figure 5.1: Comparison of average WRF-Chem and aircraft NO_2 profiles from the **(a)** SEAC4RS, **(b)** DC3, and DISCOVER-AQ campaigns, the latter in **(c)** Maryland, **(d)** California, **(e)** Texas, and **(f)** Colorado. Aircraft profiles are shown in black, BEHR v2.1 profiles in green, BEHR v3.0 monthly profiles in red, and (where available) BEHR v3.0 daily profiles in blue. The WRF and aircraft data are matched as described in Sect. 5.2 and binned by pressure. Uncertainties are 1 standard deviation of all profiles averaged. Note that for SEAC4RS the v2 profile reaches a maximum of $\sim$ 8000 pptv, off the plot axes.

in the profiles. The daily profiles show similar agreement to the DC3 observations as in Laughner and Cohen (2017). Restricting the DC3 data to 12:00–15:00 local standard time as we have done here reduces the strength of the lightning signal, since the strongest lighting occurs after OMI overpass (Lay et al., 2007; Williams et al., 2000). Compared to Laughner and Cohen (2017), the discrepancy between modeled and observed profiles decreased around 500 hPa, increased around 400 hPa, and is similarly small around 200 hPa. Surprisingly, the difference between the v2.1 and v3.0 profile around 200 hPa is not as significant as the difference between the lightning and no-lighting cases in Laughner and Cohen (2017). This is unexpected as the v2.1 profiles did not include lightning NO_x emission. It is possible that convection of greater surface NO_x concentrations is driving the v2.1 UT concentration, since the v2.1 profiles used 2005 NO_x emissions.

The SEAC4RS campaign covers the southeast US, which has very active lightning (Hudman et al., 2007; Travis et al., 2016). The daily profiles demonstrate a substantial overestimate in UT NO_2 (between 600 and 200 hPa). This is centered in the SE US; model-measurement discrepancies between 600 and 200 hPa in the rest of the country are < 500 pptv (not shown). As discussed in Laughner et al. (2018b), the southeast US exhibits greater NO_2 VCDs (and therefore smaller AMFs) when using daily profiles; that is opposite with the profiles seen here, as greater NO_2 at higher altitudes results in larger AMFs. Laughner et al. (2018b) showed that the 3 month average daily shape factor over the SE US had less contribution from UT NO_2 than the monthly profiles; this indicates that on average pixels in the SE US are not influenced by lightning, but that the SEAC4RS sampling tended to select for convective outflow. However, this does indicate that the simulation of the UT in the southeast US is biased high.

To investigate the cause of this bias, we compare the WRF lightning flash density to that measured by the Earth Networks Total Lightning Network (ENTLN). ENTLN is a ground-based lightning observation network with more than 900 sensors deployed in the contiguous US. The sensors record lightning-produced strokes as well as accurate time and location. Strokes are then clustered into a flash if they are within 700 milliseconds and 10 kilometers. The detection coefficient is larger than 70% across southern contiguous US (Rudlosky, 2015).

For the comparison, the WRF-Chem simulation is that described in Sect. 5.2. ENTLN and WRF-Chem are sampled from May 13 to Jun 23, 2012 over the middle and east US domain, where active lightning events are detected. Both observed and simulated lightning flashes are converted to flash density by dividing flash counts by the corresponding grid areas and time range.

Figure 5.2a and b show the spatial distribution of flash density in number per km^2 per day observed by ENTLN and simulated by WRF-Chem. The largest biases are located over the southeast US (outlined by red on the map). In this region, WRF-Chem substantially overestimates flash density in general and a detection coefficient of 70% for ENTLN cannot account for the discrepancy. The simulated flash density is the highest primarily along the coast, which is not detected by ENTLN.

The scatter plot of daily flash density over the southeast US from two datasets in Fig. 5.2c demonstrates that the WRF-Chem consistently overestimates flashes in the southeast US over the study period. However, outside of the southeast US, the agreement improves. The simulation captures the spatial pattern over the regional scale (Fig. 5.2a–b) and the simulated flash densities are consistent with the observed flash densities and the correlation improves as well (Fig. 5.2d).

Currently, the cause of the discrepancies between the flash density from WRF-Chem simulation and ENTLN observation, is unknown. However, it is clear that it is the flash density,

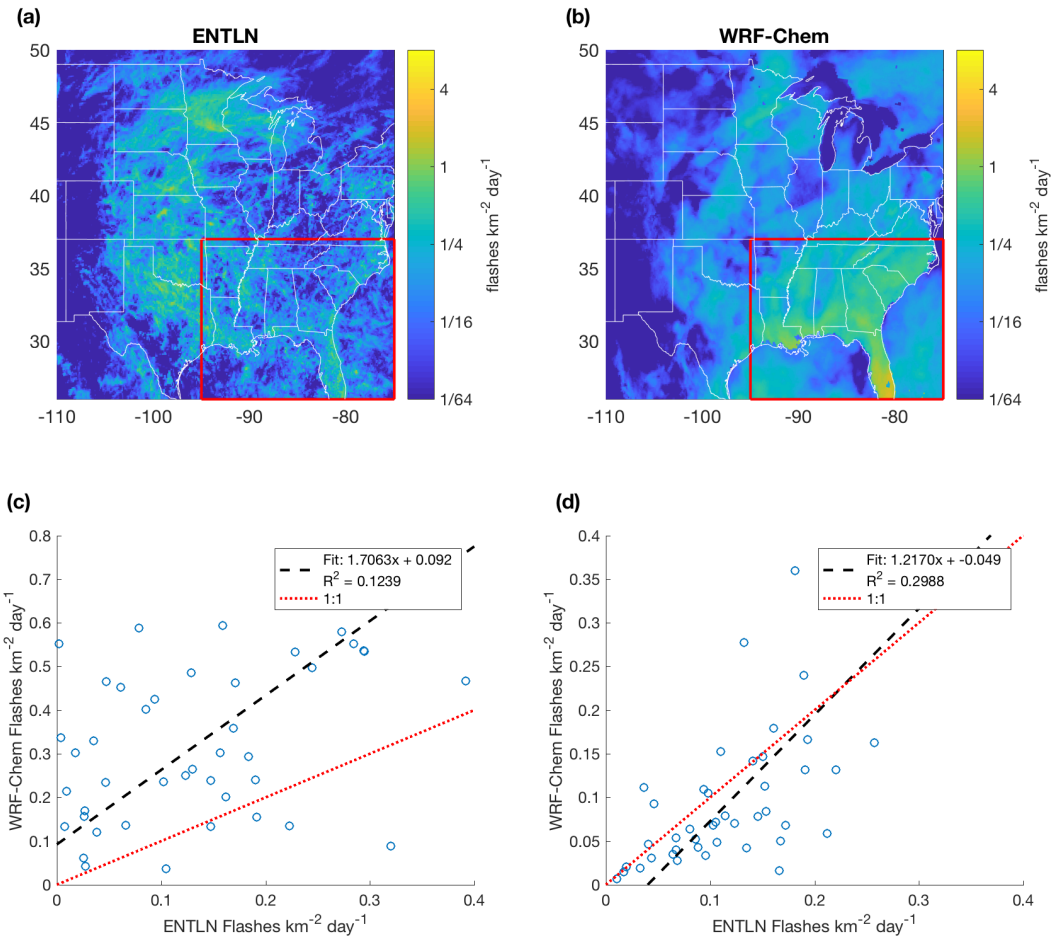

Figure 5.2: Comparison between observed and simulated flash density from May 13 to June 23 2012. **(a)** and **(b)** show the mean flash density averaged over the study period from ENTLN and WRF-Chem, respectively. Both are gridded at 12 km grid spacing. **(c)** and **(d)** show the correlation between total flash density per day between WRF and ENTLN in **(c)** the southeast US (denoted by the red box in **a** and **b**) and **(d)** elsewhere in CONUS.

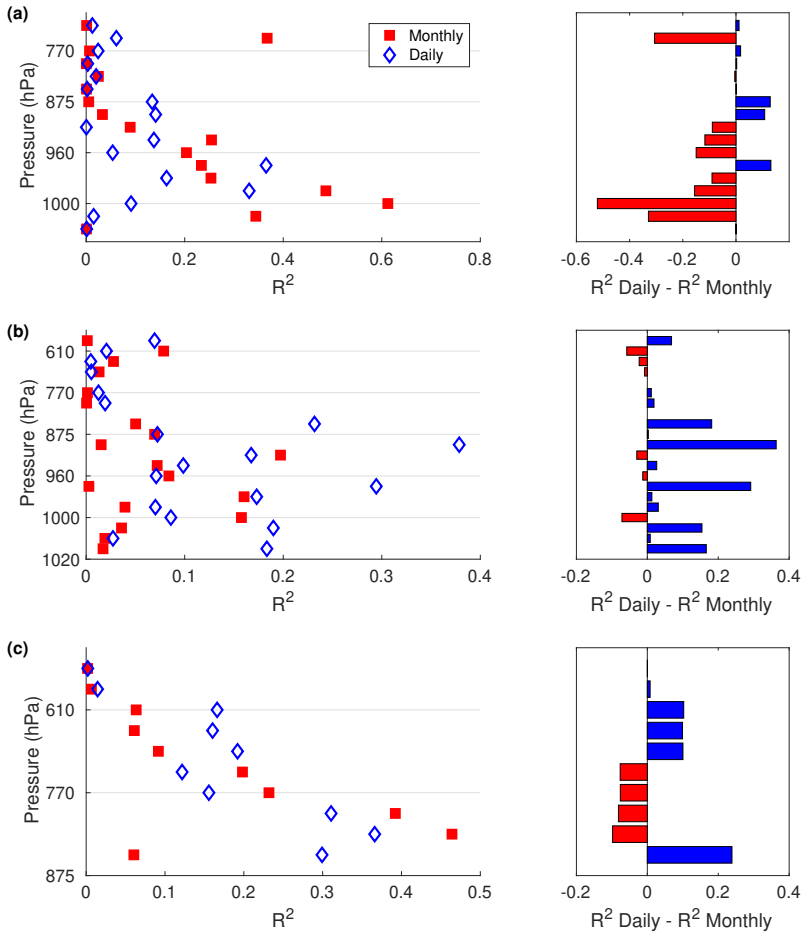

Figure 5.3: R^2 values for correlation between aircraft data and spatiotemporally matched WRF-Chem data for the **(a)** DISCOVER-CA, **(b)** DISCOVER-TX, and **(c)** DISCOVER-CO campaigns, binned by pressure. Left column: absolute R^2 values for each bin. Right column: the difference in R^2 values using monthly average and daily profiles for each bin.

rather than the per-flash production rate of NO, is the cause of the disagreement in the UT between the daily profiles and SEAC4RS data. Further research is required to optimize the lightning parameterizations and improve flash density simulations in the southeast US for our model simulation.

Evaluation of variability in daily profiles

As demonstrated in Laughner et al. (2016), simulating the day-to-day variability in the a priori NO_2 profiles can have a significant impact on the retrieved NO_2 VCDs, due primarily to the day-to-day variation in wind speed and direction driving outflow from emissions sources, e.g. cities and power plants. To examine how well WRF-Chem captures the day-to-day variability in NO_2 profiles, we compare aircraft data from three DISCOVER-AQ campaigns and the matched WRF-Chem data (Sect. 5.2). For each profile in the DISCOVER data, we binned the NO_2 concentrations by pressure and calculated the correlation between WRF-Chem and aircraft NO_2 concentrations (one data point per profile per pressure bin). The results are shown in Fig. 5.3.

In California (Fig. 5.3a), the monthly average profiles correlate better with the aircraft data. However, as mentioned before, the Californian Central Valley is known to be difficult to model accurately (Hu et al., 2010). In Colorado (Fig. 5.3c), the daily profiles do a slightly better job overall, getting the variability at the surface and in an elevated layer more accurately than the monthly average profiles. The difference in Texas is quite dramatic (Fig. 5.3b), with the daily profiles performing substantially better. This suggests that daily profiles are able to capture variability caused by small, concentrated urban plumes much more effectively than monthly average profiles.

As a second check, we also compare WRF-Chem tropospheric VCDs to OMI SCDs to evaluate the general accuracy of wind direction and speed in the daily model profiles. The OMI SCDs do not depend on modeled vertical profiles, and so constitute an independent check on the plume direction. In order to have strong isolated NO_x sources, we use Atlanta, Chicago, Las Vegas, Los Angeles, New York, and the Four Corners power plant for this study. For each of these sites, 5 days from 2007 are randomly chosen. If insufficient OMI SCDs are available for any day ($> 10\%$ of OMI pixels are cloud covered or in the row anomaly), another day is randomly chosen.

For each day, the agreement between the relative spatial distribution of WRF-Chem VCDs and OMI SCDs is manually evaluated, focusing on whether the model plume is advected in the same direction as the OMI SCDs indicate. Each day's agreement is evaluated qualitatively as good or bad. This, whether the WRF-Chem daily VCDs are significantly different from the monthly average WRF-Chem VCDs, and the confidence in the comparison are recorded for each comparison. Because of the number of factors that affect the absolute magnitude of SCDs, we look for qualitative, rather than statistically quantitative, agreement between the modeled VCDs and OMI SCDs. This is relevant since Laughner et al. (2016) noted that it is primarily the plume shape that drives the day-to-day variability in AMFs, therefore a direct, qualitative evaluation of the plume shape is desirable.

Figures 5.4 and 5.5 show two example comparisons, one good (Fig. 5.4) and one poor (Fig. 5.5). By studying randomly chosen days for 6 large NO_x sources, we find that about 67–73%

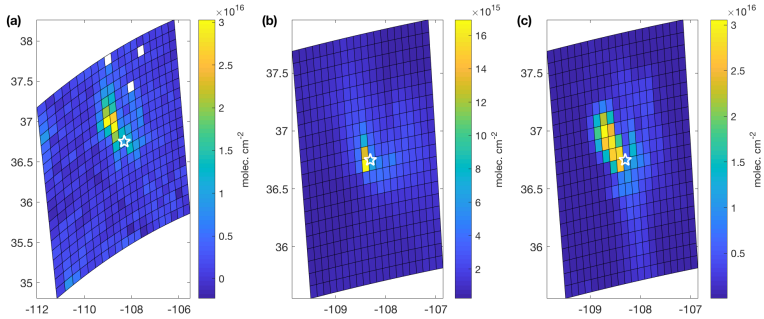

Figure 5.4: A comparison of OMI SCDs **(a)** and WRF monthly average **(b)** and daily **(c)** VCDs. The star marks the location of the Four Corners power plant. Data are from 4 Mar 2007.

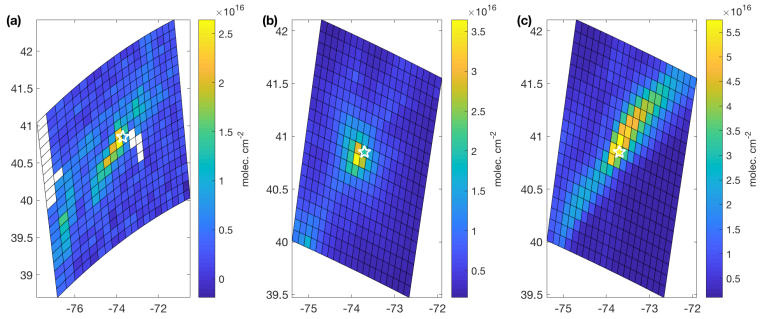

Figure 5.5: A comparison of OMI SCDs **(a)** and WRF monthly average **(b)** and daily **(c)** VCDs. The star marks the location of New York, NY, USA. Data are from 29 Sept 2007.

of days with sufficient data to be evaluated show good agreement between the OMI SCDs and WRF-Chem daily VCDs. (The range is due to different levels of confidence filtering.) This indicates that the WRF-Chem simulated NO_2 profiles are adequately capturing the day-to-day variability due to wind speed and direction.

Both comparisons (vs. OMI SCDs and aircraft measurements) show that daily WRF-Chem profiles do, on average, a better job than monthly average profiles capturing the day-to-day variation in profile shape. Therefore, the core improvement in BEHR v3.0, the transition to daily, high-resolution a priori profiles, is fundamentally sound. Daily profiles are especially important for applications that focus on upwind/downwind differences in NO_2 columns around a NO_x source (Laughner et al., 2016) and, as we will see in Sect. 5.4, generally improve the retrieval in dense urban areas.

5.4 Column density evaluation

For the DISCOVER campaigns, we compare BEHR against aircraft-derived and Pandora VCDs together, calculating a single regression line for the combined dataset. We use two comparisons, in one, only Pandora data that has a coincident aircraft profile is included ("matched"), in the other, all cloud-free Pandora data is used ("all"). Slopes and their 1σ uncertainties for combined aircraft and Pandora VCDs are shown in Table 5.2. For the DISCOVER-CO aircraft comparison, negative VCDs were removed. Such VCDs result from an overestimated stratosphere; since all versions of BEHR use the same stratosphere as their respective NASA SP products, an error in stratospheric subtraction will be present in all products, and since they cannot be corrected in the BEHR retrieval, do not contribute useful information to the evaluation. To evaluate the southeast US, we use the SENEX and SEAC4RS campaigns, which only have aircraft data. These results are shown in Table 5.3. More details (slope, intercepts, R^2 values) can be found in Tables E.1, E.2, and E.3.

In the following sections, we will evaluate the new BEHR v3.0 VCDs from three perspectives: performance compared to the current NASA SP, performance compared to the previous version of BEHR, and performance using daily a priori profiles compared to using monthly a priori profiles.

Comparison vs. SP v3.0

For all the DISCOVER campaigns, BEHR v3.0 shows better agreement with combined aircraft and Pandora measurements than the NASA SP v3.0 (slopes closer to 1). This is expected, since these campaigns generally centered on one or more cities, and a key feature of the BEHR retrieval are the $\sim$ 12 km a priori profiles ($\sim 10x$ high resolution than the NASA SP v3.0 profiles) which better capture the urban profile shape.

In the SENEX and SEAC4RS campaigns, BEHR's performance is more mixed. These campaigns include the southeast US, where we found that the WRF-Chem simulation that generated the a priori profiles overestimated the lightning flash density (Sect. 5.3). In SEAC4RS, whether BEHR v3.0 (M) performs better or worse than the NASA SP v3.0 depends on the method used to extend the profile (Sect. 5.2). This indicates that uncertainty in the measurement is greater than the difference between these two products. BEHR v3.0 (D) performs poorly in the SENEX campaign; this will be explored in Sect. 5.4. Overall, BEHR v3.0 (M) is not significantly affected by the overestimated lightning flash density in the southeast US, as the monthly average profiles smooth out the overlarge UT lightning NO_2 signal.

Campaign	Product	Slope (Matched)	Slope (All)
DISCOVER-MD	BEHR v3.0B (D)	N/A	N/A
	BEHR v3.0B (M)	0.80 ± 0.08	0.64 ± 0.03
	BEHR v2.1C	1.3 ± 0.1	0.87 ± 0.05
	SP v3.0	0.79 ± 0.08	0.50 ± 0.03
DISCOVER-CA	BEHR v3.0B (D)	0.49 ± 0.04	0.68 ± 0.04
	BEHR v3.0B (M)	0.51 ± 0.04	0.66 ± 0.04
	BEHR v2.1C	0.57 ± 0.05	0.68 ± 0.04
	SP v3.0	0.41 ± 0.04	0.54 ± 0.03
DISCOVER-TX	BEHR v3.0B (D)	0.69 ± 0.07	1.00 ± 0.06
	BEHR v3.0B (M)	0.60 ± 0.05	0.87 ± 0.05
	BEHR v2.1C	1.1 ± 0.1	1.33 ± 0.08
	SP v3.0	0.53 ± 0.05	0.74 ± 0.05
DISCOVER-CO	BEHR v3.0B (D)	0.66 ± 0.06	0.66 ± 0.03
	BEHR v3.0B (M)	0.70 ± 0.06	0.63 ± 0.03
	BEHR v2.1C	0.74 ± 0.06	0.68 ± 0.03
	SP v3.0	0.53 ± 0.05	0.50 ± 0.02

Table 5.2: Slopes and 1σ uncertainties of BEHR vs. combined aircraft (extended with GEOS-Chem profiles) and Pandora VCDs. Matched slopes use only Pandora data approximately coincident with aircraft profiles to get similar sampling; all uses all valid Pandora data. Outliers and negative VCDs are removed before computing slopes.

Campaign	Product	Slope (GEOS-Chem)	Slope (Extrap.)
SENEX	BEHR v3.0B (D)	2.3 ± 0.5	1.7 ± 0.5
	BEHR v3.0B (M)	1.0 ± 0.2	0.9 ± 0.3
	BEHR v2.1C	1.4 ± 0.4	1.5 ± 0.5
	SP v3.0	1.1 ± 0.2	0.8 ± 0.3
SEAC4RS	BEHR v3.0B (D)	0.9 ± 0.4	0.7 ± 0.3
	BEHR v3.0B (M)	1.2 ± 0.4	1.0 ± 0.3
	BEHR v2.1C	2.6 ± 0.5	2.5 ± 0.7
	SP v3.0	1.0 ± 0.3	0.8 ± 0.3

Table 5.3: Slopes and 1σ uncertainties for RMA regression of satellite VCDs against in situ calculated VCDs. Both methods of extending the profiles (using GEOS-Chem modeled profiles or extrapolating the top/bottom ten points) are included. Outliers are removed before calculating these parameters.

Comparison vs. BEHR v2.1

Using just Pandora data coincident with aircraft spirals, v2.1 performs better in all DISCOVER campaigns except MD. However, using all Pandora data, v3.0 (D) performs better than or similar to v2.1 in all DISCOVER campaigns where daily profiles are available. The Pandoras provide more observations than the aircraft profiles, and, due to their small footprint, are more sensitive to narrow, highly concentrated NO_2 plumes. The v2.1 profiles used 2005 emissions; as seen in Fig. 5.1, this led to too much NO_2 being placed at the surface, which will increase the retrieved VCD. This suggests that the better performance of v2.1 compared to v3.0 (M) in some cases is due to cancellation of errors; overestimated surface NO_2 is canceling out the lack of temporal variation in the profiles. That is, the higher average surface concentration in the v2.1 profiles may be similar to the in-plume concentrations resolved by the daily v3.0 profiles.

In v3.0, when daily profiles are available, the agreement is similar to or better than v2.1 if all Pandora data is used. Therefore, daily profiles are able to capture at least some enhancements in surface NO_2 where and when they occur, without overestimating the average profile. This is not evident using just the coincident Pandora data because of the smaller number of comparisons. As the comparison expands (using all Pandora data), the improvement becomes evident. The better performance of daily profiles suggests that even though Laughner et al. (2016) did not see large effects in a multi-month average using daily instead of monthly profiles, daily profiles will provide a more accurate representation of urban VCDs over longer averaging periods.

BEHR v3.0 performs better in the SENEX and SEAC4RS comparisons than v2.1 (excluding 3.0 (D) in SENEX). The v2.1 profiles did not include lightning emissions, as it was a limitation of WRF-Chem at that time (Laughner et al., 2018b). This indicates that, even though the contribution of lightning to the southeast US profiles is too large, the inclusion of lightning NO_2 in the profiles did improve the representation of the southeast and midwest US. Laughner et al. (2018b) also showed that implementing a variable tropopause pressure decreased VCDs in the southeast US during summer; this also would help reduce the high bias compared to SENEX and SEAC4RS seen in BEHR v2.1.

Comparison of BEHR v3.0 (M) vs BEHR v3.0 (D) in the SE US

In the SENEX campaign, v3.0 (D) performs significantly worse than v3.0 (M). From Fig. 5.1 we know that the daily a priori profiles overestimate the UT NO_2, and from Fig. 5.2 we know that this is due to a significant overestimate of the flash density in our WRF simulation. The comparison in Table 5.3 would seem to indicate that this overestimate has a severe impact on the retrieved VCDs, but we must also consider the uncertainty in the SENEX-derived VCDs.

Figure 5.6a shows the ensemble of profiles from SENEX used to calculate VCDs. The circles

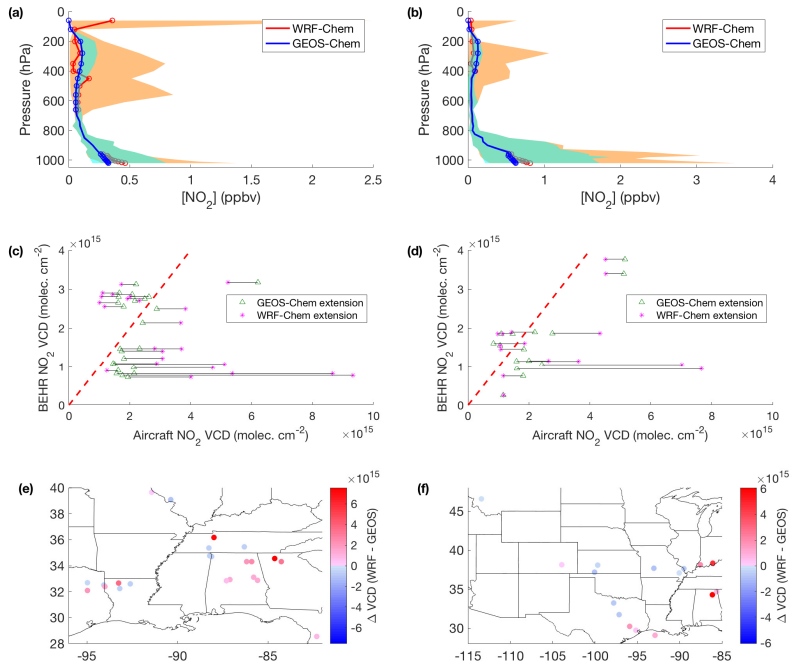

Figure 5.6: **(a,b)** The profiles used to calculate the aircraft VCDs extended using WRF-Chem or GEOS-Chem profiles; the solid line is the median of all profiles, the shading represents the 10th and 90th percentiles for each binned level. Circles indicate levels that were derived from the models in at least 50% of the profiles. **(c,d)** Comparison of BEHR v3.0 (D) VCDs vs. aircraft-derived VCDs using GEOS-Chem and WRF-Chem profiles to extend the profile to the surface and tropopause. The black lines connect corresponding comparisons between the two methods and the red dashed line represents the 1:1 agreement. **(e,f)** Difference between aircraft VCDs extended with WRF-Chem and GEOS-Chem profiles. **(a,c,e)** are for the SENEX campaign, **(b,d,f)** are for SEAC4RS.

mark levels that had to be calculated using model data for > 50% of the profiles. In SENEX, that is all levels about ∼ 700 hPa, which means that the SENEX aircraft data provides very little constraint on the UT. The lightning contribution to the SENEX columns must come from the GEOS-Chem monthly averages or extrapolation from a lower altitude, which means the spatial and temporal variation is lost.

Figure 5.6c shows the effect of using the WRF-Chem a priori profiles instead of the GEOS-Chem profiles to extend the SENEX profiles. The WRF-Chem profiles do include spatial and temporal variation of the UT, but using them reinforces the AMF errors, moving all points away from the 1:1 line. Without either in situ measurements of the UT in the southeast US or Pandora total column observations we cannot separate the errors in AMF caused by the overestimated UT NO_2 in the a priori profiles from the error caused by the lack of spatiotemporal variation in the extended aircraft profiles. For example, the error in the cluster of points below the 1:1 line in Fig. 5.6c could be corrected if either the UT NO_2 in the a priori profile was reduced, decreasing the AMFs and so increasing the BEHR VCDs, or if the aircraft profile had less NO_2, thus moving the points left onto the 1:1 line. (In the case, there would still be a discrepancy between the BEHR VCD and the VCD derived from combining aircraft and WRF-Chem profiles, suggesting that the WRF-Chem UT NO_2 is still too great.)

Other campaigns do have better sampling of the UT, e.g. SEAC4RS (Fig. 5.6b,d,f), but do not have as many profiles in the southeast US (Fig. 5.6e,f). Therefore, we must currently assign an uncertainty of ±100% to VCDs retrieved with daily profiles in the southeast US (east of 95° W and south of 37.5° N). This is almost certainly overly conservative, as Laughner et al. (2018b) showed that the frequency distribution of UT NO_2 in the southeast apriori profiles was skewed to lower values in the daily profiles, and a three month average using daily a priori profiles resulted in greater VCDs than using monthly a priori profiles, which would not be the case if the daily profiles always overestimated the UT. This suggests that days with little or no lightning in both the real world and WRF-Chem simulations are more numerous than days with significant lightning contribution, and so a multi-month average using daily profiles would in fact accurately capture this. However, without long term independent column measurements in the southeast, we cannot confirm this hypothesis. Future work will focus on improving the simulation of lightning in the southeast US. If successful, improved WRF-Chem profiles for the southeast can be implemented.

Comparison of BEHR v3.0 (M) vs BEHR v3.0 (D) in urban areas

In the DISCOVER campaigns, BEHR v3.0 (D) using daily profiles has regression slopes similar to or closer to 1 than BEHR v3.0 (M) using monthly profiles except in the DISCOVER-CA aircraft comparisons. There is a clear improvement in DISCOVER-TX using daily profiles. This suggests that the daily profiles are capturing small, concentrated plumes in the urban area (Fig. 5.3b), which is improving the retrieval overall in an urban area with many highly

concentration industrial NO_x sources. Therefore, we argue that daily profiles improve the retrieval in many ways, not only for applications that select for upwind/downwind pixels as shown in Laughner et al. (2016), but also for multi-month averages in dense urban areas.

5.5 Discussion: future efforts to validate daily profiles

Using space-based SCDs to evaluate the spatial distribution of NO_2 in a CTM is powerful (Sect. 5.3), because both provide a spatially continuous field of NO_2 columns. As we have shown here, this makes a qualitative evaluation straightforward and illustrative. However, a quantitative metric is more challenging to devise, as the direct correlation of model and satellite columns is less important than the more abstract agreement between the overall plume direction and extent. As we have shown here, daily, high-resolution profiles provide important benefits to an NO_2 retrieval; therefore, development of more quantitative methods to evaluate model performance in this manner should be a priority.

There are several possibilities. First, an algorithm that identifies the plume and computes the direction and length of its major axis could be used. This would allow a comparison of the direction and extent of the plumes more directly. Such an algorithm would not be trivial to develop; comparisons such as the one shown in Fig. 5.5a,c would likely be difficult for the algorithm to distinguish the plume direction accurately.

Second, this problem could be treated as an image recognition problem. A neural network could be trained on modeled VCDs and SCDs. A training set of good and bad days could be constructed from the WRF-Chem simulations used in BEHR v3.0D. Development of this approach is beyond the scope of this paper.

Third, dense sensor networks (e.g. Shusterman et al., 2016; Kim et al., 2018) may also be useful to evalulate daily profiles by permitting a simpler correlation test between modeled and observed surface concentrations than is possible between modeled VCDs and observed SCDs. Development of these networks is a topic of active research. This method may be necessary for future retrievals, especially over the US and European domains, where decreasing NO_x emissions mean that the contrast between plumes and background in SCDs is much weaker now than in 2007.

5.6 Conclusions

We have evaluated version 3.0B of the BEHR OMI NO_2 product against multiple datasets. We find that the WRF simulation used to generate the a priori NO_2 profiles generally agrees well with the available aircraft data; however, the number of lightning flashes is significantly overestimated in the southeast US leading to an overestimate of the UT NO_2 in that region, although broadly consistent with ENTLN observations elsewhere. When compared against

aircraft-derived and Pandora VCDs, BEHR v3.0B performs better than SP v3.0, with regionally varying low biases of 0–51% compared to in situ and Pandora measurements. Using daily profiles yields better results than monthly profiles, except in the southeast US.

The lessons learned here are applicable to geostationary satellites scheduled to launch in the near future. Because the BEHR retrieval focuses on the continental United States, it serves as a useful prototype for future NO_2 retrievals from geostationary satellites such as GEMS (Bak et al., 2013; Choi and Ho, 2015), Sentinel-5 (Ingmann et al., 2012), and TEMPO (Chance et al., 2013), which also will be inherently restricted to regional areas. This offers the opportunity to use higher-resolution a priori data than global retrievals.

Here, the results from the SENEX and SEAC4RS campaign here demonstrate that verifying the chemical transport model's reproduction of the day-to-day variability in lightning flashes is vital to obtain reliable results in such regions. With the sub-daily temporal resolution available to geostationary satellites, this will only become more important. Therefore, geostationary retrievals should evaluate the diurnal variation in lightning flashes in their a priori models using ground- and space- based lightning detectors (e.g. NLDN, ENTLN, or the GOES-R lightning mapper), and plans should be made to validate retrieved VCDs in multiple regions that have strong, but different, lightning influence. Such validations must include measurement of the UT NO_2 profile and/or total column observations in order to reliably separate errors in the a priori profiles from errors in the observations used for evaluation.

Evaluating the day-to-day performance of the a priori profiles in future geostationary retrievals is crucial. Daily profiles have been shown to significantly affect retrieved NO_2, especially in applications that systematically focus on NO_2 VCDs downwind of a source (Laughner et al., 2016), and we have shown here that daily profiles also improve performance in urban areas. With the WRF-Chem model configuration used here, urban NO_2 plumes are simulated with the correct spatial pattern $\sim$ 70% of the time. Planned campaigns to evaluate geostationary satellite retrievals should be designed with an eye towards also evaluating the day-to-day accuracy of the a priori profiles.

Code and data availability

The analysis code for this paper is available at `https://github.com/behr-github/BEHR-v3-evaluation/` (Laughner, 2018). Supporting datasets generated or used by this code is hosted by UC Dash (Laughner et al., 2018a). The BEHR v3.0B product is hosted as four subproducts by UC Dash (Laughner et al., 2018c; Laughner et al., 2018e; Laughner et al., 2018d; Laughner et al., 2018f) as well as on `behr.cchem.berkeley.edu`. The BEHR algorithm is available at `https://github.com/CohenBerkeleyLab/BEHR-core/tree/master` (Laughner and Zhu, 2018a).

Chapter 6

Observations of the NO_x concentration-lifetime relationship in US cities

6.1 Introduction

NO_x ($\equiv$ NO + NO_2) is a pollutant trace gas emitted anthropogenically as a byproduct of combustion and naturally by lightning, soil bacteria, and biomass burning. NO_x plays a key role in air quality; it itself is toxic (Kagawa, 1985; Chauhan et al., 1998; Wegmann et al., 2005; Kampa and Castanas, 2008), it participates in the formation of particulate matter (Izumi and Fukuyama, 1990; Pandis et al., 1992) and is a key catalyst in the production of tropospheric ozone (Jacob et al., 1993; Perring et al., 2013) Because of this, NO_x emissions have been a key target of air quality regulations in many developed countries (e.g. US Environmental Protection Agency, 1970; Vestreng et al., 2009; Liu et al., 2017), with the ultimate goal of reducing NO_x concentrations to improve air quality, especially in urban areas.

However, reducing NO_x emissions does not lead to a linear improvement in air quality. The rates of chemical reactions leading to ozone production, PM formation, and NO_x loss are nonlinearly dependent on NO_x concentration, total volatile organic compound reactivity with OH (VOC_R), and the branching ratio (α) of the alkyl peroxy (RO_2) and NO reaction (Browne and Cohen, 2012; Perring et al., 2013; Romer et al., 2016). The nonlinear relationship between NO_x concentration and lifetime is particularly relevant when evaluating the effectiveness of emissions controls. If lifetime decreases with decreasing concentration, the effectiveness of emissions controls will be enhanced; conversely, if lifetime increases with decreasing concentrations, then reducing emissions has less effect on the NO_x concentrations. In the latter case if the change in lifetime is not accounted for when constraining emissions with a top-down approach, changes in NO_x emissions will be underestimated.

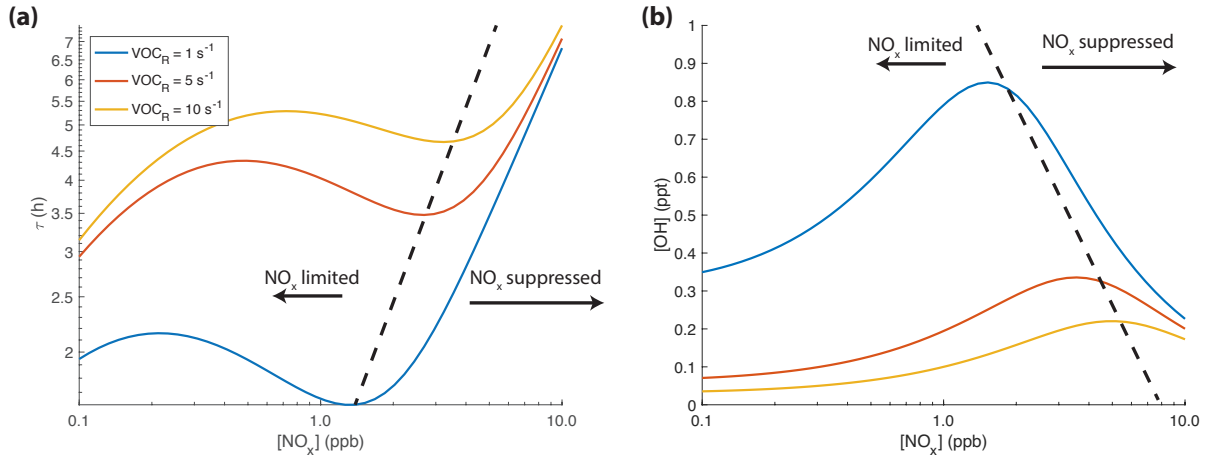

Figure 6.1: Theoretical calculation of **(a)** NO_x lifetime and **(b)** OH concentration vs. NO_x concentration for three different VOC_R values. The lifetime is calculated assuming a steady-state of HO, HO_2, and RO_2 radicals for each fixed NO_x concentration. The black dashed line demarcates the separation between NO_x-limited and NO_x-suppressed chemistry.

The theoretical relationship between NO_x lifetime and concentration is shown in Fig. 6.1a. At high NO_x concentrations (>5 ppb), the lifetime is primarily controlled by loss to HNO_3 (by the reaction NO_2 + OH); the lifetime increases with NO_x concentration because HO_x production is limited by the photolysis of ozone and formaldehyde (Thornton et al., 2002), therefore the amount of OH present is limited (Fig. 6.1b). At low concentrations (<1 ppb), NO_x lifetime is governed by loss to alkyl nitrates (ANs), a minor product of the NO + RO_2 reaction. A minimum in lifetime occurs at a NO_x concentration between 1 ppb to 3 ppb when both loss the ANs and HNO_3 are active loss processes.

The NO_x lifetime can be calculated from in situ measurements, given that the VOC_R is adequately captured by the VOC species measured and the important reactions are known a priori. However, this introduces an uncertainty from the possibility of unaccounted for reactions. An alternative method of constraining lifetime is to use satellite observations, where the distance from the source and wind speed together serve as a proxy for time (Beirle et al., 2011; Valin et al., 2013; Liu et al., 2016).

In theory, a change in chemical lifetime between weekdays and weekends should be observed (the "weekend effect", e.g. Murphy et al., 2007; Valin et al., 2014). In the US, this is due to the reduction in heavy truck traffic on weekends (Dreher and Harley, 1998; Marr and Harley, 2002; Vukovich and Scarborough, 2004), which results in a change of NO_x concentration with a smaller change in VOC_R. This causes a shift in NO_x chemical lifetime along one of the curves in Fig. 6.1.

It is common to apply the terms "NO_x-limited" and "NO_x-suppressed" to the part of the

lifetime curves left and right, respectively, of the minimum between 1 ppb to 3 ppb. These terms come from the dependence of ozone production on NO_x concentration; at low concentrations, NO_x is the limiting reagent in ozone production, while at high NO_x concentrations, NO_x suppressed the oxidation of VOCs necessary to the production of ozone. These terms are convenient descriptors of chemical regimes, and have carried over into the discussion of NO_x lifetime.

In this work, we use satellite observations of two US cities between 2005 and 2014 to show that there is a change in the weekend vs. weekday NO_x lifetimes that is generally consistent with our understanding of NO_x chemistry at intermediate concentrations. To our knowledge, this is the first direct observation of the NO_x lifetime-concentration relationship, made possible by the use of high-resolution, daily NO_2 a priori profiles in the latest version of the Berkeley High Resolution (BEHR) NO_2 retrieval.

6.2 Methods

The Berkeley High Resolution (BEHR) NO_2 retrieval

The Berkeley High Resolution (BEHR) retrieval, version 3.0B, is described in detail in Laughner et al. (2018b). Briefly, the BEHR retrieval is a regional tropospheric NO_2 retrieval that calculates a custom air mass factor over the continental US using high resolution a priori inputs, most notably daily, high resolution NO_2 profiles. As noted in Laughner et al. (2016), such profiles are necessary to simultaneously retrieval NO_2 vertical column densities and loss downwind of sources accurately. These profiles are simulated with WRF-Chem v3.5.1 (Grell et al., 2005) at 12 km resolution. For details of the model simulation, refer to Laughner et al. (2018b). Daily profiles are currently available for 2005, 2007–2009, and 2012–2014. Additional years will be added as the simulations complete. These air mass factors are used to convert the tropospheric slant column densities from the NASA Standard Product version 3.0 (Krotkov et al., 2017) into vertical column densities (VCDs) that take advantage of the high resolution a priori data.

Exponentially modified gaussian fitting

To calculate lifetime from satellite observations, we use a method of fitting wind-aligned satellite VCDs with an exponentially modified gaussian (EMG) function (Beirle et al., 2011; Valin et al., 2013; Lu et al., 2015). For each OMI orbit, the wind direction is obtained from the same WRF-Chem simulation that provides the BEHR a priori NO_2 profiles by averaging the first five model layers of the 3×3 subset of model grid cells centered on the location of interest from the WRF-Chem output file closest in time to the OMI overpass.

The observed BEHR VCDs are rotated such that the wind direction points east in order to align the plumes, then averaged in time. Only VCDs marked as good quality in the BEHR

quality flags and days with the wind speed $>3\,\mathrm{m\,s^{-1}}$ are used. VCDs from 1° upwind and 2° downwind of the city center are included. Averages are over April to September for two or three years (represented by a slash, e.g. 2005/07, and dash, e.g. 2012–14, respectively), depending on the availability of daily profiles. The time averaged VCDs are then integrated perpendicular to the wind direction ±1° from the city center to produce a one-dimensions "line density", which is a 1D representation of the NO_2 plume. These line densities are then fit by the EMG function,

$$F(x|a, x_0, \mu_x, \sigma_x, B) = \frac{a}{2x_0} \exp\left(\frac{\mu_x}{x_0} + \frac{\sigma_x^2}{2x_0^2} - \frac{x}{x_0}\right) \mathrm{erfc}\left(-\frac{1}{\sqrt{2}}\left[\frac{x-\mu_x}{\sigma_x} - \frac{\sigma_x}{x_0}\right]\right) + B \quad (6.1)$$

where a, x_0, μ_x, σ_x, and B are fitting parameters and erfc is the error function complement. This is fit to the line densities with a constrained nonlinear, least-squares optimization using an interior-point algorithm. The constraints used are the same as in Laughner et al. (2016). Uncertainties in the fitting parameters are calculated as the diagonal elements of the inverse Hessian matrix computed at the final step of the optimization, multiplied by the sum of squared errors:

$$\vec{e} = \frac{t(0.95|n-5)}{\sqrt{n}} \left[\frac{1}{n-5}\sum_x (L_x - F_x)^2\right] \mathbf{H}^{-1} \quad (6.2)$$

where n is the number of points in the line density, $t(0.95|n-5)$ is Student's two-tailed 95% confidence t for $n-5$ degrees of freedom, L_x and F_x are the discrete line density and EMG fit, respectively, at coordinate x, and $\mathbf{H}$ is the 5×5 Hessian matrix for the five fitting parameters.

Lifetime is computed from the fitting parameter x_0 and average wind speed for all orbits contributing to the line density (w):

$$\tau = \frac{x_0}{w} \quad (6.3)$$

Uncertainty is propagated to τ by using the 95% confidence intervals of x_0 and w:

$$e_\tau^2 = \left(\frac{\partial \tau}{\partial x_0} e_{x_0}\right)^2 + \left(\frac{\partial \tau}{\partial w} e_w\right)^2 \quad (6.4)$$

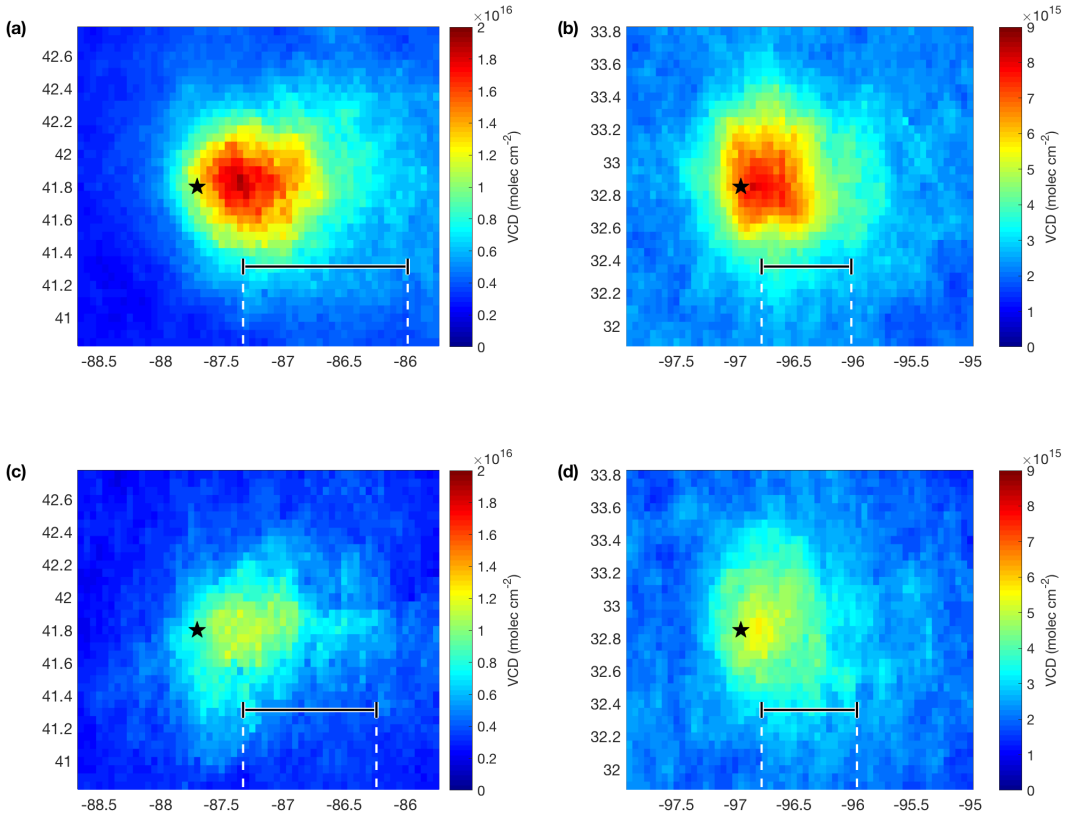

Figure 6.2: Wind aligned NO_2 plumes (aligned so the wind blows west to east) in **(a, c)** Chicago, IL, USA and **(b, d)** Dallas, TX, USA, averaged Apr.–Sept. from 2005 and 2007. **(a)** and **(b)** are weekdays only (Tue.–Fri.) and **(c)** and **(d)** are weekends (Sat.–Sun.) only. The star marks the location of Chicago or Dallas, and the line below the plume marks the distance between the maximum in the plume and the distance at which the enhancement above background has reduced to $1/e$ of its peak value.

6.3 Results

Figure 6.2 shows the impact of the weekend effect in Chicago, IL and Dallas, TX. It shows the summertime (April to September) VCDs averaged from 2005 to 2007 (omitting 2006 because daily a priori profiles were not available for 2006 at the time of writing). The VCDs are rotated such that the wind directions align (blowing west to east in this frame of reference) before averaging. In both cities, the NO_2 VCDs decrease by nearly 50% on the weekends (Fig. 6.2c,d) compared to the weekdays (Fig. 6.2a,b), due to the absence of heavy truck traffic on weekends.

In Chicago, this reduction in VCDs also leads to a shift in the chemical loss. The black lines in Fig. 6.2 denote the e-folding distance from the maximum NO_2 VCDs (specifically, the right end of the line is the distance at which the NO_2 enhancement over background has reduced to $1/e$ of its original value). Figure 6.2c shows that the e-folding distance decreased by $\sim 20\%$ on the weekends compared to the weekday (Fig. 6.2a). From Fig. 6.1, such a change can occur if Chicago is in the NO_x-suppressed regime, where its lifetime is positively correlated with its concentration. In contrast, Dallas shows no such change, which would occur if the weekday and weekend NO_x concentrations were on opposite sides of the lifetime minimum seen in Fig. 6.1.

Figure 6.3 provides another view of this phenomenon. Weekday and weekend line densities and the corresponding EMG fits for Chicago and Dallas are shown for two time periods, 2005/2007 (a,b) and 2012–2014 (c,d). The line densities in figure 6.3a,b are the result of integrating the VCDs in Fig. 6.2 perpendicular to the wind direction. To help compare the lifetimes, the line densities and EMG fits are normalized to the range $[0, 1]$. The decrease in lifetime on the weekends relative to the weekdays during 2005/2007 in Chicago manifests in Fig. 6.3a as a more rapid decline in the NO_2 line densities downwind of the city (to the right of 0 in Fig. 6.3). In contrast, there is little difference between the weekend and weekday lifetimes in Dallas in 2005/2007 (Fig. 6.3b).

In 2012–2014, NO_x concentrations have reduced to the point that both cities are approaching the NO_x-limited part of the lifetime curve. Chicago now exhibits no noticeable difference in lifetime between weekdays and weekends (Fig. 6.3c) but in Dallas, the weekend lifetime is now longer than the weekday lifetime (Fig 6.3d).

We can use this shift to examine the relationship between NO_x lifetime and concentration empirically by plotting the change in lifetime against the average VCDs over the urban area for that time period. This is shown in Fig. 6.4. Weekend-weekday pairs for four time periods (2005/2007, 2007–2009, 2012/2013, and 2012–2014) are drawn as connected pairs of points. In each pair, both the weekend and weekday points have similar VOC_R, but different NO_x concentrations. Therefore, each pair will move along one of the VOC_R curves in Fig. 6.1. In Chicago, we see a distinct shift from decreased lifetime on weekends before 2010

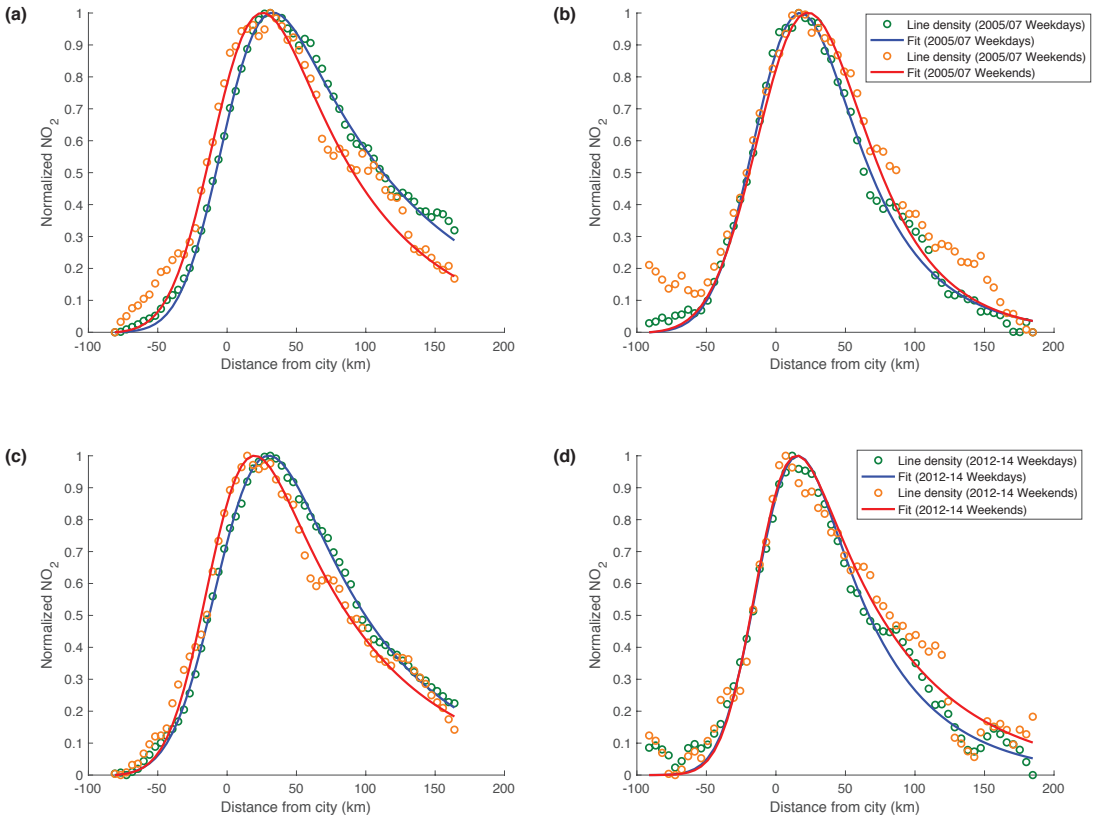

Figure 6.3: Line densities and the corresponding EMG fits for Chicago, IL **(a,c)** and Dallas, TX **(b,d)**, normalized to the range $[0, 1]$. **(a)** and **(b)** are from 2005 and 2007 data; **(c)** and **(d)** are from 2012–2014 data.

to increased or unchanged weekend lifetime after 2010. In Dallas, before 2007, there is no significant change in weekend vs. weekday lifetime, but after 2007, lifetime increases on weekends relative to weekdays. In all cases, weekends have smaller VCDs than weekdays.

6.4 Discussion

This shift toward increased lifetime on weekends with decreased VCDs after 2007/2010 indicates that these two cities are in the process of or have shifted from NO_x-suppressed to NO_x-limited chemistry. This has important implications for constraining emissions trends from VCDs or concentration measurements, for future efforts to reduce ozone pollution, as well as our basic understanding of NO_x chemistry.

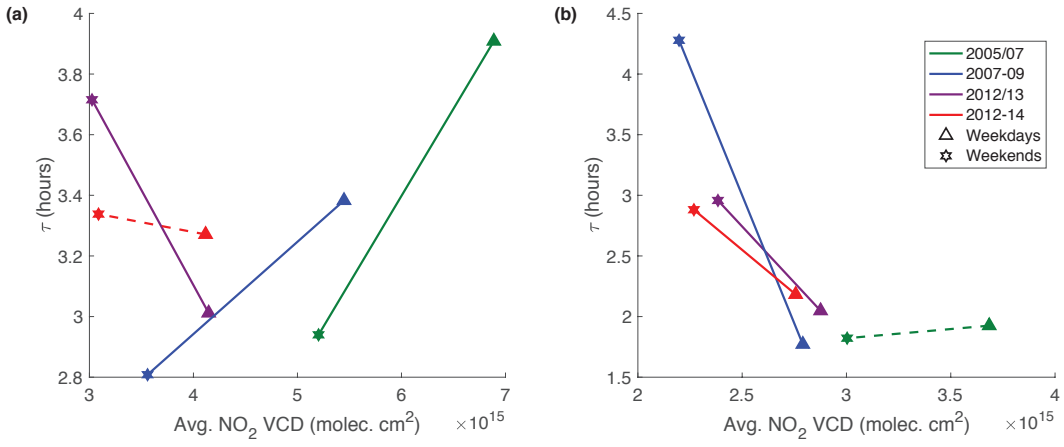

Figure 6.4: Weekday-weekend change in lifetime for six US cities: **(a)** Chicago, IL and **(b)** Dallas, TX. Four time periods are shown: 2005 and 2007, 2007–2009, 2012–2013, and 2012–2014. Each weekday/weekend pair is connected by a solid line if the difference in lifetimes is statistically significant, a dashed line if it is not.

Implications for emissions

A number of studies have examined trends in US emissions by assuming that they are linearly related to trends in VCDs (e.g. Russell et al., 2012; Jiang et al., 2018). However, we see evidence that not only does the NO_x lifetime change with decreasing VCDs, but the sign of that dependence changes.

Interestingly, we see that the turning point, where lifetimes begin increasing with decreasing VCDs, occurs in both Chicago and Illinois between 2007 and 2012. This is approximately the time period when Jiang et al. (2018) identified a flattening out in NO_2 VCD trends. Jiang et al. (2018) attribute this to a slowdown in US emissions reductions, which certainly may play a part. However, increasing NO_x lifetime with decreasing NO_x concentrations will counteract the emissions reductions to some extent, since NO_x will not be removed as quickly from the atmosphere.

In contrast, Lu et al. (2015) used the EMG method with the OMI standard product, and did not observe a significant slowdown in top-down NO_x emissions. Since the EMG method explicitly accounts for lifetime, this suggests that once changes in lifetime are taken into account, the reduction in US NO_x emissions is fairly consistent over the past decade.

Further research is necessary to expand our analysis to multiple cities and show that the transition from NO_x-suppressed to NO_x-limited chemistry has indeed occurred throughout the US, but we already see strong evidence that changes in the NO_x lifetime cannot be ignored when constraining emissions.

Implications for ozone production

Ozone production depends nonlinearly on NO_x concentration in a similar but inverse manner compared to NO_x lifetime; that is, ozone production is minimized at low and high NO_x concentrations but maximized at intermediate concentrations (Perring et al., 2013). The mechanistic cause of the nonlinear dependence of both NO_x lifetime and ozone production are related, and so the maximum in ozone production usually (but not always) occurs at a similar NO_x concentration as the minimum in NO_x lifetime. Therefore, observing a shift in the dependence of lifetime on NO_x concentration from NO_x-suppressed to NO_x-limited chemistry implies that a similar shift will happen in ozone production.

Under NO_x-suppressed conditions, ozone production increases as NO_x concentration decreases, while under NO_x-limited conditions, the reverse is true. Therefore, reducing NO_x emissions is effective at reducing peak ozone only if the atmosphere is in a NO_x-limited regime. We see both Chicago and Dallas entering the NO_x-limited regime based on the behavior of NO_x-lifetime; therefore, we predict that NO_x emissions reductions will be a viable method of reducing ozone concentrations in the future for these cities.

Testing our understanding of NO_x chemistry

The ability to observe changes in NO_x lifetime and VCDs simultaneously allows us to test our understanding of NO_x chemistry in new ways. The pattern shown in Fig. 6.4a, where the lifetime reaches a minimum around 3×10^{15} molec. cm^{-2} to 4×10^{15} molec. cm^{-2}, is qualitatively similar to the pattern predicted by the steady state model (Fig. 6.1).

We can relate the results in Fig. 6.4 to the model in Fig. 6.1 more quantitatively by establishing the relationship between BEHR VCDs and boundary layer NO_x concentration. Lamsal et al. (2015) showed that there is a linear relationship between a tropospheric NO_2 VCD and surface NO_2 concentration. We calculate the linear relationship as

$$\mathrm{NO}_{x\,\mathrm{BEHR}}(p) = \frac{\mathrm{NO}_{x\,\mathrm{WRF}}(p)}{V_{\mathrm{NO_2,WRF}}} \cdot V_{\mathrm{NO_2,BEHR}} \tag{6.5}$$

where p represents the vertical coordinate as pressure, $\mathrm{NO}_{x\,\mathrm{WRF}}(p)$ is the WRF NO_x ($\equiv$ NO+ NO_2) profile at pressure p, and $V_{\mathrm{NO_2,BEHR}}$ and $V_{\mathrm{NO_2,WRF}}$ are the NO_2 vertical column densities from BEHR and integrating the WRF-Chem NO_2 profile, respectively. The quantities on the right hand side are averaged within 0.35° of the city center, to focus on the active urban chemistry.

Using this approach, we calculate the average NO_x concentration in the bottom 10 WRF-Chem layers (corresponding to an $\sim$2 km boundary layer, chosen as the altitude in Chicago at which the concentration profile is clearly controlled by the free troposphere). The 2012/13

and 2012–14 weekdays in Chicago are approximately the point at which the transition from NO_x-suppressed to NO_x-limited chemistry occurs, and correspond to a boundary layer NO_x concentration of ∼2.5 ppb. Likewise, the 2007–09, 2012/13, and 2012–14 weekdays in Dallas correspond to a transition at ∼1 ppb. This agrees well with the steady-state model (Fig. 6.1), where the shift in chemistry occurs at 1 ppb to 3 ppb, depending on the VOC_R.

This is, to our knowledge, the first direct observation of the relationship between NO_x lifetime and concentration. That it generally agrees with the steady-state model is confirmation that such a model can capture the shift in chemical regime, at least in urban areas.

6.5 Conclusions

We have shown that, using the latest version of the BEHR product, we are able to observe how changes in NO_x lifetime correspond to changes in NO_2 VCDs. This is, to our knowledge, the first time this relationship has been directly observed. The observed behavior in Chicago, IL, USA and Dallas, TX, USA is mostly consistent with our current understanding of urban NO_x chemistry, principally that there is a transition around 1 ppb to 3 ppb NO_x between the NO_x-suppressed and NO_x-limited regimes. This has implications for emissions trends and ozone production as well. New questions about our current understanding of NO_x chemistry as well as a more detailed examination of the implications for NO_x emissions and ozone production will be addressed in future work.

Chapter 7

Concluding remarks

Understanding how NO_x lifetime has changed in the past decade is crucial to be able to accurately constrain emissions changes and to predict the effect of NO_x transport from sources to cleaner areas. Satellite observations provide a powerful tool to evaluate this, as the ability to see spatial patterns in NO_2 concentration allows us to directly observe transport in the patterns seen and observe the rate of chemical loss by examining how quickly the NO_2 enhancement decreases downwind of a source. However, measuring both the magnitude and spatial gradients presents a challenge for standard space-based NO_2 retrievals.

In this dissertation, I have designed and implemented a new NO_2 retrieval over the continental US specifically optimized for this problem. In Chapter 2, I showed that, in order to simultaneously retrieve the NO_2 VCDs of a source and the decay downwind from it accurately, a space-based NO_2 retrieval must use a priori profiles of NO_2 at a spatial and temporal resolution equal or greater to the spatial and temporal resolution of the satellite pixels: using spatially coarse profiles will underestimate the magnitude of the NO_2 VCDs, and using temporally coarse profiles will overestimate the loss rate of NO_2 downwind of a source. Constructing and evaluating a full retrieval with sufficiently detailed profiles was a significant undertaking, detailed in Chapters 3, 4, and 5. Finally, in Chapter 6 I showed that this retrieval is capable of identifying a change in the chemical regime in two US cities (Chicago and Dallas) and that the transition occurs at the range of NO_x concentrations predicted by a straightforward steady-state model (1 ppb to 3 ppb).

This result opens the door to detailed analysis of changes in NO_x lifetime from space. Future work can use this approach to test our fundamental understanding of NO_x chemistry by comparing changes in lifetime in the real atmosphere to that in models. For example, by examining the lifetime for different time periods that have similar average VCDs, we could infer the effect of changing VOC reactivity. By comparing the observed change in lifetime from satellite observations against lifetimes calculated in models, we can see if our current models are able to capture the same observed change, and if not, investigate why.

Other future work could focus on further refining the new NO_2 retrieval. As shown in Chapter 5, the profiles in the southeast US overpredict upper tropospheric NO_2 due to far greater simulated lightning flash rates than actual flashes, although the simulation is reasonably accurate elsewhere in the country. Further research is necessary to identify the root cause for this discrepancy. Additionally, the need to simulate high resolution NO_2 profiles for every day retrieved is the limiting factor in extending the new product to additional years, as each year takes 3 to 6 months to simulate. As 7+ complete years of NO_2 profiles have been simulated for this dissertation, this provides a consistent data set that may be used as a training set for a neural network-based approach in the future. Future work could design a method to train a neural network to predict the daily NO_2 profiles with inputs such as latitude, longitude, month, year, temperature, NO_2 slant column density, etc. which are readily available without the need for modeling.

Bibliography

Acarreta, J. R., J. F. De Haan, and P. Stammes (2004). "Cloud pressure retrieval using the O2-O2 absorption band at 477 nm". *J. Geophys. Res. Atmos.* 109.D5, p. D05204. ISSN: 2156-2202. DOI: 10.1029/2003JD003915.

Ahmad, Z. and P. K. Bhartia (1995). "Effect of molecular anisotropy on the backscattered UV radiance". *Appl. Opt.* 34, pp. 8309–8314.

Allen, D. J. et al. (2012). "Impact of lightning-NO on eastern United States photochemistry during the summer of 2006 as determined using the CMAQ model". *Atmos. Chem. Phys.* 12, pp. 1737–1758. DOI: 10.5194/acp-12-1737-2012.

Anderson, D. C. et al. (2014). "Measured and modeled CO and NO_y in DISCOVER-AQ: An evaluation of emissions and chemistry over the eastern US". *Atmos. Environ.* 96, pp. 78 –87. ISSN: 1352-2310. DOI: https://doi.org/10.1016/j.atmosenv.2014.07.004.

Apel, E. C. et al. (2010). "Chemical evolution of volatile organic compounds in the outflow of the Mexico City Metropolitan area". *Atmos. Chem. Phys.* 10.5, pp. 2353–2375. DOI: 10.5194/acp-10-2353-2010.

Apel, E. C. et al. (2012). "Impact of the deep convection of isoprene and other reactive trace species on radicals and ozone in the upper troposphere". *Atmos. Chem. Phys.* 12.2, pp. 1135–1150. DOI: 10.5194/acp-12-1135-2012.

Bacak, A. et al. (2011). "Kinetics of the HO_2 + NO_2 Reaction: On the impact of new gas-phase kinetic data for the formation of HO_2NO_2 on HO_x, NO_x and HO_2NO_2 levels in the troposphere". *Atmos. Environ.* 45.35, pp. 6414–6422. DOI: 10.1016/j.atmosenv.2011.08.008.

Bak, J. et al. (2013). "Evaluation of ozone profile and tropospheric ozone retrievals from GEMS and OMI spectra". *Atmos. Meas. Tech.* 6, pp. 239–249. DOI: 10.5194/amt-6-239-2013.

Bard, Y. (1974). "Interpretation of the Estimates". In: *Nonlinear Parameter Estimation*. London: Academic Press Inc. Chap. VII. ISBN: 0-12-078250-2.

Barth, M. C. et al. (2015). "The Deep Convective Clouds and Chemistry (DC3) Field Campaign". *Bull. Am. Met. Soc.* 96.8, pp. 1281–1309. DOI: 10.1175/bams-d-13-00290.1.

Beirle, S. et al. (2004). "Estimate of nitrogen oxide emissions from shipping by satellite remote sensing". *Geophys. Res. Lett.* 31. DOI: 10.1029/2004GL020312.

Beirle, S. et al. (2009). "Sensitivity of satellite observations for freshly produced lightning NO_x". *Atmos. Chem. Phys.* 9.3, pp. 1077–1094. DOI: 10.5194/acp-9-1077-2009.

Beirle, S., H. Huntrieser, and T. Wagner (2010a). "Direct satellite observations of lightning-produced NO_x". *Atmos. Chem. Phys.* 10, pp. 10965–10986. DOI: 10.5194/acp-10-10965-2010.

Beirle, S. et al. (2010b). "Retrieval of tropospheric column densities of NO_2 from combined SCIAMACHY nadir/limb measurements". *Atmos. Meas. Tech.* 3.1, pp. 283–299. DOI: 10.5194/amt-3-283-2010.

Beirle, S. et al. (2011). "Megacity Emissions and Lifetimes of Nitrogen Oxides Probed from Space". *Science* 333, pp. 1737–1739.

Belmonte Rivas, M. et al. (2014). "Intercomparison of daytime stratospheric NO_2 satellite retrievals and model simulations". *Atmos. Meas. Tech.* 7.7, pp. 2203–2225. DOI: 10.5194/amt-7-2203-2014.

Bertram, T. H. et al. (2007). "Direct Measurements of the Convective Recycling of the Upper Troposphere". *Science* 315, pp. 816–820. DOI: 10.1126/science.1134548.

Bertram, T. H. et al. (2005). "Satellite measurements of daily variations in soil NO_x emissions". *Geophys. Res. Lett.* 32.24. DOI: 10.1029/2005gl024640.

Bey, I. et al. (2001). "Global modeling of tropospheric chemistry with assimilated meteorology". *J. Geophys. Res.* 106, pp. 23073–23096.

Boccippio, D. et al. (2001). "Combined Satellite- and Surface-Based Estimation of the Intracloud–Cloud-to-Ground Lightning Ratio over the Continental United States". *Mon. Weather Rev.* 129, pp. 108–122.

Boersma, K. et al. (2002). "NO_2, in: OMI Algorithm Theoretical Basis Document, vol 4, OMI Trace Gas Algorithms, ATB-OMI-04, version 2.0", pp. 13–36. URL: http://eospso.nasa.gov/sites/default/files/atbd/ATBD-OMI-04.pdf.

Boersma, K., H. Eskes, and E. Brinksma (2004). "Error analysis for tropospheric NO_2 retrieval from space". *J. Geophys. Res. Atmos.* 106, p. D04311. DOI: 10.1029/2003JD003962.

Boersma, K. et al. (2007). "Near-real time retrieval of tropospheric NO_2 from OMI". *Atmos. Chem. Phys.* 7, pp. 2103–2118.

Boersma, K. et al. (2008). "Validation of OMI tropospheric NO_2 observations during INTEX-B and application to constrain NO_x emissions over the eastern United States and Mexico". *Atmos. Environ.* 42.19, pp. 4480–4497. DOI: 10.1016/j.atmosenv.2008.02.004.

Boersma, K. et al. (2011). "An improved tropospheric NO_2 column retrieval algorithm for the Ozone Monitoring Instrument". *Atmos. Meas. Tech.* 4, pp. 1905–1928. DOI: 10.5194/amt-4-1905-2011.

Boucher, O. et al. (2013). "Climate Change 2013: The Physical Science Basis. Contribution of Working Group I to the Fifth Assessment Report of the Intergovernmental Panel on Climate Change [Stocker, T.F., D. Qin, G.-K. Plattner, M. Tignor, S.K. Allen, J. Boschung, A. Nauels, Y. Xia, V. Bex, and P.M. Midgley (eds)]". In: Cambridge, United Kingdom and New York, NY, USA: Cambridge University Press. Chap. Clouds and Aerosols, p. 571.

Bousserez, N. (2014). "Space-based retrieval of NO_2 over biomass burning regions: quantifying and reducing uncertainties". *Atmos. Meas. Tech.* 7.10, pp. 3431–3444. DOI: 10.5194/amt-7-3431-2014.

Brown, S. S. et al. (2009). "Reactive uptake coefficients for N_2O_5 determined from aircraft measurements during the Second Texas Air Quality Study: Comparison to current model parameterizations". *J. Geophys. Res.* 114. DOI: 10.1029/2008jd011679.

Browne, E. C. and R. C. Cohen (2012). "Effects of biogenic nitrate chemistry on the NO_x lifetime in remote continental regions". *Atmos. Chem. Phys.* 12.24, pp. 11917–11932. DOI: 10.5194/acp-12-11917-2012.

Browne, E. C. et al. (2011). "Global and regional effects of the photochemistry of $CH_3O_2NO_2$: evidence from ARCTAS". *Atmos. Chem. Phys.* 11.9, pp. 4209–4219. DOI: 10.5194/acp-11-4209-2011.

Browne, E. C. et al. (2014). "On the role of monoterpene chemistry in the remote continental boundary layer". *Atmos. Chem. Phys.* 14, pp. 1225–1238. DOI: 10.5194/acp-14-1225-2014.

Bucsela, E. J. et al. (2006). "Algorithm for NO_2 vertical column retrieval from the ozone monitoring instrument". *IEEE T. Geosci. Remote* 44.5, pp. 1245–1258. DOI: 10.1109/TGRS.2005.863715.

Bucsela, E. J. et al. (2008). "Comparison of tropospheric NO_2 from in situ aircraft measurements with near-real-time and standard product data from OMI". *J. Geophys. Res. Atmos.* 113.D16, D16S31. ISSN: 2156-2202. DOI: 10.1029/2007JD008838.

Bucsela, E. et al. (2013). "A new tropospheric and stratospheric NO_2 retrieval algorithm for nadir-viewing satellite instruments: applications to OMI". *Atmos. Meas. Tech.* 6, pp. 2607–2626. DOI: 10.5194/amt-6-2607-2013.

Bucsela, E. J. et al. (2010). "Lightning-generated NO_x seen by the Ozone Monitoring Instrument during NASA's Tropical Composition, Cloud and Climate Coupling Experiment (TC4)". *J. Geophys. Res. Atmos.* 115.D10, D00J10. ISSN: 2156-2202. DOI: 10.1029/2009JD013118.

Burrows, J. P. and S. Noel (2011). "Appendix D: Timelines for Present and Future Missions". In: *The Remote Sensing of Tropospheric Composition from Space*. Ed. by J. Burrows, U. Platt, and P. Borrell. New York: Springer.

Burrows, J. P. et al. (1999). "The Global Ozone Monitoring Experiment (GOME): Mission Concept and First Scientific Results". *J. Atmos. Sci.* 56, pp. 151–175. DOI: 10.1175/1520-0469(1999)056<0151:TGOMEG>2.0.CO;2.

Cahalan, R. F. et al. (1994). "Independent Pixel and Monte Carlo Estimates of Stratocumulus Albedo". *J. Atmos. Sci.* 51.24, pp. 3776–3790. DOI: 10.1175/1520-0469(1994)051<3776:ipamce>2.0.co;2.

Carlton, A. G., C. Wiedinmyer, and J. H. Kroll (2009). "A review of Secondary Organic Aerosol (SOA) formation from isoprene". *Atmos. Chem. Phys.* 9.14, pp. 4987–5005. DOI: 10.5194/acp-9-4987-2009.

Castellanos, P., K. F. Boersma, and G. R. van der Werf (2014). "Satellite observations indicate substantial spatiotemporal variability in biomass burning NO_x emission factors

for South America". *Atmos. Chem. Phys.* 14, pp. 3929–3943. DOI: 10.5194/acp-14-3929-2014.

Castellanos, P. et al. (2015). "OMI tropospheric NO_2 air mass factors over South America: effects of biomass burning aerosols". *Atmos. Meas. Tech.* 8.9, pp. 3831–3849. DOI: 10.5194/amt-8-3831-2015.

Castellanos, P. and K. F. Boersma (2012). "Reductions in nitrogen oxides over Europe driven by environmental policy and economic recession". *Sci. Rep.* 2.1. DOI: 10.1038/srep00265.

Chance, K. et al. (2013). *Tropospheric emissions: monitoring of pollution (TEMPO)*. DOI: 10.1117/12.2024479.

Chatterjee, S. and A. Hadi (2012). *Regression Analysis by Example, Ch 8: The Problem of Correlated Errors*. Hoboken, New Jersey, USA: John Wiley & Sons Inc.

Chauhan, A. et al. (1998). "Exposure to nitrogen dioxide (NO_2) and respiratory disease risk". *Rev. Environ. Health* 13.1-2, pp. 73–90. URL: https://www.scopus.com/inward/record.uri?eid=2-s2.0-0031842694&partnerID=40&md5=129866ddd76a17bb4f29b71e09ca636e.

Choi, S. et al. (2014). "First estimates of global free-tropospheric NO_2 abundances derived using a cloud-slicing technique applied to satellite observations from the Aura Ozone Monitoring Instrument (OMI)". *Atmos. Chem. Phys.* 14.19, pp. 10565–10588. DOI: 10.5194/acp-14-10565-2014.

Choi, Y.-S. and C.-H. Ho (2015). "Earth and environmental remote sensing community in South Korea: A review". *Remote Sensing Applications: Society and Environment* 2, pp. 66–76. DOI: 10.1016/j.rsase.2015.11.003.

Chun, Z. and W. Yuhang (2009). "Assimilated inversion of NO_x emissions over east Asia using OMI NO_2 column measurements". *Geophys. Res. Lett.* 36.6. DOI: 10.1029/2008GL037123.

Ciais, P. et al. (2013). "Carbon and Other Biogeochemical Cycles". In: *Climate Change 2013: The Physical Science Basis. Contribution of Working Group I to the Fifth Assessment Report of the Intergovernmental Panel on Climate Change*. Ed. by T. Stocker et al. Cambridge University Press, Cambridge, United Kingdom and New York, NY, USA. URL: http://www.ipcc.ch/pdf/assessment-report/ar5/wg1/WG1AR5_Chapter06_FINAL.pdf.

Cohan, D. S., Y. Hu, and A. G. Russell (2006). "Dependence of ozone sensitivity analysis on grid resolution". *Atmos. Environ.* 40.1, pp. 126–135. DOI: 10.1016/j.atmosenv.2005.09.031.

Computational and Information Systems Laboratory (2017). *Cheyenne: HPE/SGI ICE XA System (NCAR Community Computing). Boulder, CO: National Center for Atmospheric Research*. DOI: 10.5065/D6RX99HX.

Cooray, V., M. Rahman, and V. Rakov (2009). "On the NO_x production by laboratory electrical discharges and lightning". *J. Atmos. Sol. Terr. Phys.* 71, pp. 1877–1889. DOI: 10.1016/j.jastp.2009.07.009.

Crisp, D. et al. (2017). "The on-orbit performance of the Orbiting Carbon Observatory-2 (OCO-2) instrument and its radiometrically calibrated products". *Atmos. Meas. Tech.* 10.1, pp. 59–81. DOI: 10.5194/amt-10-59-2017.

Curier, R. et al. (2014). "Synergistic use of OMI NO_2 tropospheric columns and LOTOS–EUROS to evaluate the NO_x emission trends across Europe". *Rem. Sens. Environ.* 149, pp. 58 –69. ISSN: 0034-4257. DOI: https://doi.org/10.1016/j.rse.2014.03.032.

Davé, J. V. (1964). "Meaning of successive iteration of the auxiliary equation in the theory of radiative transfer". *Astrophys. J.* 140, pp. 1292–1303.

Davé, J. (1965). "Multiple scattering in a nonhomogeneous, Rayleigh atmosphere". *J. Atmos. Sci.* 22, pp. 273–279.

Day, D. A. et al. (2002). "A thermal dissociation laser-induced fluorescence instrument for in situ detection of NO_2, peroxy nitrates, alkyl nitrates, and HNO_3". *J. Geophys. Res. Atmos.* 107.D6, ACH 4–1–ACH 4–14. ISSN: 2156-2202. DOI: 10.1029/2001JD000779.

Day, D. A. (2003). "On alkyl nitrates, O_3, and the "missing NO_y"". *J. Geophys. Res.* 108.D16. DOI: 10.1029/2003jd003685.

de Foy, B. et al. (2014). "Model evaluation of methods for estimating surface emissions and chemical lifetimes from satellite data". *Atmos. Environ.* 98, pp. 66–77. DOI: 10.1016/j.atmosenv.2014.08.051.

de Foy, B. et al. (2015). "Estimates of power plant NO_x emissions and lifetimes from OMI NO_2 satellite retrievals". *Atmos. Environ.* 116, pp. 1–11. DOI: 10.1016/j.atmosenv.2015.05.056.

Ding, J. et al. (2015). "NO_x emission estimates during the 2014 Youth Olympic Games in Nanjing". *Atmos. Chem. Phys.* 15.16, pp. 9399–9412. DOI: 10.5194/acp-15-9399-2015.

Douglass, A. R. et al. (2003). "Evaluation of transport in the lower tropical stratosphere in a global chemistry and transport model". *J. Geophys. Res.* 108.D9. DOI: 10.1029/2002JD002696.

Dovì, V., O. Paladino, and A. Reverberi (1991). "Some remarks on the Use of the Inverse Hessian Matrix of the Likelihood Function in the Estimation of Statistical Properties of Parameters". *Appl. Math. Lett.* 4.1, pp. 87–90.

Dreher, D. B. and R. A. Harley (1998). "A Fuel-Based Inventory for Heavy-Duty Diesel Truck Emissions". *J. Air Waste Manage. Assoc.* 48.4, pp. 352–358. DOI: 10.1080/10473289.1998.10463686.

Duncan, B. N. et al. (2013). "The observed response of Ozone Monitoring Instrument (OMI) NO_2 columns to NO_x emission controls on power plants in the United States: 2005–2011". *Atmos. Environ.* 81, pp. 102 –111. ISSN: 1352-2310. DOI: https://doi.org/10.1016/j.atmosenv.2013.08.068.

Duncan, B. N. et al. (2016). "A space-based, high-resolution view of notable changes in urban NO_x pollution around the world (2005-2014)". *J. Geophys. Res. Atmos.* 121.2, pp. 976–996. DOI: 10.1002/2015jd024121.

Emmons, L. K. et al. (2010). "Description and evaluation of the Model for Ozone and Related chemical Tracers, version 4 (MOZART-4)". *Geosci. Model Dev.* 3.1, pp. 43–67. DOI: 10.5194/gmd-3-43-2010.

Endlick, R., R. Singleton, and J. Kaufman (1969). "Spectral Analysis of Detailed Vertical Wind Speed Profiles". *J. Atmos. Sci.* 26, pp. 1030–1041.

EPA (2016). *Air Pollutant Emissions Trends Data*. URL: https://www.epa.gov/air-emissions-inventories/air-pollutant-emissions-trends-data (visited on 05/03/2016).

Evans, M. J. and D. J. Jacob (2005). "Impact of new laboratory studies of N_2O_5 hydrolysis on global model budgets of tropospheric nitrogen oxides, ozone, and OH". *Geophys. Res. Lett.* 32.9. DOI: 10.1029/2005gl022469.

Follette-Cook, M. et al. (2015). "Spatial and temporal variability of trace gas columns derived from WRF/Chem regional model output: Planning for geostationary observations of atmospheric composition". *Atmos. Environ.* 118, pp. 28–44. DOI: 10.1016/j.atmosenv.2015.07.024.

Foy, B. de et al. (2014). "Model evaluation of methods for estimating surface emissions and chemical lifetimes from satellite data". *Atmos. Environ.* 98, pp. 66–77. DOI: 10.1016/j.atmosenv.2014.08.051.

Freeborn, P. H. et al. (2008). "Relationships between energy release, fuel mass loss, and trace gas and aerosol emissions during laboratory biomass fires". *J. Geophys. Res.* 113.D1. DOI: 10.1029/2007jd008679.

Fujita, E. M. et al. (2012). "Comparison of the MOVES2010a, MOBILE6.2, and EMFAC2007 mobile source emission models with on-road traffic tunnel and remote sensing measurements". *J. Air Waste Manage. Assoc.* 62.10, pp. 1134–1149. DOI: 10.1080/10962247.2012.699016.

Goldberg, D. L. et al. (2017). "A high-resolution and observationally constrained OMI NO_2 satellite retrieval". *Atmos. Chem. Phys.* 17.18, pp. 11403–11421. DOI: 10.5194/acp-17-11403-2017.

Goliff, W. S., W. R. Stockwell, and C. V. Lawson (2013). "The regional atmospheric chemistry mechanism, version 2". *Atmos. Environ.* 68, pp. 174 –185. DOI: 10.1016/j.atmosenv.2012.11.038.

Grell, G. A. (1993). "Prognostic Evaluation of Assumptions Used by Cumulus Parameterizations". *Mon. Weather Rev.* 121.3, pp. 764–787. DOI: 10.1175/1520-0493(1993)121<0764:PEOAUB>2.0.CO;2.

Grell, G. A. and D. Dévényi (2002). "A generalized approach to parameterizing convection combining ensemble and data assimilation techniques". *Geophys. Res. Lett.* 29.14, pp. 38–1–38–4. DOI: 10.1029/2002gl015311.

Grell, G. A. et al. (2005). "Fully coupled "online" chemistry within the WRF model". *Atmos. Environ.* 39, pp. 6957 –6975. DOI: 10.1016/j.atmosenv.2005.04.027.

Gu, D. et al. (2013). "Reduction in NO_x Emission Trends over China: Regional and Seasonal Variations". *Environ. Sci. Technol.* 47.22, pp. 12912–12919. DOI: 10.1021/es401727e.

Guenther, A. et al. (2006). "Estimates of global terrestrial isoprene emissions using MEGAN (Model of Emissions of Gases and Aerosols from Nature)". *Atmos. Chem. Phys.* 6.11, pp. 3181–3210. DOI: 10.5194/acp-6-3181-2006.

Haagen-Smit, A. J. (1952). "Chemistry and Physiology of Los Angeles Smog". *Ind. Eng. Chem.* 44.6, pp. 1342–1346. DOI: 10.1021/ie50510a045.

Haagen-Smit, A. et al. (1952). "Investigation on Injury to Plants from Air Pollution in the Los Angeles Area". *Plant Physiol.* 27, pp. 18–34.

Hains, J. C. et al. (2010). "Testing and improving OMI DOMINO tropospheric NO_2 using observations from the DANDELIONS and INTEX-B validation campaigns". *J. Geophys. Res.* 115.D5. DOI: 10.1029/2009jd012399.

Harris, D. (2010). "Comparison of Means with Student's *t*". In: *Quantitative Chemical Analysis*. 8th. W.H. Freeman. Chap. 4-3, pp. 76–78.

Hastings, D. and P. Dunbar (1999). *Global Land One-kilometer Base Elevation (GLOBE) Digital Elevation Model, Documentation, Volume 1.0. National Oceanic and Atmospheric Administration, National Geophysical Data Center, 325 Broadway, Boulder, Colorado 80303, U.S.A.* Key to Geophysical Records Documentation (KGRD) 34.

Heath, R. L. (1975). "Ozone". In: *Responses of plants to air pollution*. Ed. by J. Mudd. San Francisco, CA: Academic Press, p. 23.

Heckel, A. et al. (2011). "Influence of low spatial resolution a priori data on tropospheric NO_2 satellite retrievals". *Atmos. Meas. Tech.* 4.9, pp. 1805–1820. DOI: 10.5194/amt-4-1805-2011.

Henderson, B. H. et al. (2012). "Combining Bayesian methods and aircraft observations to constrain the $HO^{\cdot} + NO_2$ reaction rate". *Atmos. Chem. Phys.* 12.2, pp. 653–667. DOI: 10.5194/acp-12-653-2012.

Herman, J. et al. (2009). "NO_2 column amounts from ground-based Pandora and MFDOAS spectrometers using the direct-sun DOAS technique: Intercomparisons and application to OMI validation". *J. Geophys. Res. Atmos.* 114.D13. DOI: 10.1029/2009jd011848.

Hönninger, G., C. von Friedeburg, and U. Platt (2004). "Multi axis differential optical absorption spectroscopy (MAX-DOAS)". *Atmos. Chem. Phys.* 4.1, pp. 231–254. DOI: 10.5194/acp-4-231-2004.

Hu, J. et al. (2010). "Particulate air quality model predictions using prognostic vs. diagnostic meteorology in central California". *Atmos. Environ.* 44.2, pp. 215 –226. ISSN: 1352-2310. DOI: https://doi.org/10.1016/j.atmosenv.2009.10.011.

Hu, L. et al. (2018). "Global simulation of tropospheric chemistry at 12.5 km resolution: performance and evaluation of the GEOS-Chem chemical module (v10-1) within the NASA GEOS Earth System Model (GEOS-5 ESM)". *Geoscientific Model Development Discussions* 2018, pp. 1–32. DOI: 10.5194/gmd-2018-111.

Huang, M. et al. (2014). "Changes in nitrogen oxides emissions in California during 2005–2010 indicated from top-down and bottom-up emission estimates". *J. Geophys. Res. Atmos.* 119, pp. 12,928–12,952. DOI: 10.1002/2014JD022268.

Hudman, R. C. et al. (2007). "Surface and lightning sources of nitrogen oxides over the United States: Magnitudes, chemical evolution, and outflow". *J. Geophys. Res. Atmos.* 112.D12. ISSN: 2156-2202. DOI: 10.1029/2006JD007912.

Hudman, R. C. et al. (2010). "Interannual variability in soil nitric oxide emissions over the United States as viewed from space". *Atmos. Chem. Phys.* 10.20, pp. 9943–9952. DOI: 10.5194/acp-10-9943-2010.

Hudman, R. C. et al. (2012). "Steps towards a mechanistic model of global soil nitric oxide emissions: implementation and space based-constraints". *Atmos. Chem. Phys.* 12.16, pp. 7779–7795. DOI: 10.5194/acp-12-7779-2012.

Hudson, R., J.-H. Kim, and A. Thompson (1995). "On the derivation of tropospheric column ozone from radiances measured by the total ozone mapping spectrometer". *J. Geophys. Res. Atmos.* 100, pp. 11,134–11,145.

Huijnen, V. et al. (2012). "Hindcast experiments of tropospheric composition during the summer 2010 fires over western Russia". *Atmos. Chem. Phys.* 12.9, pp. 4341–4364. DOI: 10.5194/acp-12-4341-2012.

Hunt, B. R., E. J. Kostelich, and I. Szunyogh (2007). "Efficient data assimilation for spatiotemporal chaos: A local ensemble transform Kalman filter". *Physica D* 230.1, pp. 112 –126. ISSN: 0167-2789. DOI: https://doi.org/10.1016/j.physd.2006.11.008.

Hunter, S. M. et al. (2001). "Winter Lightning and Heavy Frozen Precipitation in the Southeast United States". *Weather Forecasting* 16, pp. 478–490. DOI: 10.1175/1520-0434(2001)016<0478:wlahfp>2.0.co;2.

Ialongo, I. et al. (2014). "Characterization of OMI tropospheric NO_2 over the Baltic Sea region". *Atmos. Chem. Phys.* 14, pp. 7795–7805. DOI: 10.5194/acp-14-7795-2014.

Ialongo, I. et al. (2016). "Comparison of OMI NO_2 observations and their seasonal and weekly cycles with ground-based measurements in Helsinki". *Atmos. Meas. Tech.* 9.10, pp. 5203–5212. DOI: 10.5194/amt-9-5203-2016.

Ingmann, P. et al. (2012). "Requirements for the GMES Atmosphere Service and ESA's implementation concept: Sentinels-4/-5 and -5p". *Remote Sens. of Environ.* 120, pp. 58–69. DOI: 10.1016/j.rse.2012.01.023.

Izumi, K. and T. Fukuyama (1990). "Photochemical aerosol formation from aromatic hydrocarbons in the presence of NO_x". *Atmos. Environ. Part A* 24.6, pp. 1433 –1441. ISSN: 0960-1686. DOI: https://doi.org/10.1016/0960-1686(90)90052-O.

Jacob, D. J. et al. (1993). "Factors regulating ozone over the United States and its export to the global atmosphere". *J. Geophys. Res. Atmos.* 98.D8, pp. 14817–14826. ISSN: 2156-2202. DOI: 10.1029/98JD01224.

Jaeglé, L. et al. (2004). "Satellite mapping of rain-induced nitric oxide emissions from soils". *J. Geophys. Res. Atmos.* 109, p. D21310. DOI: 10.1029/2004jd004787.

Jaeglé, L. et al. (2005). "Global partitioning of NO_x sources using satellite observations: Relative roles of fossil fuel combustion, biomass burning and soil emissions". *Faraday Discuss.* 130, p. 407. DOI: 10.1039/b502128f.

Jaeglé, L. et al. (1998). "Sources and chemistry of NO_x in the upper troposphere over the United States". *Geophys. Res. Lett.* 25.10, pp. 1705–1708. ISSN: 1944-8007. DOI: 10.1029/97GL03591.

Jiang, Z. et al. (2018). "Unexpected slowdown of US pollutant emission reduction in the past decade". *PNAS* 115.20, pp. 5099–5104. DOI: 10.1073/pnas.1801191115.

Jin, Z. et al. (2006). "Analytical solution of radiative transfer in the coupled atmosphere-ocean system with a rough surface". *Appl. Opt.* 45.28, pp. 7443–7455.

Kagawa, J. (1985). "Evaluation of biological significance of nitrogen oxides exposure". *Tokai J. Exp. Clin. Med.* 10, p. 348.

Kalnay, E. (2010). "Ensemble Kalman Filter: Current Status and Potential". In: *Data Assimilation: Making Sense of Observations*. Ed. by W. Lahoz, B. Khattatov, and R. Ménard. Springer, pp. 69–92.

Kampa, M. and E. Castanas (2008). "Human health effects of air pollution". *Environ. Pollut.* 151.2, pp. 362 –367. ISSN: 0269-7491. DOI: https://doi.org/10.1016/j.envpol.2007.06.012.

Kiehl, J. and S. Solomon (1986). "On the Radiative Balance of the Stratosphere". *J. Atmos. Sci.* 43, pp. 1525–1534. DOI: 10.1175/1520-0469(1986)043<1525:OTRBOT>2.0.CO;2.

Kim, J. et al. (2018). "The BErkeley Atmospheric CO_2 Observation Network: field calibration and evaluation of low-cost air quality sensors". *Atmos. Meas. Tech.* 11.4, pp. 1937–1946. DOI: 10.5194/amt-11-1937-2018.

Kim, S.-W. et al. (2006). "Satellite-observed U.S. power plant NO_x emission reductions and their impact on air quality". *Geophys. Res. Lett.* 33.22. DOI: 10.1029/2006gl027749.

Kim, S.-W. et al. (2009). "NO_2 columns in the western United States observed from space and simulated by a regional chemistry model and their implications for NO_x emissions". *J. Geophys. Res. Atmos.* 114.D11. DOI: 10.1029/2008jd011343.

Kleipool, Q. L. et al. (2008). "Earth surface reflectance climatology from 3 years of OMI data". *J. Geophys. Res.* 113.D18. DOI: 10.1029/2008jd010290.

Koelemeijer, R. B. A. (2003). "A database of spectral surface reflectivity in the range 335–772 nm derived from 5.5 years of GOME observations". *J. Geophys. Res.* 108.D2. DOI: 10.1029/2002jd002429.

Koelemeijer, R. B. A. and P. Stammes (1999). "Effects of clouds on ozone column retrieval from GOME UV measurements". *J. Geophys. Res. Atmos.* 104.D7, pp. 8281–8294. ISSN: 2156-2202. DOI: 10.1029/1999JD900012.

Konovalov, I. B. et al. (2010). "Multi-annual changes of NO_x emissions in megacity regions: nonlinear trend analysis of satellite measurement based estimates". *Atmos. Chem. Phys.* 10.17, pp. 8481–8498. DOI: 10.5194/acp-10-8481-2010.

Krotkov Nickolay, A. and P. Veefkind (2016). *OMI/Aura Nitrogen Dioxide (NO2) Total and Tropospheric Column 1-orbit L2 Swath 13x24 km V003, Greenbelt, MD, USA, Goddard Earth Sciences Data and Information Services Center (GES DISC)*. DOI: 10.5067/Aura/OMI/DATA2017.

Krotkov, N. A. et al. (2016). "Aura OMI observations of regional SO_2 and NO_2 pollution changes from 2005 to 2015". *Atmos. Chem. Phys.* 16.7, pp. 4605–4629. DOI: 10.5194/acp-16-4605-2016.

Krotkov, N. A. et al. (2017). "The version 3 OMI NO_2 standard product". *Atmos. Meas. Tech.* 10.9, pp. 3133–3149. DOI: 10.5194/amt-10-3133-2017.

Krotkov, N. and P. Veefkind (2006). "OMI/Aura Nitrogen Dioxide (NO2) Total and Tropospheric Column 1-orbit L2 Swath 13x24 km V003, version 003, Greenbelt, MD, USA,

Goddard Earth Sciences Data and Information Services Center (GES DISC), accessed 23 Oct 2016". DOI: 10.5067/Aura/OMI/DATA2017.

Kuhlmann, G. et al. (2014). "A novel gridding algorithm to create regional trace gas maps from satellite observations". *Atmos. Meas. Tech.* 7.2, pp. 451–467. DOI: 10.5194/amt-7-451-2014.

Kuhlmann, G. et al. (2015). "Development of a custom OMI NO_2 data product for evaluating biases in a regional chemistry transport model". *Atmos. Chem. Phys.* 15.10, pp. 5627–5644. DOI: 10.5194/acp-15-5627-2015.

Kurosu, T. P. and E. A. Celarier (2010). *OMI/Aura Global Ground Pixel Corners 1-Orbit L2 Swath 13x24km V003, Greenbelt, MD, USA, Goddard Earth Sciences Data and Information Services Center (GES DISC)*. DOI: 10.5067/Aura/OMI/DATA2020.

Lamsal, L. N. et al. (2010). "Indirect validation of tropospheric nitrogen dioxide retrieved from the OMI satellite instrument: Insight into the seasonal variation of nitrogen oxides at northern midlatitudes". *J. Geophys. Res. Atmos.* 115. DOI: 10.1029/2009JD013351.

Lamsal, L. N. et al. (2014). "Evaluation of OMI operational standard NO_2 column retrievals using in situ and surface-based NO_2 observations". *Atmos. Chem. Phys.* 14.21, pp. 11587–11609. DOI: 10.5194/acp-14-11587-2014.

Lamsal, L. (2018). "NO_2 activities at GSFC". In: *Sixth TEMPO Science Team Meeting*.

Lamsal, L. N. et al. (2015). "U.S. NO_2 trends (2005–2013): EPA Air Quality System (AQS) data versus improved observations from the Ozone Monitoring Instrument (OMI)". *Atmos. Environ.* 110, pp. 130–143. DOI: 10.1016/j.atmosenv.2015.03.055.

Laughner, J. L. (2017). *AutoWRFChem-Base v1.2.0: Automation for the WRF-Chem model*. DOI: 10.5281/zenodo.839040.

— (2018). *Analysis code for Laughner et al., AMT (discussion), 2018*. DOI: 10.5281/zenodo.1320469.

Laughner, J. L. and R. C. Cohen (2017). "Quantification of the effect of modeled lightning NO_2 on UV–visible air mass factors". *Atmos. Meas. Tech.* 10.11, pp. 4403–4419. DOI: 10.5194/amt-10-4403-2017.

Laughner, J. L. and Q. Zhu (2018a). *CohenBerkeleyLab/BEHR-Core: BEHR Core code*. DOI: 10.5281/zenodo.998275.

— (2018b). *ESSD Discussion - Supporting Code*. DOI: 10.5281/zenodo.1247564.

Laughner, J. L., A. Zare, and R. C. Cohen (2016). "Effects of daily meteorology on the interpretation of space-based remote sensing of NO_2". *Atmos. Chem. Phys.* 16.23, pp. 15247–15264. DOI: 10.5194/acp-16-15247-2016.

Laughner, J. L., Q. Zhu, and R. C. Cohen (2018a). *Supporting data for "Evaluation of version 3.0B of the BEHR OMI NO2 product"*. DOI: 10.6078/D1JT28.

— (2018b). "The Berkeley High Resolution Tropospheric NO_2 Product". *Earth Syst. Sci. Data Discuss.* 2018, pp. 1–33. DOI: 10.5194/essd-2018-66.

Laughner, J., Q. Zhu, and R. Cohen (2018c). *Berkeley High Resolution (BEHR) OMI NO2 - Gridded pixels, daily profiles, v3, UC Berkeley Dash, Dataset*. DOI: 10.6078/D12D5X.

— (2018d). *Berkeley High Resolution (BEHR) OMI NO2 - Gridded pixels, monthly profiles, UC Berkeley Dash, Dataset*. DOI: 10.6078/D1RQ3G.

Laughner, J., Q. Zhu, and R. Cohen (2018e). *Berkeley High Resolution (BEHR) OMI NO2 - Native pixels, daily profiles, UC Berkeley Dash, Dataset*. DOI: 10.6078/D1WH41.

— (2018f). *Berkeley High Resolution (BEHR) OMI NO2 - Native pixels, monthly profiles, UC Berkeley Dash, Dataset*. DOI: 10.6078/D1N086.

Lay, E. H. et al. (2007). "Local time variation in land/ocean lightning flash density as measured by the World Wide Lightning Location Network". *J. Geophys. Res. Atmos.* 112.D13. DOI: 10.1029/2006JD007944.

Lee, H.-J. et al. (2014). "Transport of NO_x in East Asia identified by satellite and in situ measurements and Lagrangian particle dispersion model simulations". *J. Geophys. Res. Atmos.* 119.5, pp. 2574–2596. DOI: 10.1002/2013jd021185.

Leitão, J. et al. (2010). "On the improvement of NO_2 satellite retrievals—aerosol impact on the airmass factors". *Atmos. Meas. Tech.* 3.2, pp. 475–493. DOI: 10.5194/amt-3-475-2010.

Levelt, P. et al. (2006). "The Ozone Monitoring Instrument". *IEEE Trans. Geosci. Remote Sense.* 44, pp. 1093–1101. DOI: 10.1109/TGRS.2006.872333.

Lin, J.-T. (2012). "Satellite constraint for emissions of nitrogen oxides from anthropogenic, lightning and soil sources over East China on a high-resolution grid". *Atmos. Chem. Phys.* 12.6, pp. 2881–2898. DOI: 10.5194/acp-12-2881-2012.

Lin, J.-T., M. B. McElroy, and K. F. Boersma (2010). "Constraint of anthropogenic NO_x emissions in China from different sectors: a new methodology using multiple satellite retrievals". *Atmos. Chem. Phys.* 10, pp. 63–78. DOI: 10.5194/acp-10-63-2010.

Lin, J.-T. et al. (2014a). "Retrieving tropospheric nitrogen dioxide from the Ozone Monitoring Instrument: effects of aerosols, surface reflectance anisotropy, and vertical profile of nitrogen dioxide". *Atmos. Chem. Phys.* 14.3, pp. 1441–1461. DOI: 10.5194/acp-14-1441-2014.

Lin, J.-T. et al. (2015). "Influence of aerosols and surface reflectance on satellite NO_2 retrieval: seasonal and spatial characteristics and implications for NO_x emission constraints". *Atmos. Chem. Phys.* 15.19, pp. 11217–11241. DOI: 10.5194/acp-15-11217-2015.

Lin, J. et al. (2014b). "China's international trade and air pollution in the United States". *Proceedings of the National Academy of Sciences* 111.5, pp. 1736–1741. DOI: 10.1073/pnas.1312860111.

Lin, Y.-L., R. D. Farley, and H. D. Orville (1983). "Bulk Parameterization of the Snow Field in a Cloud Model". *J. Clim. Appl. Meteorol.* 22, pp. 1065–1092.

Liu, F. et al. (2016). "NO_x lifetimes and emissions of cities and power plants in polluted background estimated by satellite observations". *Atmos. Chem. Phys.* 16.8, pp. 5283–5298. DOI: 10.5194/acp-16-5283-2016.

Liu, F. et al. (2017). "NO_x emission trends over Chinese cities estimated from OMI observations during 2005 to 2015". *Atmos. Chem. Phys.* 17.15, pp. 9261–9275. DOI: 10.5194/acp-17-9261-2017.

Liu, Y. et al. (2006). "Implementation of the observation-nudging based on FDDA into WRF for supporting AFEC test operations." In: *6th WRF Conference, NCAR, Boulder, CO, USA*.

Lorente, A. et al. (2017). "Structural uncertainty in air mass factor calculation for NO_2 and HCHO satellite retrievals". *Atmos. Meas. Tech.* 10.3, pp. 759–782. DOI: 10.5194/amt-10-759-2017.

Lu, Z. et al. (2015). "Emissions of nitrogen oxides from US urban areas: estimation from Ozone Monitoring Instrument retrievals for 2005–2014". *Atmos. Chem. Phys.* 15, pp. 10367–10383. DOI: 10.5194/acp-15-10367-2015.

Marchenko, S. et al. (2015). "Revising the slant column density retrieval of nitrogen dioxide observed by the Ozone Monitoring Instrument". *J. Geophys. Res. Atmos.* 120.11, pp. 5670–5692. ISSN: 2169-8996. DOI: 10.1002/2014JD022913.

Marle, M. J. E. van et al. (2017). "Historic global biomass burning emissions for CMIP6 (BB4CMIP) based on merging satellite observations with proxies and fire models (1750–2015)". *Geosci. Model Dev.* 10.9, pp. 3329–3357. DOI: 10.5194/gmd-10-3329-2017.

Marr, L. C. and R. A. Harley (2002). "Modeling the Effect of Weekday-Weekend Differences in Motor Vehicle Emissions on Photochemical Air Pollution in Central California". *Environ. Sci. Technol.* 36.19, pp. 4099–4106. DOI: 10.1021/es020629x.

Marshak, A. et al. (1998). "Nonlocal independent pixel approximation: direct and inverse problems". *IEEE Trans. Geosci. Rem. Sens.* 36.1, pp. 192–205. DOI: 10.1109/36.655329.

Martin, R. V. (2003). "Global inventory of nitrogen oxide emissions constrained by space-based observations of NO_2 columns". *J. Geophys. Res.* 108.D17. DOI: 10.1029/2003jd003453.

Martin, R. V. et al. (2002). "An improved retrieval of tropospheric nitrogen dioxide from GOME". *J. Geophys. Res. Atmos.* 107.D20. 4437. ISSN: 2156-2202. DOI: 10.1029/2001JD001027.

Martin, R. et al. (2007). "Space-based constraints on the production of nitric oxide by lightning". *J. Geophys. Res. Atmos.* 112. DOI: 10.1029/2006JD007831.

Martini, M. et al. (2011). "The impact of North American anthropogenic emissions and lightning on long-range transport of trace gases and their export from the continent during summers 2002 and 2004". *J. Geophys. Res. Atmos.* 116.D7. DOI: 10.1029/2010JD014305.

McKenzie, R. et al. (1991). "Altitude distributions of stratospheric constituents from ground-based measurements at twilight". *J. Geophys. Res. Atmos.* 96.D8, pp. 15499–15511. DOI: 10.1029/91JD01361.

McLinden, C. A. et al. (2014). "Improved satellite retrievals of NO_2 and SO_2 over the Canadian oil sands and comparisons with surface measurements". *Atmos. Chem. Phys.* 14.7, pp. 3637–3656. DOI: 10.5194/acp-14-3637-2014.

Mebust, A. K. et al. (2011). "Characterization of wildfire NO_x emissions using MODIS fire radiative power and OMI tropospheric NO_2 columns". *Atmos. Chem. Phys.* 11.12, pp. 5839–5851. DOI: 10.5194/acp-11-5839-2011.

Mebust, A. and R. Cohen (2013). "Observations of a seasonal cycle in NO_x emissions from fires in African woody savannas". *Geophys. Res. Lett.* 40, pp. 1451–1455. DOI: 10.1002/grl.50343.

— (2014). "Space-based observations of fire NO_x emissions coefficients: a global biome-scale comparison". *Atmos. Chem. Phys.* 14, pp. 2509–2524. DOI: 10.5194/acp-14-2509-2014.

Menzel, D. B. (1984). "Ozone: An overview of its toxicity in man and animals". *J. Toxicol. Environ. Health* 13.2-3, pp. 181–204. DOI: 10.1080/15287398409530493.

Miyazaki, K., H. Eskes, and K. Sudo (2012a). "Global NO_x emissions estimates derived from an assimilation of OMI tropospheric NO_2 columns". *Atmos. Chem. Phys.* 12, pp. 2263–2288. DOI: 10.5194/acp-12-2263-2012.

Miyazaki, K., H. J. Eskes, and K. Sudo (2012b). "Global NO_x emission estimates derived from an assimilation of OMI tropospheric NO_2 columns". *Atmos. Chem. Phys.* 12.5, pp. 2263–2288. DOI: 10.5194/acp-12-2263-2012.

Miyazaki, K. et al. (2014). "Global lightning NO_x production estimated by an assimilation of multiple satellite data sets". *Atmos. Chem. Phys.* 14, pp. 3277–3305. DOI: 10.5194/acp-14-3277-2014.

Miyazaki, K. et al. (2017). "Decadal changes in global surface NO_x emissions from multi-constituent satellite data assimilation". *Atmos. Chem. Phys.* 17.2, pp. 807–837. DOI: 10.5194/acp-17-807-2017.

Munro, R. et al. (2016). "The GOME-2 instrument on the Metop series of satellites: instrument design, calibration, and level 1 data processing – an overview". *Atmos. Meas. Tech.* 9.3, pp. 1279–1301. DOI: 10.5194/amt-9-1279-2016.

Murphy, J. G. et al. (2006). "The weekend effect within and downwind of Sacramento: Part 2. Observational evidence for chemical and dynamical contributions". *Atmos. Chem. Phys. Discuss.* 6, pp. 11971–12019. DOI: 10.5194/acpd-6-11971-2006.

— (2007). "The weekend effect within and downwind of Sacramento—Part 1: Observations of ozone, nitrogen oxides, and VOC reactivity". *Atmos. Chem. Phys.* 7.20, pp. 5327–5339. DOI: 10.5194/acp-7-5327-2007.

Myhre, G. et al. (2013). "Climate Change 2013: The Physical Science Basis. Contribution of Working Group I to the Fifth Assessment Report of the Intergovernmental Panel on Climate Change [Stocker, T.F., D. Qin, G.-K. Plattner, M. Tignor, S.K. Allen, J. Boschung, A. Nauels, Y. Xia, V. Bex, and P.M. Midgley (eds)]". In: Cambridge, United Kingdom and New York, NY, USA: Cambridge University Press. Chap. Anthropogenic and Natural Radiative Forcing, p. 659.

Nault, B. A. et al. (2015). "Measurements of $CH_3O_2NO_2$ in the upper troposphere". *Atmos. Meas. Tech.* 8.2, pp. 987–997. DOI: 10.5194/amt-8-987-2015.

Nault, B. A. et al. (2016). "Observational Constraints on the Oxidation of NO_x in the Upper Troposphere". *J. Phys. Chem. A* 120.9, pp. 1468–1478. DOI: 10.1021/acs.jpca.5b07824.

Nault, B. A. et al. (2017). "Lightning NO_x Emissions: Reconciling Measured and Modeled Estimates With Updated NO_x Chemistry". *Geophys. Res. Lett.* ISSN: 1944-8007. DOI: 10.1002/2017GL074436.

Noel, S. et al. (1998). "SCIAMACHY instrument on ENVISAT-1". In: *Sensors, Systems, and Next-Generation Satellites II*. Ed. by H. Fujisada. SPIE. DOI: 10.1117/12.333621.

Nunnermacker, L. J. et al. (1998). "Characterization of the Nashville urban plume on July 3 and July 18, 1995". *J. Geophys. Res. Atmos.* 103, pp. 28129–28148. DOI: 10.1029/98JD01961.

Orville, R. E. et al. (2001). "Enhancement of cloud-to-ground lightning over Houston, Texas". *Geophys. Res. Lett.* 28.13, pp. 2597–2600. ISSN: 1944-8007. DOI: 10.1029/2001GL012990.

Ott, L. E. et al. (2010). "Production of lightning NO_x and its vertical distribution calculated from three-dimensional cloud-scale chemical transport model simulations". *J. Geophys. Res.* 115. DOI: 10.1029/2009jd011880.

Otte, T. (2008). "The Impact of Nudging in the Meteorological Model for Retrospective Air Quality Simulations. Part I: Evaluation against National Observation Networks." *J. Appl. Meteorol. Clim.* 47, pp. 1853–1867. DOI: 10.1175/2007JAMC1790.1.

Palmer, P. et al. (2001). "Air mass factor formulation for spectroscopic measurements from satellites: Applications to formaldehyde retrievals from the Global Ozone Monitoring Experiment". *J. Geophys. Res. Atmos.* 106, pp. 14539–14550.

Pandis, S. N. et al. (1992). "Secondary organic aerosol formation and transport". *Atmos. Environ. Part A* 26.13, pp. 2269 –2282. ISSN: 0960-1686. DOI: https://doi.org/10.1016/0960-1686(92)90358-R.

Perring, A. E., S. E. Pusede, and R. C. Cohen (2013). "An Observational Perspective on the Atmospheric Impacts of Alkyl and Multifunctional Nitrates on Ozone and Secondary Organic Aerosol". *Chem. Rev.* 113.8, pp. 5848–5870. DOI: 10.1021/cr300520x.

Pickering, K. E. et al. (1998). "Vertical distributions of lightning NO_x for use in regional and global chemical transport models". *J. Geophys. Res.* 103.D23, pp. 31203–31216.

Pickering, K. E. et al. (2016). "Estimates of lightning NO_x production based on OMI NO_2 observations over the Gulf of Mexico". *J. Geophys. Res. Atmos.* 121.14. 2015JD024179, pp. 8668–8691. ISSN: 2169-8996. DOI: 10.1002/2015JD024179.

Platnick, S. et al. (2015). *MODIS/Aqua Clouds 5-Min L2 Swath 1km and 5km. NASA MODIS Adaptive Processing System, Goddard Space Flight Center, USA*. DOI: 10.5067/MODIS/MYD06_L2.006.

Platt, U. and D. Perner (1980). "Direct Measurements of Atmospheric CH_2, HNO_2, O_3, NO_2, and SO_2 by Differential Optical Absorption in the Near UV". *J. Geophys. Res.* 85.C12, pp. 7453–7458.

Pope, C. A., M. Ezzati, and D. W. Dockery (2009). "Fine-Particulate Air Pollution and Life Expectancy in the United States". *N. Engl. J. Med.* 360.4, pp. 376–386. DOI: 10.1056/nejmsa0805646.

Price, C. and D. Rind (1992). "A simple lightning parameterization for calculating global lightning distributions". *J. Geophys. Res. Atmos.* 97.D9, pp. 9919–9933. ISSN: 2156-2202. DOI: 10.1029/92JD00719.

Richter, A. and T. Wagner (2011). "The Use of UV, Visible and Near IR Solar Back Scattered Radiation to Determine Trace Gases". In: *The Remote Sensing of Tropospheric Composition from Space*. Ed. by J. Burrows, U. Platt, and P. Borrell. New York: Springer.

Richter, A. et al. (2005). "Increase in tropospheric nitrogen dioxide over China observed from space". *Nature* 437.7055, pp. 129–132. DOI: 10.1038/nature04092.

Robere, R. (2012). "Interior Point Methods and Linear Programming". University of Toronto. URL: http://www.cs.toronto.edu/~robere/paper/interiorpoint.pdf.

Rollins, A. W. et al. (2012). "Evidence for NO_x Control over Nighttime SOA Formation". *Science* 337.6099, pp. 1210–1212. DOI: 10.1126/science.1221520.

Romer, P. S. et al. (2016). "The lifetime of nitrogen oxides in an isoprene-dominated forest". *Atmos. Chem. Phys.* 16.12, pp. 7623–7637. DOI: 10.5194/acp-16-7623-2016.

Roujean, J.-L., M. Leroy, and P.-Y. Deschamps (1992). "A bidirectional reflectance model of the Earth's surface for the correction of remote sensing data". *J. Geophys. Res. Atmos.* 97.D18, pp. 20455–20468. ISSN: 2156-2202. DOI: 10.1029/92JD01411.

Rozanov, A. et al. (2005). "SCIATRAN 2.0 – A new radiative transfer model for geophysical applications in the 175–2400 nm spectral region". *Advances in Space Research* 36.5, pp. 1015–1019. DOI: 10.1016/j.asr.2005.03.012.

Rudlosky, S. D. (2015). "Evaluating ENTLN Performance Relative to TRMM/LIS." *Journal of Operational Meteorology* 3.2.

Russell, A. R., L. C. Valin, and R. C. Cohen (2012). "Trends in OMI NO_2 observations over the United States: effects of emission control technology and the economic recession". *Atmos. Chem. Phys.* 12, pp. 12197–12209. DOI: 10.5194/acp-12-12197-2012.

Russell, A. et al. (2011). "A high spatial resolution retrieval of NO_2 column densities from OMI: method and evalutation". *Atmos. Chem. Phys.* 11, pp. 8543–8554. DOI: 10.5194/acp-11-8543-2011.

Russell, A. R. et al. (2010). "Space-based Constraints on Spatial and Temporal Patterns of NO_x Emissions in California, 2005-2008". *Environ. Sci. Technol.* 44.9, pp. 3608–3615. DOI: 10.1021/es903451j.

Ryerson, T. B. et al. (1999). "Design and initial characterization of an inlet for gas-phase NOymeasurements from aircraft". *J. Geophys. Res. Atmos.* 104.D5, pp. 5483–5492. DOI: 10.1029/1998jd100087.

Sander, S. P. et al. (2011). *Chemical Kinetics and Photochemical Data for Use in Atmospheric Studies: Evaluation Number 17*. Tech. rep. Jet Propulsion Laboratory.

Schaaf, C. and Z. Wang (2015). *MCD43C3 MODIS/Terra+Aqua BRDF/Albedo Albedo Daily L3 Global 0.05Deg CMG V006, NASA EOSDIS Land Processes DAAC*. DOI: 10.5067/MODIS/MCD43C3.006.

Schaaf, C. Z. W. (2015a). *MCD43D07 MODIS/Terra+Aqua BRDF/Albedo Parameter1 Band3 Daily L3 Global 30ArcSec CMG V006. NASA EOSDIS Land Processes DAAC*. DOI: 10.5067/modis/mcd43d07.006.

— (2015b). *MCD43D08 MODIS/Terra+Aqua BRDF/Albedo Parameter2 Band3 Daily L3 Global 30ArcSec CMG V006. NASA EOSDIS Land Processes DAAC*. DOI: 10.5067/modis/mcd43d08.006.

— (2015c). *MCD43D09 MODIS/Terra+Aqua BRDF/Albedo Parameter3 Band3 Daily L3 Global 30ArcSec CMG V006. NASA EOSDIS Land Processes DAAC*. DOI: 10.5067/modis/mcd43d09.006.

Schaaf, C. Z. W. (2015d). *MCD43D31 MODIS/Terra+Aqua BRDF/Albedo QA BRDFQuality Daily L3 Global 30ArcSec CMG V006. NASA EOSDIS Land Processes DAAC*. DOI: 10.5067/modis/mcd43d31.006.

Schaaf, C. B. et al. (2010). "Aqua and Terra MODIS Albedo and Reflectance Anisotropy Products". In: *Land Remote Sensing and Global Environmental Change*. Springer New York, pp. 549–561. DOI: 10.1007/978-1-4419-6749-7_24.

Schaap, M. et al. (2015). "Performance of European chemistry transport models as function of horizontal resolution". *Atmos. Environ.* 112, pp. 90–105. DOI: 10.1016/j.atmosenv.2015.04.003.

Schaepman-Strub, G. et al. (2006). "Reflectance quantities in optical remote sensing—definitions and case studies". *Remote Sens. Environ.* 103.1, pp. 27–42. DOI: 10.1016/j.rse.2006.03.002.

Schreier, S. F. et al. (2014). "The empirical relationship between satellite-derived tropospheric NO_2 and fire radiative power and possible implications for fire emission rates of NO_x". *Atmos. Chem. Phys.* 14.5, pp. 2447–2466. DOI: 10.5194/acp-14-2447-2014.

Schumann, U. and H. Huntrieser (2007). "The global lightning-induced nitrogen oxides source". *Atmos. Chem. Phys.* 7, pp. 3823–3907.

Schütt, A. (2017). "Improved Gridding Routine of OMI NO_2 data and its applications". MA thesis. Ludwig-Maximilians-University Munich.

Schwantes, R. H. et al. (2015). "Isoprene NO_3 Oxidation Products from the RO_2 + HO_2 Pathway". *J. Phys. Chem. A* 119.40, pp. 10158–10171. DOI: 10.1021/acs.jpca.5b06355.

Seiler, W. and P. J. Crutzen (1980). "Estimates of gross and net fluxes of carbon between the biosphere and the atmosphere from biomass burning". *Clim. Change* 2, pp. 207–247. URL: https://link.springer.com/article/10.1007/BF00137988.

Seltzer, K. M., W. Vizuete, and B. H. Henderson (2015). "Evaluation of updated nitric acid chemistry on ozone precursors and radiative effects". *Atmos. Chem. Phys.* 15, pp. 5973–5986. DOI: 10.5194/acp-15-5973-2015.

SENEX Science Team (2013). *SENEX 2013 WP-3D Data: NOAA/Earth System Research Laboratory, Chemical Sciences Division*. URL: https://esrl.noaa.gov/csd/groups/csd7/measurements/2013senex/P3/DataDownload/.

Shusterman, A. A. et al. (2016). "The BErkeley Atmospheric CO_2 Observation Network: initial evaluation". *Atmos. Chem. Phys.* 16.21, pp. 13449–13463. DOI: 10.5194/acp-16-13449-2016.

Slusser, J. et al. (1996). "Comparison of air mass computations". *J. Geophys. Res. Atmos.* 101.D5, pp. 9315–9321. DOI: 10.1029/96JD00054.

Sneep, M. et al. (2008). "Three-way comparison between OMI and PARASOL cloud pressure products". *J. Geophys. Res. Atmos.* 113.D15. D15S23. ISSN: 2156-2202. DOI: 10.1029/2007JD008694.

Spicer, C. (1982). "Nitrogen Oxide Reactions in the Urban Plume of Boston". *Science* 215, pp. 1095–1097. DOI: 10.1126/science.215.4536.1095.

Stahler, A. et al. (1999). "MODIS BRDF/Albedo Product: Algorithm Theoretical Basis Document Version 5.0", pp. 7–15. URL: https://lpdaac.usgs.gov/sites/default/files/public/product_documentation/atbd_mod09_v5.pdf.

Stammes, P (Jan. 2001). "Spectral radiance modelling in the UV-Visible range, in: IRS 2000: Current problems in atmospheric radiation". In: *Proceedings of the International Radiation Symposium, A. Deepak Publishing*, pp. 385–388.

Stammes, P. et al. (2008). "Effective cloud fractions from the Ozone Monitoring Instrument: Theoretical framework and validation". *J. Geophys. Res. Atmos.* 113.D16. D16S38. ISSN: 2156-2202. DOI: 10.1029/2007JD008820.

Sullivan, J. T. et al. (2016). "Quantifying the contribution of thermally driven recirculation to a high ozone event along the Colorado Front Range using lidar". *J. Geophys. Res. Atmos.* 121.17, pp. 10,377–10,390. DOI: 10.1002/2016JD025229.

Tapley, B. D. et al. (2004). "The gravity recovery and climate experiment: Mission overview and early results". *Geophys. Res. Lett.* 31, p. L09607. DOI: 10.1029/2004gl019920.

Thornton, J. et al. (2002). "Ozone production rates as a function of NO_x abundances and HO_x production rates in the Nashville urban plume". *J. Geophys. Res.* 107.D12. DOI: 10.1029/2001jd000932.

Thornton, J. A., P. J. Wooldridge, and R. C. Cohen (2000). "Atmospheric NO_2: In Situ Laser-Induced Fluorescence Detection at Parts per Trillion Mixing Ratios". *Anal. Chem.* 72.3. PMID: 10695138, pp. 528–539. DOI: 10.1021/ac9908905.

Tie, X. et al. (2007). "Characterizations of chemical oxidants in Mexico City: A regional chemical dynamical model (WRF-Chem) study". *Atmos. Environ.* 41.9, pp. 1989 –2008. ISSN: 1352-2310. DOI: 10.1016/j.atmosenv.2006.10.053.

Tong, D. Q. et al. (2015). "Long-term NO_x trends over large cities in the United States during the great recession: Comparison of satellite retrievals, ground observations, and emission inventories". *Atmos. Environ.* 107, pp. 70–84. DOI: 10.1016/j.atmosenv.2015.01.035.

Toon, O. B. et al. (2016). "Planning, implementation, and scientific goals of the Studies of Emissions and Atmospheric Composition, Clouds and Climate Coupling by Regional Surveys (SEAC4RS) field mission". *J. Geophys. Res. Atmos.* 121.9, pp. 4967–5009. DOI: 10.1002/2015jd024297.

Travis, K. R. et al. (2016). "Why do models overestimate surface ozone in the Southeast United States?" *Atmos. Chem. Phys.* 16.21, pp. 13561–13577. DOI: 10.5194/acp-16-13561-2016.

ul-Haq, Z., S. Tariq, and M. Ali (2015). "Tropospheric NO_2 Trends over South Asia during the Last Decade (2004–2014) Using OMI Data". *Adv. Meteorol.* 2015, pp. 1–18. DOI: 10.1155/2015/959284.

United States Census Bureau. *Annual Estimates of the Resident Population: April 1, 2010 to July 1, 2015. Metropolitan and Micropolitan Statistical Area; and for Puerto Rico.* URL: http://www.census.gov/popest/data/metro/totals/2015/index.html (visited on 06/02/2016).

US Environmental Protection Agency (1970). *Clean Air Act.* URL: https://www.epa.gov/clean-air-act-overview/clean-air-act-text.

Valin, L. C., A. R. Russell, and R. C. Cohen (2014). "Chemical feedback effects on the spatial patterns of the NO_x weekend effect: a sensitivity analysis". *Atmos. Chem. Phys.* 14.1, pp. 1–9. DOI: 10.5194/acp-14-1-2014.

Valin, L. et al. (2011). "Effects of model resolution on the interpretation of satellite NO_2 observations". *Atmos. Chem. Phys.* 11, pp. 11647–11655. DOI: 10.5194/acp-11-11647-2011.

Valin, L., A. Russell, and R. Cohen (2013). "Variations of OH radical in an urban plume inferred from NO_2 column measurements". *Geophys. Res. Lett.* 40, pp. 1856–1860. DOI: 10.1002/grl.50267.

van der A, R. J. et al. (2006). "Detection of the trend and seasonal variation in tropospheric NO2 over China". *J. Geophys. Res. Atmos.* 111, p. D12317. DOI: 10.1029/2005JD006594.

van der A, R. J. et al. (2008). "Trends, seasonal variability and dominant NO_x source derived from a ten year record of NO_2 measured from space". *J. Geophys. Res. Atmos.* 113.D4, p. D04302. ISSN: 2156-2202. DOI: 10.1029/2007JD009021.

van Geffen, J. H.G. M. et al. (2015). "Improved spectral fitting of nitrogen dioxide from OMI in the 405-465 nm window". *Atmos. Meas. Tech.* 8.4, pp. 1685–1699. DOI: 10.5194/amt-8-1685-2015.

Vasilkov, A. et al. (2017). "Accounting for the effects of surface BRDF on satellite cloud and trace-gas retrievals: a new approach based on geometry-dependent Lambertian equivalent reflectivity applied to OMI algorithms". *Atmos. Meas. Tech.* 10.1, pp. 333–349. DOI: 10.5194/amt-10-333-2017.

Veefkind, J. et al. (2012). "TROPOMI on the ESA Sentinel-5 Precursor: A GMES mission for global observations of the atmospheric composition for climate, air quality and ozone layer applications". *Remote Sens. Environ.* 120, pp. 70–83. DOI: 10.1016/j.rse.2011.09.027.

Verstraeten, W. W. et al. (2015). "Rapid increases in tropospheric ozone production and export from China". *Nat. Geosci.* 8.9, pp. 690–695. DOI: 10.1038/ngeo2493.

Vestreng, V. et al. (2009). "Evolution of NO_x emissions in Europe with focus on road transport control measures". *Atmos. Chem. Phys.* 9.4, pp. 1503–1520. DOI: 10.5194/acp-9-1503-2009.

Vinken, G. C. M. et al. (2014a). "Constraints on ship NO_x emissions in Europe using GEOS-Chem and OMI satellite NO_2 observations". *Atmos. Chem. Phys.* 14.3, pp. 1353–1369. DOI: 10.5194/acp-14-1353-2014.

Vinken, G. C. M. et al. (2014b). "Worldwide biogenic soil NO_x emissions inferred from OMI NO_2 observations". *Atmos. Chem. Phys.* 14.18, pp. 10363–10381. DOI: 10.5194/acp-14-10363-2014.

Vukovich, F. M. and J. Scarborough (2004). "15-year simulation of ozone in Baltimore using SIPM". *Atmos. Environ.* 38.29, pp. 4825–4837. DOI: 10.1016/j.atmosenv.2004.06.009.

Wang, W. et al. (2014). "Chapter 7: Objective Analysis (OBSGRID)". In: *WRF-ARW Version 3.5 User's Guide*.

Wang, Y. et al. (2007). "Seasonal variability of NO_x emissions over east China constrained by satellite observations: Implications for combustion and microbial sources". *J. Geophys. Res.* 112.D6. DOI: 10.1029/2006jd007538.

Wanner, W., X. Li, and A. H. Strahler (1995). "On the derivation of kernels for kernel-driven models of bidirectional reflectance". *J. Geophys. Res. Atmos.* 100.D10, pp. 21077–21089. ISSN: 2156-2202. DOI: 10.1029/95JD02371.

Wegmann, M. et al. (2005). "NO_2-induced airway inflammation is associated with progressive airflow limitation and development of emphysema-like lesions in C57BL/6 mice". *Exp. Toxicol. Pathol* 56.6, pp. 341–350. DOI: 10.1016/j.etp.2004.12.004.

Wenig, M. et al. (2003). "Intercontinental transport of nitrogen oxide pollution plumes". *Atmos. Chem. Phys.* 3.2, pp. 387–393. DOI: 10.5194/acp-3-387-2003.

Wiedinmyer, C. et al. (2006). "Estimating emissions from fires in North America for air quality modeling". *Atmos. Environ.* 40.19, pp. 3419–3432. DOI: 10.1016/j.atmosenv.2006.02.010.

Wild, O. and M. J. Prather (2006). "Global tropospheric ozone modeling: Quantifying errors due to grid resolution". *J. Geophys. Res. Atmos.* 111, p. D11305. DOI: 10.1029/2005JD006605.

Williams, E. et al. (2000). "Global Lightning Variations Caused by Changes in Thunderstorm Flash Rate and by Changes in the Number of Thunderstorms". *J. Appl. Meteorol.* 39.12, pp. 2223–2230. DOI: 10.1175/1520-0450(2001)040<2223:glvcbc>2.0.co;2.

Wolfe, W. L. (1998). *Introduction to Radiometry*. SPIE–The International Society for Optical Engineering.

Wong, J., M. C. Barth, and D. Noone (2013). "Evaluating a lightning parameterization based on cloud-top height for mesoscale numerical model simulations". *Geosci. Model Dev.* 6.2, pp. 429–443. DOI: 10.5194/gmd-6-429-2013.

Wooldridge, P. J. et al. (2010). "Total Peroxy Nitrates (ΣPNs) in the atmosphere: the Thermal Dissociation-Laser Induced Fluorescence (TD-LIF) technique and comparisons to speciated PAN measurements". *Atmos. Meas. Techn.* 3.3, pp. 593–607. DOI: 10.5194/amt-3-593-2010.

Wooster, M. J. et al. (2005). "Retrieval of biomass combustion rates and totals from fire radiative power observations: FRP derivation and calibration relationships between biomass consumption and fire radiative energy release". *J. Geophys. Res.* 110.D24. DOI: 10.1029/2005jd006318.

Wooster, M. J. (2002). "Small-scale experimental testing of fire radiative energy for quantifying mass combusted in natural vegetation fires". *Geophys. Res. Lett.* 29.21. DOI: 10.1029/2002gl015487.

Wright, M. (2005). "The interior-point revolution in optimization: History, recent developments, and lasting consequences". *Bull. Amer. Math. Soc.* 42, pp. 39–56. URL: http://www.ams.org/journals/bull/2005-42-01/S0273-0979-04-01040-7/.

Yamaji, K. et al. (2014). "Influence of model-grid resolution on NO_2 vertical column densities over East Asia". *J. Air. Waste. Manage.* 64, pp. 436–444. DOI: 10.1080/10962247.2013.827603.

Yang, K. et al. (2014). "Advancing measurements of tropospheric NO_2 from space: New algorithm and first global results from OMPS". *Geophys. Res. Lett.* 41.13, pp. 4777–4786. DOI: 10.1002/2014gl060136.

Yegorova, E. A. et al. (2011). "Characterization of an eastern U.S. severe air pollution episode using WRF/Chem". *J. Geophys. Res. Atmos.* 116.D17. D17306. ISSN: 2156-2202. DOI: 10.1029/2010JD015054.

Yienger, J. and H. Levy II (1995). "Empirical model of global soil-biogenic NO_x emissions". *J. Geophys. Res.* 100.D6, pp. 11447–11464. URL: https://agupubs.onlinelibrary.wiley.com/doi/epdf/10.1029/95JD00370.

Zare, A. et al. (2018). "A comprehensive organic nitrate chemistry: insights into the lifetime of atmospheric organic nitrates". *Atmos. Chem. Phys. Discuss.* 2018, pp. 1–33. DOI: 10.5194/acp-2018-530.

Zhang, Y. et al. (2009). "Comparisons of WRF/Chem simulations in Mexico City with ground-based RAMA measurements during the 2006-MILAGRO". *Atmos. Chem. Phys.* 9.11, pp. 3777–3798. DOI: 10.5194/acp-9-3777-2009.

Zhao, C. and Y. Wang (2009). "Assimilated inversion of NO_x emissions over east Asia using OMI NO_2 column measurements". *Geophys. Res. Lett.* 36.6. DOI: 10.1029/2008gl037123.

Zhou, Y. et al. (2009). "An improved tropospheric NO_2 retrieval for OMI observations in the vicinity of mountainous terrain". *Atmos. Meas. Tech.* 2.2, pp. 401–416. DOI: 10.5194/amt-2-401-2009.

Zhou, Y. et al. (2010). "Accounting for surface reflectance anisotropy in satellite retrievals of tropospheric NO_2". *Atmos. Meas. Tech.* 3.5, pp. 1185–1203. DOI: 10.5194/amt-3-1185-2010.

Zhou, Y. et al. (2012). "Changes in OMI tropospheric NO_2 columns over Europe from 2004 to 2009 and the influence of meteorological variability". *Atmos. Environ.* 46, pp. 482–495. DOI: 10.1016/j.atmosenv.2011.09.024.

Ziemke, J., S. Chandra, and P. Bhartia (2001). "Cloud slicing: A new technique to derive upper tropospheric ozone from satellite measurements". *J. Geophys. Res. Atmos.* 106, pp. 9853–9867.

Zörner, J. et al. (2016). "Multi-satellite sensor study on precipitation-induced emission pulses of NO_x from soils in semi-arid ecosystems". *Atmos. Chem. Phys.* 16.14, pp. 9457–9487. DOI: 10.5194/acp-16-9457-2016.

Appendix A

Summary of global and regional OMI NO_2 retrievals

Here we will review existing NO_2 retrievals for the Ozone Monitoring Instrument (OMI). OMI, launched in October 2004, had the highest spatial resolution of any space-based NO_2 sensors with a spatial resolution at nadir of 13×24 km^2 (Levelt et al., 2006) until the launch of TROPOMI in October 2017. With its wide viewing swath, OMI was initially able to observe the entire globe in one day; however, between June 2007 and July 2011, anomalous radiances (termed the "row anomaly") developed that made approximately one-third of OMI's viewing swath unusable. Consequently, OMI now observes the entire globe once every two days.

The high resolution of the OMI sensor compared to previous NO_2 satellite instruments (GOME, 40×320 km^2, Burrows et al. 1999; SCIAMACHY, 30×60 km^2, Beirle et al. 2010b) offered tremendous opportunity to study NO_2 on spatial scales that make it possible to resolve physical processes operating on it (e.g. Valin et al., 2013) but also opened up significant challenges in producing AMF calculations that resolved the pixel-to-pixel difference at such a fine scale. Generally, *a priori* information used to retrieve the NO_2 column density should be given at equal or finer resolution than the OMI observations in order to capture the pixel to pixel variability in those *a priori* data. Some of the *a priori* data, most notably the NO_2 profiles calculated with CTMs, are computationally expensive to produce at the $\sim$13 km resolution needed by OMI, particularly for global retrievals. In response, alongside the major global retrievals, a number of regional retrievals, focusing on a subset of the Earth, have emerged, trading global coverage for high resolution *a priori* data.

Product	SCD Fitting	Strat. Sep.	RTM	Surf. refl.	Surf. elev.	Clouds	CTM	Citation
NASA SPv1	DOAS modified for ring effect	Mask and fill with wave-2 fits	TOMRAD LUT	GOME monthly climatology	3 km DEM, pressure at pixel center	O_2-O_2 OMI cloud product	GSFC CTM (strat, annual global mean) + GEOS-Chem (trop. $2.5^\circ \times 2.0^\circ$ annual mean)	Bucsela et al. (2006)
NASA SPv2	DOAS fitting with static solar spectrum	Iterative masking and interpolation	TOMRAD LUT, Lagrange polynomial interpolation	OMI monthly LER climatology	3 km DEM with hyposmetric eqn.	O_2-O_2 OMI cloud product	Monthly mean GMI-CTM profiles (Averaged 2005-07, $2.5^\circ \times 2.0^\circ$)	Bucsela et al. (2013)
NASA SPv3	Microwindow spectral DOAS fitting	Iterative masking and interpolation	TOMRAD LUT, Langrange polynomial interpolation	OMI monthly LER climatology	3 km DEM with hyposmetric eqn.	O_2-O_2 OMI cloud product	Year specific $1.25^\circ \times 1.0^\circ$ monthly average profiles, 2004–2014 (2014 used all later years)	Krotkov et al. (2017)
DOMINOv1	DOAS fitting modified for ring effect	Total-column assimilation in TM4	LUT calculated with the pseudo-spheric DAK model	TOMS+GOME monthly climatology	Interpolated TM4 surface pressure	O_2-O_2 OMI cloud product	Daily TM4 profiles ($3^\circ \times 2^\circ$ at 13:30 local)	Boersma et al. (2007)
DOMINOv2	DOAS fitting modified for ring effect	Total-column assimilation in TM4	LUT calculated with plane-parallel DAK including polarization	OMI monthly LER climatology	DEM 3km with hyposmetric eqn.	O_2-O_2 OMI cloud product	Improved daily TM4 profiles ($3^\circ \times 2^\circ$ at 13:30 local)	Boersma et al. (2011)

Table A.1: Summary of the retrieval choices for several versions of the NASA Standard Product and KNMI Dutch OMI NO_2 global OMI NO_2 retrievals.

Product (Region)	SCD Fitting	Strat. Sep.	RTM	Surf. refl.	Surf. elev.	Clouds	CTM	Citation
EOMINO (Europe)	Same as DOMINO v1		Online LIDORT calculation	MODIS BRDF (MOD43B, collection 5)	GTOPO30 elevation with hypsometric eqn.	OMI O_2-O_2 algorithm using MODIS black-sky albedo, GTOPO30 surf. elev., and LIDORT (cld. rad. frac.)	Same as DOMINO v1	Zhou et al. (2009) and Zhou et al. (2010)
BEHRv2 (Cont. US)	Same as NASA SPv2			MODIS MCD43C3 0.05° black-sky albedo	GLOBE 1 km elevation with 7.4 km scale height	OMI O_2-O_2 + MODIS MYD06 cloud fraction	WRF-Chem (12 km, monthly)	Russell et al. (2011) and Russell et al. (2012)
OMI-EC (Canadian Oil Sands)	Used both SP and DOMINO trop. SCDs		Clear and cloudy LUTs from VECTOR RTM	MODIS blue-sky albedo, wavelength adjusted with OMI climatology	GEM-MACH surf. pressure	Same as DOMINO v2	Hybrid GEM-MACH (15 km) + GEOS-Chem ($0.67° \times 0.5°$, monthly avg.)	McLinden et al. (2014)
DOMINO2_GC (Europe)	Same as DOMINO v2						GEOS-Chem ($0.67° \times 0.5°$, daily w/plume-in-grid ship emissions	Vinken et al. (2014a)
POMINO (China)	Same as DOMINO v2		Online LIDORT v3.6, explicit aerosol treatment	MODIS BRDF (MCD43C2, collection 5)	GMTED2010 elevation with hypsometric eqn.	Rederived from OMI O_2-O_2 SCDs with LIDORT RTM	GEOS-Chem ($0.67° \times 0.5°$, daily)	Lin et al. (2014a) and Lin et al. (2015)
HKOMI (Pearl River Delta, China)	Same as NASA SPv2		SCIATRAN, online, explicit and implicit aerosol treatment	MODIS SZA-dependent black-sky alb. (MCD43C2)	WRF-derived	OMI O_2-O_2 product	WRF-CMAQ (3 km, daily)	Kuhlmann et al. (2015)
OMI-CMAQ (Baltimore, MD, USA and surrounding area)	Same as NASA SP v3.0						WRF-CMAQ (1.33 km); daily for June–July 2011, monthly otherwise	Goldberg et al. (2017)

Table A.2: Summary of the retrieval choices for all known custom or regional OMI NO_2 retrievals.

A.1 Global retrievals

The NASA Standard Product, version 1

There are two primary global retrievals of NO_2 from OMI. The first is the NASA Standard Product (SP). The first version fit the observed Earthshine radiances using a DOAS technique modified to account for the Ring effect, or the filling in of the Fraunhofer lines of the solar spectrum by Raman scattering in the atmosphere. The initial total SCDs resulting from this fit were temporarily converted to VCDs using an AMF that assumes a standard stratospheric NO_2 profile.

The contributions of stratospheric vs. tropospheric NO_2 to the total column were derived from these initial VCDs. The stratosphere-tropospheric separation (STS) algorithm employed in the SP first masked areas known to have significant tropospheric NO_2 from the initial VCD field. The remaining areas were assumed to have little tropospheric NO_2, and were therefore assumed to be entirely stratospheric NO_2. A first-guess stratospheric VCD field was calculated by filling in the masked areas with a 10° running boxcar average in the north-south direction, then assuming that the east-west variation is described by

$$\mathrm{NO_2}(L) = a_1 L + a_2 \sin(L) + a_3 \sin(2L) \tag{A.1}$$

where L is the longitude and the a_i's are fitting coefficients. To avoid contamination from tropospheric NO_2 not known *a priori* in the first masking step, the wave structure analysis was repeated after masking areas where the initial VCDs and the first-guess stratospheric field differ by $> 1\sigma$. The result of this second wave-fitting step was the final stratospheric VCD field.

Finally, to accurately retrieve tropospheric columns in polluted areas with substantial tropospheric NO_2, the tropospheric VCD was calculated by subtracting the stratospheric SCD from the total SCD and dividing by a tropospheric air mass factor.

In this algorithm, the AMFs were calculated with scattering weights computed using the TOMRAD radiative transfer model (Davé, 1964; Davé, 1965; Ahmad and Bhartia, 1995) and NO_2 profiles simulated using the GEOS-Chem (for tropospheric profiles, Bey et al., 2001) and GSFC (for the stratospheric profile, Douglass et al., 2003) chemical transport models. The scattering weights were precomputed and stored in a look up table (LUT) and depended on several input parameters: the solar and viewing angles, the surface reflectance, and the surface pressure. The solar and viewing angles can be calculated very precisely, given knowledge of OMI's orbital trajectory. The surface reflectance and elevation must be taken from other datasets; in SP v1, the surface reflectance was taken from a climatological surface reflectance database generated from GOME-1 observations (Koelemeijer, 2003). The surface pressure is derived from the SDP Toolkit 90 arcsec (∼3 km) DEM database, taken at the

center of the OMI pixel (Russell et al., 2011). The tropospheric NO_2 profiles were simulated at $2.5° \times 2°$ (longitude $\times$ latitude) resolution and averaged over the entire simulated year. A single, global average stratospheric profile from the GSFC CTM was used.

The NASA Standard Product, version 2

Changes between version 1 and version 2 of the NASA SP focused on the STS method and the calculation of the tropospheric AMF.

The version 2 STS was redesigned to use local data to fill in the stratospheric NO_2 field, rather than the global analysis used in version 1. The general process was similar: an initial, *a priori* tropospheric NO_2 column was subtracted from the total column to give a first-guess stratospheric NO_2 field; regions where the *a priori* tropospheric VCD exceeded a given threshold are masked. This masking considered the sensitivity of OMI to the tropospheric NO_2 column (represented by the tropospheric AMF), so e,g. a cloud-covered pixel can be used even if the *a priori* NO_2 profile indicated significant tropospheric NO_2. Similar to the version 1 algorithm, the masked areas were filled in, then remaining tropospheric contamination was remasked and reinterpolated. However, unlike the version 1 algorithm, the interpolation was carried out by averaging unmasked values within a box centered on the stratospheric VCD to be calculated. The size of the box varied with latitude.

The tropospheric AMF calculated was significantly modified. The TOMRAD RTM was still used to generate an LUT, but the scattering weights were calculated for a larger number of input values compared to version 1 (resulting in a denser LUT), and the method of interpolation modified to reduce errors in the lookup process. The input *a priori* data was also updated: the albedo used changed from one derived from GOME (Koelemeijer, 2003) to one derived from OMI itself (Kleipool et al., 2008) and the surface pressure was found by scaling modeled surface pressure by the surface elevation from a high resolution digital elevation map. The NO_2 profiles were kept at the same spatial resolution, but updated to use monthly averages (rather than a single yearly average). Both stratospheric and tropospheric NO_2 profiles were drawn from the same model simulation, which was run from 2005 to 2007.

The NASA Standard Product, version 3

Version 3 of the NASA SP further refined the tropospheric AMF calculation as well as implemented a new total SCD fitting approach that reduced a positive bias recently identified in the OMI SCDs.

Belmonte Rivas et al. (2014) identified a +20% bias in OMI stratospheric VCDs by comparing them to limb measurements. This was traced to a bias in the initial total SCD fitting procedure, leading to a revised fitting procedure developed by Marchenko et al. (2015) and incorporated into the version 3 Standard Product. The Marchenko et al. (2015) approach

differs from the more traditional DOAS approach used previously in several ways. The first step remains to compute a baseline absorbance accounting for broad atmospheric effects, represented as a second order polynomial of wavelength. The new approach divided the 402–465 nm fitting window into seven "microwindows," each of which may have a different wavelength shift between the solar irradiance and Earthshine radiance spectra. In contrast to the previous approach, the new method used the Ring effect to guide the spectral alignment. The Ring spectrum was subtracted from the radiances at this step, rather than fit simultaneously with the desired trace gases, as was done in the previous DOAS algorithm.

Next, NO_2, H_2O, and CHOCHO differential absorption features above the second order polynomial baseline were fit. The trace gases were fit in sequence, rather than simultaneously, as in the prior DOAS algorithm. The fitting process was iterated several times, removing the trace gas absorbances and identifying, in turn, instrument noise and undersampling artifacts, in the radiances, refitting the trace gas SCDs after each correction.

The tropospheric AMF calculation was also updated in version 3 by an upgrade to the *a priori* NO_2 profiles. In version 3, the spatial resolution of the *a priori* profiles was increased to $1.25° \times 1°$ (from $2.5° \times 2°$ previously) and used year-specific monthly average profiles for 2004 to 2014. This allowed *a priori* profiles to respond to changes in emissions over that decade. Years after 2014 were retrieved with 2014 profiles.

The KNMI DOMINO Product v1

The first independent OMI retrieval developed by the Royal Netherlands Meteorological Institute (KNMI) was the near-real time retrieval described in Boersma et al. (2007). This product used the same total SCDs as the NASA SP v1, but handled STS and tropospheric AMF calculation differently. The STS is carried out by assimilating total OMI SCDs into the TM4 CTM. By nudging the CTM to be consistent with the total column, the stratospheric component can be taken directly from the model. The assimilation weighted the OMI observations such that regions predicted by TM4 to have substantial tropospheric columns had only a weak effect during the assimilation.

The tropospheric AMF calculation was conceptually similar to that in the SP v1, but the particulars differed. The scattering weigh look-up table was computed with the Doubling-Adding KNMI (DAK) RTM (Stammes, 2001). The surface albedo used was the TOMS reflectivity at 380 nm scaled by the ratio of GOME reflectivity at 440 nm to 380 nm (Boersma et al., 2004), rather than using the GOME reflectivity directly. Finally, daily NO_2 profiles from TM4 were used rather than yearly averaged NO_2 profiles.

The KNMI DOMINO Product v2

The second iteration of the Dutch OMI NO_2 (DOMINO) algorithm, as the near-real time KNMI algorithm became known, focused primarily on improvements to the tropospheric AMF calculation. Similarly to the NASA SP v2, DOMINO v2 increased the density of the scattering weight LUT. Two improvements suggested by Zhou et al. (2009) were also added. First, the scattering weights were extrapolated as necessary to pressure levels below the CTM surface pressure rather than set to 0; second, the surface pressure for each pixel now combined modeled surface pressure with a high resolution topographic database. The second enhancement was also included in the NASA SP v2 retrieval. The surface reflectance product used in the AMF calculations was updated from the combined GOME/TOMS climatology of version 1 to the OMI climatology developed by Kleipool et al. (2008); this albedo was also used in the NASA SP v2. Finally, DOMINO v2 updated the TM4 model to explicitly simulate NO_2, rather than simulate NO_x and calculate NO_2 from the total NO_x concentration; this solved an issue identified by Hains et al. (2010) where vertical mixing of NO_2 was underrepresented in the TM4 profiles.

A.2 Lessons learned from regional retrievals

Regional retrievals are those that trade global coverage of the retrieval for improved a priori inputs, primarily by increasing the inputs' resolution to a level that cannot be achieved in the global retrievals due to computational constraints.

Effect of spatial resolution of the a priori profiles

Many studies have examined the effect of increasing the spatial resolution of the a priori NO_2 profiles on the retrieved satellite VCDs. Russell et al. (2011) found that increasing the resolution from $2.5^\circ \times 2.0^\circ$ (longitude by latitude, approximately 275×220 km) to 4 km altered the retrieved NO_2 by up to -75% in rural areas and $+10\%$ in urban areas.

The OMI_EC retrieval (McLinden et al., 2014) also demonstrated that the a priori profile resolution is especially critical for dense point sources, i.e. the Canadian Oil Sands. Using a retrieval at 15×15 km^2 with updated Oil Sands NO_x emissions, McLinden et al. (2014) saw an increase of nearly 100% in NO_2 VCDs over the Oil Sands compared to the standard products. This was due to both the out-of-date (underestimated) NO_x emissions in the standard product a priori profile simulations and the coarse resolution diluting the NO_2 emitted with background concentrations.

Vinken et al. (2014a) designed a regional NO_2 retrieval that used a $0.667^\circ \times 0.5^\circ$ GEOS-Chem simulation with a plume-in-grid method that parameterized the sub-grid scale NO_2 emitted by ships in order to avoid instantaneous dilution to the grid cell size. Compared to the DOMINO v2.0 product, Vinken et al. (2014a) retrieved 10% lower VCDs using these

new profiles. When the spatial distribution is considered in more detail, it is evident that the DOMINO2_GC retrieval from Vinken et al. (2014a) retrieves smaller VCDs over most of Europe, but higher VCDs over shipping tracks in the Mediterranean Sea and several large European cities (e.g. Barcelona, Valencia). This is consistent with Russell et al. (2011), in that rural areas have decreased NO_2 VCDs and urban, or more generally locations with significant emissions, have increased VCDs when the resolution of the a priori profiles is increased.

The POMINO retrieval (Lin et al., 2014a; Lin et al., 2015) uses NO_2 a priori profiles simulated at $0.667^\circ \times 0.5^\circ$ by GEOS-Chem. In comparison to a retrieval using profiles simulated with TM4 (the model used in the DOMINO v2 retrieval upon which their retrieval is based), they found that VCDs decreased by $\sim 13\%$. They attribute this to a tendency of TM4 to place more NO_2 near the surface compared to GEOS-Chem. Previous work had identified a bias in TM4 that overestimated near-surface NO_2 (Hains et al., 2010), but this was corrected in DOMINO v2 (Boersma et al., 2011). Lin et al. (2014a) do not show the spatial distribution of the change in VCDs attributed to the NO_2 profiles, but we suspect that similar patterns to e.g. Russell et al. (2011) should be expected, where the overall change is negative, but is positive within cities.

The HKOMI and OMI-CMAQ retrievals use the highest resolution a priori profiles known to date, ~ 1 km. HKOMI retrieves NO_2 VCDs over Hong Kong, China (Kuhlmann et al., 2015). Compared to the NASA SP v2.1, they find that using the 1 km resolution increases VCDs by $\sim 10\%$. The top tenth of VCDs (likely mostly urban VCDs) increased by $\sim 13\%$, Interestingly this is similar to the increase identified in Russell et al. (2011), indicating that increasing from 4 km to 1 km a priori profiles offers little benefit. The OMI-CMAQ product retrieves the area around Baltimore, MD, USA using a priori profiles from CMAQ adjusted based on observational data to correct a high bias in total reactive nitrogen and NO/NO_2 ratios. Using these corrected profiles, they see an increase of $\sim 20\%$ in VCDs within Baltimore and a $\sim 40\%$ decrease in rural areas.

All the retreivals discussed here show a similar pattern of modest increases in NO_2 VCDs within cities and larger decreases in VCDs outside of cities when the resolution of the a priori profiles is increased. At coarser resolutions, the a priori profiles represent an average of an urban and rural NO_2 profile; meaning that rural areas will have too much surface NO_2 and urban areas too little. Additional NO_2 near the surface, where the satellite's sensitivity is low, requires a smaller AMF to account for the reduced sensitivity, and thus retrieves larger VCDs.

Most of the regional retrievals described here saw smaller percent increases in urban areas than percent decreases in surrounding rural areas. This suggests that, in most cases, the urban NO_2 profile had an outsized impact on the coarse resolution NO_2 profiles. For example, Russell et al. (2011) compared the NASA SP v2.1 (which used a priori profiles based on 2005–

2007 emissions) to a retrieval using 4 km profiles simulated with 2005 NO_x emissions. Large US NO_x emissions in 2005–2007 would contribute to a large urban effect even in coarse a priori profiles. This effect may be reversing as NO_x emissions reduce and the urban profile influences the coarse grid cell less. Goldberg et al. (2017) did not see this, instead seeing a similar pattern to the other studies despite studying 2008–2012; this may be because the Baltimore-Washington D.C. metropolitan area is quite large geographically, and so will continue to have significant influence on coarse a priori profiles, even as its NO_x emissions reduce.

Surface reflectivity

Background

As the lower boundary condition for atmospheric radiative transfer, surface reflectivity is an important input parameter to a trace gas retrieval. There are three elements to consider in a retrieval's treatment of surface reflectivity:

1. Resolution of the observations it is derived from and of the final product
2. Treatment of anisotropy in the surface itself
3. Treatment of indirect illumination in addition to direct illumination

The resolution of the surface reflectance matters in two ways. First, sufficiently high resolution observations can "look between" clouds. This is crucial because the presence of clouds will bias the surface reflectance high (Kleipool et al., 2008). In a surface reflectance product using OMI (in which the pixels are large enough to frequently have some degree of cloud contamination), Kleipool et al. (2008) attempted to address this by using the 1st percentile of the monthly reflectivity observations after filtering, but there is evidence that cloud contamination remains an issue (e.g. Zhou et al., 2010). Higher resolutions (≤ 1 km) increase the chance of obtaining cloud-free observations, producing a less biased representation of surface reflectance.

Second, representation of surface reflectance can also be improved by changing from an isotropic to anisotropic representation. In the standard NO_2 retrievals, the surface is treated as an isotropic reflector that scatters light equally in all directions and for all incident angles. This is an idealized representation; in reality, the amount of light scattered in a particular direction varies. An extreme example is the ocean surface; very little light is scattered in most directions, but at the glint angle, a significant fraction of incident light is scattered. Two terms are used to describe this directional dependence, the *bidirectional reflectance distribution function* (BRDF) is the ratio of outgoing radiance to incoming irradiance for a particular incidence and viewing geometry. The second, the *bidirectional reflectance factor*

(BRF) is the BRDF normalized by that expected for a fully reflective, isotropic surface (Schaepman-Strub et al., 2006; Wolfe, 1998). It is worth noting that these two terms are not always used correctly in the literature.

Finally, surface reflectance may measure the reflected direct sunlight, indirect sunlight (that is, sunlight scattered in the atmosphere so that it impinges on the ground from a direction other than the direct line from the sun), or both. A surface reflectance only considering the direct sunlight is called a black-sky reflectance, one considering only the indirect reflectance is called a white-sky reflectance, and one considering both is a blue-sky reflectance. A blue-sky reflectance is most accurate, as it accounts for both direct and indirect sunlight, weighted by the fraction of light that is indirect. This requires a radiative transfer model (or a look-up table generated by one) to calculate that fraction.

Effects observed in regional retrievals

Currently, the operational NASA SP and KNMI DOMINO retrievals use a $0.5^\circ \times 0.5^\circ$ monthly climatological surface reflectivity product derived from OMI (Kleipool et al., 2008). For use in an OMI retrieval, this has the advantage of being derived at the same wavelengths as the trace gas retrieval operates at, but the coarse spatial and temporal resolution loses information about the fine scale variability in surface reflectivity (Russell et al., 2011).

The EOMINO retrieval addressed both the resolution and directional dependence of surface reflectance by using the MODIS (Moderate Resolution Imaging Spectrometer) BRDF product MOD43B1 (Zhou et al., 2010). Comparing NO_2 VCDs retrieved using the $1^\circ \times 1^\circ$ surface reflectivity derived from GOME and TOMS observations used in DOMINO v1 (Boersma et al., 2004; Boersma et al., 2007), Zhou et al. (2010) found that the source of the surface reflectivities has a larger impact (15–60%) than the treatment of anisotropic reflectances (0–20%). They suggested that this is due to unavoidable snow and cloud contamination in the larger GOME and TOMS pixels, which biases the surface reflectance high, while the small pixel size of MODIS ($\leq 1\,\text{km}$) allows it to "look between" clouds, reducing cloud contamination.

Zhou et al. (2010) further quantified the difference using a MODIS black-sky, nondirectional, black-sky directional, and blue-sky directional surface reflectance. The black-sky nondirectional is the simplest case, assuming isotropic reflectance and only considering direct sun illumination. The blue-sky directional case is the most complex, using a radiative transfer model to treat the indirect illumination from scattered sunlight and accounting for the directionality of surface reflectance. They found differences in retrieved NO_2 VCDs mostly $\leq 12\%$ among these cases, with most summertime differences $\leq 4\%$. This indicates that the surface anisotropy and indirect illumination is primarily important in winter, with larger solar zenith angles leading to more scattered light and more extreme illumination angles.

Russell et al. (2011) focused on the resolution of the surface reflectance, using the MODIS combined black-sky albedo product. The version used in the BEHR v2 retrieval was released

every 8 days at $0.05^\circ \times 0.05^\circ$ resolution, allowing it to capture small scale variations in albedo and (since it is not a climatological reflectance product) medium-term changes in surface reflectivity. Compared to the Kleipool et al. (2008) OMI reflectance used in the standard retrievals, Russell et al. (2011) found up to 100% differences in surface reflectivity, causing up to 40% differences in the retrieved NO_2 columns over California and Nevada.

Similarly, McLinden et al. (2014) uses a weighted sum of MODIS black-sky and white-sky reflectivities, but adjusted to the OMI retrieval wavelengths (440 nm for NO_2) using a ratio of reflectivities at the OMI and MODIS wavelengths from the Kleipool et al. (2008) climatology. Although they did not explicitly evaluate the effect of reflectance on the retrieved columns, they demonstrated that the MODIS reflectivity was able to capture the higher reflectivity of the Oil Sands compared to the surrounding area.

The POMINO retrieval implemented a bidirectional reflectance function (BRF) surface reflectance in their retrieval. A BRF accounts for the angular dependence of surface reflectivity. Compared to Russell et al. (2011), they found a much smaller impact of surface reflectance on retrieved NO_2 columns, $\leq$ 10% ($\sim$ 1% difference in overall normalized mean bias versus MAX-DOAS observations) compared to using the Kleipool et al. (2008) product. A difference between the POMINO and BEHR retrievals is that that POMINO retrieval also retrieves cloud properties with the new surface reflectance; Lin et al. (2014a) suggested that the change in cloud properties balances the effect of the change to surface reflectance.

Finally the HKOMI retrieval (Kuhlmann et al., 2015) used a black-sky surface reflectivity calculated from the MODIS MCD43C2 product for the solar zenith angle appropriate for each pixel. They did not include a wavelength correction or white-sky contribution. They found, on average, an 11% difference compared to the NASA SP v2. Again, this is smaller than observed by Russell et al. (2011). Unlike POMINO, the HKOMI retrieval did not retrieve the cloud properties with the updated surface reflectance, so it cannot be due to changes in the cloud properties counteracting the surface reflectance. Since both POMINO and HKOMI retrieved over East Asia, this may indicate that the difference between the Kleipool et al. (2008) and MODIS surface reflectivities are less in East Asia than other parts of the world. Lin et al. (2014a) speculate to this effect, noting that Zhou et al. (2010) found effects of up to 20% in Europe.

In summary, several studies found that switching from coarser OMI, GOME, or TOMS albedos to higher resolution MODIS products had a larger impact than accounting for surface anisotropy or indirect illumination, but that the latter still introduced important effects on the NO_2 VCDs especially in winter.

Terrain pressure

Terrain pressure can generally be treated three ways in retrievals:

1. Directly extracted from the chemical transport model used to simulate the NO_2 a priori profiles (e.g. NASA SP v1, DOMINO v1, HKOMI)

2. Derived from a high resolution terrain height data base and converted to pressure using a fixed scale height relationship (e.g. BEHR v2)

3. Scale the CTM surface pressure using a high resolution terrain height database and the hypsometric equation (e.g. EOMINO, POMINO, NASA SP v2/v3, DOMINO v2)

The EOMINO retrieval was the first to evaluate the effect of a high resolution terrain height (Zhou et al., 2009) finding biases of up to 20% (winter, 5% summer) in DOMINO v1 NO_2 VCDs over mountainous regions due to the coarse surface pressure used in that retrieval. Zhou et al. (2009) used the hypsometric relationship to downscale coarse TM4 surface pressures to OMI pixel sizes using a 1 km terrain height database.

Other retrievals used more straightforward methods to achieve high resolution surface pressures. the OMI-EC (McLinden et al., 2014) and HKOMI (Kuhlmann et al., 2015) retrievals took surface pressures directly from high resolution models. The BEHR v2 retrieval (Russell et al., 2011) used a surface pressure directly calculated from a 1 km terrain height database assuming a fixed scale height. Only Russell et al. (2011) specifically evaluated the effect of increasing the surface pressure resolution, finding summertime differences in the NO_2 VCD compared to the NASA SP v1 of $\sim$ 20% for individual pixels. Both results indicate that accurately representing surface pressure at the resolution of the satellite pixels has a significant impact on the retrieval in regions with significant orography. However, to date, no comparison of these three methods of achieving that resolution has been carried out.

Clouds and aerosols

The presence of aerosols in the atmosphere can significantly alter its scattering properties. Most retrievals implicitly account for this effect by combining cloud and aerosol effects (Boersma et al., 2004; Boersma et al., 2011), as aerosols and clouds both shield NO_2 below them from observation. However, two retrievals, POMINO (Lin et al., 2015) and HKOMI (Kuhlmann et al., 2015) explicitly treat aerosols in their retrievals. It is worth noting that both retrievals focus on China or regions within, which have extremely high aerosol optical depth (AOD).

The HKOMI (Kuhlmann et al., 2015) retrieval tested several ways of explicitly including aerosols in the retrieval. They found only a small increase in VCDs when explicitly treating aerosol (+6–12%) except in their least sophisticated approach (+24–30%). The POMINO retrieval (Lin et al., 2015), which covered a much larger area of East Asia, also most frequently saw changes of $\sim$ +10% when explicitly accounting for aerosols, but did see rarer occurrences of +50–100% increases in NO_2 VCD. Further, Lin et al. (2015) also noted that the magnitude

and even the sign of the aerosol effect varied from region to region within their domain. This is likely due to the effects of the relative position of the NO_2 and aerosol layers described in Leitão et al. (2010) and Bousserez (2014).

In general, Lin et al. (2015) and Castellanos et al. (2015) both found that, in the majority of cases, the implicit treatment of aerosols as clouds in NO_2 retrievals is accurate to within $\sim 10\%$, but the effect could be much larger ($\sim 100\%$) under the right conditions. Castellanos et al. (2015) used aerosol profiles measured by the CALIOP satellite instrument to evaluate the effect of aerosols on NO_2 retrievals and found similar results. Both also agree that the magnitude of the effect is not simply a function of AOD, but also depends on single scattering albedo and the aerosol profile.

Lin et al. (2015) also noted that because the implicit treatment of aerosols will usually increase effective cloud fraction, and since most applications of satellite NO_2 data will remove pixels with a cloud fraction above a certain threshold, that the implicit treatment of aerosols can cause high pollution days to be preferentially and erroneously excluded from averages. Therefore, they argue that even if the effect on the retrieved column is small, implicitly treating aerosols as clouds biases statistics of NO_2 columns in highly polluted areas.

A.3 Summary

A consistent theme through all the above regional retrievals is that improving the spatial resolution of the a priori input improves the retrieval. NO_2 vertical profiles, surface reflectances, and terrain pressure that are given at coarser spatial resolution than the OMI pixels used in the retrieval process obscure key variability in the atmosphere and surface that is necessary to accurately account for all factors affecting the outgoing radiance, and therefore the NO_2 VCDs. This has led to a push in the global retrievals towards higher resolution a priori data, as evidenced by the increase to $1.25^\circ \times 1.0^\circ$ NO_2 profiles in the NASA SP v3. Future versions of the SP v3 retrieval are planned that use 0.25° profiles (Lamsal, 2018).

Appendix B

Supplemental material for "Effects of daily meteorology on the interpretation of space-based remote sensing of NO_2"

The chapter was adapted from the supplement of: J. L. Laughner, A. Zare, and R. C. Cohen (2016). "Effects of daily meteorology on the interpretation of space-based remote sensing of NO_2". *Atmos. Chem. Phys.* 16.23, pp. 15247–15264. DOI: 10.5194/acp-16-15247-2016

B.1 Choice of weights for the monthly average profiles

When computing the monthly average profiles, it is necessary to use profiles that represent OMI's overpass time, typically quoted as 13:30 to 13:45 local standard time (e.g. McLinden et al. 2014; Levelt et al. 2006). To average the profiles output from WRF-Chem, weights were calculated that fulfilled two requirements:

1. The weights should be 1 at OMI overpass time and 0 when more than 1 hour away from overpass time.
2. The transition between profiles from different hours should be smooth.

For #1, we assume that the average overpass time is 1330 local standard time. We compute local standard time as:

$$t_{\text{apriori, local}} = \frac{l}{15} + t_{\text{apriori, utc}} \tag{B.1}$$

where $t_{\text{apriori, local}}$ is the local standard time in hours past midnight, $t_{\text{apriori, utc}}$ the UTC time in hours past midnight, and l the longitude (west is negative). To meet the second requirement, this is a continuous function, rather than a step function (where each 15° longitudinal segment/time zone has a single local time). Areas further west in a time zone are more likely to be observed on the east edge of a later OMI swath, and vice versa for areas further east. This weighting includes some influence from later profiles to account for this.

The weights from Eq. (2.5) are derived from:

$$w = 1 - |t_{\text{overpass}} - t_{\text{apriori, local}}| = 1 - \left|13.5 - \frac{l}{15} - h\right| \tag{B.2}$$

where t_{overpass} is the assumed overpass time for OMI and $h \equiv t_{\text{apriori, utc}}$. If $w < 0$, w is set to 0. This gives us the desired form where the weights smoothly vary in time.

B.2 Influence of boundary layer vs. free troposphere

Figure B.2 illustrates the possible effects on the AMF of day-to-day changes in the a priori upper troposphere NO_2 profile. From Sect. 2.2, Eq. (2.2) and Eq. (2.3) show that it is the relative contribution of each altitude to the a priori profile that determines the AMF. Therefore, if an increase in near-surface NO_2 is balanced by an increase in upper tropospheric NO_2, there may be no or very little net change to the AMF. This is the case to the left of the city in Fig. B.2. However, the reverse can also occur, where changes in the upper tropospheric a priori profile accentuate the effect of changes near the surface. This occurs to the right of the city in Fig. B.2.

Here we consider the magnitude of the effect day-to-day changes in the free tropospheric NO_2 profile have on the retrieval. Figure B.3 compares the difference in pseudo-retrieval AMFs among the three a priori types used: the daily profiles over the full extent of the troposphere, "hybrid" daily profiles which include day-to-day variation in boundary layer but use a monthly average above 750 hPa, and the monthly average profiles. These statistics are derived over the entire pseudo-retrieval domain for the entire time period. Comparing either the full or hybrid daily profile to the monthly average profile yields very similar statistics. Both exhibit a positive median change (+1.7% full, +2.0% hybrid) and show similar upper and lower quartiles. When using the full daily profile, the range of the most

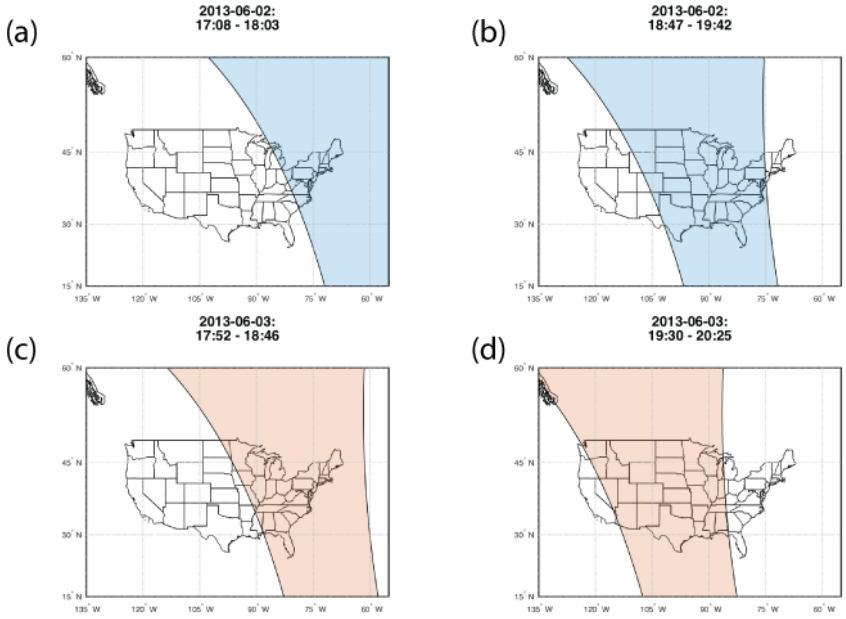

Figure B.1: Swaths covering the east coast of the US for 2 June 2013 (a,b) and 3 June 2013 (c,d). The times given are the start and end times of the daytime half of the orbit in UTC. As shown, on different days, the time of the OMI swath that covers Atlanta can vary by up to an hour.

extreme values is slightly greater, occurring when the changes in the boundary layer and free troposphere act in the same direction on the AMF.

The third column shows the difference between the hybrid and full daily profile AMFs. The mean and median differences are nearly 0 (-0.4% and -0.2% respectively), with upper and lower quartile values of $+2.20\%$ and -2.88%. This is $\sim 35\%$ of the interquartile range of the difference between AMFs resulting from either the full or hybrid daily profiles and the monthly average profile. Day-to-day changes in the free tropospheric a priori profile are smaller in magnitude than those in the boundary layer, but usually occur over a much greater vertical extent. Further, the scattering weights are greater at these altitudes ($\sim$2–8 times those near the surface), amplifying the effect of small changes in the profile shape at these altitudes. This explains why the effect on the AMF is as large as it is, although day-to-day changes in the boundary layer still dominate the effect using daily profiles has on the AMFs. It should be noted that these a priori are derived from a model without lightning NO emission; therefore this should be considered a lower bound for the effect of the free tropospheric profile. The presence of lightning NO_x would likely lead to larger increases in AMF due to the higher upper tropospheric sensitivity.

The implications of this response are varied. For applications (such as data assimilation)

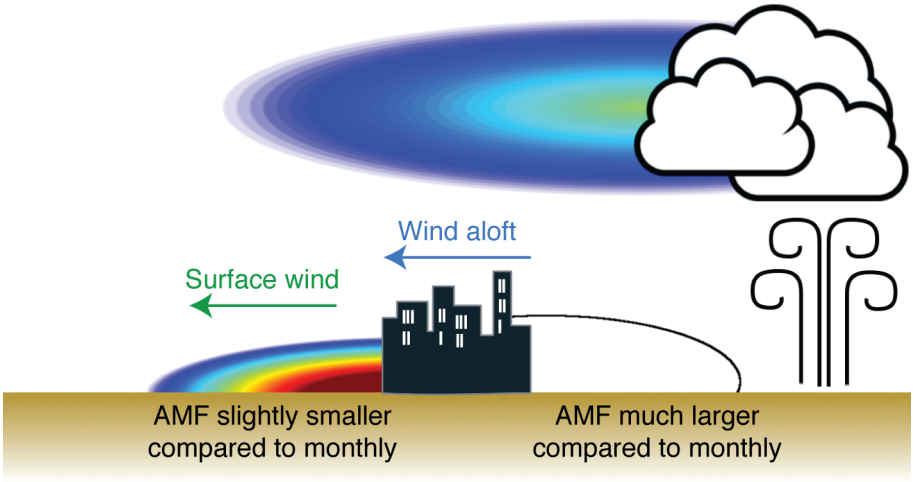

Figure B.2: An illustration of how day-to-day variations in the upper troposphere impact the calculation of the AMF. The colored gradients represent the day-to-day NO_2 plumes, the black outline represents the monthly average plume. To the left of the city, the increase in near-surface NO_2 compared to the monthly average would result in a much smaller AMF; however the addition of NO_2 in the upper troposphere balances this, keeping the difference in AMF smaller. To the right, both the lack of near-surface NO_2 and the introduction of NO_2 in the upper troposphere result in a much greater AMF than the monthly average.

where reducing the uncertainty in a single day's observations is critical, this result indicates that accurate modeling of upper tropospheric NO_2 is important. However, over the 91 days of this study, the effect of including a daily free tropospheric a priori profile averages out to nearly 0. Winds in the free troposphere are not correlated with surface winds (Endlick et al., 1969). In methods sorting observations by wind speed or direction (Valin et al., 2013; Lu et al., 2015), day-to-day variations in the AMF due to changes in the free troposphere will therefore be random in character. Over long periods of averaging, the impact due to these variations will have no net impact. Only changes associated with the surface winds will lead to systematic changes in the results obtained by these methods.

B.3 EMG fitting algorithm details

The EMG fitting was carried out by minimizing the residuals between the EMG function and the line densities using the Matlab function `fmincon`, which allows constrained non-linear fitting using an interior-point algorithm. Additionally, the following three refinements were necessary.

- The constraints listed in Table B.1 must be imposed to ensure physically realistic values

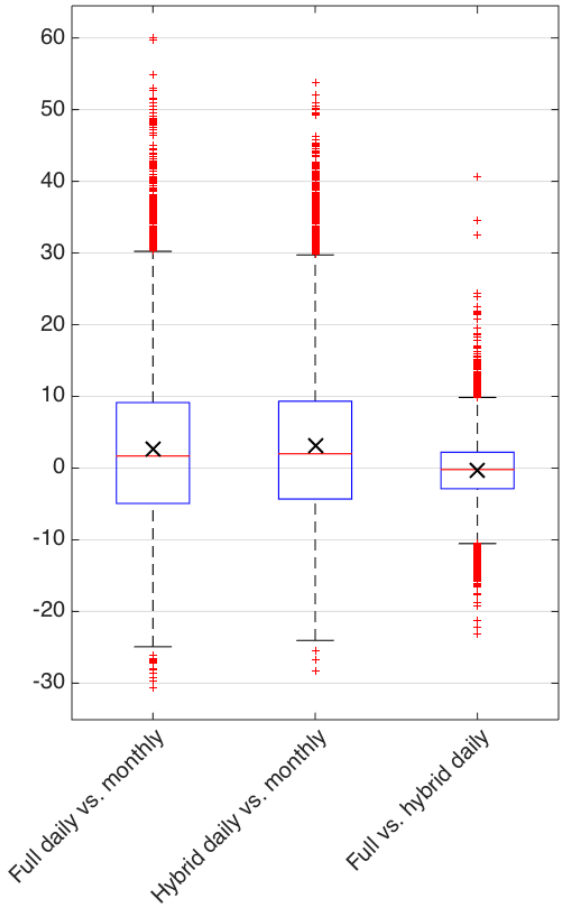

Figure B.3: Percent changes in the AMF for the pseudo-retrieval over the full time period (1 June to 30 Aug) among the three a priori used in the pseudo-retrieval. For "new vs. base," the percent change is calculated as (new − base)/base × 100%. The red line is the median, the box edges are the 25th and 75th percentiles, the whiskers cover the remainder of the data not considered outliers, and the red pluses are outliers. A point is considered an outlier if it is more than 1.5 times the interquartile range from the closer quartile. The black X marks the average.

of a, x_0, μ_x, σ_x, and B are obtained.

- Any not-a-number (NaN) values in the EMG function (Eq. 2.8) are replaced with infinity, thus making the fitting function (Eq. 2.9) report that the current values of a, x_0, μ_x, σ_x, and B are unacceptable. NaNs occur in the EMG function when the exponential goes to infinity and the error function to zero, typically when the fitting parameters are unrealistically large or small and the fit is incorrectly a flat line. By doing this replacement and treating NaNs as 0 in the summation in Eq. (2.9), we allow NaNs to occur in the line densities (representing missing data, which is thus ignored) but not the fit.

- The minimization algorithm requires an initial value for a, x_0, μ_x, σ_x, and B. For the first minimization, best-guess values for these are computed as specified in Table B.1 (see supplement for rationale for each). However, an interior-point minimization algorithm uses a line search strategy which minimizes a function by following the derivative at the current point "downhill" (Robere, 2012; Wright, 2005). If the algorithm begins in a region from which the downhill path leads to a local, rather than global, minimum, the global minimum may never be found by this algorithm. This can be alleviated by carrying out multiple minimizations, starting from a different point each time, and choosing the result with the smallest residual. The randomization draws from the range of values defined by the upper and lower limits for each parameter with a uniform probability distribution. For a and x_0, upper bounds of 5×10^6 mol and 1000 km, respectively, are used during the randomization process, as a finite upper bound is necessary for the randomization algorithm. This randomization and reoptimization was carried out nine times per fit. Additional randomization of the initial point does not improve the fit. Each time the optimum value of the fitting function is compared to the previous minimum; if it is less, the new fit is accepted.

The constraints listed in Table B.1 were found to be necessary to ensure that a physically realistic fit was obtained. The following upper and lower limits for each of the parameters were imposed:

- $a \in [0, \infty)$: a corresponds to the total NO_2 burden and therefore must be a positive value.

- $x_0 \in [1.6, \infty)$: x_0 is the distance traveled by the plume in one lifetime. Therefore it must be positive; however, if it becomes too small, the fit fails (returning a flat line). At very slow wind speeds of 1 m s^{-1}, a short lifetime of 1 h would translate to an x_0 of 3.6 km, we choose a minimum value for x_0 shorter than this to allow for the possibility of very short lifetimes. 1.6 km was specifically chosen as one-third the distance between adjacent data points in the line densities on the oversampled $0.05^\circ \times 0.05^\circ$ ($\approx 5 \times 5$ km) grid. This means that three lifetimes would pass and $> 95\%$ of the NO_x enhancement

Parameter	Physical significance	Lower Bound	Upper Bound	Best guess initial value
a (mol)	NO_2 burden	0	∞	$\int_{x_{\min}}^{x_{\max}} NO_2(x)\, dx$
x_0 (km)	Distance traveled in 1 lifetime	1.6	∞	54
μ_x (km)	Emission center	$\min(x)$	$\max(x)$	$x_{\max(NO2)}$
σ_x (km)	Gaussian smoothing	2.5	$x_{\max(NO2)} - \min(x)$	FWHM / 2.355
B (mol)	Background	0	$\max(NO_2)$	$\min(NO_2)$
Additional constraints				
$\mu_x + x_0 \leq \max(x)$				
$\exp\left(\frac{\mu_x}{x_0} + \frac{\sigma_x^2}{2x_0^2} - \frac{x}{x_0}\right) \leq 20$				

Table B.1: Constraints imposed on the solutions permitted to the interior point algorithm, in the form of upper and lower bounds, with additional linear and nonlinear constraints. x refers to the x-coordinates associated with the data, i.e. distance from the city center. $x_{\max(NO2)}$ indicates the x coordinate where the greatest NO_2 line density is present. NO_2 refers to the values of the line density. FWHM is the full width at half maximum of the Gaussian. For additional discussion of the reasoning for the selection of these values, see the supplement.

due to a source would be removed; shorter lifetimes than this are unlikely to be resolved at this grid resolution.

- $\mu_x \in [\min(x), \max(x)]$: μ_x is the apparent position of the emission center relative to the geographic city center. It must be within the domain of distances chosen, otherwise the domain was chosen poorly.

- $\sigma_x \in [2.5, x_{\max NO_2} - \min(x)]$: σ_x is the Gaussian smoothing parameter, serving the same role as the σ parameter in any Gaussian function. 2.5 km was chosen as the lower bound under the assumption that the smallest observable Gaussian requires at least 3 data points (the base on either side and the maximum). As 4σ = full width at base this implies that the smallest observable signal is $\frac{1}{2}$ the oversampled grid resolution: if only 3 points defined the Gaussian, one-half the full width at the base ($= 2\sigma$) would fit within one grid cell. The upper limit simply specifies that σ_x cannot be larger than the distance from the upwind edge of the domain to the x-coordinate of maximum line density, i.e. that the Gaussian build-up on the upwind side is fully captured in the domain.

- $B \in [0, \max(NO_2)]$: B is the background line density. It must be positive, and should not be larger than the maximum observed line density.

Two additional constraints were imposed using the ability of `fmincon` to accept linear and nonlinear relationships between the fitting parameters:

- $x_0 + \mu_x \leq \max(x)$: Simply, one lifetime must pass between the apparent emissions center and the downwind edge of the domain. If not, the domain was chosen poorly.
- $\exp\left(\frac{\mu_x}{x_0} + \frac{\sigma_x^2}{2x_0^2} - \frac{x}{x_0}\right) \leq 20$: This is a second numerical constraint to prevent the case where the exponential goes to infinity and the error function complement goes to 0, thus creating a return value of NaN from the fitting function. (The first numerical constraint is the replacement of NaNs with infinity discussed in the main text.)

For the best-guess initial values:

- $a = \int_{x_{\min}}^{x_{\max}} \mathrm{NO_2}(x)\, dx$: Since a corresponds to the total burden of $\mathrm{NO_2}$ present, we use the integral over the domain as the initial guess.
- $x_0 = 54$: A best guess of 54 km follows from an average summer lifetime of 3 h (Lu et al., 2015) and a wind speed of 5 m $\mathrm{s^{-1}}$.
- $\mu_x = x_{\max(\mathrm{NO2})}$: Logically, one would expect the apparent emission source to be somewhat near the maximum concentration, the fitting procedure can then identify if it is slightly displaced.
- $\sigma_x = \mathrm{FWHM}/2.355$: This uses the relationship between the full width at half max and the standard deviation of a Gaussian. The half maximum line density is computed as:

$$\mathrm{HM} = \frac{\max(\mathrm{NO_2}) - \mathrm{NO_2}(x_{\min})}{2} \tag{B.3}$$

  The FWHM is then:

$$\mathrm{FWHM} = |x_{\mathrm{HM}} - x_{\max(\mathrm{NO2})}| \tag{B.4}$$

  where x_{HM} is the x-coordinate where the half-max exists, found by interpolating to the half maximum line density.
- $B = \min(\mathrm{NO_2})$: It is a natural guess that the background is simply the lowest observed line density.

B.4 Computation of uncertainty in EMG parameters (a, x_0, μ_x, σ_x, B, E, and τ)

To compute the uncertainty in both the fitting parameters and the values of E and τ derived from them, we base our calculation off those in Beirle et al. (2011) and Lu et al. (2015). Lu

Source	Uncertainty	Citation
VCD	25%	Lu et al. (2015)
Across wind integration dist.	10%	Beirle et al. (2011)
Choice of wind fields	10%	Beirle et al. (2011)
Fitting uncertainty	Computed	Sect. B.5
NO_x:NO_2 ratio	10%	Beirle et al. (2011)

Table B.2: Values of uncertainty for the various steps of the EMG fitting process.

et al. (2015) use the values in Table B.2. The value of 25% for the uncertainty in the VCDs used in Lu et al. (2015) is below the lower bound of uncertainty given in Boersma et al. (2004), likely reflecting improvements such as the temperature correction of the NO_2 cross section used in determining the scattering weights.

Our computation of uncertainty differs from Lu et al. (2015) in that we include the uncertainty for the VCDs in the calculation of uncertainty for τ. As shown in this paper, the choice of a priori profiles can introduce a spatial bias into the exponential decay related to effective lifetime, therefore the inclusion of the VCD uncertainty in the lifetime uncertainty is logical.

To compute the uncertainty due to the fitting process itself, we first need the standard deviations of the fitting parameters. We begin by computing the variance-covariance matrix as (Bard, 1974; Dovì et al., 1991):

$$Cov([a, x_0, \mu_x, \sigma_x, B]) \approx \text{diag}(s^2\ \mathbf{H}^{-1});\ \text{where} \tag{B.5}$$

$$s^2 = \frac{1}{n_{\text{fit}} - 5} \sum_x \left[\text{NO}_2(x) - F(x|a, x_0, \mu_x, \sigma_x, B)\right]^2 \tag{B.6}$$

that is, the variance-covariance matrix of the fitting parameters is approximately equal to the inverse Hessian matrix for the fitting function (Eq. 2.9) evaluated at the optimum values of the fitting parameters and scaled by s^2, the sum of squared residuals for the optimum fit divided by the number of degrees of freedom. The variance for each parameter is, as usual, the corresponding element on the diagonal of the variance-covariance matrix.

In Eq. B.5, we use the Hessian matrix returned by the unconstrained Matlab minimization function `fminunc`. The documentation for `fmincon` states that the Hessian matrix returned can be inaccurate; therefore we pass the fitting function (Eq. 2.9) to `fminunc` and initialize

it at the optimum values of the fitting parameters. `fminunc` is set to only evaluate the fitting function once; this returns the unconstrained Hessian at the constrained optimum found by `fmincon`.

As in Beirle et al. (2011), we represent the uncertainty in the fitting parameters due to the fitting process as 95% confidence intervals. We compute these for each individual parameter with:

$$c_{95} = \frac{t\sigma}{\sqrt{n_{\text{fit}}}} \tag{B.7}$$

where t is Student's t-value and is computed in Matlab as `tinv(0.975, n_fit - 5)`. (0.975 is used as the p value because `tinv` returns one-tailed t values, so 0.975 returns the 0.95 two-tailed value.) n_{fit} is the number of points used to obtain the fit, and $n_{\text{fit}} - 5$ degrees of freedom are used for determinine the value of t because 5 degrees of freedom have been fixed in the fitting process, one each for the five parameters fit. The standard deviation, σ, is taken as the square root of the corresponding diagonal element of the variance-covariance matrix from Eq. (B.5). This treatment assumes that each of the fitting parameters is independent. Both the covariance matrix and an analysis of the change in optimum values for four of the parameters if one is fixed shows that the parameters are not fully independent, but using individual confidence intervals for each parameter lends itself to a more intuitive understanding of the uncertainty than would attempting to derive a five-dimensional confidence region for the five fitting parameters.

To combine this uncertainty with the other sources identified in Beirle et al. (2011) (VCD, across wind distance, and wind field), the uncertainties are then simply added in quadrature:

$$u_p = p \cdot \sqrt{\left(\frac{c_{95,p}}{p}\right)^2 + (\%u_{\text{VCD}})^2 + (\%u_b)^2 + (\%u_{\text{wf}})^2} \tag{B.8}$$

where p is the value of the fitting parameter, u_p the total uncertainty for the parameter, $c_{95,p}$ the confidence interval for that parameter, and $\%u_{\text{VCD}}$, $\%u_b$, and $\%u_{\text{wf}}$ are the percent uncertainties in VCDs, across wind integration direction, and choice of wind fields given in Table B.2 as decimal values (i.e. $\%u_b = 0.1$).

The uncertainty for lifetime (τ) and emissions (E) are then propagated from the fitting parameter uncertainties. For lifetime:

$$\tau = \frac{x_0}{w} \tag{B.9}$$

$$u_\tau^2 = \left(\frac{\partial \tau}{\partial x_0} u_{x_0}\right)^2 + \left(\frac{\partial \tau}{\partial w} u_w\right)^2$$
$$= \left(\frac{1}{w} u_{x_0}\right)^2 + \left(\frac{-x_0}{w^2} u_w\right)^2 \tag{B.10}$$

where w is the average wind speed. We compute u_w as the 95% confidence interval of the distribution of winds that fall within the bin used; that is, if we consider all days with wind speed > 3 m s^{-1}, then this is the 95% confidence interval of the distribution of wind speeds > 3 m s^{-1}. This helps account for the uncertainty in lifetime introduced because different wind speeds lead to different NO_x lifetimes (Valin et al., 2013).

For emissions:

$$E = \frac{raw}{x_0} = \frac{ra}{\tau} \tag{B.11}$$

$$u_E^2 = \left(\frac{\partial E}{\partial r} u_r\right)^2 + \left(\frac{\partial E}{\partial a} u_a\right)^2 + \left(\frac{\partial E}{\partial \tau} u_\tau\right)^2$$
$$= \left(\frac{a}{\tau} u_r\right)^2 + \left(\frac{r}{\tau} u_a\right)^2 + \left(\frac{-ra}{\tau^2} u_\tau\right)^2 \tag{B.12}$$

where r is the NO_x:NO_2 ratio of 1.32 from (Beirle et al., 2011).

B.5 Validation of EMG fitting

To determine if the EMG fitting process is returning good fits to the data, we consider several criteria. First, we examine each fit to the data; all the best fits reproduce the shape of the data very well. Second, we consider the R value of the fits. Beirle et al. (2011) required an $R > 0.9$ for a fit to be considered acceptable. Out of 30 fits with an across-wind distance of 1° (2 wind bins for Atlanta and 3 for Birmingham times 3 a priori), only 2 had $R < 0.9$, and even then were > 0.89. The algorithm is finding good fits in nearly every case.

We also consider whether the `fmincon` algorithm is finding the global minimum of the fitting function or becoming trapped in a local minimum. As described in Sect. 2.2, we carry out 9 optimizations from random starting points, in addition to that from the best guess initial values, to sample different parts of the parameter space. We tested increasing the number of

random starting points to 99 and found no change in the optimal fitting parameter values. In a separate experiment, we found only one case in which a local minimum, rather than the global minimum, was returned, but repeated fitting with 9 random start point optimizations returned the global minimum. Therefore we find that optimizing from 9 random starting points plus one best guess is a good balance between accuracy and computational efficiency.

B.6 Model lifetime calculation

To compare the EMG derived NO_x lifetime against that from the WRF-Chem model, two loss processes were considered:

$$NO_2 + OH \longrightarrow HNO_3 \quad \text{(R B.1)}$$

$$NO + RO_2 \longrightarrow \alpha\, RONO_2 \quad \text{(R B.2)}$$

where α is the $RONO_2$ branching ratio. This leads to a total lifetime:

$$\tau_{\text{total}} = \left(\frac{1}{\tau_{HNO_3}} + \frac{1}{\tau_{RONO_2}} \right)^{-1} \quad \text{(B.13)}$$

The lifetime with respect to HNO_3 is simply:

$$\tau_{HNO_3} = \frac{1}{k_1[OH]} \quad \text{(B.14)}$$

while the lifetime with respect to $RONO_2$ is:

$$\tau_{RONO_2} = \left(\sum_i \alpha_i k_{2,i} [RO_2]_i \right)^{-1} \quad \text{(B.15)}$$

The concentrations of the RO_2 species are not stored in the model output, so we assume steady state (Murphy et al., 2006):

$$\frac{d[RO_2]}{dt} = 0 = -k_2[RO_2][NO] + \sum_i k_{RH_i+OH}[RH]_i[OH] \quad \text{(B.16)}$$

$$\Rightarrow [RO_2]_{SS,i} = \left(\sum_i k_{RH_i+OH}[RH]_i[OH] \right) / \left(k_2[NO] \right) \quad \text{(B.17)}$$

The overall lifetime is then:

$$\tau_{\text{total}} = \left(k_1[OH] + \sum_i \alpha_i k_{2,i} [RO_2]_{SS,i} \right)^{-1} \quad \text{(B.18)}$$

Appendix C

Supplemental material for "Quantification of the effect of modeled lightning NO_2 on UV-visible air mass factors"

The chapter was adapted from the supplement of: J. L. Laughner and R. C. Cohen (2017). "Quantification of the effect of modeled lightning NO_2 on UV–visible air mass factors". *Atmos. Meas. Tech.* 10.11, pp. 4403–4419. DOI: 10.5194/amt-10-4403-2017

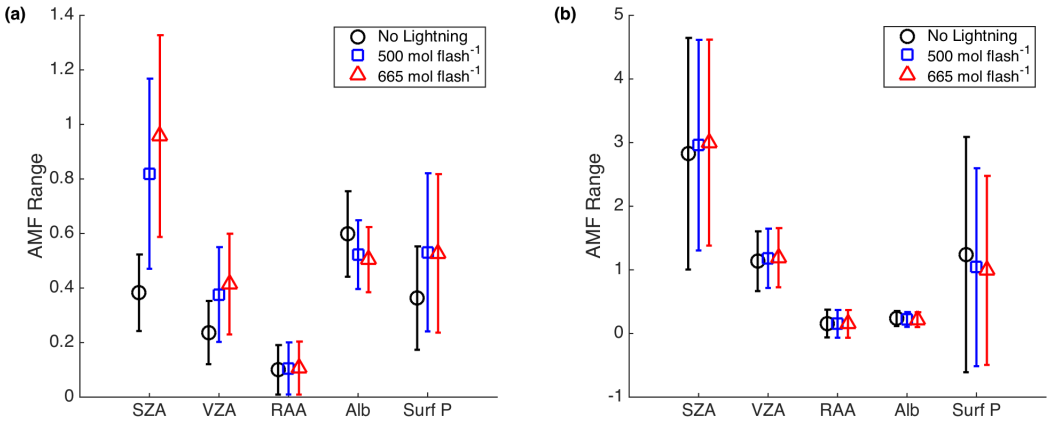

Figure C.1: The sensitivity of the AMF to different input parameters to the TOMRAD lookup table for conditions relevant to clear sky pixels (a) and cloudy pixels (b) using the WRF-Chem profile averaged over the entire domain. The marker (circle, square, or triangle) represents the average range of the AMF (max − min) due to varying a given parameter while holding the other four constant; the error bars represent the 1σ variability in that range for all combinations of the other four parameters.

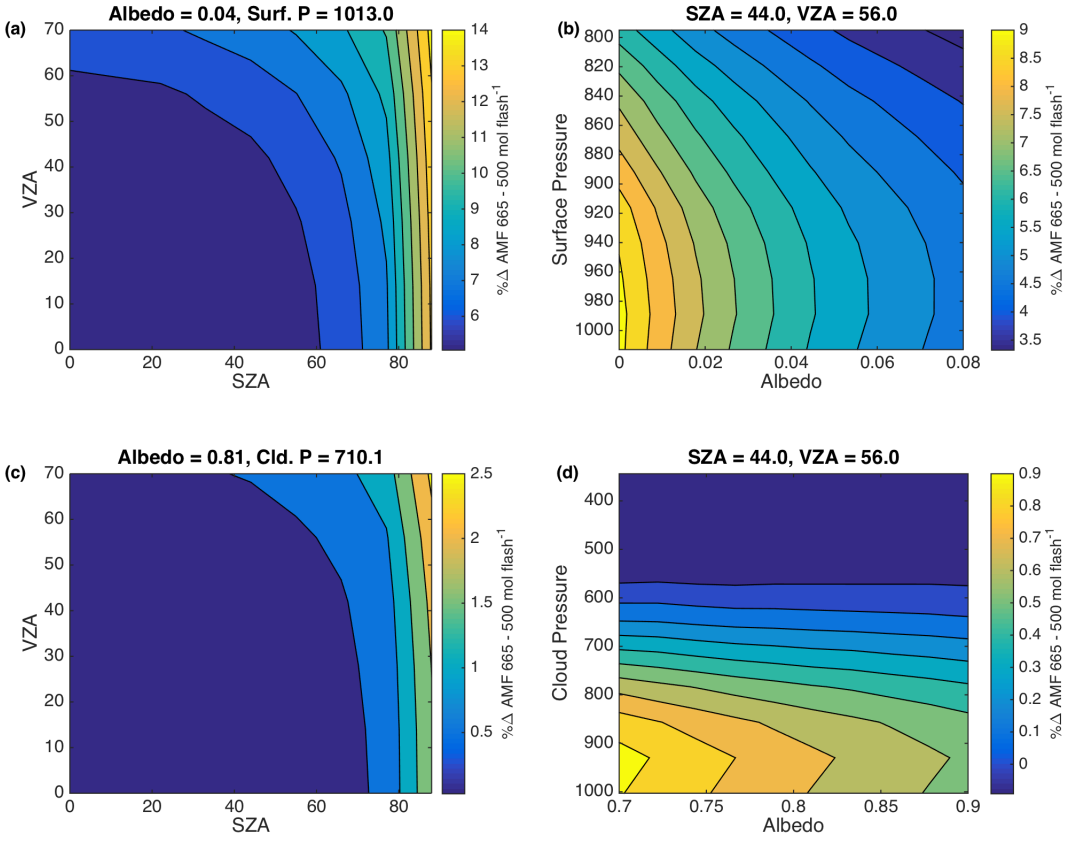

Figure C.2: As in Fig. 3.2, but now the percent difference in AMF between using profiles generated with 665 and 500 mol NO flash^{-1}.

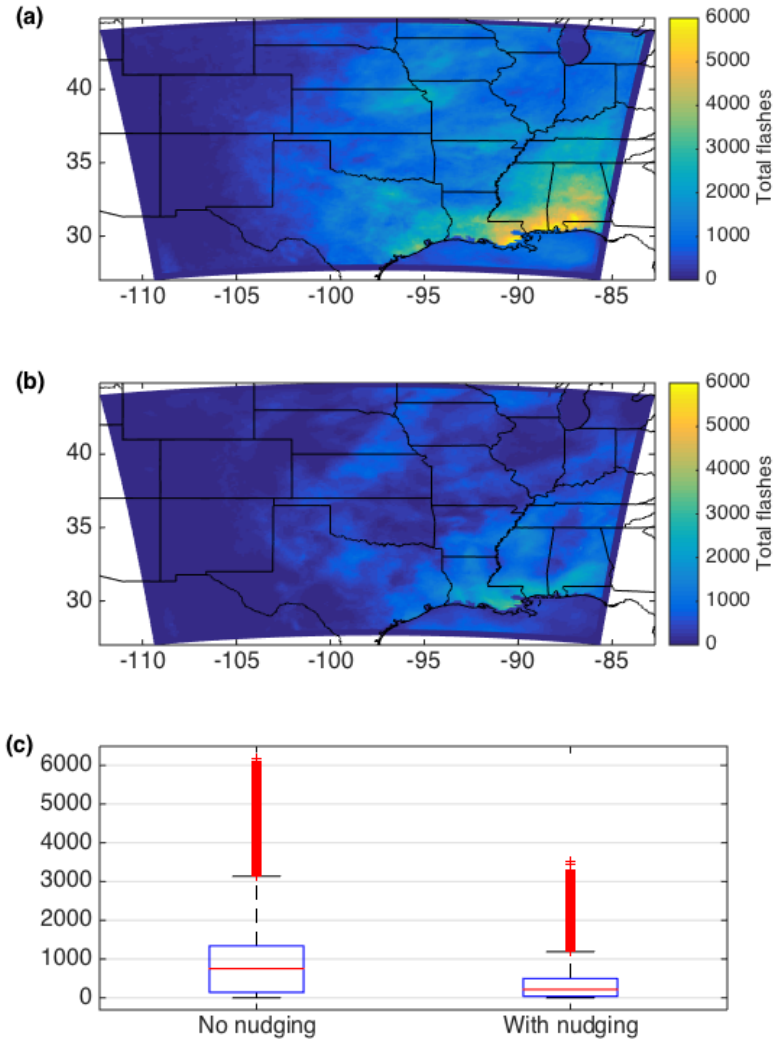

Figure C.3: The effect of FDDA nudging on number of lightning flashes. (a) Total number of modeled lightning flashes during the entire modeled time period (13 May to 24 June 2012) without nudging. (b) Same as (a), but for the model run with nudging. (c) Box plot of the statistics for total number of modeled flashes across the domain. The central mark is the median, the box edges the upper and lower quartiles, the ends of the whiskers are the greatest and least non-outlier value, and the individual marks are outliers.

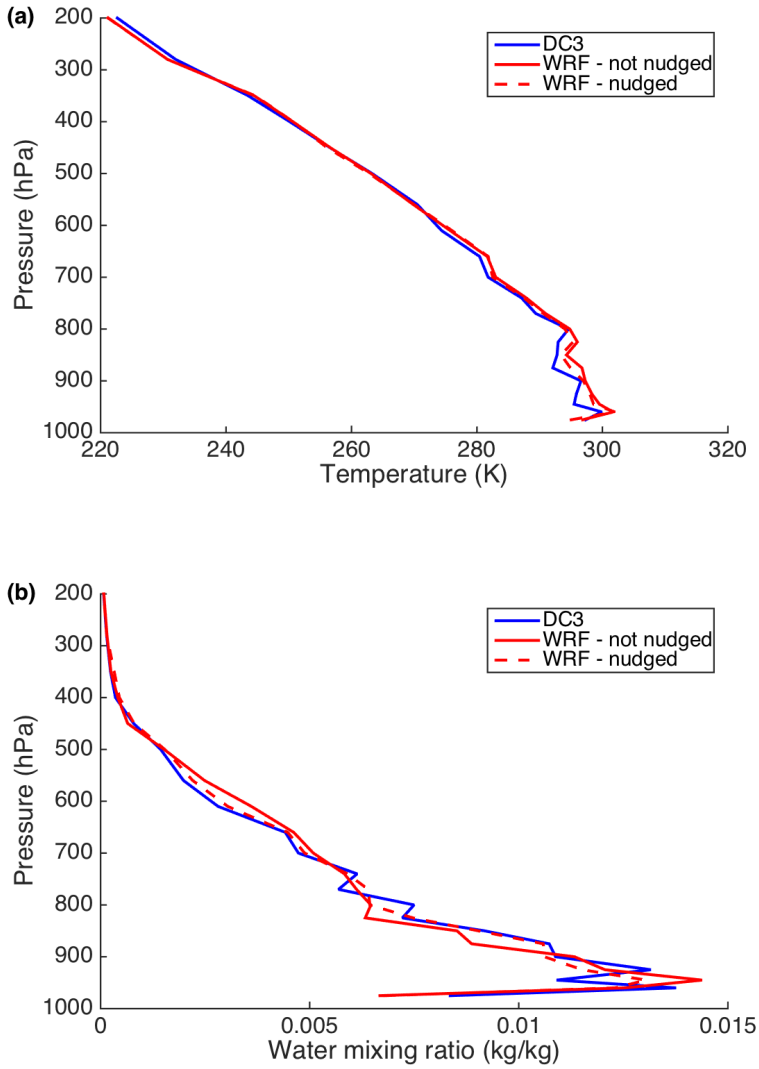

Figure C.4: (a) Temperature and (b) water vapor profiles averaged over the DC3 campaign (blue) or WRF data matched to the DC3 flight path as described in Sect. 3.2 (red). WRF data resulting from the unnudged run is the solid line, data from the nudged run is the dashed line. Note that both the nudged and unnudged runs' temperature profiles agree with the DC3 profile similarly well, while the nudged water vapor profile exhibits better agreement with the DC3 profile than the unnudged one.

Appendix D

Supplemental material to "The Berkeley High Resolution Product"

The chapter was adapted from the supplement of: J. L. Laughner, Q. Zhu, and R. C. Cohen (2018b). "The Berkeley High Resolution Tropospheric NO_2 Product". *Earth Syst. Sci. Data Discuss.* 2018, pp. 1–33. DOI: 10.5194/essd-2018-66

D.1 Published Format

File structure

BEHR data is published as HDF version 5 files. Each file contains a single, top-level group "Data", which in turn contains each orbit as a child group named "SwathX" where X is the orbit number. The datasets for each orbit are contained in the "SwathX" groups.

Separate HDF files contain data at the native OMI pixel resolution and regridded to $0.05° \times 0.05°$ resolution. The regridded files only contain a subset of the variables stored in the native pixel files. The regridded files contain each orbit gridded separately; each orbit's grid covers the entire domain retrieved. Grid cells outside each orbit's observed swath contain fill values. Users can identify whether a file contains gridded information by the dataset level attribute "gridding_method", if present, the file is a gridded file; if absent, the file is a native pixel file. Additionally, the "Description" attribute contained in each swath indicates whether the data is at native or regridded resolution.

Retrievals using daily vs. monthly NO_2 a priori profiles are available separately. Retrievals using monthly profiles will be updated as new OMI and MODIS data becomes available. Retrievals using daily profiles are limited by the need to model said profiles; these will become available as modeled NO_2 profiles are simulated.

BEHR files are named with the format "OMI_BEHR-**profile_region_version_yyyymmdd**.hdf", where:

- **profile** will be DAILY or MONTHLY, indicating whether daily or monthly NO_2 a priori profiles were used
- **region** region retrieved, currently, US = continental United States.
- **version** is the version string (Sect. D.1).
- **yyyymmdd** is the date of the observation

This information is also contained as swath level attributes "BEHRProfileMode", "BEHRRegion", "Version", and "Date", respectively.

Quality flagging

BEHR data contains a 32-bit unsigned integer quality flag field that summarizes quality errors and warnings from both the NASA processing and BEHR processing. Each bit in the integer value represents a specific error or warning flagged during processing. The bits are divided into three categories; the bit number is the position of the bit (1-based) starting from the least significant bit.

- **Bits 1 & 2: summary bits.** These summarize the other 30 bits. Users interested in simple filtering can focus only on these.
- **Bits 3–16: error bits.** These are set to 1 for significant errors in the retrieval that preclude the use of the corresponding NO_2 data in any capacity.
- **Bits 17–32: warning bits.** These are set to 1 as non-fatal warnings about the processing of the corresponding data. These do not automatically preclude the use of the corresponding data, but rather provide warnings of potentially lower-quality data or information about decisions made during the retrieval. The flags for low quality BRDF data (Sect. 4.2) fall into this category.

The meaning of each used bit is given in the "FlagMeanings" attribute of the BEHRQualityFlags dataset; here, we will only discuss the two summary bits.

Bit 2 is the error summary bit; it is set to 1 if any error bit is set. Therefore, NO_2 columns from any pixel with this bit set should not be used. In v3.0B, this is set if the NASA

VcdQualityFlags or XTrackQualityFlags fields indicate the pixel should not be used, or if the BEHR AMF is invalid (usually because a WRF profile is not available for that pixel).

Bit 1 is the quality summary bit; in v3.0B, it is set to 1 if bit 2 is set, the MODIS BRDF coefficients are low quality, or the OMI geometric cloud fraction exceeds 20%. Therefore, the NO_2 data can be restricted to high quality, total tropospheric column data by using only pixels where this bit is not set.

These quality flags focus on the quality of the NO_2 retrieval; therefore ancillary data (such as the MODIS surface reflectance or MODIS clouds) is not necessarily unusable for pixels flagged with a retrieval error.

In the gridded product, the quality flags field is a bitwise OR of all contributing pixels' quality flags. Therefore, any error or warning in a pixel that contributes to a grid cell is propagated to the grid cell.

Versioning

BEHR versions follow the format "vX-XYrevZ", e.g. v3-0Arev0. The "X-X" indicates the version of the NASA Standard Product that was ingested as the basis for that BEHR retrieval. "Y" is a sequential letter (A, B, C, etc.) indicating the major version of BEHR produced from the same NASA SP base; i.e., v3-0A indicates the first major BEHR version based on the NASA SPv3. "revZ" (short for "revision") indicates a small update to the BEHR product. Revisions are reserved for small changes that are not expected to significantly affect scientific results obtained from the data; e.g. updates to file format or attributes, or very uncommon error corrections. A revision of 0 may be omitted from the version string, i.e. "v3-0A" and "v3-0Arev0" are the same version.

Traceability

To ensure traceability, files ingested during processing from other satellite products or models are recorded in the swath level attributes "OMNO2File" (NASA NO_2 SP data), "OMPIXCORFile" (pixel corner data), "MODISCloudFiles" (MYD06 files that MODIS cloud data is taken from), "MODISAlbedoFile" (MCD43Dxx files that BRDF parameters are taken from), and "BEHRWRFFile" (WRF-Chem output files the NO_2 profiles are taken from; are post-processed for monthly average profiles).

The BEHR code is available on GitHub at `https://github.com/CohenBerkeleyLab/BEHR-core` (Laughner and Zhu, 2018a). Each release will be tagged with the same version string as the data. Additionally, eleven swath level attributes contain the Git SHA-1 hash of the most recent commit of the core BEHR code and additional dependencies at the time each of the three major steps in processing BEHR data. These attribute names have the form "GitHead_**repo_step**", where **repo** will be one of:

- **Core**: the core BEHR repository (`https://github.com/CohenBerkeleyLab/BEHR-core`)
- **BEHRUtils**: the repository of BEHR satellite utility functions (`https://github.com/CohenBerkeleyLab/BEHR-core-utils`)
- **GenUtils**: the repositiory of general Matlab utilities (`https://github.com/CohenBerkeleyLab/Matlab-Gen-Utils`)
- **PSM**: the repository containing the modified "omi" python package used for gridding (`https://github.com/CohenBerkeleyLab/BEHR-PSM-Gridding`)
- **MatPyInt**: the Matlab-Python type conversion interface (`https://github.com/CohenBerkeleyLab/MatlabPythonInterface`)
- **WRFUtils**: the repository containing Matlab utilities for working with WRF data.

and **step** will be one of:

- **Read**: step in which OMI, MODIS, and GLOBE data are ingested into Matlab and (where necessary) averaged to OMI pixels.
- **Main**: step in which scattering weights and NO_2 profiles are matched to OMI pixels, the BEHR AMFs and VCDs are calculated, and the data is gridded.
- **Pub**: step in which the BEHR Matlab files are converted to HDF files.

D.2 WRF-Chem Model

For years 2005–2006, the chemical initial and boundary conditions for WRF-Chem are taken from the GEOS-Chem v9-02 model with the following changes to the chemistry:

- The rate of the reaction $NO_2 + OH \longrightarrow HNO_3$ is changed from that recommended in Sander et al. (2011) to that in Henderson et al. (2012).
- The rates of the formation and dissociation of HNO_4 are changed from that recommended in Sander et al. (2011) to that in Bacak et al. (2011).
- The rate of hydrolysis of N_2O_5 to HNO_3 was reduced to 10% of the value from Evans and Jacob (2005), as recommended in Brown et al. (2009).

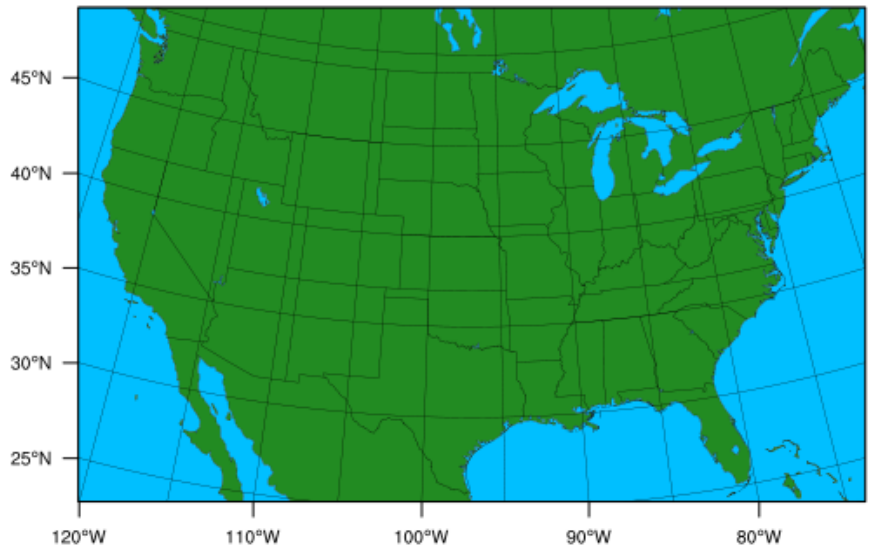

Figure D.1: The WRF-Chem model domain.

- The number of moles of NO emitted per lightning flash was increased by 33% to 665 mol NO flash^{-1} (midlatitudes) and 346 mol NO flash^{-1} (tropics) based on the findings of Nault et al. (2017)

To provide output for WRF-Chem boundary conditions from 2005–2006, the GEOS-Chem model is spun up for the calendar year 2004.

D.3 Difference in average VCDs due to profile temporal resolution

The difference in the NO_2 VCDs when using daily vs. monthly profiles must ultimately be due to differences in the AMFs. Consider an average AMF for a given location defined by:

$$\overline{A} = \frac{1}{n}\sum_{i=1}^{n}\frac{\int_{p_{s_i}}^{p_t} w_i(p)g_i(p)\,dp}{\int_{p_{s_i}}^{p_t} g_i(p)\,dp} \tag{D.1}$$

For a given location, the surface pressure and (over the course of a month) surface reflectivity will be fairly constant, and additionally let us assume that the sun-satellite geometry will average in such a way that the scattering weights, w_i can be taken as an average, $\overline{w}$. With this assumption and assuming that $p_{s_i} = p_s$ for all i:

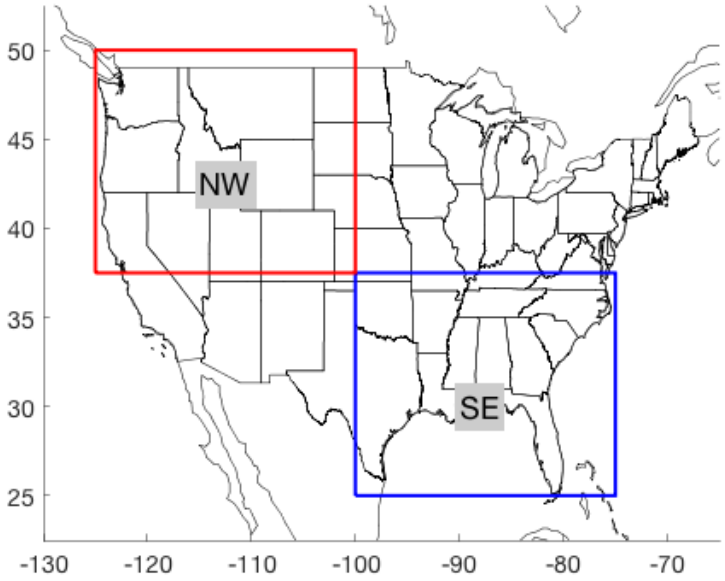

Figure D.2: Regions used in testing the differences between using monthly and daily a priori NO_2 profiles.

$$\overline{A} = \frac{1}{n}\sum_{i=1}^{n} \frac{\int_{p_s}^{p_t} \overline{w}(p) g_i(p)\, dp}{\int_{p_s}^{p_t} g_i(p)\, dp} \tag{D.2}$$

$$= \int_{p_s}^{p_t} \overline{w}(p) \frac{1}{n}\sum_{i=1}^{n} S_i(p)\, dp \tag{D.3}$$

where

$$S_i(p) = \frac{g_i(p)}{\int_{p_s}^{p_t} g_i(p)\, dp} \tag{D.4}$$

i.e. $S_i(p)$ is the shape factor.

For the monthly average profiles, $g(p)$ is averaged temporally. Within each day, individual hours are weighted by their proximity to OMI overpass; the resulting daily average profiles are given equal weight in the monthly average:

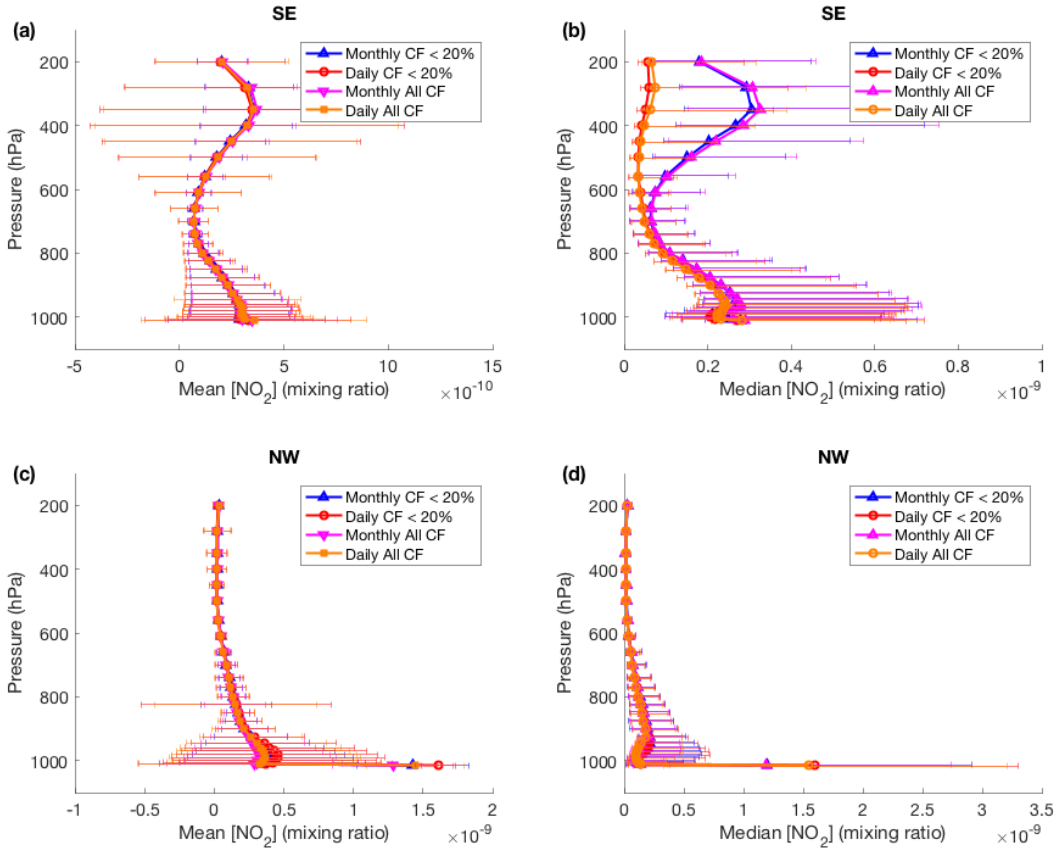

Figure D.3: Mean (a,c) and median (b,d) NO_2 a priori profiles for the regions defined in D.2 (southeast, a–b; northwest, c–d). Error bars for means are 1σ standard deviation, medians are the 25th and 75th percentiles. As in the main paper, the blue and red lines only include pixels with cloud fraction $< 20\%$, while the magenta and orange lines include all pixels.

$$\overline{g}(p) = \frac{1}{n}\sum_{i=1}^{n} g_i(p) \tag{D.5}$$

where $g_i(p)$ represents one day's profile. Therefore, the monthly average shape factor is

$$\overline{S}_M(p) = \frac{1}{n}\sum_{i=1}^{n} \frac{\overline{g}(p)}{\int_{p_s}^{p_t} \overline{g}(p)\, dp} \tag{D.6}$$

$$= \frac{\overline{g}(p)}{\int_{p_s}^{p_t} \overline{g}(p)\, dp} \tag{D.7}$$

$$= \frac{\frac{1}{n}\sum_{i=1}^{n} g_i(p)}{\int_{p_s}^{p_t} \frac{1}{n}\sum_{i=1}^{n} g_i(p)\, dp} \tag{D.8}$$

In contrast, the average shape factor using daily profiles would be:

$$\overline{S}_D(p) = \frac{1}{n}\sum_{i=1}^{n} \frac{g_i(p)}{\int_{p_s}^{p_t} g_i(p)\, dp} \tag{D.9}$$

Eq. (D.8) and (D.9) are not mathematically equivalent. From Figs. D.3 and 4.6, we can infer that the daily variation in surface NO_2 does not significantly affect the average AMF, which is consistent with Laughner et al. (2016), where implementing daily profiles led to small changes in the average over most of the domain. In Eq. (D.9), profiles influenced by lightning will have a larger denominator than those not influenced, and so the increase in UT NO_2 is offset by the increase in total VCD. This causes the shift towards more surface influence in the average daily shape factors in Fig. 4.6c. Alternately, the denominator of Eq. (D.9) can be viewed as a weighting factor that is inherently smaller for lightning-influenced profiles; thus, such profiles have less influence in the shape factor.

D.4 Additional figures

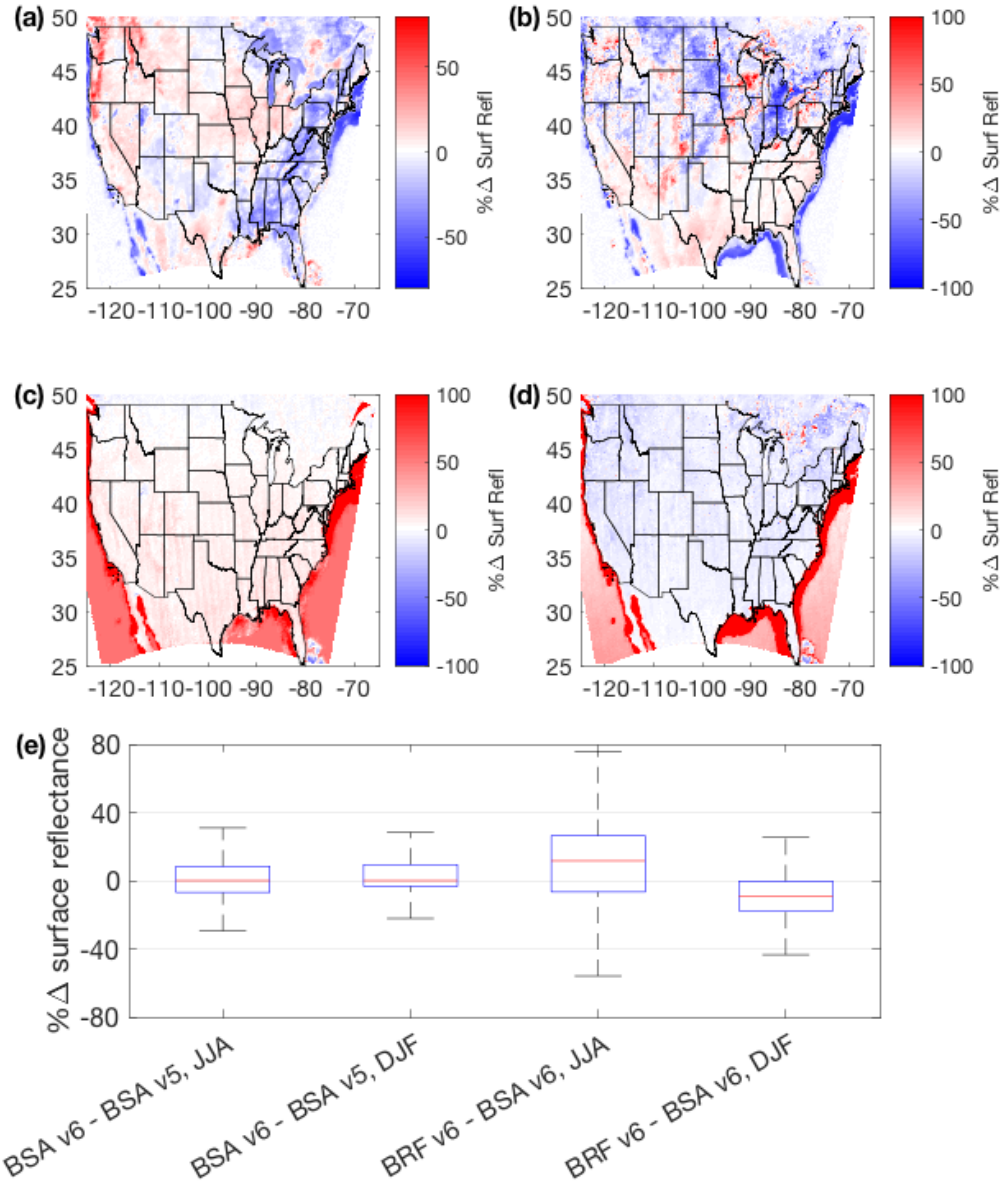

Figure D.4: Attribution of changes in surface reflectance to the version 5 to version 6 MODIS product upgrade vs. the black sky to BRF upgrade. **(a,b)** Percent difference in surface reflectance using version 6 – version 5 of the MODIS black-sky albedo product (MCD43C3). **(c,d)** Percent difference in surface reflectance using a BRF – black sky, both version 6. **(a,c)** differences averaged over Jun, Jul, and Aug 2012; **(b,d)** averaged over Jan, Feb, and Dec 2012. **(e)** Box plots of percent difference in individual pixels' surface reflectances for pixels classified as land pixels, illustrating that although the average change between a black sky and BRF surface reflectance is fairly consistent, individual pixels do have significant changes, as one would expect with a geometry dependent surface reflectance. The red line marks the median, the blue box the upper and lower quartiles, and the black lines the largest and smallest non-outlier values. Outliers are omitted.

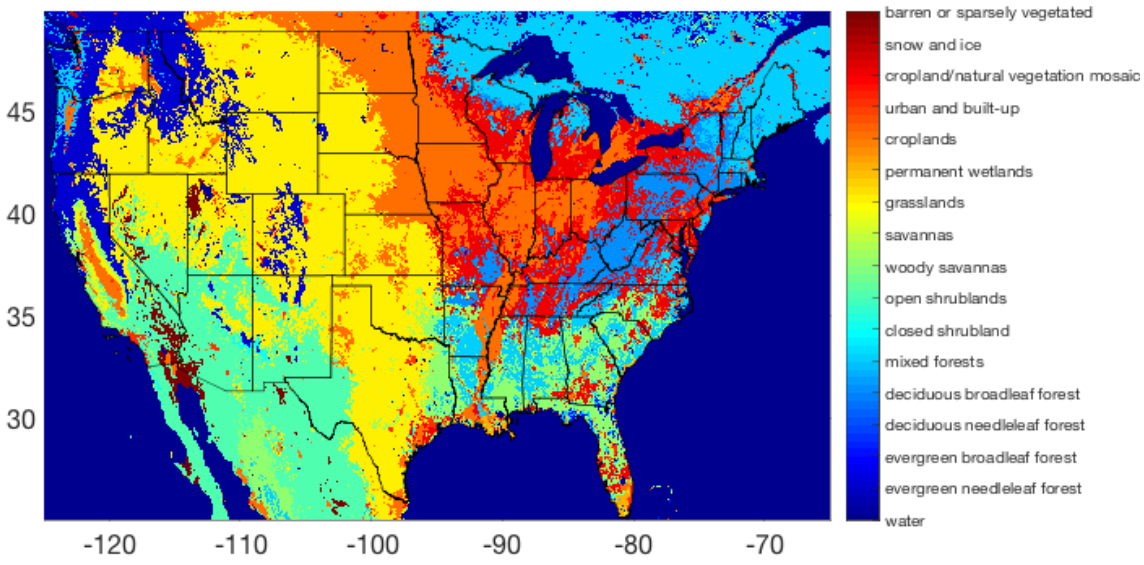

Figure D.5: IGBP land cover classifications for 2012 from the MODIS MCD12C1 product

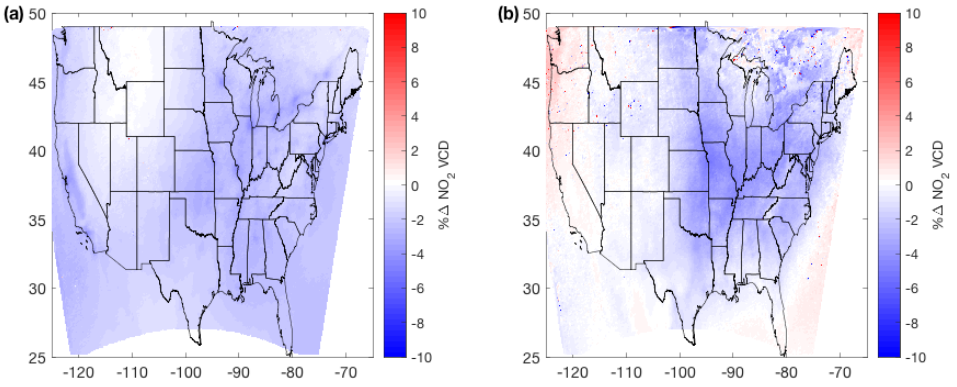

Figure D.6: The percent change in total tropospheric VCDs after fixing the temperature lookup error (a) in summer (Jun–Aug) and (b) in winter (Jan, Feb, Dec).

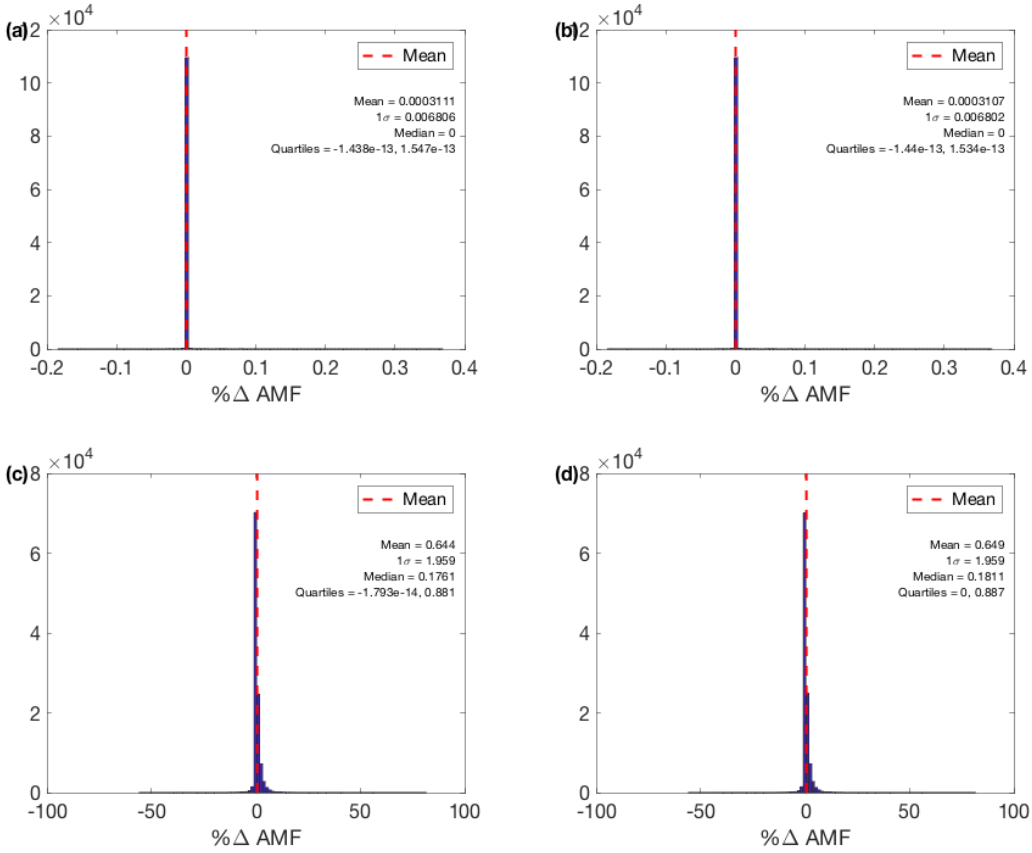

Figure D.7: Percent differences between BEHR AMFs and AMFs recalculated with the published scattering weights and NO_2 a priori profiles. **(a, b)** use separate published clear and cloudy scattering weights, **(c, d)** use the v3.0A and previous cloud radiance fraction weighted average scattering weights. **(a)** and **(c)** are for total tropospheric AMFs, **(b)** and **(d)** are for visible-only AMFs.

D.5 More detail on each incremental change

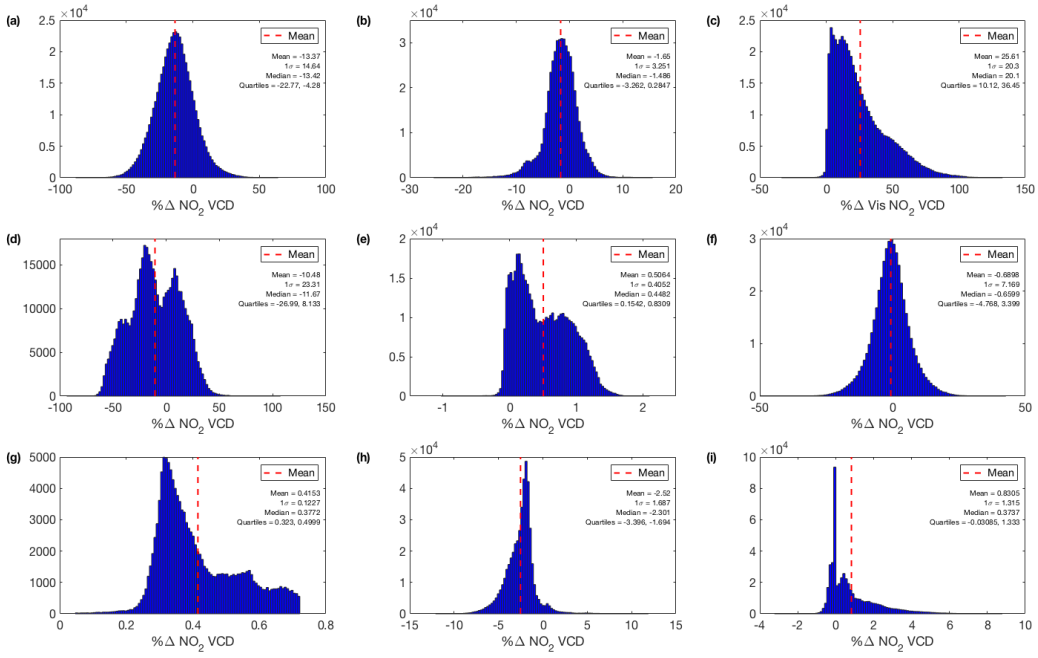

Figure D.8: Histograms of the changes in JJA VCDs from Fig. 4.1. As in Fig. 4.1: **(a)** Change due to new NASA SCDs. **(b)** Change due to updated surface reflectance. **(c)** Change in visible-only VCD due to new visible-only AMF formulation. **(d)** Change due to new monthly profiles. **(e)** Changes due to new temperature profile. **(f)** Changes due to new gridding method. **(g)** Changes due to the ocean reflectance changed to 460 nm. **(h)** Change due to implementation of the variable tropopause height. **(i)** Changes due to the Zhou et al. (2009) surface pressure formulation. All averages exclude outliers, the row anomaly, and use only cloud fraction ≤ 0.2. In **(g)**, only ocean grid cells are considered.

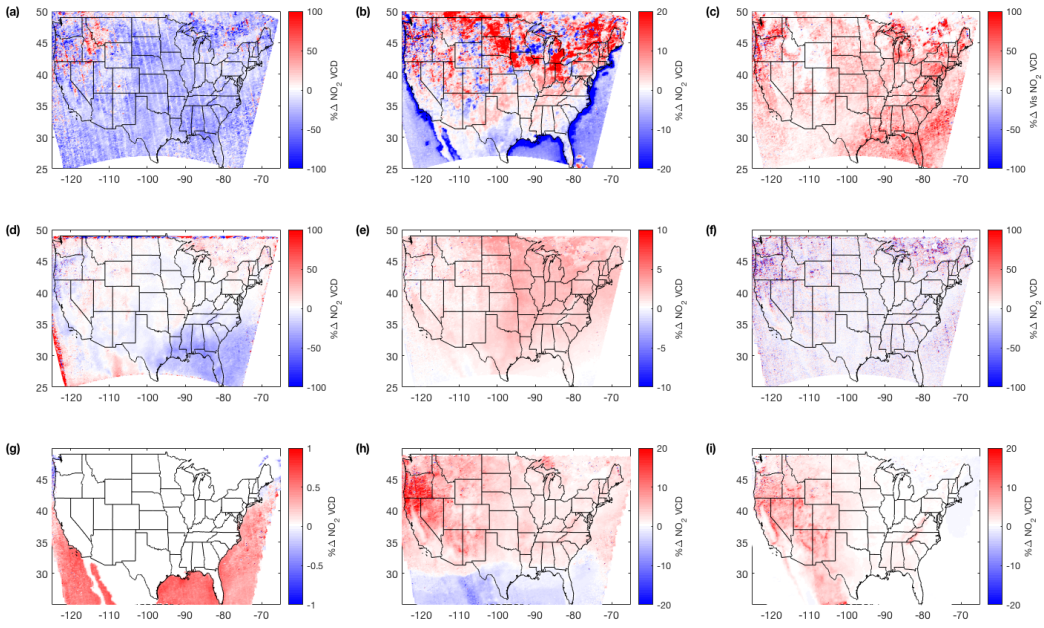

Figure D.9: As Fig. 4.1 but for Jan, Feb, Dec 2012: changes in total tropospheric or visible-only VCDs due to individual changes. **(a)** Change due to new NASA SCDs. **(b)** Change due to updated surface reflectance. **(c)** Change in visible-only VCD due to new visible-only AMF formulation. **(d)** Change due to new monthly profiles. **(e)** Changes due to new temperature profile. **(f)** Changes due to new gridding method. **(g)** Changes due to the ocean reflectance changed to 460 nm. **(h)** Change due to implementation of the variable tropopause height. **(i)** Changes due to the Zhou et al. (2009) surface pressure formulation. All averages exclude the row anomaly and use only cloud fraction ≤ 0.2.

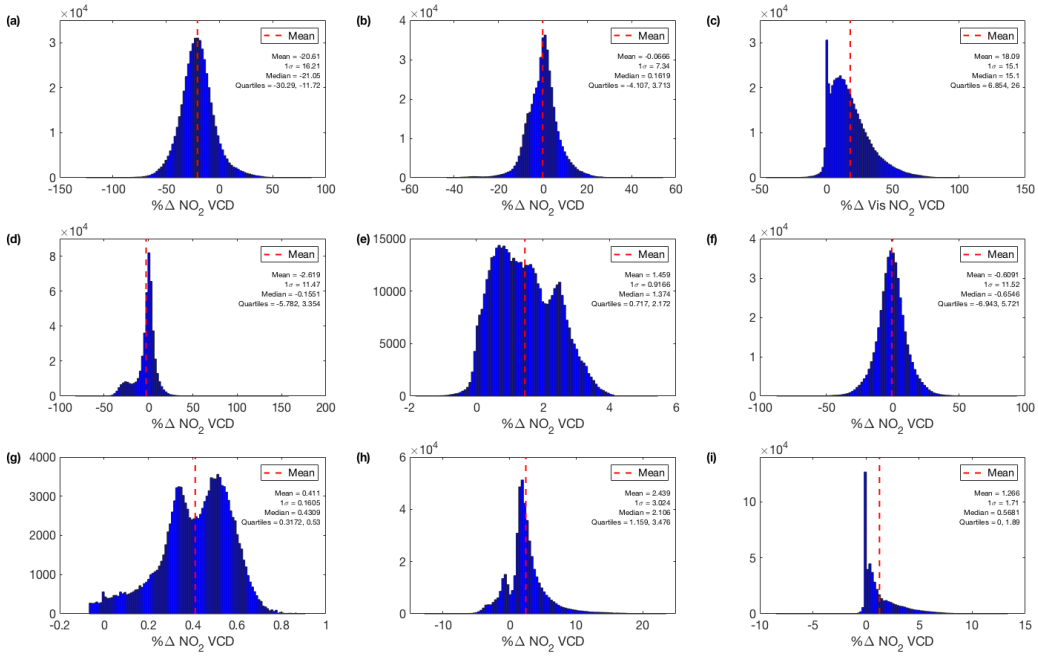

Figure D.10: Histograms of the changes in DJF VCDs from Fig. D.9, with outliers removed. In **(g)**, only ocean grid cells are considered.

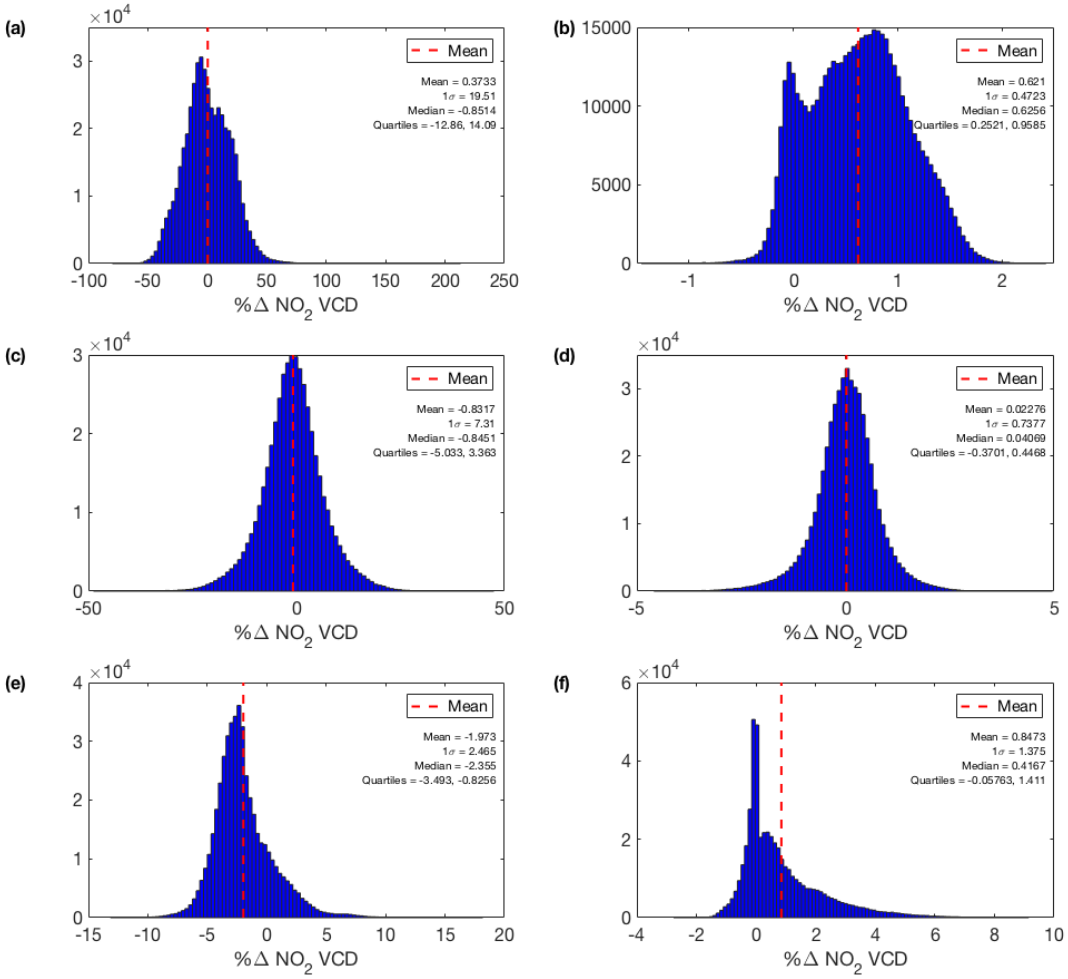

Figure D.11: Histograms of the differences shown in Fig. 4.4.

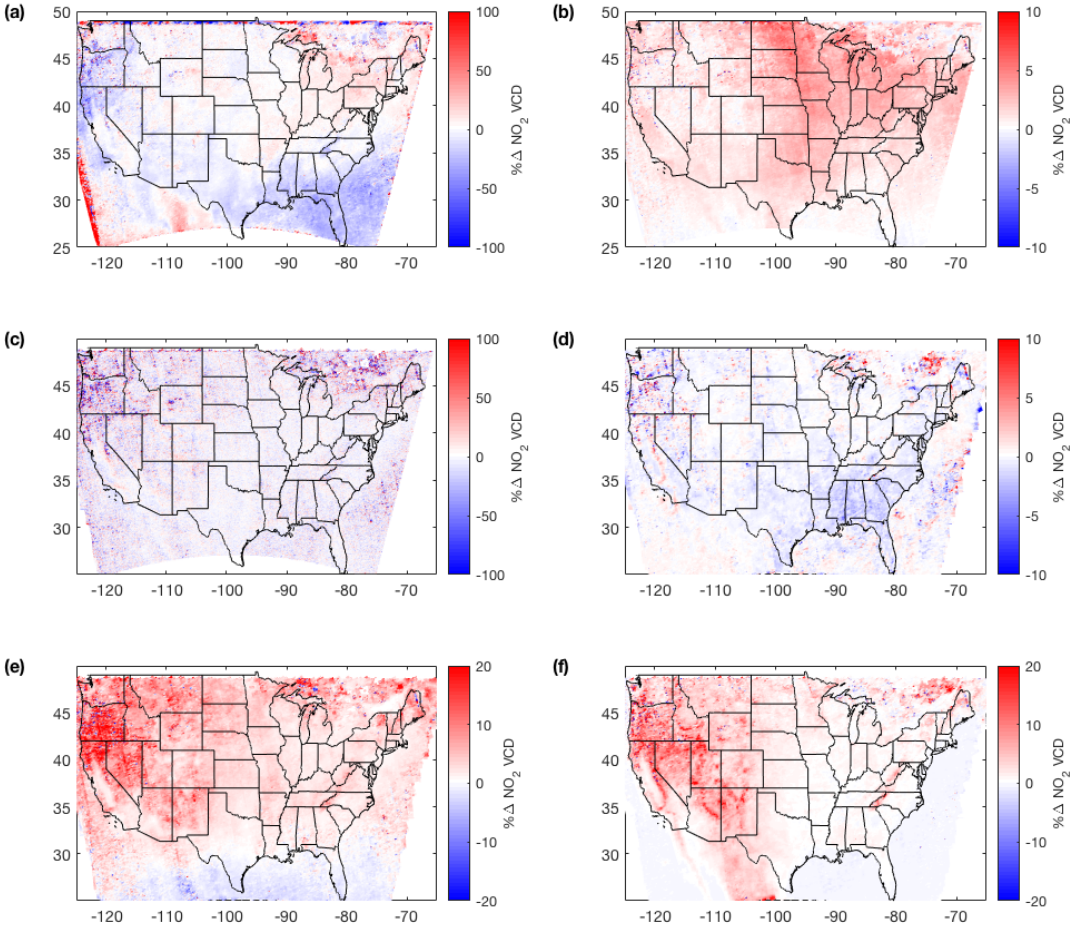

Figure D.12: Similar to Fig. 4.4, but for DJF. Changes in the average VCDs in the subproduct using daily profiles due to: **(a)** implementation of new profiles, **(b)** new temperature profiles, **(c)** new gridding method, **(d)** change to temporal matching of daily profiles with OMI overpass and changing the ocean reflectance LUT to 460 nm, **(e)** implementing the variable tropopause height, and **(f)** the Zhou et al. (2009) surface pressure formulation. All averages exclude the row anomaly only use cloud fraction ≤ 0.2.

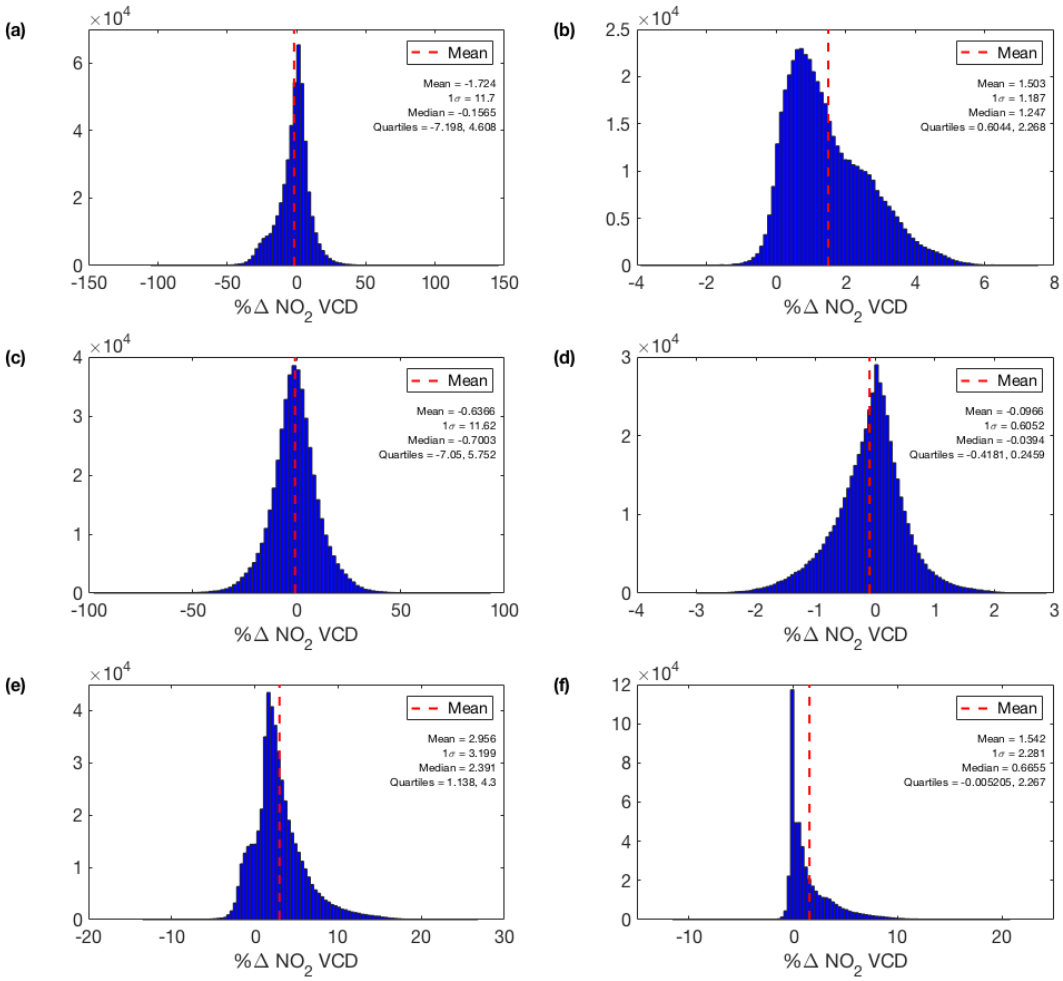

Figure D.13: Histogram of the differences in Fig. D.12, with outliers removed.

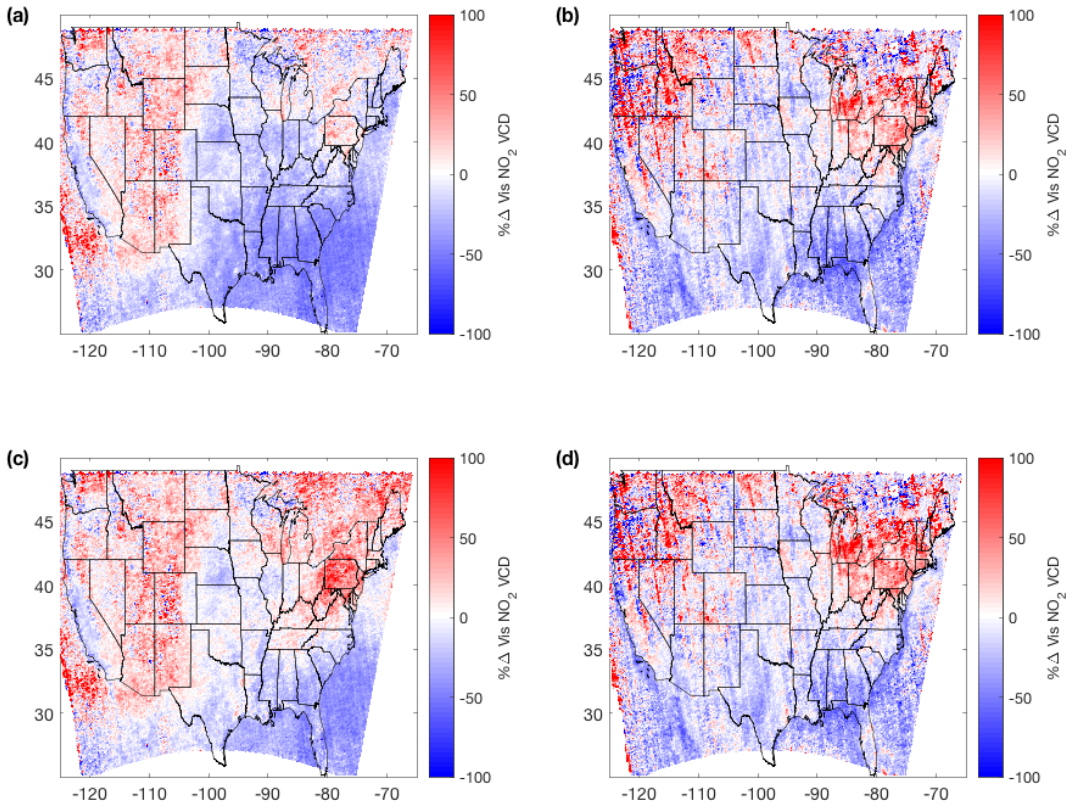

Figure D.14: As Fig. 4.7 but for the visible-only VCDs: differences between v2.1C and v3.0B **(a,b)** v3.0B uses monthly profiles. **(c,d)** v3.0B uses daily profiles. **(a,c)** average over Jun–Aug 2012. **(b,d)** average over Jan, Feb, Dec 2012. All averages exclude the row anomaly and use only cloud fraction ≤ 0.2.

Appendix E

Supplemental material to "Evaluation of the BEHR v3.0 product"

E.1 VCD comparison detail

BEHR v3.0 intercepts and R^2 values are generally similar to or better than NASA SP v3.0, though the discrepancy in intercepts is greater when comparing against Pandora data alone. In theory, comparing against aircraft data, the intercepts would indicate a bias in the stratospheric separation or total column (for Pandora comparisons, it can only be in the total column). In practice, it is not fully orthogonal to errors in the AMF. However, the stratospheric separation and total column will still be a significant component to the intercept, so it is reasonable that the BEHR and NASA intercepts are similar, as both use the same stratospheric separation and total columns.

		Extended with GEOS-Chem			Extended by extrapolation		
Campaign	Product	Slope	Intercept	R^2	Slope	Intercept	R^2
DISCOVER-MD	BEHR v3.0B (D)	N/A	N/A	N/A	N/A	N/A	N/A
	BEHR v3.0B (M)	0.888	-8.96×10^{14}	0.149	0.998	1.28×10^{14}	0.0813
	BEHR v2.1C	1.92	-2.69×10^{15}	0.0747	2.27	-7.24×10^{14}	0.0921
	SP v3.0	0.774	-5.35×10^{14}	0.0806	0.884	3.67×10^{14}	0.0469
DISCOVER-CA	BEHR v3.0B (D)	0.627	1.12×10^{15}	0.567	0.716	9.6×10^{14}	0.587
	BEHR v3.0B (M)	0.665	9.91×10^{14}	0.521	0.775	7.98×10^{14}	0.554
	BEHR v2.1C	0.944	8.29×10^{14}	0.554	1.14	5.25×10^{14}	0.625
	SP v3.0	0.512	9.66×10^{14}	0.291	0.513	9.93×10^{14}	0.311
DISCOVER-TX	BEHR v3.0B (D)	0.483	2.66×10^{14}	0.295	0.512	4.54×10^{14}	0.275
	BEHR v3.0B (M)	0.407	3.9×10^{14}	0.321	0.425	5.54×10^{14}	0.238
	BEHR v2.1C	0.867	1.03×10^{15}	0.386	0.836	1.58×10^{15}	0.359
	SP v3.0	0.299	7.15×10^{14}	0.352	0.317	7.9×10^{14}	0.355
DISCOVER-CO ($V > 0$)	BEHR v3.0B (D)	1.03	-5.82×10^{14}	0.0279	1.01	1.26×10^{14}	0.0234
	BEHR v3.0B (M)	0.915	-5.27×10^{14}	0.0244	0.957	8.24×10^{13}	0.062
	BEHR v2.1C	1.84	-1.32×10^{15}	0.018	1.84	-1.65×10^{14}	0.0186
	SP v3.0	0.705	-4.04×10^{14}	0.0553	0.65	1.69×10^{14}	0.0423
SENEX	BEHR v3.0B (D)	2.25	-2.59×10^{15}	0.154	1.72	-1.2×10^{15}	0.0549
	BEHR v3.0B (M)	0.953	-4.6×10^{14}	0.265	0.879	-8.89×10^{13}	0.153
	BEHR v2.1C	1.43	-2.25×10^{14}	0.164	1.48	-2.44×10^{14}	0.111
	SP v3.0	1.07	-5.84×10^{14}	0.274	0.835	2.35×10^{13}	0.107
SEAC4RS	BEHR v3.0B (D)	0.888	-1.51×10^{14}	0.0122	0.695	5.89×10^{14}	0.0473
	BEHR v3.0B (M)	1.22	-4.56×10^{14}	0.228	0.971	5.81×10^{14}	0.376
	BEHR v2.1C	2.63	-1.55×10^{15}	0.597	2.53	-7.82×10^{13}	0.422
	SP v3.0	1.01	-3.97×10^{14}	0.236	0.823	4.31×10^{14}	0.154

Table E.1: Slopes, intercepts, and R^2 values for RMA regression of satellite VCDs against in situ calculated VCDs. Outliers are removed before calculating these parameters; negative VCDs are retained unless noted.

Campaign	Product	Slope	Intercept	R^2
DISCOVER-MD	BEHR v3.0B (D)	N/A	N/A	N/A
	BEHR v3.0B (M)	0.443	2.55×10^{15}	0.139
	BEHR v2.1C	0.766	3.2×10^{15}	0.128
	SP v3.0	0.355	3.02×10^{15}	0.125
DISCOVER-CA	BEHR v3.0B (D)	0.813	-9.99×10^{14}	0.175
	BEHR v3.0B (M)	0.781	-8.66×10^{14}	0.16
	BEHR v2.1C	0.774	-1.22×10^{14}	0.178
	SP v3.0	0.599	-1.01×10^{14}	0.169
DISCOVER-TX	BEHR v3.0B (D)	1.08	-7.57×10^{14}	0.152
	BEHR v3.0B (M)	0.868	2.05×10^{14}	0.173
	BEHR v2.1C	1.43	6.54×10^{14}	0.102
	SP v3.0	0.688	9.54×10^{14}	0.136
DISCOVER-CO (V > 0)	BEHR v3.0B (D)	0.655	7.71×10^{14}	0.211
	BEHR v3.0B (M)	0.628	8.26×10^{14}	0.243
	BEHR v2.1C	0.658	1.5×10^{15}	0.224
	SP v3.0	0.468	1.38×10^{15}	0.213

Table E.2: Slopes, intercepts, and R^2 values for RMA regression of satellite VCDs against Pandora VCDs. Outliers are removed before calculating these parameters.

		Matched Data			All Data		
Campaign	Product	Slope	Intercept	R2	Slope	Intercept	R2
DISCOVER-MD	BEHR v3.0B (D)	N/A	N/A	N/A	N/A	N/A	N/A
	BEHR v3.0B (M)	0.804	-4.16×10^{14}	0.407	0.637	8.46×10^{14}	0.361
	BEHR v2.1C	1.27	-2.92×10^{14}	0.292	0.874	2.23×10^{15}	0.304
	SP v3.0	0.788	-4.65×10^{14}	0.383	0.496	1.72×10^{15}	0.286
DISCOVER-CA	BEHR v3.0B (D)	0.493	1.3×10^{15}	0.525	0.677	1.27×10^{14}	0.321
	BEHR v3.0B (M)	0.509	1.18×10^{15}	0.514	0.661	1.5×10^{14}	0.317
	BEHR v2.1C	0.568	1.46×10^{15}	0.469	0.682	6.54×10^{14}	0.321
	SP v3.0	0.407	1.31×10^{15}	0.408	0.539	4.11×10^{14}	0.282
DISCOVER-TX	BEHR v3.0B (D)	0.692	1.35×10^{14}	0.157	1	-7.39×10^{14}	0.208
	BEHR v3.0B (M)	0.598	3.22×10^{14}	0.217	0.871	-2.26×10^{14}	0.221
	BEHR v2.1C	1.06	1.07×10^{15}	0.19	1.33	7.16×10^{14}	0.173
	SP v3.0	0.527	5.25×10^{14}	0.12	0.736	2.45×10^{14}	0.136
DISCOVER-CO	BEHR v3.0B (D)	0.663	6.38×10^{14}	0.394	0.664	6.92×10^{14}	0.267
	BEHR v3.0B (M)	0.696	2.68×10^{14}	0.347	0.628	7.56×10^{14}	0.277
	BEHR v2.1C	0.741	1.09×10^{15}	0.422	0.679	1.33×10^{15}	0.326
	SP v3.0	0.531	4.32×10^{14}	0.312	0.498	1.05×10^{15}	0.224

Table E.3: Slopes and 1σ uncertainties of BEHR vs. combined aircraft (extended with GEOS-Chem profiles) and Pandora VCDs. Matched slopes use only Pandora data approximately coincident with aircraft profiles to get similar sampling; all uses all valid Pandora data. Outliers and negative VCDs are removed before computing slopes.

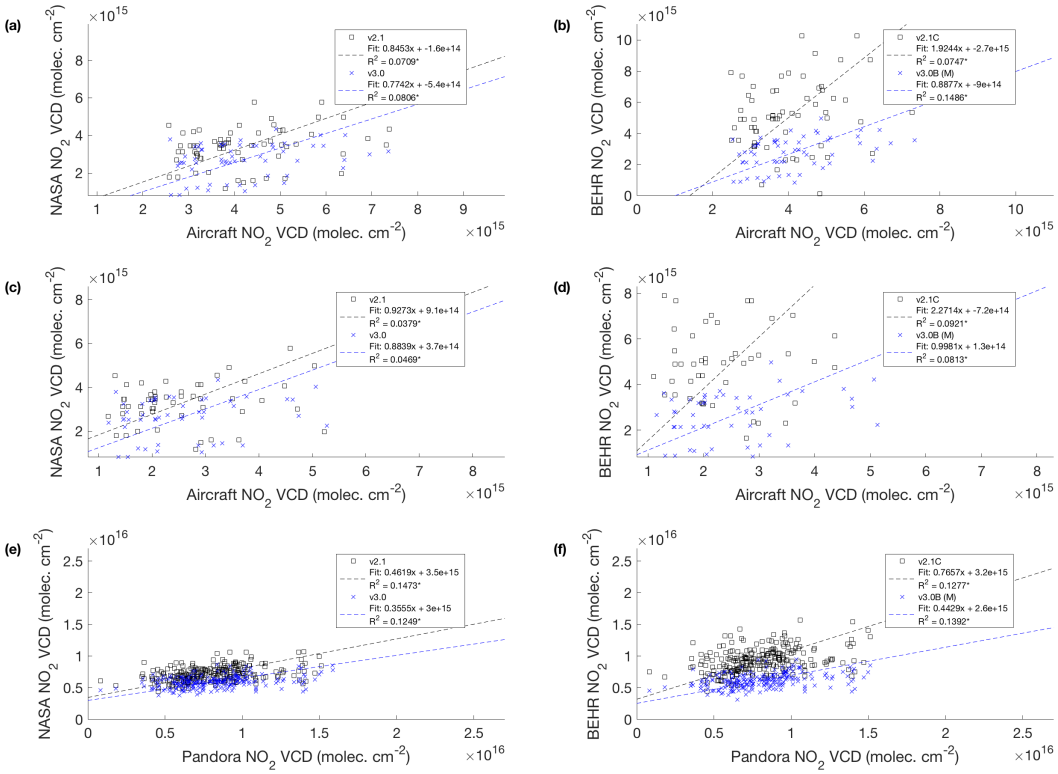

Figure E.1: Scatter plots comparing **(a,c,e)** NASA Standard Product and **(b,d,f)** the BEHR product VCDs to **(a,b)** aircraft profiles extended with GEOS-Chem, **(c,d)** aircraft profiles extended by extrapolation, **(e,f)** Pandora columns measured during the DISCOVER-AQ Maryland campaign. An asterisk (*) after the R^2 value in the legend indicates the slope is statistically different from 0 at the 95% confidence level.

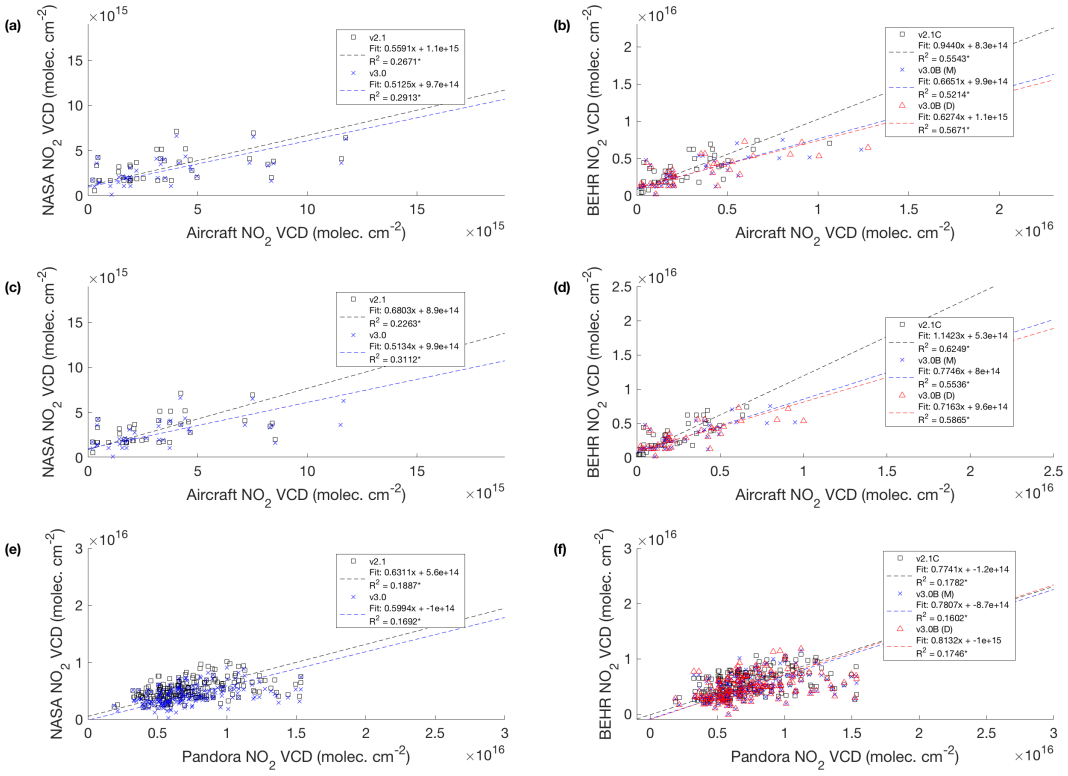

Figure E.2: Scatter plots comparing **(a,c,e)** NASA Standard Product and **(b,d,f)** the BEHR product VCDs to **(a,b)** aircraft profiles extended with GEOS-Chem, **(c,d)** aircraft profiles extended by extrapolation, **(e,f)** Pandora columns measured during the DISCOVER-AQ California campaign. An asterisk (*) after the R^2 value in the legend indicates the slope is statistically different from 0 at the 95% confidence level.

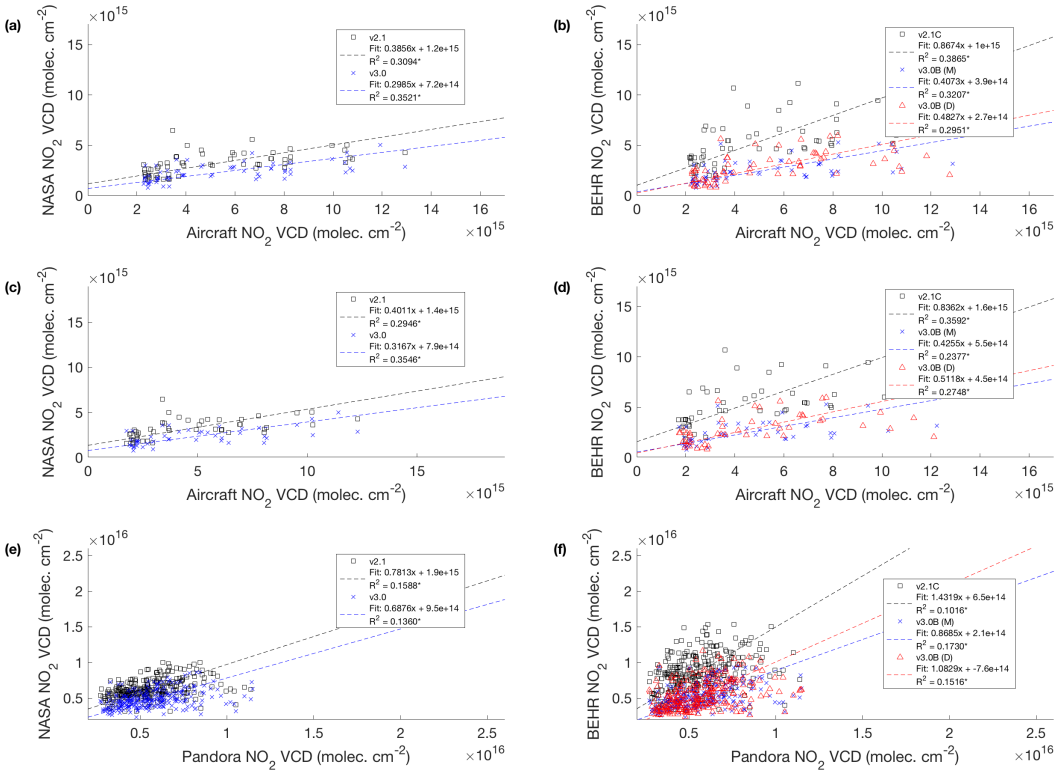

Figure E.3: Scatter plots comparing **(a,c,e)** NASA Standard Product and **(b,d,f)** the BEHR product VCDs to **(a,b)** aircraft profiles extended with GEOS-Chem, **(c,d)** aircraft profiles extended by extrapolation, **(e,f)** Pandora columns measured during the DISCOVER-AQ Texas campaign. An asterisk (*) after the R^2 value in the legend indicates the slope is statistically different from 0 at the 95% confidence level.

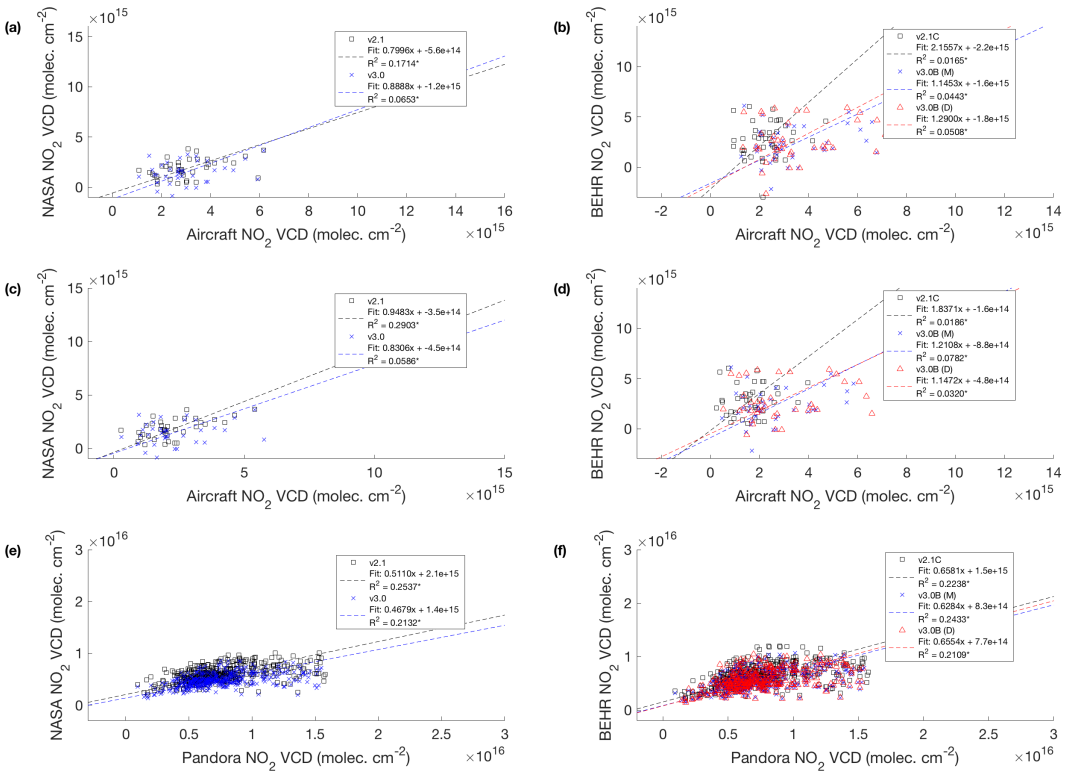

Figure E.4: Scatter plots comparing **(a,c,e)** NASA Standard Product and **(b,d,f)** the BEHR product VCDs to **(a,b)** aircraft profiles extended with GEOS-Chem, **(c,d)** aircraft profiles extended by extrapolation, **(e,f)** Pandora columns measured during the DISCOVER-AQ Colorado campaign. Negative VCDs are not removed, in contrast to Table E.3. An asterisk (*) after the R^2 value in the legend indicates the slope is statistically different from 0 at the 95% confidence level.

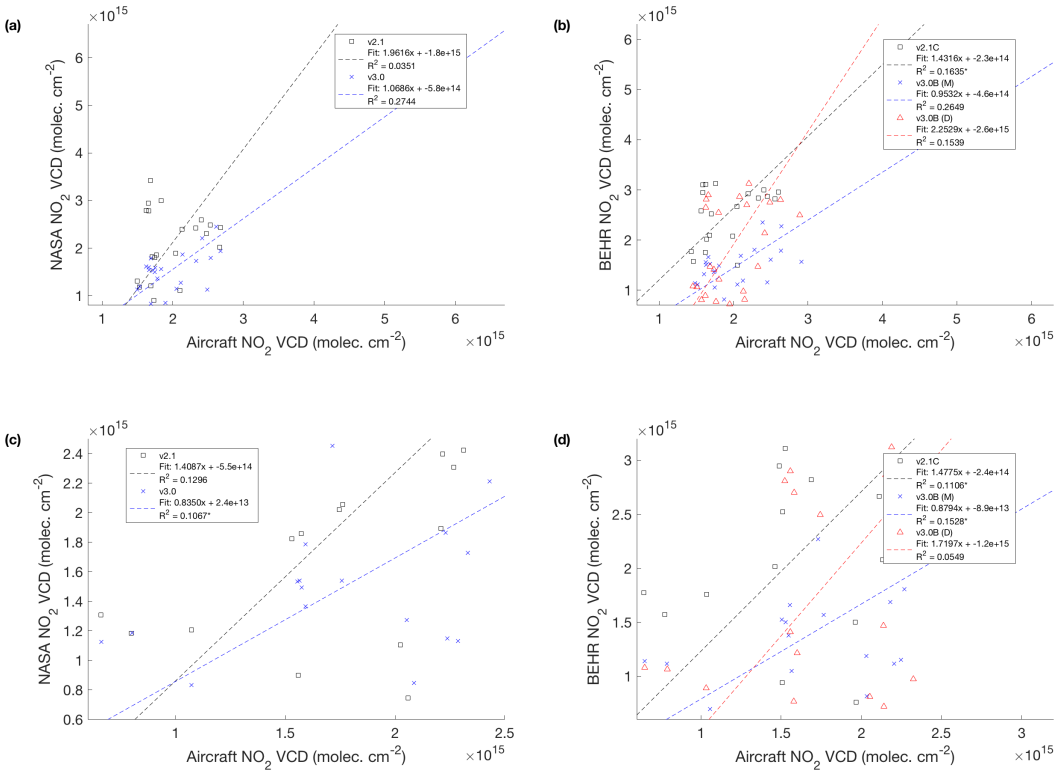

Figure E.5: Scatter plots comparing **(a,c)** NASA Standard Product and **(b,d)** the BEHR product VCDs to **(a,b)** aircraft profiles extended with GEOS-Chem and **(c,d)** aircraft profiles extended by extrapolation measured during the SENEX campaign. An asterisk (*) after the R^2 value in the legend indicates the slope is statistically different from 0 at the 95% confidence level.

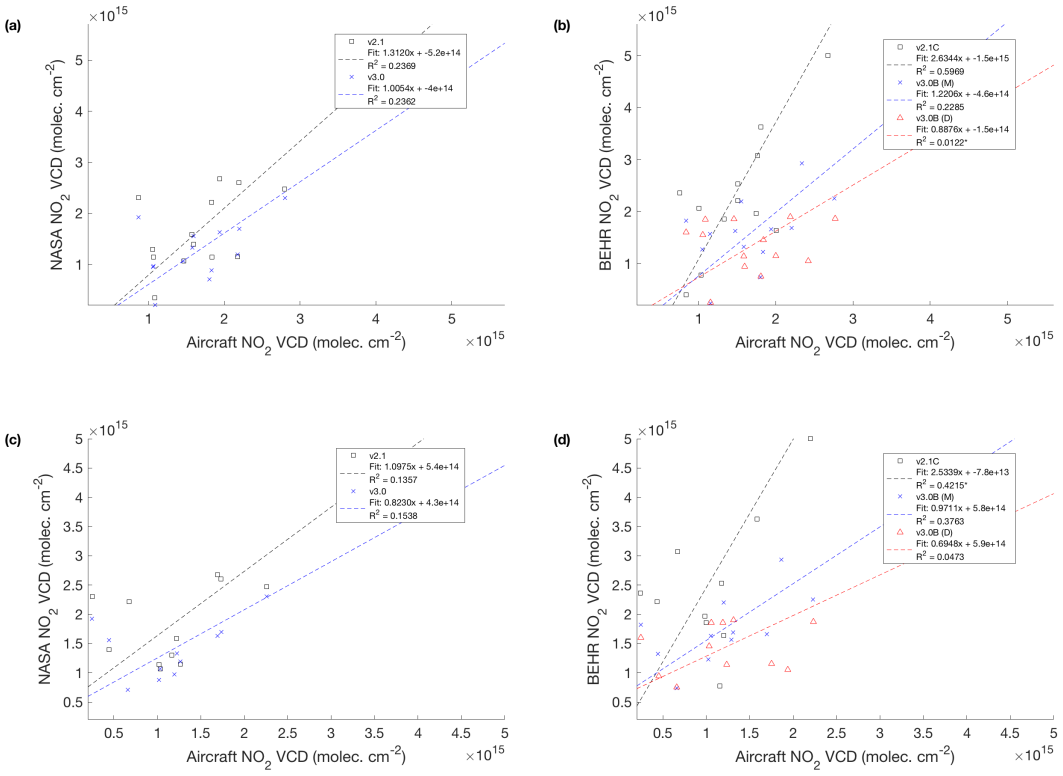

Figure E.6: Scatter plots comparing **(a,c)** NASA Standard Product and **(b,d)** the BEHR product VCDs to **(a,b)** aircraft profiles extended with GEOS-Chem and **(c,d)** aircraft profiles extended by extrapolation measured during the SEAC4RS campaign. An asterisk (*) after the R^2 value in the legend indicates the slope is statistically different from 0 at the 95% confidence level.

E.2 WRF Lightning - Individual Events

The analysis of a individual convective event taking place near the boundary of Alabama and Georgia on June 14 2012 in shown in Fig. E.7. The spatial extent of flashes simulated by WRF-Chem is much broader than that measured by ENTLN, and outside of a few grid cells, the ENTLN flash counts are substantially less than the WRF-Chem simulation.

Outside of the southeast US, although the overall agreement in flash density improves, on smaller scales, we still see that flash density observed by ENTLN is concentrated in the convective core while the simulated flash density spreads over the convective area and fails to reproduce the gradient across the convective core (Fig. E.8). The simulated flash density in the convection core is lower than observation, though the total flash counts are still comparable.

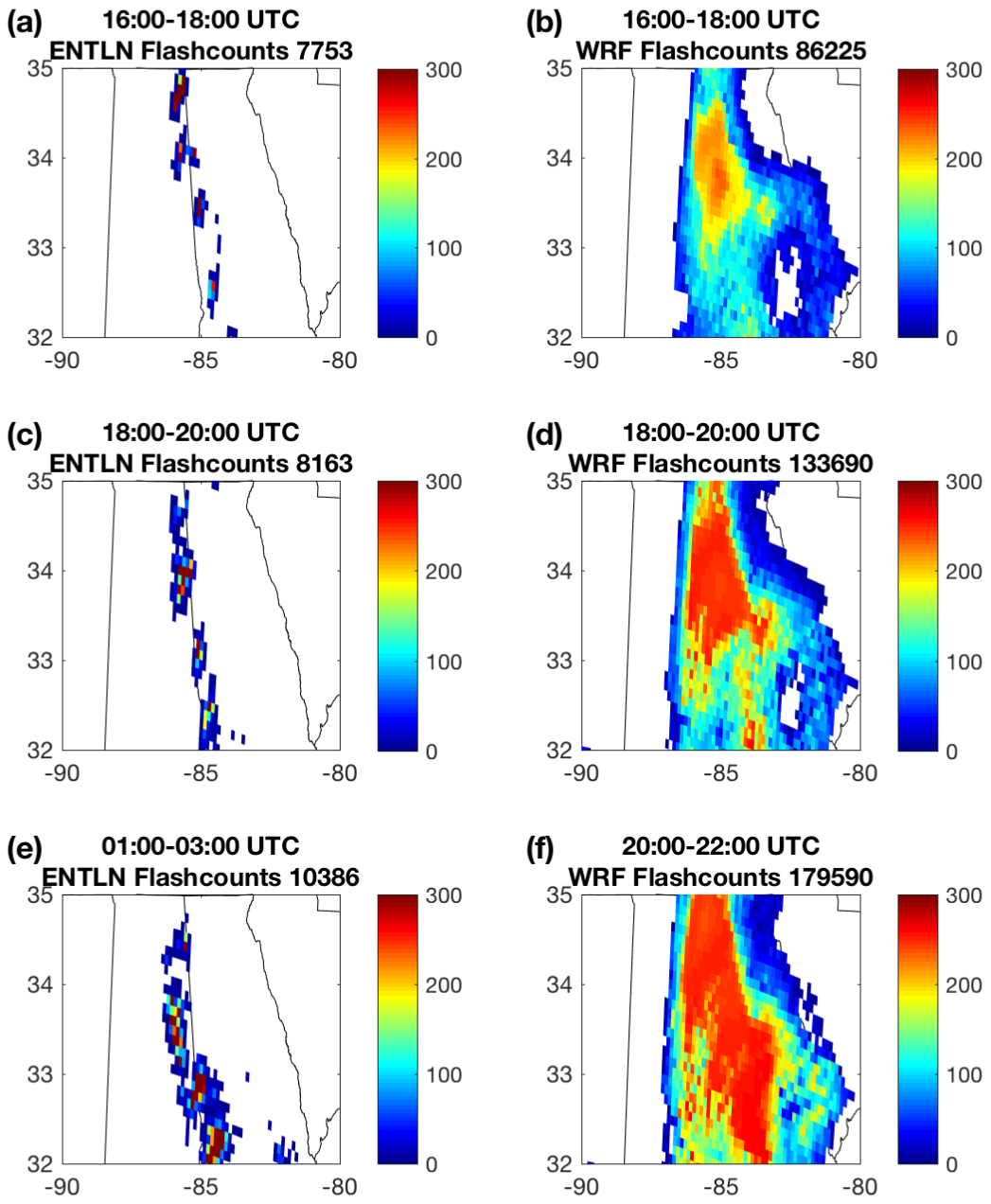

Figure E.7: Time-evolved development of storm in the southeast US illustrated by lightning flashes observed by ENTLN **(a, c, e)** and simulated by WRF-Chem **(b, d, f)** on June 14 2012. The number of flashes occurring within the time range is denoted.

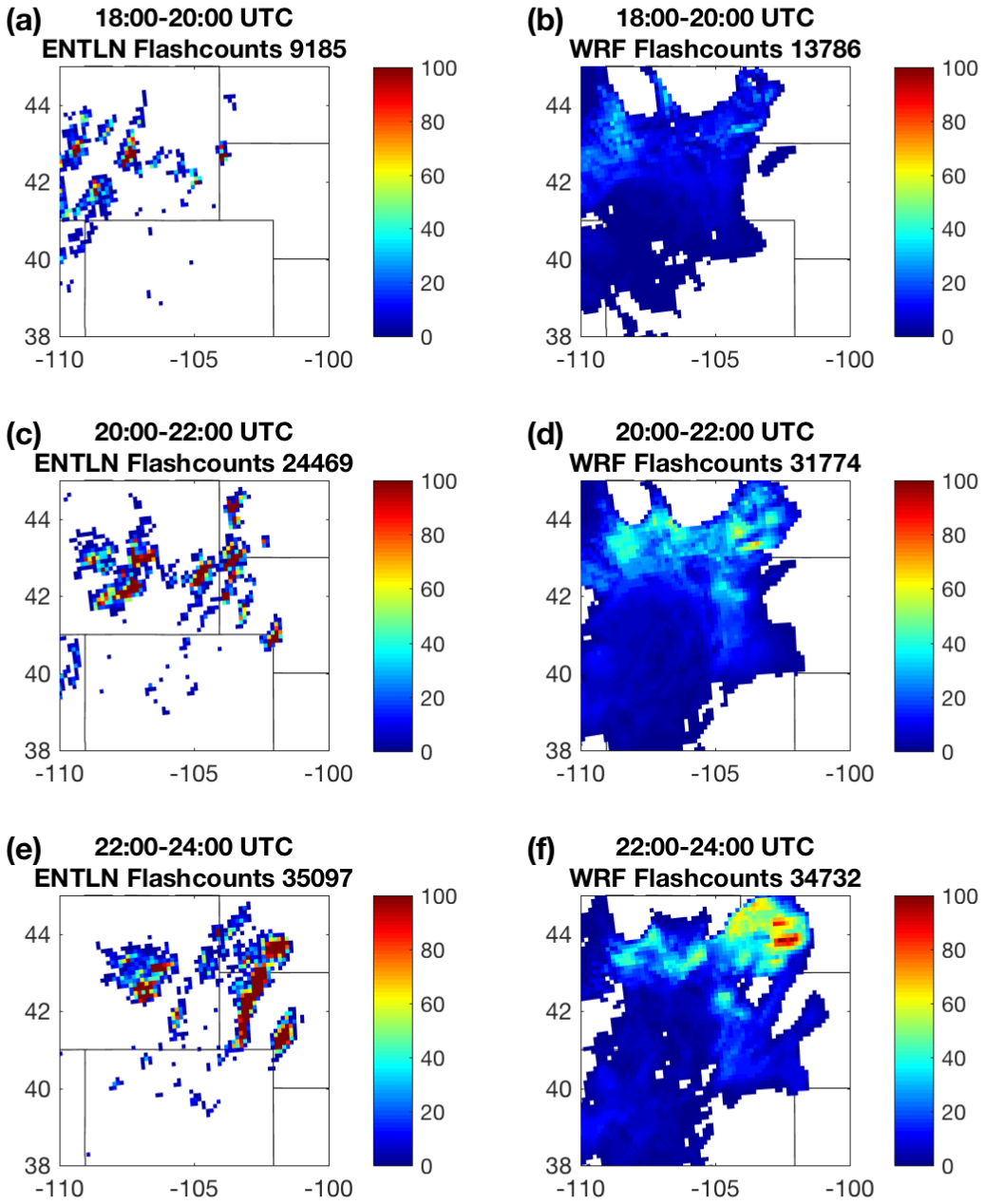

Figure E.8: Time-evolved development of storm in the central US illustrated by lightning flashes observed by ENTLN **(a, c, e)** and simulated by WRF-Chem **(b, d, f)** on May 18 2012. The number of flashes occurring within the time range is denoted.

E.3 Surface reflectivity evaluation

In BEHR v3, we use the MODIS combined Band 3 MCD43D BRDF coefficients along with the Ross-Thick Li-Sparse kernels to compute a surface reflectivity. This is a computationally simpler approach than Vasilkov et al. (2017), who combined MODIS BRDF coefficients with the VLIDORT radiative transfer model to calculate a modified Lambertian Equivalent Reflectivity (m-LER) that assumes a uniform Lambertian surface under a scattering atmosphere. Here, we evaluate the difference resulting from using the MODIS BRDF directly.

We do so using the MODIS BRDF values using the SCIATRAN radiative transfer model (Rozanov et al., 2005). SCIATRAN is run in plane-parallel scattering mode, including polarization effect. The incident beam is assumed to be unpolarized (Stokes vector [1 0 0 0]). The aerosol profile uses the included WMO aerosol scenario, with 4 layers with upper boundaries of 2 km, 12 km, 30 km, and 100 km above the ground elevation, and aerosol types of continental, continental, background, and background, respectively.

We follow Vasilkov et al. (2017) to calculate modified-LERs (m-LERs) from:

$$I(\lambda, \theta, \theta_0, \phi, P_s, R_{\text{BRDF}}) = I_0(\lambda, \theta, \theta_0, \phi, P_s) + \frac{R_{\text{LER}} \cdot T(\lambda, \theta, \theta_0, P_s)}{1 - R_{\text{LER}} \cdot S_b(\lambda, P_s)} \tag{E.1}$$

for R_{LER}, which is the m-LER. The other variables are:

- I: the top-of-atmosphere intensity at wavelength λ for the given viewing zenith angle (VZA, θ), solar zenith angle (SZA, θ_0), relative azimuth angle (RAA, ϕ), surface pressure (P_s), and BRDF function (R_{BRDF})
- I_0: the top-of-atmosphere intensity for the same wavelength, geometry, and surface pressure as I, but with a 0-reflectivity (i.e. perfectly black) surface
- T: the intensity of light transmitted through the atmosphere; specifically, it represents the solar irradiance that reaches the surface, divided by π (to account for isotropic scattering from the assumed Lambertian surface, which reduces the intensity in a given solid angle), and multiplied by the transmittance of the atmosphere along the viewing direction.
- S_b: the spherical albedo of the atmosphere under the condition of illumination from below. This accounts for additional light incident on the surface due to downward scattering by the atmosphere of light already reflected from the surface.

As in Vasilkov et al. (2017), look up tables (LUTs) are created for I_0, T, and S_b. The I_0 LUT is created from the intensity output of SCIATRAN iterated over three wavelengths

(450, 460, and 470 nm) and the same SZAs, VZAs, RAAs, and surface pressures used in the scattering weight LUT, with surface reflectivity set to 0. The LUTs for T and S_b are created by solving a system of linear equations obtained by rearranging Eq. (E.1):

$$\begin{bmatrix} (I-I_0)_{R=0.05} & 1 \\ (I-I_0)_{R=0.1} & 1 \end{bmatrix} \begin{bmatrix} S_b \\ T \end{bmatrix} = \begin{bmatrix} \left(\frac{I-I_0}{R}\right)_{R=0.05} \\ \left(\frac{I-I_0}{R}\right)_{R=0.1} \end{bmatrix} \tag{E.2}$$

where the subscripts $R = 0.05$ and $R = 0.1$ indicate that I was calculated with a Lambertian surface reflectivity of 0.05 and 0.1, respectively. These are computed for the same SZAs, VZAs, RAAs, surface pressures, and wavelengths as the I_0 table, although S_b and T are theoretically invariant with respect to some of those parameters. This holds in practice, except for S_b when both the SZA and VZA are very large.

The m-LER is then calculated at 85 sites throughout the continental United States for 189 geometries per site using MCD43D07, MCD43D08, and MCD43D09 coefficients from the first day of each month in 2005 by inputting those coefficients into SCIATRAN to calculate I in Eq. (E.1) at 466 nm. Using the previously discussed LUTs for I_0, T, and S_b, we calculate the m-LER from Eq. (E.1).

Finally, we calculate the BRDF albedo as in Laughner et al. (2018b) for each geometry and month at each site, noting that the RAA definition for SCIATRAN is reversed from that for the BRDF kernels (i.e. $\phi_{\mathrm{SCIA}} = 180 - \phi_{\mathrm{MODIS}}$). We match each m-LER to the corresponding BRDF albedo for the comparison below.

Figure E.9 shows the results for 85 sites (a combination of urban, power plant, and rural sites) with 189 geometry combinations for each site. Figure E.9a shows only a 3% variation from a 1:1 line in the regression, and Fig. E.9b and c shows a median difference of only 0.005 (8%), with the 75th percentile difference of 0.007 (14%). We retrieved 1 June 2012 with a 14% increase in surface reflectance and found, on average, only a $1.5 \pm 4\%$ (1σ) decrease in the NO_2 column. Since the overall effect of including the radiative transfer calculations on the retrieved columns is small, we choose to use the BRDF coefficients directly to account for the directional dependence of surface reflectance.

We do note that for surface reflectances < 0.3, larger differences in the surface reflectance obtained with radiative transfer calculations compared to the raw BRDF coefficients are associated with large solar zenith angles ($\sim 70°$). This indicates that the uncertainty in individual pixels due to the choice of surface reflectance will be greater during the winter months. However, when individual months are fit, the slope does not change significantly (range 1.011 ± 0.001 to 1.0395 ± 0.0005), indicating that the average uncertainty does not vary significantly with season.

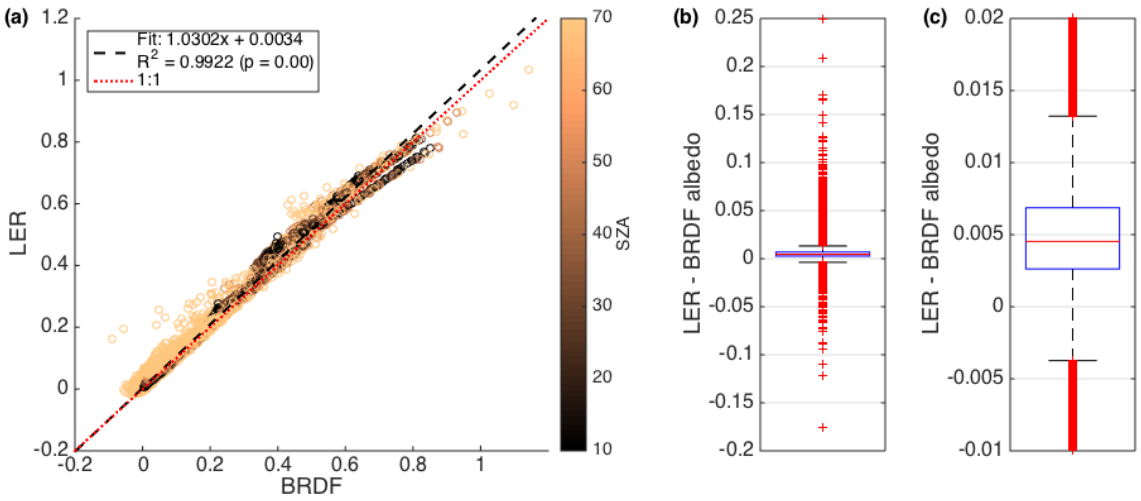

Figure E.9: Comparison of a m-LER calculated with MODIS BRDF coefficients to the surface reflectance calculated directly from MODIS BRDF coefficients and kernels. **(a)** scatter plot of the m-LER on the y-axis and direct BRDF on the x-axis, colored by solar zenith angle; a reduced major axis regression is used to fit the data. **(b)** box plot of the difference between the two quantities. The red line is the median, the blue box the 25th and 75th percentiles, the black lines are the furthest non-outlier values, and the red crosses are outliers. **(c)** same as **(b)**, but zoomed in on the interquartile range.

E.4 Uncertainty analysis

We determine the uncertainty in the AMF due to surface reflectance, surface pressure, tropopause pressure, cloud pressure, cloud radiance fraction, and profile shape numerically by perturbing each parameter in turn and re-retrieving the NO_2 VCDs with the perturbed values (Table E.4). For each perturbation, we reretrieved all of 2012 with the varied parameter.

Surface reflectivity, surface pressure and tropopause pressure are varied by fixed percentages (surface and tropopause pressure are explicitly limited to the range 1020 to 60 hPa). The error in cloud pressure is given as a function of cloud pressure and fraction by Acarreta et al. (2004); we add and subtract the given error for each pixel. Acarreta et al. (2004) also indicates that the error in cloud fraction is < 0.05; to transform that to an error in cloud radiance fraction, we use:

$$\sigma_{f_r} = 0.05 \cdot \left.\frac{\partial f_r}{\partial f_g}\right|_{f_{g,\mathrm{pix}}} \tag{E.3}$$

Quantity	Perturbation	Reasoning
Surface reflectivity	±17%	Quadrature sum of 14% LER error and 10% from Schaaf et al. (2010)
Surface pressure	±1.5%	Comparing WRF and BEHR surface pressure
Tropopause presssure	Replace w/NASA tropopause	Alternate method
Cloud pressure	Variable	Fig. 3 of Acarreta et al. (2004)
Cloud radiance fraction	Cloud fraction ±0.05	Acarreta et al. (2004) with correlation of cloud frac. and cloud rad. frac.
Profiles	Quasi-Monte Carlo	Assume variability of model profiles is a reasonable metric

Table E.4: Perturbation of input parameters to the AMF calculation used in the uncertainty analysis.

where f_r is the cloud radiance fraction and f_g the cloud fraction. We determine $\partial f_r / \partial f_g$ at $f_{g,\text{pix}}$ (the cloud fraction of a specific pixel) by binning all f_r and f_g for the current OMI orbit in increments of 0.05 and using that relationship to numerically convert the error in cloud fraction to an error in cloud radiance fraction.

To determine the error due to profile uncertainty, we take advantage of the high spatial and temporal resolution of our WRF-Chem profiles, akin to Boersma et al. (2004). We run two sensitivity retrievals, first allowing the profile to be taken from any day of the same month as the satellite observation, and second allowing each pixel to shift by -0.2, 0, or $+0.2$ degrees in the longitudinal and latitudinal directions for the purpose of matching it with the corresponding NO_2 and temperature profiles. The first is a very conservative simulation of the possible error due to erroneous meteorological drivers (especially wind speed and direction); the second effectively simulates errors in emissions location, chemical kinetics, and transport by moving the pixel so that its profile reflects different aging time since emission.

Figure E.10 shows the summed uncertainty for the four seasons as well as the individual contributions to the uncertainty. In all seasons, the a priori NO_2 profiles dominate the uncertainty. ProfileTime is the largest component in all seasons; the represents the uncertainty due primarily to errors in wind direction and speed, since it is calculated by randomly choosing profiles from a different day of the same month as the OMI data. It is unsurprising that

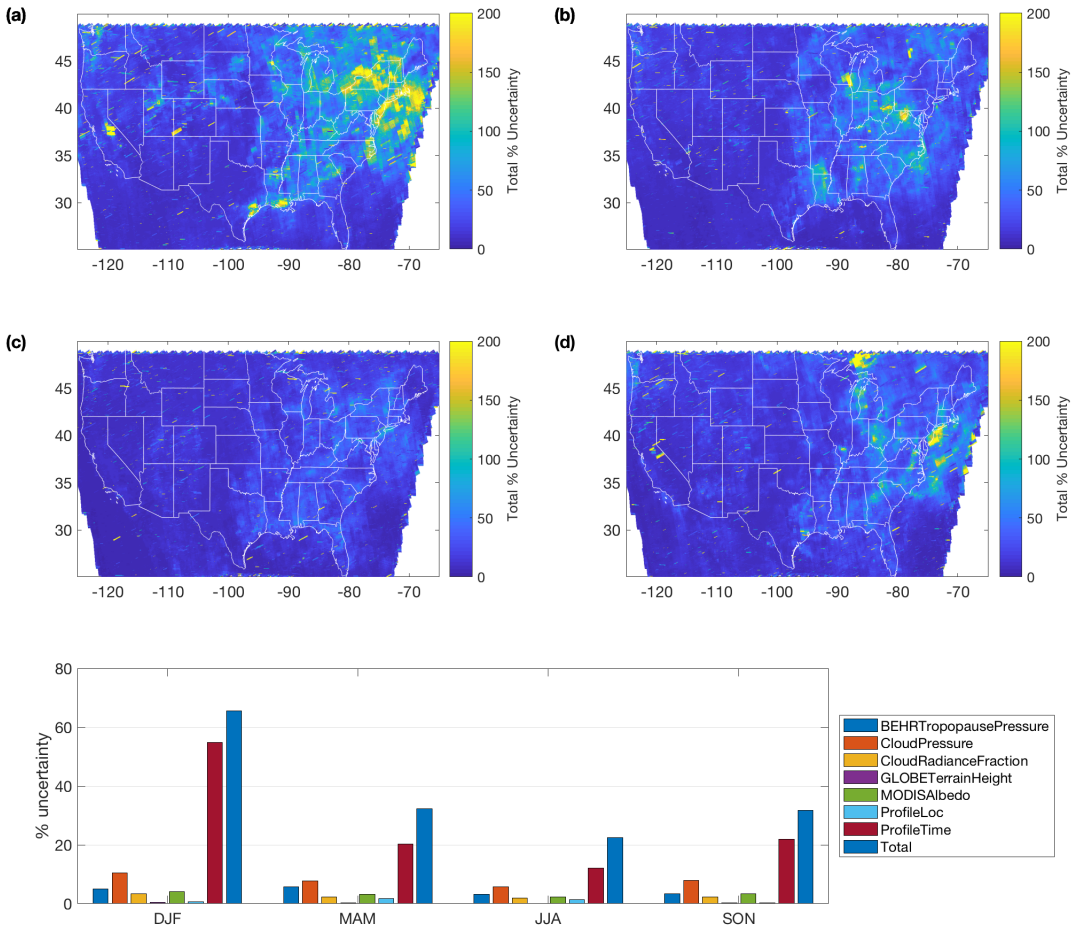

Figure E.10: **(a–d)** Total percent uncertainty in tropospheric NO_2 VCDs for **(a)** Jan, Feb, Dec; **(b)** Mar.–May, **(c)** June–Aug., and **(d)** Sept.–Nov., 2012. **(e)** The domain average effect of each varied parameter and the domain average total uncertainty for the same four time periods.

this is the greatest contributor to uncertainty, since errors in meteorology may completely change the NO_2 profile of any given pixel, i.e. is it downwind of a source or not, as well as the impact of lightning in the SE US. This is a conservative upper bound, as we saw in Sect. 5.3, WRF captures the plume direction well $\sim 70\%$ of the time, whereas the uncertainty analysis essentially assumes that the WRF winds are uncorrelated with the real winds. Reducing the uncertainty by 70% as a rough correction would make it of similar magnitude to the other contributions and significantly reduce the total uncertainty.

The tropopause and cloud pressures are the next two largest contributors to uncertainty in most seasons. Of the non-profile contributors, the retrieval is most sensitive to cloud pressure. The retrieval sensitivity to the other four non-profile parameters is similar (~ 5 to -10%) in all seasons. The tropopause pressure is generally the second largest non-profile contributor to the uncertainty as one of the integration limits in the AMF calculation; the sensitivity of the NO_2 columns to it and the terrain height ($\%\Delta V_{NO_2}/\%\Delta p_{trop}$) are generally similar ($\sim 0.25\%/\%$, not shown), but the greater uncertainty in the tropopause pressure calculation causes it to have the greater impact on the retrieved VCDs.

Overall, the uncertainty due to the AMF calculation is $\sim 70\%$ in the winter, but much smaller ($\leq 30\%$) during the remainder of the year. The 30% uncertainty is similar to that calculated for polluted conditions in Boersma et al. (2004). This seems reasonable, as in winter, longer NO_x lifetime means that more pixels will have high levels of surface NO_2, and getting the wind direction wrong (i.e. what is tested with ProfileTime) will have effects over larger ares. In the summer the error in urban plumes is still important, but over smaller areas. The highest uncertainties are found in the northeast US, which has a significant number of urban areas. Our greater average uncertainty compared to Boersma et al. (2004) likely follows from the greater variability of our 12 km a priori profiles than the $5^\circ \times 3.75^\circ$ used in Boersma et al. (2004).

Data files containing the seasonal average uncertainties may be downloaded at `behr.cchem.berkeley.edu` for users who require spatially varying uncertainty information for their applications.